

# DEVELOPMENT AND APPLICATIONS OF THE NUCLEAR LIGHTHOUSE EFFECT AT HIGH ENERGIES AND AT GRAZING INCIDENCE

Dissertation zur Erlangung des akademischen Grades  
doctor rerum naturalium (Dr. rer. nat.)  
der Mathematisch-Naturwissenschaftlichen Fakultät der Universität Rostock

vorgelegt von

THOMAS ROTH

geb. am 18. August 1972 in Darmstadt,  
aus Grenoble

in Rostock am 2. Mai 2005



# DEVELOPMENT AND APPLICATIONS OF THE NUCLEAR LIGHTHOUSE EFFECT AT HIGH ENERGIES AND AT GRAZING INCIDENCE

Thesis of

THOMAS ROTH

Universität Rostock  
European Synchrotron Radiation Facility

Supervised by:

Prof. E. Burkel,  
Universität Rostock

Dr. R. Ruffer  
European Synchrotron  
Radiation Facility

Dr. R. Röhlberger  
Hamburger Synchrotron-  
strahlungs Labor

Referees of the manuscript:

Prof. S. Sinha,  
University of California  
San Diego

Prof. G. Wortmann  
Universität Paderborn

Prof. E. Burkel

Disputation on the 6<sup>th</sup> of October 2005



# Abstract

The nuclear lighthouse effect (NLE) is a new technique to examine Mössbauer isotopes with synchrotron radiation (SR). It is closely related to nuclear forward scattering (NFS), which is the time based analogon to traditional, energy based Mössbauer spectroscopy. However, in rotating rapidly the sample, which is basis of the NLE, the time response of a NFS experiment is mapped to an angular scale. Interacting photons are deviated according to their interaction time within the rotating sample. In principle, it is an improvement of nuclear forward scattering (NFS), as it permits to apply the rules of NFS, but does not need a certain time structure of the synchrotron radiation.

In this thesis, an experimental setup for NLE measurements was established to investigate two different types of systems. The first system are model  $^{57}\text{Fe}$ -layers in a grazing incidence geometry. This was the first angle-resolved measurement of the NLE in this geometry. The second system is  $^{61}\text{Ni}$  metal. This Mössbauer isotope has a very high transition energy of 67.4 keV. This energy is twice as high as all other isotopes used in NFS or other coherent SR based nuclear resonant measurements so far. The lack of investigations on transitions with high energies is of no surprise, as the Lamb-Mössbauer factor describing the probability of nuclear resonant absorption scales with  $e^{-h^{-2}c^{-2}E_{\gamma}^2\langle x^2 \rangle}$ . Further, high resolution monochromators become difficult to realise at these energies. The NLE does not depend on a huge degree of monochromatisation of the incident radiation, as the non-interacting photons are not deviated into the detector.

This thesis describes the technical developments realised to use the NLE in grazing incidence geometry and at high energies. The latter application depends crucially on an elaborated scheme to cool the rotating sample. The performances of the beamline ID18 at the European Synchrotron Radiation Facility at high energies are presented. Small angle X-ray scattering (SAXS) leads to an undesired background and has to be minimised. Means how to minimise SAXS are presented.

The results obtained for the  $^{57}\text{Fe}$ -layer systems are presented and their magnetic properties deduced. The main emphasis however is given to the  $^{61}\text{Ni}$  resonance. The first spectra ever obtained in coherent nuclear resonant scattering of SR for a Mössbauer isotope with high transition energy is presented. The analysis of these data obtained with the NLE are compared to literature and to results of a further method, synchrotron radiation based perturbed angular correlation (SR-PAC). SR-PAC exploits the incoherent, inelastic decay channel of a nuclear excitation. It does not depend on the Lamb-Mössbauer factor and leads to higher experimental countrates as compared to NFS with a small Lamb-Mössbauer factor. Advantages and drawbacks of these two methods are discussed.



# Contents

<b>Abstract</b>	<b>1</b>
<b>1 Introduction</b>	<b>7</b>
<b>2 Theoretical background</b>	<b>13</b>
2.1 The Mössbauer effect . . . . .	13
2.1.1 Nuclear resonant absorption . . . . .	13
2.1.2 The Lamb-Mössbauer-factor . . . . .	15
2.1.3 Energy conservation and recoil energy . . . . .	18
2.1.4 Scanning the region of nuclear resonant absorption . . . . .	19
2.2 Influences on the energy of nuclear levels: hyperfine interactions . . . . .	21
2.2.1 Isomer shift . . . . .	22
2.2.2 Electric quadrupole interaction . . . . .	23
2.2.3 Magnetic hyperfine splitting . . . . .	25
2.2.4 Mössbauer spectroscopy and line intensities . . . . .	27
2.3 Absorption and scattering . . . . .	29
2.4 Nuclear forward scattering . . . . .	31
2.4.1 Coherent elastic scattering and the nuclear exciton . . . . .	31
2.4.2 Jones matrices and the refractive index of a scattering process . . . . .	32
2.4.3 The nuclear scattering amplitude . . . . .	33
2.4.4 Dynamical beats and speed-up . . . . .	35
2.4.5 Quantum beats . . . . .	36
2.4.6 Distributions of magnetic quantisation axis . . . . .	39
2.4.7 Principal experimental setup of NFS . . . . .	40
2.5 Grazing incidence scattering . . . . .	41
2.6 The nuclear lighthouse effect . . . . .	43
2.6.1 Phase shift upon rotation . . . . .	44
2.6.2 Nuclear lighthouse effect experimental scheme . . . . .	45
2.6.3 Energy shifts . . . . .	46
2.7 Introduction to small angle X-ray scattering . . . . .	47
2.7.1 Scattered intensity and correlation function . . . . .	47
2.7.2 Porod's law . . . . .	48
2.7.3 Single crystals . . . . .	48
<b>3 Investigated samples</b>	<b>49</b>
3.1 $^{61}\text{Ni}$ nuclear parameters . . . . .	49
3.2 $^{61}\text{Ni}$ -metal . . . . .	50
3.3 $^{57}\text{Fe}$ nuclear parameters . . . . .	52
3.4 Magnetic thin films . . . . .	52

3.4.1	$^{57}\text{Fe}$ layer systems . . . . .	53
3.4.2	Waveguides . . . . .	55
3.4.3	Magnetic and electric behaviour of the $^{57}\text{Fe}$ thin films . . . . .	56
<b>4</b>	<b>Experimental aspects</b>	<b>59</b>
4.1	Synchrotron radiation . . . . .	59
4.1.1	History of synchrotron radiation . . . . .	59
4.1.2	An accelerated electron . . . . .	60
4.1.3	Bending magnets, wigglers and undulators . . . . .	61
4.1.4	The ESRF storage ring . . . . .	64
4.2	The beamline ID18 . . . . .	65
4.2.1	Flux at high energies . . . . .	65
4.2.2	Monochromatisation . . . . .	67
4.2.3	Focussing and collimation with compound refractive lenses . . . . .	69
4.2.4	High resolution monochromatisation . . . . .	71
4.2.5	ID18 layout for the nuclear lighthouse effect and SR-PAC . . . . .	73
4.3	Spinning of the sample . . . . .	76
4.3.1	Stators and rotors . . . . .	76
4.3.2	Stability issues . . . . .	78
4.3.3	The lighthouse tower . . . . .	80
4.4	Cooling . . . . .	81
4.4.1	Cooling method . . . . .	81
4.4.2	Stator modifications . . . . .	82
4.4.3	Gas flows and cooling . . . . .	84
4.4.4	Top cooling . . . . .	85
4.5	Detectors . . . . .	86
4.5.1	Photon detection for nuclear resonant scattering . . . . .	86
4.5.2	Avalanche photo diode array . . . . .	88
4.5.3	APD signal electronics . . . . .	89
4.5.4	Position sensitive APD detectors or scanning detectors . . . . .	90
4.6	Beamstop and in-vacuum flux monitor . . . . .	91
<b>5</b>	<b><math>^{57}\text{Fe}</math>-layer measurements in grazing incidence</b>	<b>93</b>
5.1	13 Å thin $^{57}\text{Fe}$ layer in an aluminium and tantalum sandwich . . . . .	94
5.1.1	Electronic and nuclear reflectivity curves . . . . .	94
5.1.2	Nuclear response . . . . .	96
5.1.3	Fitting with NFS theory . . . . .	97
5.1.4	Fitting with the grazing incidence extension to CONUSS . . . . .	98
5.2	medium thick ( $\approx 75$ Å) $^{57}\text{Fe}$ layer . . . . .	100
5.2.1	Electronic and nuclear reflectivity curves . . . . .	100
5.2.2	Nuclear response . . . . .	101
5.2.3	Fitting of the nuclear response . . . . .	102
5.3	thick ( $\approx 178$ Å) $^{57}\text{Fe}$ layer . . . . .	104
5.3.1	Electronic and nuclear reflectivity curves . . . . .	104
5.3.2	Nuclear response . . . . .	105



<b>6</b>	<b>Nuclear lighthouse effect with <math>^{61}\text{Ni}</math></b>	<b>109</b>
6.1	Flux at ID18 at the $^{61}\text{Ni}$ resonance energy . . . . .	109
6.2	The energy of the first excited nuclear level of $^{61}\text{Ni}$ . . . . .	113
6.3	The lifetime of the 67.41 keV level of $^{61}\text{Ni}$ . . . . .	115
6.4	Nuclear lighthouse effect in transmission with $^{61}\text{Ni}$ . . . . .	116
6.4.1	Brief experimental review . . . . .	116
6.4.2	NLE time/angle spectra of $^{61}\text{Ni}$ and background evaluation . . . . .	117
6.4.3	Results at 180 K . . . . .	118
6.4.4	Results at 115 K . . . . .	119
6.4.5	Measurements without timing electronics for the lighthouse signal . . . . .	121
<b>7</b>	<b>SR-PAC with <math>^{61}\text{Ni}</math></b>	<b>125</b>
7.1	Nuclear levels important for TD-PAC and SR-PAC . . . . .	125
7.2	Theory of synchrotron radiation based perturbed angular correlation . . . . .	126
7.2.1	Differential angular probability of scattering . . . . .	126
7.2.2	Isotropic hyperfine interactions . . . . .	129
7.2.3	External magnetic field $\vec{B}_{ext}$ . . . . .	129
7.2.4	Special orientations of the external magnetic field $\vec{B}_{ext}$ . . . . .	130
7.3	Measurements . . . . .	131
7.4	Discussion . . . . .	133
<b>8</b>	<b>Nuclear resonant scattering with high energy Mössbauer transitions</b>	<b>135</b>
8.1	Experimental milestones . . . . .	135
8.2	Overview of Mössbauer isotopes . . . . .	135
8.3	New Mössbauer isotopes to be addressed with SR . . . . .	139
8.3.1	NLE isotopes . . . . .	139
8.3.2	SR-PAC isotopes . . . . .	141
<b>9</b>	<b>Conclusions and outlook</b>	<b>145</b>
	<b>Bibliography</b>	<b>149</b>
	<b>Acknowledgements</b>	<b>159</b>
	<b>Eidesstattliche Erklärung</b>	<b>163</b>
	<b>Curriculum Vitæ</b>	<b>165</b>



# Chapter 1

## Introduction

The aim of this thesis is the development of a recently introduced nuclear resonant scattering technique and its application to high energies and in grazing incidence geometry: the nuclear lighthouse effect. The roots of nuclear resonant scattering (NRS) date back to the late fifties.

In 1958 R. Mössbauer examined the nuclear resonant absorption of  $\gamma$ -rays in  $^{191}\text{Ir}$ . He found out that, with decreasing temperature, resonant absorption increased contrary to what was expected. His interpretation of the experiment based on works on neutron absorption by Lamb [Lam39] and Wigner and Breit [Bre36], leading to the picture of “recoilless absorption”. Although first discovered in  $^{191}\text{Ir}$ , many other isotopes proved to show the effect, the most prominent one being  $^{57}\text{Fe}$ . The effect, now called the Mössbauer effect, soon became a new spectroscopic tool to study the electronic and magnetic properties of solids via the hyperfine interactions at the Mössbauer nuclei, e.g. magnetic hyperfine fields or valence states in chemical bonds. In fact, it was immediately widely used in physics, chemistry, material science and biology [Güt78]. The sources of the  $\gamma$ -rays are radioactive mother isotopes, that are sometimes hard to obtain or impractical. With the construction of synchrotrons, the idea to excite the nuclear levels with synchrotron radiation (SR) emerged [Rub74]. The theoretical treatment of the physics involved in such an experiment was soon developed [Tra78, Kag78, and references therein for earlier work not specific to synchrotron radiation excitation].

As the natural linewidth of nuclear levels is extremely small (in the range from neV to  $\mu\text{eV}$ ), especially as compared to the typical energetic width of undulator generated synchrotron radiation (in the order of several eV), special experimental measures have to be taken in order to extract the nuclear signal from the background of non-interacting or electronically scattered photons. One is to maximise the ratio of resonant photons (i.e. photons having an energy within the natural linewidth of the nuclear transition) to overall photons. Another one is the use of a pulsed time structure of the incoming synchrotron radiation. Then, the delayed de-excitation of the excited nuclei can be observed during the absence of non-interacting or electronically scattered photons.

The first successful observation of nuclear resonant scattering with SR was achieved in 1985 [Ger85] using yttrium iron garnet single crystals containing  $^{57}\text{Fe}$ . Properties of the  $^{57}\text{Fe}$  sites in these crystals were investigated using a nuclear Bragg reflection, that is an electronically forbidden Bragg reflection, which is nonetheless allowed by a different orientation of nuclear  $^{57}\text{Fe}$  scatterers in different lattice sites. Accordingly, this type of measurements was named nuclear Bragg scattering (NBS). It is an efficient means to

extract the interacting photons from the energetically broad pulse of incoming synchrotron radiation.

With increasing quality of monochromator crystals and thanks to faster detectors, another approach became possible, which is no longer restricted to nuclear Bragg reflections of single crystals: Nuclear forward scattering (NFS) [Has91]. Coherently scattered photons are allowed for all crystalline and non-crystalline solids in the forward direction (i.e. the direction of the incoming wavevector  $\vec{k}$ ). The transmission of a synchrotron radiation pulse through such a sample is characterised by a prompt pulse of photons that did not interact with the nuclei and by a delayed signal of nuclear resonant scattering. The time discrimination of the detector signal permits its separation.

Yet, the incident radiation had to have a very well defined time structure with a sharp peak in intensity followed by a huge gap of zero intensity. This type of filling is sometimes realised in synchrotron radiation storage rings. At the ESRF, these are principally the 16 bunch and the single bunch fillings and represent about a quarter of available measurement time [ESRFa]. In 1996, a group of scientists examined X-ray optics for  $\mu\text{eV}$ -resolved spectroscopy [Röh97]. During these experiments, they observed that the phase of the nuclear excitation turns with the sample itself, if the latter is subject to a rotation. The de-excitation proceeds deviated into a certain angle as compared to the forward direction. In fact, in this case the time evolution of the decay of NFS is mapped on an angular scale. Increasing angles correspond to increasing times, and this independently from the time structure of the incident radiation. The effect became known as the nuclear lighthouse effect (NLE) [Röh99c]. Apart from the independence from the time structure of the incident radiation, the second feature of greatest importance is the separation of nuclear scattered photons and non-interacting or electronically scattered photons in space. Whereas the first are deviated off axis to the side, the latter -to a large majority- stay on the beam axis and proceed undeviated. Monochromatisation schemes like for NFS can become much less important. The first measurements demonstrating the power of this approach have been carried out with  $^{57}\text{Fe}$ ,  $^{149}\text{Sm}$  and  $^{119}\text{Sn}$  in transmission geometry [Röh00c, Röh01c, Röh01d]. As the NLE does not depend on the synchrotron radiation time structure, but obeys the rules of NFS nevertheless, it is in that respect an improvement of that last technique. Electronically scattered photons that do not stay on the beam axis originate mostly from small angle X-ray scattering (SAXS) and constitute unfortunately an undesired background to the delayed signal.

NFS and the NLE are valuable tools to investigate hyperfine interactions, as is the Mössbauer effect. Further, also dynamics like relaxation and diffusion [Leu99, Vog99, Ast01, Ser02] can be addressed with this technique. Another development of NRS to study dynamics is nuclear inelastic scattering (NIS), discovered in 1995 [Set95], which allows to measure the density of phonon states in solids and liquids [Bur00]. Despite the variety of applications of NRS, a remark often heard about NRS is the limitation to a small number of Mössbauer isotopes that are investigated in experiments. By far the most used samples contain  $^{57}\text{Fe}$ , as was the case already in traditional Mössbauer spectroscopy. But other isotopes have been addressed with SR, too.  $^{181}\text{Ta}$ ,  $^{169}\text{Tm}$ ,  $^{83}\text{Kr}$ ,  $^{151}\text{Eu}$ ,  $^{149}\text{Sm}$ ,  $^{119}\text{Sn}$ ,  $^{161}\text{Dy}$ ,  $^{40}\text{K}$ ,  $^{129}\text{I}$  and  $^{121}\text{Sb}$ . Other isotopes have just been excited and their delayed decay was observed:  $^{127}\text{I}$ ,  $^{197}\text{Au}$ . Before this thesis,  $^{61}\text{Ni}$  belonged to this category, too. For an overview and references concerning these isotopes, see chapter 8.  $^{61}\text{Ni}$  was first used in traditional Mössbauer spectroscopy by Obenshain and Wegener [Obe61]. Due to its manifold applications in magnetism and biology, it was hoped to

access this transition also with SR. Efforts by Wille *et al.* [Wil02, Ger02] did not pass the step of simply exciting the level and observing the following nuclear fluorescence. This thesis presents the first spectroscopic measurement with  $^{61}\text{Ni}$  at a synchrotron, using the nuclear lighthouse effect. It further presents first results with  $^{61}\text{Ni}$  using synchrotron radiation based perturbed angular correlation (SR-PAC), which will be explained later on in this introduction.

Nickel is a very interesting isotope for Mössbauer investigations: like iron, it exists in different valences, it shows various magnetic behaviours and it plays a key role as active centre of biomolecules [Lan88, Hau97]. Unfortunately, the use of Mössbauer spectroscopy is very much hampered by the lack of a suitable radioactive mother isotope. The two possible sources are  $^{61}\text{Co}$  with a lifetime of only 99 minutes and  $^{61}\text{Cu}$  with a lifetime of 200 minutes. The only group involved sporadically in Mössbauer spectroscopy with  $^{61}\text{Ni}$  at present is the group of Prof. Gütlich in Mainz, Germany, having the possibility to activate their sources with a nearby accelerator. A few other groups did so in the past. In the beginning, nuclear properties of  $^{61}\text{Ni}$  [Weg61, Spi68, Lov68, Eri69] and possible Mössbauer sources [Sey65, Amb69] were the main interest of the investigations. Then, most research has been on electron configurations via the isomer shift and the electric quadrupole splitting in molecules of chemical interest [Obe76, Dal79, Jan96, Got98, Güt99], the nickel contribution to magnetism in metallic alloys [Lov71, Tan72, Gör73, Tom77, Luk85] or spinel type magnetic oxides [Güt84, Gry89, Oka95] and hyperfine interactions at the copper sites of superconductors via  $^{61}\text{Cu}$ ( $^{61}\text{Ni}$ ) emission Mössbauer spectroscopy [Mas98]. Also the contribution of the nickel nuclei to the magnetism of metallic glasses and amorphous alloys [Sos81, Sta89], phase transitions in pyrites containing nickel [Kri76] and surface magnetism of nickel [Sta88] have been investigated. Very little results in the domain of material science [Rum82, Kse02] and biology [Jan96] are published, to finish this almost comprehensive picture of the literature available on  $^{61}\text{Ni}$  Mössbauer spectroscopy.

Another obstacle in Mössbauer spectroscopy with  $^{61}\text{Ni}$  is the Lamb-Mössbauer factor, that strongly decreases at high transition energies and with increasing temperature (see equation 2.21). As the transition energy of the  $^{61}\text{Ni}$  Mössbauer level is fixed at 67.41 keV, it is therefore indispensable to cool the sample. In traditional Mössbauer spectroscopy, this is done down to 4 K. Using the nuclear lighthouse effect and thus a sample that spins inside a gas bearing and driven by another gas flow, these temperatures are out of reach. The stator-rotor system with its tolerances is conceived for ambient temperature. Nevertheless, we can finally report the feasibility to cool the sample down to 100 K. During the development of a functional cooling scheme, several options were thought of and also led to an approach with the spinning sample sticking out of the stator block, allowing for an "external" cooling. Although rotors having a hollow sample chamber at their outer end became too brittle and broke repeatedly in this region, the method of having the sample at the outer end of the rotor was maintained for a different idea: measurements in grazing incidence geometry on surface samples.

$^{57}\text{Fe}$  layers allow the creation of manifold systems to study magnetic behaviour in reduced dimensions (e.g. interfaces and layer structures) [Bla94]. NFS in grazing incidence geometry [Röh99b] with  $^{57}\text{Fe}$  has led to remarkable results in this field of research [Chu99, Röh03, Röh04b]. This technique can be combined with the NLE. We therefore went on to conceive bulk rotors with a polished top surface, which were covered with layered structures containing  $^{57}\text{Fe}$ . The advantage of the grazing incidence geometry is the fact that no sample container, e.g. the rotor walls, has to be passed by the synchrotron radiation. The rotor walls represent a key part of the SAXS background, that tends to

obscure the nuclear resonant signal, as it is likewise deviated into the same angular range. Our measurements with the nuclear lighthouse effect in grazing incidence geometry on these systems are the first of their kind.

Unfortunately in both cases ( $^{61}\text{Ni}$  sample in transmission geometry and  $^{57}\text{Fe}$  surface layers) the SAXS, coming either from the transmitted sample and rotor wall or from the surface roughness of the sample, turned out to be too big, if no further measures had been taken. Luckily, SAXS is a scattering effect on a prompt time scale as compared to nuclear resonant scattering. If the synchrotron is filled in "timing mode", an electronic gating of the detector or the amplifiers allows to distinguish between prompt SAXS and delayed nuclear resonant scattering. (Prompt non-interacting photons are not deviated and do not need to be suppressed by electronics.) The drawback is the loss of a main advantage of the NLE, namely its principal independence of the filling mode of the synchrotron. For grazing incidence measurements with  $^{57}\text{Fe}$  layered structures, it is therefore advantageous to use the less problematic NFS setup with sophisticated, but available and reliable high resolution monochromators. However, to perform coherent nuclear resonant measurements with  $^{61}\text{Ni}$ , NFS is *no* alternative, as sophisticated monochromatisation schemes do not work at photon energies above 30 or 40 keV, if Bragg backscattering is used. The angular acceptance of Bragg reflections at these energies is too low to match the angular divergence of current synchrotron sources. But without sophisticated monochromatisation and in forward geometry, the ratio of nuclear resonant photons to overall photons is too bad even for modern detectors. Here, the separation in space with the NLE is the only method to overcome this problem to date.

Only recently [Ser04], a further nuclear scattering technique has been reactivated. After exciting a set of individual nuclei with synchrotron radiation, their exponential decay is slightly modulated in time and angle, if the excited level consists of several sublevels that interfere. It was first observed in 1996 and then called single nucleus quantum beats [Bar96]. It is in fact an incoherent process, therefore involving just individual nuclei. Due to the angular behaviour of the decay, nowadays the effect is termed synchrotron radiation based perturbed angular correlation (SR-PAC). In time differential perturbed angular correlation, a radioactive source decays into an excited state of nuclei showing a further intermediate level between the primary excited state and the ground state. An angular correlation between the two subsequent decays of the investigated nuclei provides information about its hyperfine interactions. Here, the radioactive source and the first step of the two-stepped decay is replaced by the synchrotron and the direction of the incoming radiation. No three level system is needed anymore. Possible candidates for this technique are thus all Mössbauer isotopes. The great advantage in the context of energetically high lying nuclear levels like in the case of  $^{61}\text{Ni}$  is its independence from the Lamb-Mössbauer factor. The Lamb-Mössbauer factor decreases with increasing energy and temperature. So far, SR-PAC was used to investigate  $^{57}\text{Fe}$  samples, but the advantages cited above made it obvious to apply it to  $^{61}\text{Ni}$ . The interference structure on top of the exponential decay reveals the hyperfine splitting of the excited state. The magnetic hyperfine field of  $^{61}\text{Ni}$  was thus determined by an alternative method.

NLE and SR-PAC can be complementary. Especially the NLE is sensitive to a splitting of the nuclear ground state. On the other side, SR-PAC works in the region of vanishing Lamb-Mössbauer factor. If this factor becomes bigger, SR-PAC data will be disturbed by the propagation of the coherent wave field in the sample. Both methods, NLE and SR-PAC, will hopefully allow to address still other isotopes with synchrotron radiation in the near future. A few isotopes seem to be in reach.

This thesis continues as follows: chapter 2 introduces the theory of nuclear resonant experiments and the hyperfine interactions. After focussing on the Mössbauer effect, it treats especially the nuclear scattering technique and finishes with non-resonant SAXS. Chapter 3 presents the different types of samples used and the nuclear properties of  $^{57}\text{Fe}$  and  $^{61}\text{Ni}$ . Chapter 4 shows in detail the experimental setup used for the experiments, in particular the lighthouse setup. It further explains synchrotron relevant instrumentation. Chapter 5 presents nuclear resonant scattering in grazing incidence geometry on  $^{57}\text{Fe}$  layers. It compares NLE results with the standard method of grazing incidence on a stationary sample. Chapter 6 starts with flux and energy considerations at the  $^{61}\text{Ni}$  energy and treats the measurements obtained on the  $^{61}\text{Ni}$  with the NLE in transmission. Alternative results are obtained using SR-PAC measurements with  $^{61}\text{Ni}$  which are presented in a separate chapter 7, together with a short theoretical part. The question whether the techniques of NLE and SR-PAC can be applied to other Mössbauer isotopes with a high transition energy is elucidated in chapter 8 including an overview over past and present Mössbauer isotopes addressed with SR. The conclusions to take from this work are drawn in chapter 9.





## Chapter 2

# Theoretical background

The main interest of this chapter is to review the theory of coherent nuclear resonant scattering. It starts with the Mössbauer effect, which historically was the starting point of nuclear resonance investigations in solid state physics. Then, with the advent of powerful synchrotron light sources, nuclear forward scattering (NFS) and recently the nuclear lighthouse effect (NLE) developed, as the time-based analogon of the energy domain Mössbauer spectroscopy. Both depend on the coherence of the scattering process, thus on its elastic behaviour. Into the same category falls grazing incidence scattering on thin films containing Mössbauer isotopes, which will be discussed as well. In the case of the  $^{61}\text{Ni}$  isotope, it turned out that nuclear lighthouse experiments are rather difficult, as compared to investigations of the isotope with synchrotron radiation based perturbed angular correlation (SR-PAC). This technique exploits the incoherent, inelastic scattering channel of the nuclear excitation, especially the deviation from an exponential decay. It will be discussed later in the dedicated chapter 7. Of further interest is small angle X-ray scattering (SAXS), which presents an undesired background in NLE experiments. An introduction to SAXS is found at the end of this chapter.

### 2.1 The Mössbauer effect

#### 2.1.1 Nuclear resonant absorption

Nuclear resonant absorption of photons treats subsequent absorption and re-emission of a photon by nuclei. An important issue concerning this effect is the recoil of the nucleus after emission, or absorption, of a photon. Let's consider a free nucleus. Apart from its ground state, where all its nucleons occupy the energetically lowest configuration allowed by the Pauli-principle, a variety of excited states exist, which can be reached by supplying energy, e.g. by electromagnetic radiation or through the decay of a radioactive mother-isotope [May94]. An excited nucleus of energy  $E_e$  will decay into a lower level  $E_g$ , e.g. its ground state, after a characteristic time, the mean lifetime  $\tau_o$  of this excited level. The difference in energy is  $E_o = E_e - E_g$ . This decay can be radiative. The energetic width  $\Gamma_o$  of the level and the lifetime are correlated via the Heisenberg's uncertainty principle:

$$\Gamma_o = \frac{\hbar}{\tau_o} \quad (2.1)$$

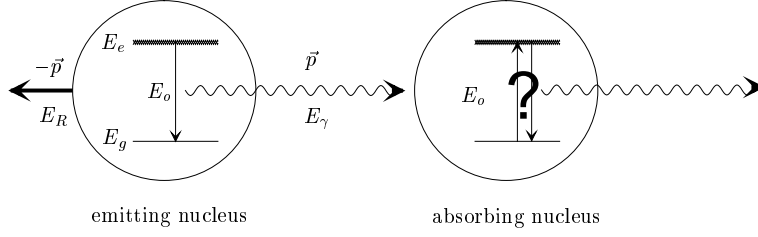


Figure 2.1: Principle of resonant absorption

The energy distribution  $N(E)$  of photons emitted by such nuclei is of Lorentzian shape with  $\Gamma_o$  being the full width at half maximum. A photon carries a momentum  $p = E_\gamma/c$ , which has to be balanced by the emitting free nucleus, due to momentum conservation. Therefore, the nucleus of mass  $m$  recoils with an energy

$$E_R = \frac{p^2}{2m} = \frac{E_\gamma^2}{2mc^2} \quad (2.2)$$

The Lorentzian energy distribution of the emitted photons is thus centred around the reduced value  $E_\gamma = E_o - E_R$ :

$$N(E) = N_o \frac{\left(\frac{\Gamma_o}{2}\right)^2}{(E - (E_o - E_R))^2 + \left(\frac{\Gamma_o}{2}\right)^2} \quad (2.3)$$

The same accounts for the absorption of photons by nuclei. The incoming photons have to provide a surplus of energy needed for the recoil of the absorbing nuclei:  $E_\gamma = E_o + E_R$ . Thus, energy dependant absorption cross section,  $\sigma(E)$  is centred at an increased value  $E_o + E_R$ :

$$\sigma(E) = \sigma_o \frac{\left(\frac{\Gamma_o}{2}\right)^2}{(E - (E_o + E_R))^2 + \left(\frac{\Gamma_o}{2}\right)^2} \quad (2.4)$$

Resonant absorption is only possible, if both distributions 2.3 and 2.4 overlap at least partly. This is not the case for a free nucleus at rest: A prominent example is  $^{57}\text{Fe}$  with  $E_\gamma = 14.4$  keV, leading to a recoil energy  $E_R = 2 \cdot 10^{-3}$  eV. Its mean lifetime is  $\tau_o = 141$  ns, which translates into a natural linewidth  $\Gamma_o = 4.7 \cdot 10^{-9}$  eV. Hence, there is no overlap.

Things change, if we consider thermal motion of the nuclei, like in gases and liquids. Due to the Doppler shift, the widths of 2.3 and 2.4 increase, as thermal velocities are distributed over a wide range according to the Maxwell distribution. Thermal velocities correspond to kinetic energies in the range of  $E_R$ , so some overlap between 2.4 and 2.3 will be observed at the center  $E_o$ . The probability of resonant absorption stays nevertheless small, as just the flanks overlap.

Nuclei in a crystal structure are bound. While absorbing a photon, a nucleus cannot recoil freely, as  $E_R$  is smaller than typical binding energies (several eV). Energy might be transferred to excite lattice vibrations, phonons. The energy of phonons in a crystal is in the order of recoil energies of a free nucleus. Nevertheless, with a certain probability, the absorption or emission of photons can occur without changing the phonon state of the system. Then, the recoil has to be taken by the crystal as a whole. The mass of the crystal  $M$  is comparatively huge and  $E_R = \frac{E_\gamma^2}{2Mc^2}$  is negligible. The energy of the emitted or absorbed photon then matches the energy of the nuclear transition, the difference between ground and excited state:  $E_\gamma = E_o = E_e - E_g$ . Nuclear resonant absorption can

take place. It has been observed first in 1958 by Rudolf Mössbauer and is therefore called the Mössbauer effect [Möb59][Möb58, theory]. The probability for transitions without phonon interaction, zero-phonon  $\gamma$ -transitions, is called the Lamb-Mössbauer-factor  $f_{\text{LM}}$  [Lam39]. Although confusing, one speaks about the recoilless fraction. Remember that there is still a recoil, only it is taken by the crystal as a whole and does not lead to a perceptible energy shift of the  $\gamma$ -ray.

### 2.1.2 The Lamb-Mössbauer-factor

It is evident that the knowledge of the Lamb-Mössbauer-factor is of great importance for nuclear resonant scattering. We will first calculate it using classical physics [Bar80, Fra63] and investigate a moving emitter of electromagnetic radiation. The result for the Lamb-Mössbauer factor turns out to be the same as obtained with the correct quantum mechanical treatment. This is surprising, as recoil losses do not appear in the classical picture of a radiating emitter. Nevertheless, the temperature dependence in this approach is not satisfactory. The transition to quantum mechanics will be sketched later.

Imagine a nucleus at rest bound in a crystal at zero temperature, emitting continuously radiation of energy  $E_\gamma = \hbar\omega_o$ . The vector potential is then:

$$A(t) = A_o e^{i\omega_o t} \quad \text{with: } |A_o|^2 = 1 \quad (2.5)$$

At higher temperatures, the nucleus oscillates around its equilibrium position. The frequency changes:  $\omega(t) = \omega_o(1 + \frac{v(t)}{c})$ , with  $v$  being the non-relativistic velocity of the nucleus. The vector potential becomes:

$$A(t) = A_o e^{i\int_o^t \omega(t')dt'} = A_o e^{i\omega_o t} e^{ikx(t)} \quad (2.6)$$

$x$  is the displacement of the nucleus and  $k = |\vec{k}| = \frac{\omega_o}{c}$  the wave vector of the emitted radiation. If we apply the Einstein model of lattice vibrations, we assume only one vibration frequency of the lattice  $\Omega$  and replace  $x(t) = x_o \sin \Omega t$ , obtaining:

$$A(t) = A_o e^{i\omega_o t} e^{ikx_o \sin \Omega t} \quad (2.7)$$

Introducing the Bessel function with  $e^{ikx_o \sin \Omega t} = \sum_{n=-\infty}^{\infty} J_n(kx_o) e^{in\Omega t}$ , we get:

$$A(t) = A_o \sum_{n=-\infty}^{\infty} J_n(kx_o) e^{i(\omega_o + n\Omega)t} \quad (2.8)$$

The frequency spectrum of the emitted radiation splits thus into the frequencies  $\omega_o$ ,  $\omega_o \pm \Omega$ ,  $\omega_o \pm 2\Omega$ , .... The unshifted central line with  $n = 0$  is the line of zero-phonon  $\gamma$ -transition. It's intensity is given by

$$f = |A_{n=0}|^2 = J_o^2(kx_o) \quad (2.9)$$

If we consider a real crystal with  $N$  atoms, there exist  $3N$  independent vibration modes. The displacement of the emitter  $x(t)$  in the exponent of equation 2.6 is the sum of the different components:  $x(t) = \sum_m^{3N} x_m \sin \Omega_m t$ . For  $f$  we now obtain:

$$f = \prod_{m=1}^{3N} J_o^2(kx_m) \quad (2.10)$$

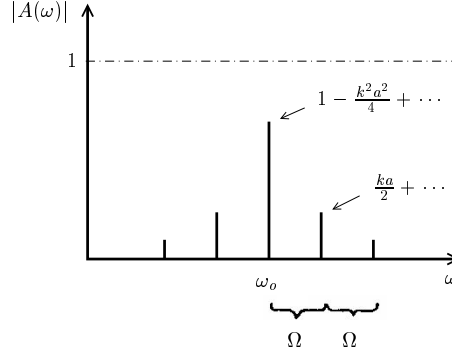


Figure 2.2: Model of a classical oscillating emitter [Sch92]

As  $f$  cannot exceed 1, and  $3N$  is large, each factor of 2.10 is close to 1, also the amplitudes  $x_m$  are very small. Then, we can develop the Bessel function as a series  $J_0(kx_m) = 1 - \frac{1}{4}(kx_m)^2 + \dots$  and stop after the quadratic term. We calculate:

$$\ln f = 2 \sum_{m=1}^{3N} \ln J_0(kx_m) \approx 2 \sum_{m=1}^{3N} \ln \left( 1 - \frac{k^2 x_m^2}{4} \right) \quad (2.11)$$

We use  $\ln(1 + a) = a - \frac{1}{2}a^2 + \dots$  and introduce the mean square displacement  $\langle x^2 \rangle = \frac{1}{2} \sum_m x_m^2$  to obtain:

$$\ln f \approx -2 \sum_{m=1}^{3N} \frac{k^2 x_m^2}{4} = -k^2 \langle x^2 \rangle \quad (2.12)$$

This is even exact for the limit  $N \rightarrow \infty$ . The value is called the Lamb-Mössbauer factor.

$$f_{\text{LM}} = e^{-k^2 \langle x^2 \rangle} \quad (2.13)$$

The quantum mechanical result is very similar, we just have to interpret  $\langle x^2 \rangle$  in terms of probability amplitudes. We can already see the following: To have a significant value for  $f_{\text{LM}}$ , we need  $k^2 \langle x^2 \rangle \ll 1$ . The nuclei need to be bound, e.g. in a crystal or in an amorphous solid. It further implies that the wave vector shouldn't be too big, which translates to an upper limit of the  $\gamma$ -energy  $E_\gamma = \hbar c k$ , for traditional Mössbauer spectroscopy below 200 keV. For nuclear resonant scattering with synchrotron radiation, this limit is much lower due to technical problems, as we will discuss in chapter 4. As it decreases the atom displacements and thus  $\langle x^2 \rangle$ , cooling will help to increase the resonant fraction  $f_{\text{LM}}$ .

When considering aspects of quantum mechanics, two problems arise from our preceding treatment. First, even at zero temperature, oscillations in a crystal exist. Second, the  $\gamma$ -ray emission is not continuously, but implies a  $\gamma$ -quantum, a photon. It carries a recoil that we did not consider above. A very nice way of introducing quantum mechanics at this point is given in [Weg66, chapter 2 and 3]. Here, we will just replace the energy of a classical oscillator by the energy of a quantum mechanical oscillator to obtain the right temperature dependence of the Lamb-Mössbauer factor [Sch92].

The energy of a one dimensional classical oscillator with  $x_m$  being its maximum displacement is given by  $E_{cl} = \frac{1}{2}m\Omega^2 x_m^2$ . The mean square displacement is  $\langle x^2 \rangle = \frac{1}{2}x_m^2$ . Thus

$$E_{cl} = m \Omega^2 \langle x^2 \rangle \quad (2.14)$$

In quantum mechanics, the energy of a harmonic oscillator being in the state  $n$  is

$$E_{qm} = \hbar\Omega \left( n + \frac{1}{2} \right) \quad (2.15)$$

In a large set of identical oscillators, each energy level  $n$  is occupied with a probability  $P_n$  according to Bose-Einstein statistics.

$$P_n = \frac{e^{-\frac{n\hbar\Omega}{k_B T}}}{\sum_n e^{-\frac{n\hbar\Omega}{k_B T}}} \quad (2.16)$$

We compare the classical and the quantum mechanical energy of one oscillator. For the quantum mechanical oscillator, we average over all possible states  $n$ :

$$m\Omega^2 \langle x^2 \rangle = \hbar\Omega \left( \sum_{n=0}^{\infty} n P_n + \frac{1}{2} \right) \quad (2.17)$$

Combining 2.16 and 2.17 we thus get the desired expression for the mean quadratic displacement of the atoms of the crystal:

$$\langle x^2 \rangle_E = \frac{\hbar}{2m\Omega} \left( 1 + \frac{2}{e^{\frac{\hbar\Omega}{k_B T}} - 1} \right) \quad (2.18)$$

The index  $E$  standing for the Einstein model of lattice vibrations. If we assume a general distribution of phonon frequencies,  $Z(\Omega)$  with  $\int Z(\Omega) d\Omega = 3N$ , with  $N$  being the number of atoms in the lattice, we obtain:

$$\langle x^2 \rangle = \frac{1}{3N} \int_0^{\infty} Z(\Omega) \langle x^2 \rangle_E d\Omega = \frac{\hbar}{6mN} \int_0^{\infty} \frac{Z(\Omega)}{\Omega} \left( 1 + \frac{2}{e^{\frac{\hbar\Omega}{k_B T}} - 1} \right) d\Omega \quad (2.19)$$

If the phonon density of states is known, it is thus possible to calculate the Lamb-Mössbauer factor. A good approximation for an unknown density of states is given by the Debye model of lattice vibrations with

$$Z(\Omega) = \frac{9N\hbar^3}{k_B^3} \frac{\Omega^2}{\Theta_D^3} \quad \text{for } \Omega < \Omega_D = \frac{k_B \Theta_D}{\hbar} \quad \text{and } Z(\Omega) = 0 \quad \text{above} \quad (2.20)$$

$\Theta_D$  is the Debye temperature. Combining 2.19 and 2.20 and using  $f_{\text{LM}} = e^{k^2 \langle x^2 \rangle}$ , we are able to find the Lamb-Mössbauer factor as a function of temperature:

$$f_{\text{LM}} = e^{-\frac{3\hbar^2 k^2}{mk_B \Theta_D} \left( \frac{1}{4} + \frac{T^2}{\Theta_D^2} \int_0^{\Theta_D/T} \frac{y}{e^y - 1} dy \right)} \quad (2.21)$$

For low temperatures  $T \ll \Theta_D$  we get:

$$f_{\text{LM}} = e^{-\frac{3\hbar^2 k^2}{4mk_B \Theta_D} \left( 1 + \frac{2\pi^2}{3} \frac{T^2}{\Theta_D^2} \right)} \quad (2.22)$$

We state again that neither  $E_\gamma = \hbar c k$  nor  $T$  should be too large, in order to have a significant  $f_{\text{LM}}$  value. For  $T$ , we appreciate  $T \ll \Theta_D$ . Especially when investigating Mössbauer isotopes of large transition energy  $E_\gamma$ , like in the case for the 67.14 keV transition of  $^{61}\text{Ni}$ , cooling becomes a must when investigating coherent nuclear forward scattering. As we will see in chapter 2.4, this method depends on  $f_{\text{LM}}^2$ . This is not the case for nuclear inelastic scattering or synchrotron radiation based perturbed angular correlation.

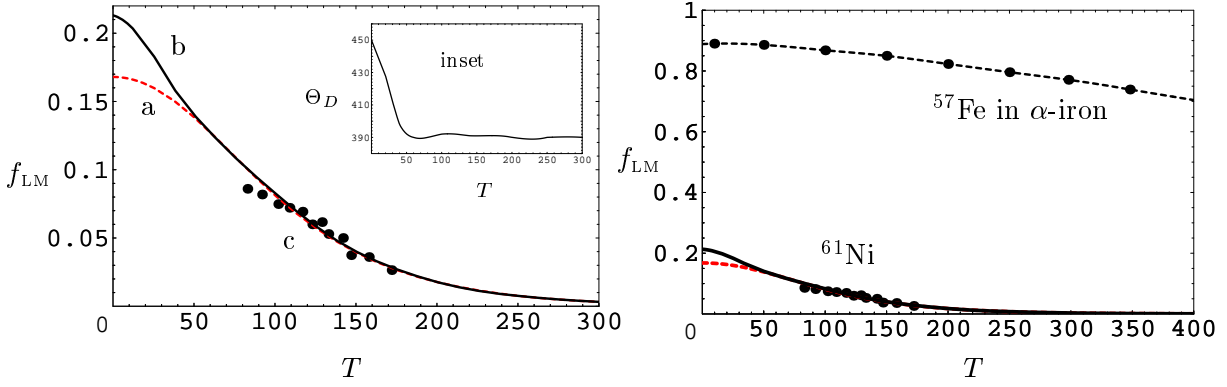


Figure 2.3: The Lamb-Mössbauer-factor in  $^{61}\text{Ni}$  metal <sup>a)</sup> following the Debye model with  $\Theta_D = 390\text{ K}$ , <sup>b)</sup> with a variable Debye temperature as shown in the inset and <sup>c)</sup> measured [Obe61]. Results of the inset taken from [Bir64]. On the right a comparison to  $f_{LM}$  of  $^{57}\text{Fe}$  in  $\alpha$ -iron [Ber94b].

### 2.1.3 Energy conservation and recoil energy

So far, we considered the probability of a transition in which the  $\gamma$ -ray energy did match exactly the energy difference between ground and excited state. This is given by  $f_{LM}$ . Thus, there is the probability  $1 - f_{LM}$ , that the energy does not match. How will the energy be conserved in this case? The recoil energy could be taken between the nucleus, the crystal and phonons. The nucleus cannot leave the lattice, so it cannot take translational energy. The mass of the crystal  $M$  is too big to take a non negligible amount of translational energy, as we had  $E_R = E_\gamma^2/2 M c^2$ . This leaves the phonons. Lipkin derived the average energy transfer between the  $\gamma$  quantum and the phonons [Lip60]. His law, the Lipkin sum rule, will be explained below [Weg66].

The Hamiltonian of the lattice of atoms with momentum  $\vec{p}_i$  and position  $\vec{x}_i$  is given by

$$H = \sum_i \frac{\vec{p}_i^2}{2m} + V(x_o, x_1, \dots) \quad (2.23)$$

If we calculate the commutator  $[H, e^{-i\vec{k}\vec{x}_o}]$ , the only term of  $H$  that does not commute with  $\vec{x}_o$  is  $\frac{1}{2m}\vec{p}_o^2$ . We get:

$$\begin{aligned} e^{i\vec{k}\vec{x}_o} H e^{-i\vec{k}\vec{x}_o} - H &= e^{i\vec{k}\vec{x}_o} [H, e^{-i\vec{k}\vec{x}_o}] = \frac{1}{2m} e^{i\vec{k}\vec{x}_o} [\vec{p}_o^2, e^{-i\vec{k}\vec{x}_o}] \\ &= \frac{\hbar^2 k^2}{2m} - \frac{\hbar}{m} \vec{k} \vec{p}_o \end{aligned} \quad (2.24)$$

The eigenstates of  $H$  are  $|E_{G'}\rangle$  with eigenvalues  $E_{G'}$ . We thus have  $H = \sum |G'\rangle E_{G'} \langle G'|$ . We further multiply  $\langle G|$  from the left and  $|G\rangle$  from the right.

$$\begin{aligned} \sum_{G'} \langle G| e^{i\vec{k}\vec{x}_o} |G'\rangle E_{G'} \langle G'| e^{-i\vec{k}\vec{x}_o} |G\rangle - \sum_{G'} \langle G| G'\rangle E_{G'} \langle G'| G\rangle &= \langle G| \frac{\hbar^2 k^2}{2m} |G\rangle - \langle G| \frac{\hbar}{m} \vec{k} \vec{p}_o |G\rangle \\ \sum_{G'} |\langle G'| e^{-i\vec{k}\vec{x}_o} |G\rangle|^2 E_{G'} - E_G &= \frac{\hbar^2 k^2}{2m} - \langle G| \frac{\hbar}{m} \vec{k} \vec{p}_o |G\rangle \end{aligned} \quad (2.25)$$

The term  $\langle G| \frac{\hbar}{m} \vec{k} \vec{p}_o |G\rangle$  vanishes, as the operator  $\vec{p}_o$  can be written as a linear combination of phonon creation and annihilation operators, thus changing the eigenstate  $|G\rangle$ , when

acting on it and  $\langle G|G'\rangle = 0$  for  $G \neq G'$ .  $|\langle G'|e^{-i\vec{k}\vec{x}_o}|G\rangle|^2$  on the other side is the probability, that the crystal changes its state from  $|G\rangle$  to  $|G'\rangle$ , while emitting a  $\gamma$ -quantum. The term  $e^{-i\vec{k}\vec{x}_o}$  is part of the Hamiltonian that describes the interaction of the  $\gamma$  wave field and the lattice. The other parts of that Hamiltonian are independent of the lattice state and do not interest here [Weg66]. We rewrite:

$$\sum_{G'} P(G \rightarrow G') E_{G'} - E_G = \frac{\hbar^2 k^2}{2m} = \frac{p_\gamma^2}{2m} = E_R \quad (2.26)$$

The mean energy transfer to the crystal equals the recoil energy of a free emitting nucleus. With this point clarified, we can understand Fig. 2.4 which summarises the values for the Lamb-Mössbauer factor and visualises the distribution of processes involving creation or annihilation of phonons.

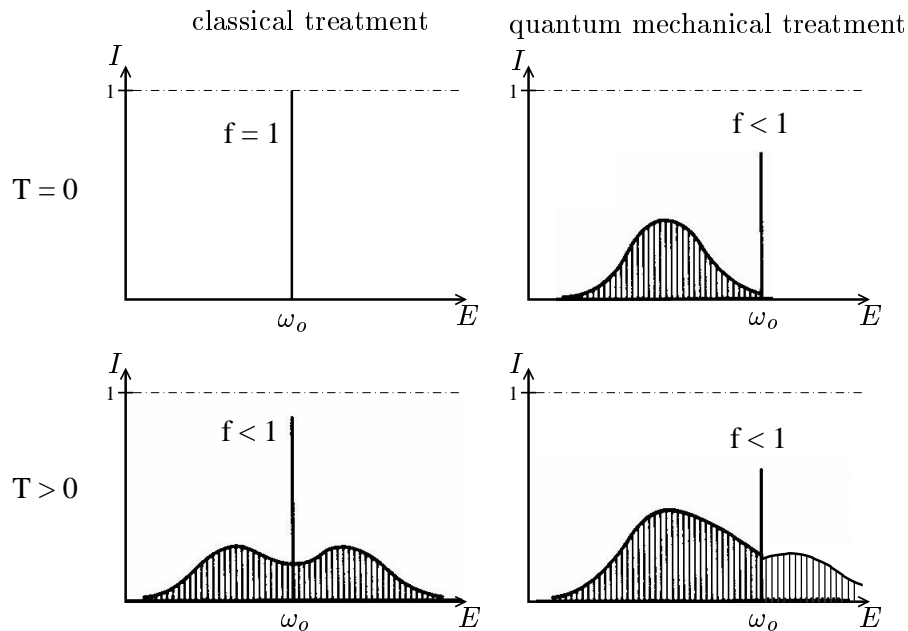


Figure 2.4: The frequency spectrum of a single line Mössbauer-source at and above zero temperature in classical and quantum mechanical treatment. In the latter case, the center of the spectra is shifted to smaller frequencies and energies, corresponding to the recoil energy that would have been transferred to a free nucleon. [Weg66]

#### 2.1.4 Scanning the region of nuclear resonant absorption

We calculated the probability, that a  $\gamma$ -ray emission or absorption process takes place without creation or annihilation of phonons. In this case, we do not transfer recoil energy to the crystal. The probability is referred to as the Lamb-Mössbauer-factor  $f_{LM}$ . Now, we will consider a source of  $\gamma$ -rays on one side, and an absorber of the same nuclei at some distance. As stated at the beginning, the source contains radioactive mother-isotopes, that in performing the radioactive decay, populate the level  $E_e$  of our Mössbauer isotope. We will then displace the source with the speed  $v$ .

We remember the energetic width of emitted radiation 2.3, now of course in the case

of  $E_R = 0$  and modify it slightly, the index  $s$  standing for the source:

$$I_s(v, E) = \frac{f_{\text{LM}}^s \cdot \Gamma_o/2\pi}{(E - E_o(1 - \frac{v}{c}))^2 + (\Gamma_o/2)^2} \quad (2.27)$$

The constant is chosen as to obtain  $\int_{-\infty}^{\infty} I_{\text{source}} = f_{\text{LM}}^{\text{source}}$ . This radiation should pass the absorber and hit a detector on the other side. The countrate will depend on the absorber density, thickness and the absorption cross section. This splits into absorption due to interaction with the electron cloud and nuclear resonant absorption. We remember the nuclear absorption cross section 2.4 and write for the transmission

$$T(E) = e^{-dn\sigma(E)} \quad (2.28)$$

$$\sigma(E) = \sigma_{el} + \sigma_n(E) \quad (2.29)$$

$$\sigma_n(E) = \beta f_{\text{LM}} \sigma_o \frac{(\Gamma_o/2)^2}{(E - E_o)^2 + (\Gamma_o/2)^2} \quad (2.30)$$

$$\sigma_o = \frac{2\pi}{k^2} \frac{1}{1 + \alpha} \frac{2J_e + 1}{2J_g + 1} \quad (2.31)$$

The value for  $\sigma_o$  is obtained from quantum electrodynamics [Ach62, deS74]. One first calculates the partial cross section of  $\gamma$ -ray absorption by a nucleus of certain angular momentum and certain z-component of it. If we do not know the initial state of the emitting or absorbing nucleus with respect to its z-component of the angular momentum, we have to average over  $2J_i + 1$  possible values. Further, after the transition, the z-component will be in one of  $2J_f + 1$  states. Here we have to sum over all these possibilities. The factor  $\frac{2\pi}{k^2}$  is a very general behaviour of  $\gamma$ -ray scattering. The factor  $\frac{1}{1+\alpha}$  originates from the fact, that in addition to a radiative decay of the excited state, a de-excitation via electron conversion is an alternative possibility, but then no  $\gamma$ -ray is emitted, reducing the resonant scattering (but not the resonant absorption) cross section. The probability of emitting a  $\gamma$ -ray is just  $\frac{1}{1+\alpha}$ . For  $^{61}\text{Ni}$ ,  $\alpha = 0.14$  and thus in 87%, the decay will be radiative.  $^{57}\text{Fe}$  is much worse with  $\alpha = 8.14$  and thus only 11% of radiative decay.  $\beta$  is the isotopic enrichment of the sample. Only the right isotope has the resonance energy under consideration.  $d$  is the sample thickness,  $n$  the number of sample atoms per volume. The detector measures the countrate

$$Z(v) = (1 - f_{\text{LM}}^s) e^{-dn\sigma_{el}} + \int_0^{\infty} I_s(v, E) \cdot e^{-dn\sigma_{el}} e^{-dn\sigma_r(E)} dE \quad (2.32)$$

The first part originates from the non-resonant part of the source intensity. It is convenient to compare the velocity dependant detector signal  $Z(v)$  to its value at Doppler shifts far away from the resonance,  $Z(\infty) = e^{-dn\sigma_{el}}$ . If the sample is thin, then  $e^{-dn\sigma_r(E)} \approx 1 - dn\sigma_r(E)$  and we get

$$\begin{aligned} \frac{Z(v)}{Z(\infty)} &= 1 - dn \int_0^{\infty} I^s(v, E) \sigma_r(E) d(E) \\ &= 1 - \frac{1}{2} dn \beta f_{\text{LM}}^s f_{\text{LM}}^a \sigma_o \frac{(\Gamma_o/E_o)^2}{(v/c)^2 + (\Gamma_o/E_o)^2} \end{aligned} \quad (2.33)$$

The index  $a$  designates the absorber. In 1957, R. Mössbauer was the first to measure this nuclear resonant absorption, using a  $^{191}\text{Ir}$  source and absorber. The setup and the result is shown in Fig. 2.5. The word 'spectroscopy' for this case seems exaggerated, but if the nuclear levels in the sample shift or split due to hyperfine interactions, this change can be investigated.



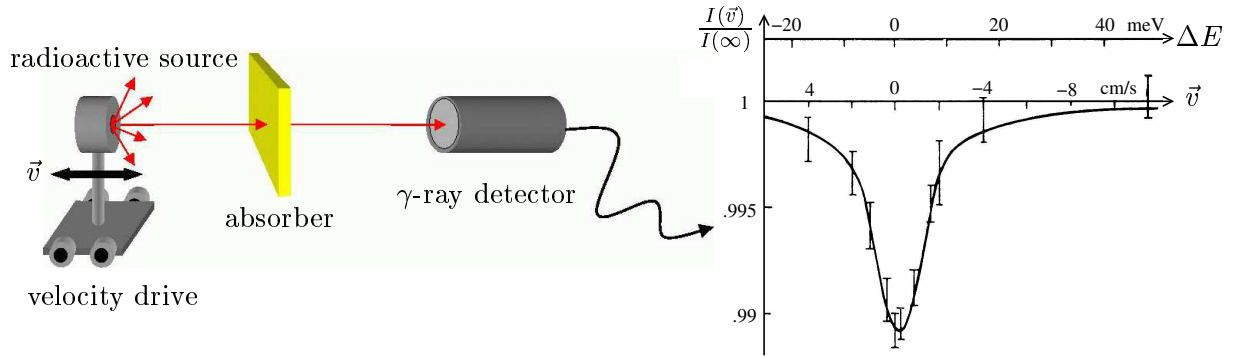


Figure 2.5: Schematic setup for Mössbauer-spectroscopy and the historic results on  $^{191}\text{Ir}$  [Möβ59].

## 2.2 Influences on the energy of nuclear levels: hyperfine interactions

In the preceding chapter, we analysed nuclear resonant absorption in the case of a nuclear transition between an excited state  $E_e$  and the ground state  $E_g$ , the difference being  $E_o$ . As only influence to this energy, we dealt with the Doppler shift that arose from thermal motion, lattice vibrations and crystal velocity. There can be different influences to a nucleus which might furthermore split possibly degenerate levels. As a nucleus is charged and a composition of particles with spin, the presence of its atomic electron cloud and magnetic fields, external or internal, affects the energy of the nuclear levels. Compared to the energy of the nuclear level, these influences are very small and can be treated as a perturbation. The set of possible perturbations is summarised with the term "hyperfine interactions". For the Hamiltonian of the perturbed nucleus, we can write [Bar80]:

$$\hat{H} = \hat{H}_o + \hat{H}_{hf} \quad \hat{H}_{hf} = \hat{H}_{el} + \hat{H}_{magn} \quad (2.34)$$

We will treat the electric and magnetic influences only individually, starting with the electric part. The electrostatic interaction energy between the charged nucleus and the surrounding electric fields can be expressed classically by

$$E_{el} = \int_n \rho_n(\vec{r}) V(\vec{r}) d^3r \quad (2.35)$$

with  $\rho_n(\vec{r})$  being the nuclear charge density (the protons) and  $V(\vec{r})$  the scalar potential of all surrounding charges (the electrons). We develop the potential in a Taylor series at point  $r = 0$  in the center of the nucleus, as the potential does not vary rapidly inside the small nuclear volume:

$$V(\vec{r}) = V_o + \sum_{i=1}^3 V_i x_i + \frac{1}{2} \sum_{i,j=1}^3 V_{ij} x_i x_j + \dots; \quad V_i = \left. \frac{\partial V}{\partial x_i} \right|_{r=0}; \quad V_{ij} = \left. \frac{\partial^2 V}{\partial x_i \partial x_j} \right|_{r=0} \quad (2.36)$$

$$E_{el} = V_o \underbrace{\int_n \rho_n(\vec{r}) d^3r}_{eZ} + \sum_{i=1}^3 V_i \underbrace{\int_n \rho_n(\vec{r}) x_i d^3r}_{=0} + \frac{1}{2} \sum_{i,j=1}^3 V_{ij} \int_n \rho_n(\vec{r}) x_i x_j d^3r + \dots \quad (2.37)$$

The first term is  $V_o eZ$  and represents the interaction of a point-like nucleus with the surrounding charges. It does not matter whether the nucleus is in its excited state or its

ground state. Thus, the term is of no interest here. The second term is zero, as  $\rho(\vec{r})$  is an even function with respect to  $\vec{r}$ . The third term can be rearranged. We add and subtract the term  $\frac{1}{3}\delta_{ij}\rho_n(\vec{r})r^2$  inside the integral. Rearranging gives

$$E_{el} = \underbrace{\frac{1}{6} \sum_{i=1}^3 V_{ii} \int_n \rho_n(\vec{r}) r^2 d^3r}_{E_{is}} + \underbrace{\frac{1}{6} \sum_{i,j} V_{ij} \int_n (3x_i x_j - \delta_{ij} r^2) \rho_n(\vec{r}) d^3r}_{E_Q} \quad (2.38)$$

### 2.2.1 Isomer shift

The first part of equation 2.38 is called the Isomer shift or Chemical shift. To analyse it, we first state that the scalar potential  $V$  obeys the Poisson equation. Especially at the nucleus,  $\vec{r} = 0$  we have:

$$\Delta V(\vec{r} = 0) = \sum_{i=1}^3 V_{ii} \Big|_{\vec{r}=0} = -4\pi\rho_e(0) = 4\pi e |\Psi(0)|^2 \quad (2.39)$$

Here,  $-e|\Psi(0)|^2$  is the charge density of the electrons, that are responsible for the existence of  $V$ .  $\Psi(0)$  is the probability of finding a charge at the center of the nucleus. Further, for  $\int_n \rho_n(\vec{r}) r^2 d^3r$  we consider a spherical nucleus of uniform charge density  $\rho_n(\vec{r}) = Ze \cdot \frac{3}{4\pi R^3}$  and radius  $R$ . This implies

$$\int_n \rho_n(\vec{r}) r^2 d^3r = \frac{3}{4\pi R^3} \int_n r^2 d^3r = \frac{3}{5} R^2 \quad (2.40)$$

Finally, we get

$$E_{is} = \frac{2\pi}{5} e |\Psi(0)|^2 R^2 \quad (2.41)$$

The nuclear radius for the ground state is not the same as for the excited state. In exciting a nucleus, we thus get an energy shift  $\Delta E_{is} = \frac{2\pi}{5} e |\Psi(0)|^2 (R_e^2 - R_g^2)$ . As the radii are almost the same, we approximate  $R_e - R_g = \delta R$  and  $R_e + R_g = 2R$ .

$$\Delta E_{is} = \frac{4\pi}{5} e |\Psi(0)|^2 \frac{\delta R}{R} R^2 \quad (2.42)$$

In a traditional Mössbauer experiment, there is the source and the absorber. The values  $R^2$  and  $\frac{\delta R}{R}$  are nuclear properties and are identical for absorber  $A$  and source  $S$ . This is different for the electron density at the nucleus  $|\Psi(0)|^2$ . s-electrons can penetrate the nucleus and spend a certain fraction of time there, as they have zero angular momentum. Also p<sub>1/2</sub>-electrons can do this, if we consider relativistic effects [Güt78]. Depending on the valence state of the Mössbauer isotope in its lattice and chemical bonding properties, the electrons are attributed to different orbits and thus the electron density at the nucleus changes. This either by changing directly the population of s-electrons or indirectly by p-, d- or f- electrons shielding more or less the s-electrons. We thus get in a Mössbauer experiment a shift of energy for the transition by:

$$\delta_{is} = \Delta E_{is}^A - \Delta E_{is}^S = \frac{4\pi}{5} e S(Z) [|\Psi^A(0)|^2 - |\Psi^S(0)|^2] \frac{\delta R}{R} R^2 \quad (2.43)$$

$S(Z)$  is a relativistic dimensionless correction factor which is 1.29 for <sup>57</sup>Fe and 1.34 for <sup>61</sup>Ni. The values for  $R^2$  are 24 fm<sup>2</sup> for <sup>57</sup>Fe and 24.8 fm<sup>2</sup> for <sup>61</sup>Ni, for  $\frac{\delta R}{R}$  we have very roughly

$-0.9 \cdot 10^{-3}$  for  $^{57}\text{Fe}$  and  $-2.6 \dots -0.9 \cdot 10^{-4}$  for  $^{61}\text{Ni}$  [Tra68, Gol68, Obe73, Ing75, Güt78]. In a Mössbauer experiment,  $\delta_{is}$  is given by an offset in velocity concerning the position of maximum overlap in the case of an unsplit absorber level and unsplit source level, see figure 2.6. With synchrotron radiation, as we will see later, this isomer shift is invisible, unless we take two different nuclear resonant samples to obtain the difference in isomer shift between them. Frequently, the isomer shift is also called electric monopole interaction.

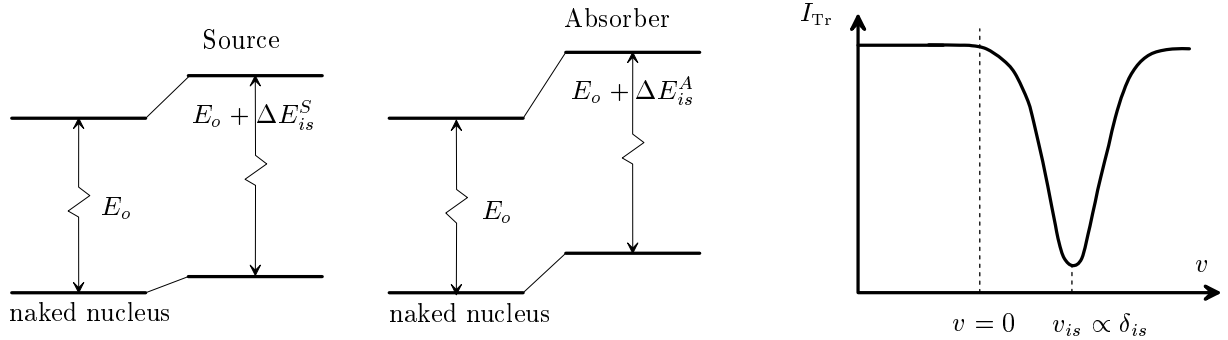


Figure 2.6: Nuclear levels and the isomer shift. On the left the corresponding Mössbauer spectra. *A* stands for absorber, *S* for source.

Actually, it is just part of it. To understand this, one has to express the interaction energy not with a Taylor series like in equation 2.37, but with the help of spherical harmonics, see for example [Möb67]. Measurements of the isomer shift with  $^{61}\text{Ni}$  samples are in general quite difficult for several reasons: the linewidth of the excited level is rather broad, due to the short lifetime. The change in nuclear radius during the transition is an order of magnitude smaller than in the case of iron. Finally, the second order Doppler shift, a relativistic temperature effect that will not be treated here, see for example [Weg66], is in this case of small isomer shifts comparable in magnitude and has to be corrected for, using theoretical models of the concerning lattice dynamics.

### 2.2.2 Electric quadrupole interaction

The second part of equation 2.38 is called the electric quadrupole term. We remember

$$E_Q = \frac{1}{6} \sum_{i,j}^3 V_{ij} \int_n (3x_i x_j - \delta_{ij} r^2) \rho_n(\vec{r}) d^3 r \quad \text{or} \quad \hat{H}_Q = \frac{1}{6} e \sum_{i,j}^3 V_{ij} \sum_p (3x_{p_i} x_{p_j} - \delta_{ij} r_p^2) \quad (2.44)$$

if we replace the classical expression for  $\rho_n(\vec{r})$  by the quantum mechanical density operator and sum over all protons  $p$ :  $\hat{\rho}(\vec{r}) = \sum_p e \delta(\vec{r} - \vec{r}_p)$  [Bar80].

For the determination of the energy eigenstates of a nucleus in the ground state  $I = I_g$  or in the excited state  $I = I_e$ , one uses perturbation theory and needs to calculate the matrix elements  $\langle I, m | \hat{H}_Q | I, m \rangle$ , so in particular  $\langle I, m | \sum_p (3x_{p_i} x_{p_j} - \delta_{ij} r_p^2) | I, m \rangle$ . The sum describes elements of the nuclear quadrupole moment. The nuclear quadrupole moment as written here is a symmetric tensor of rank 2 with trace zero. We can apply the Wigner-Eckart theorem for such a tensor, as for the operator of angular momentum. Their matrix elements are proportional:

$$\langle I, m | \sum_p (3x_{p_i} x_{p_j} - \delta_{ij} r_p^2) | I, m' \rangle = c_1 \cdot \langle I, m | 3 \frac{I_i I_j + I_j I_i}{2} - \delta_{ij} I^2 | I, m' \rangle \quad (2.45)$$

To determine  $c_1$ , we solve equation 2.45 for a special case  $m = m' = I$  and  $i = j = z$ :

$$\underbrace{\langle I, m | \sum_p (3z_p^2 - r_p^2) | I, m \rangle}_Q = c_1 \cdot \underbrace{\langle I, I | 3I_z^2 - I^2 | I, I \rangle}_{I(2I-1)} \quad (2.46)$$

The left side represents just the quadrupole moment of the nuclear charge distribution. Defining a nuclear angular momentum implies an axial symmetry, so only one value  $Q$  is of importance [Bar80]. The quadrupole moment is positive for a cigar shape like nucleus and negative for an oblate shaped one. We obtain:

$$\hat{H}_Q = \frac{eQ}{6I(2I-1)} \sum_{i,j} V_{ij} \left[ \frac{3}{2}(I_i I_j + I_j I_i) - \delta_{ij} I^2 \right] \quad (2.47)$$

The perturbation  $\hat{H}_Q$  vanishes, if either the nuclear charge density  $\rho_n(\vec{r})$  is of spherical symmetry and thus  $Q = 0$ .  $Q$  is also zero, if  $I = 0$  or  $I = \frac{1}{2}$ , as  $Q = I(2I-1) \cdot c_1$ . Further,  $\hat{H}_Q$  vanishes if the nucleus is embedded in a cubic crystal structure. This can be verified, if a coordinate system is chosen, so that  $V_{ij}$  are diagonalised. Then,  $V_{xx} = V_{yy} = V_{zz}$ , with the other values  $V_{ij}$  vanishing. Also, contributions from s-electrons and  $p_{1/2}$ -electrons can be neglected here, as they give rise to a potential of spherical symmetry. Excluding these electrons, we have no charges at  $\vec{r} = 0$  and can write the Laplace equation for the potential of the "charge free" region at  $\vec{r} = 0$ :  $\sum_i V_{ii} = 0$ . In a coordinate system that diagonalises  $V_{ij}$  and with the axes chosen so that  $V_{zz} \geq V_{xx} \geq V_{yy}$  we finally get:

$$\hat{H}_Q = \frac{eQV_{zz}}{4I(2I-1)} \left[ 3\hat{I}_z - \hat{I}^2 + \frac{\eta}{2}(\hat{I}_+^2 + \hat{I}_-^2) \right] \quad (2.48)$$

$V_{zz}$  is often called the electric field gradient, as  $\vec{\nabla} \vec{E} = -\vec{\nabla} \vec{\nabla} V$ . The asymmetry parameter is defined as  $\eta = \frac{V_{xx} - V_{yy}}{V_{zz}}$ .

With the perturbation Hamiltonian  $\hat{H}_Q$ , it is possible to determine its eigenstates, leading to

$$E_Q = \frac{eQV_{zz}}{4I(2I-1)} [3m_I^2 - I(I+1)] \sqrt{1 + \frac{\eta^2}{3}} \quad (2.49)$$

This equation is correct for  $\eta = 0$  and all possible values of  $I$  and  $m$ . If  $I = \frac{3}{2}$ , it is correct even for  $\eta \neq 0$ , whatever  $m$  is, also for  $I = 2$  with  $m = 0$  or  $m = +2$ . In other cases with  $\eta \neq 0$  and  $I > 2$ , only numerical results for the eigenvalues exist [Dun72]. Except for  $I = 2$  and  $\eta \neq 0$ , a two-fold degeneracy remains between substates of  $\pm m$ .

In the case of  $^{57}\text{Fe}$ , the ground state does not have a quadrupole moment, as  $I_g = \frac{1}{2}$ . If the electric field gradient  $V_{zz}$  at the nucleus does not vanish due to crystal symmetry, the excited state splits into two two-fold degenerated sublevels with

$$E(\pm \frac{1}{2}) = -\frac{eQ_e V_{zz}}{4} \sqrt{1 + \frac{\eta^2}{3}} \quad (2.50)$$

$$\text{and } E(\pm \frac{3}{2}) = +\frac{eQ_e V_{zz}}{4} \sqrt{1 + \frac{\eta^2}{3}} \quad (2.51)$$

The quadrupole moment of the excited state of  $^{57}\text{Fe}$  was a subject of debate until recently. The most recent value is  $Q_e = 0.15(2)$  barn [Mar01] and seems to settle the debate. There are two possible transitions between the ground state and both of the split sublevels of the excited state.

The angular moments of  $^{61}\text{Ni}$  are  $I_g = \frac{3}{2}$  and  $I_e = \frac{5}{2}$ . Therefore, in the presence of an electric field gradient, the ground state splits twice and the excited state into 3 sublevels. For the electric quadrupole moments, we have  $Q_g = +0.16$  barn and  $Q_e = -0.2$  barn. The Mössbauer transition in  $^{61}\text{Ni}$  is of M1 character. With the selection rules of  $\Delta m = -1, 0, +1$  for transitions between ground state and excited state, of the 6 transitions between these sublevels, only 5 are allowed, see figure 2.7.

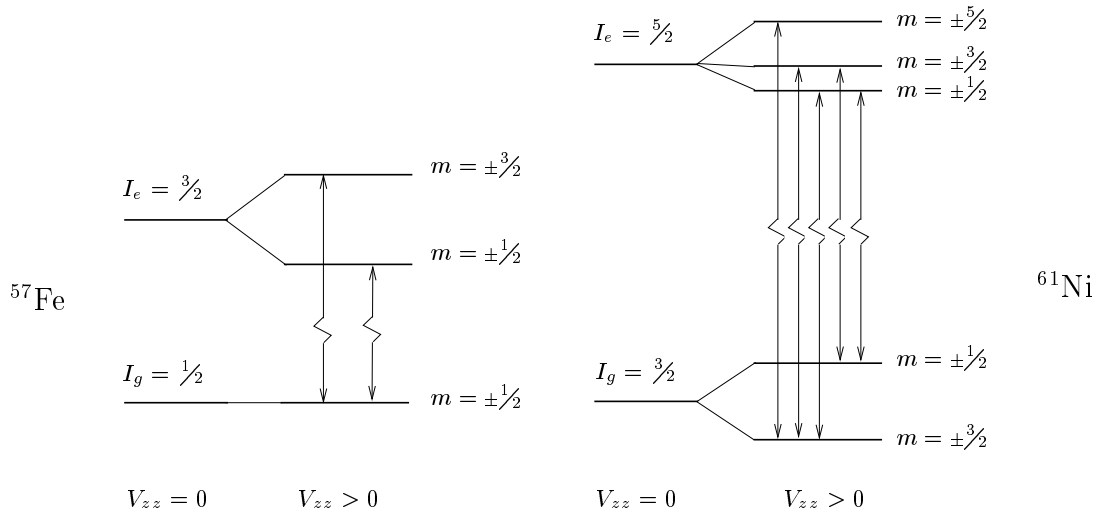


Figure 2.7: Nuclear levels and the quadrupole splitting for  $^{57}\text{Fe}$  and  $^{61}\text{Ni}$  in a non-magnetic material and for  $\eta = 0$ . (The scaling of the  $^{57}\text{Fe}$  levels and the  $^{61}\text{Ni}$  levels are different.)

$V_{zz}$  depends principally on two factors: First the contribution from distant ions that surround the Mössbauer atom in a non-cubic crystal, it is called the lattice contribution  $V_{zz}^{\text{lat}}$ . Second, in the Mössbauer atom itself, the valence electrons can be distributed anisotropically. This is called the valence contribution  $V_{zz}^{\text{val}}$ . The lattice contribution actually is still enhanced by the fact that the field gradient from the distant ions polarises the electron shells of the Mössbauer atom. The valence contribution on contrast is diminished by a shielding from the core electrons. All together, the sum off both contributions is often expressed as:

$$V_{zz} = V_{zz}^{\text{lat}}(1 - \gamma_{\infty}) + V_{zz}^{\text{val}}(1 - R) \quad (2.52)$$

$\gamma_{\infty}$  is the Sternheimer anti-shielding factor,  $R$  the Sternheimer shielding factor. For  $^{57}\text{Fe}$  we have  $\gamma_{\infty} \approx -9$  for iron compounds and  $R = 0.25 - 0.35$ , for  $^{61}\text{Ni}$ ,  $R$  should be similar as there are just two electrons more and  $\gamma_{\infty} = -4.3$  for the closed shells of  $^{61}\text{Ni}$ , [Bar80, Güt78, Obe76].

### 2.2.3 Magnetic hyperfine splitting

In classical physics, the magnetic moment of a nuclei is proportional to its angular momentum:  $\vec{\mu} = \gamma \vec{I}$ , with  $\gamma$  being the gyromagnetic ratio. In quantum mechanics, the definition for the magnetic moment is  $\mu = \langle I, m=I | \mu_z | I, m=I \rangle$ , implying that only the z-component of  $\vec{\mu}$  is observable. This leads to

$$\mu = \gamma \hbar I = g \mu_N I \quad (2.53)$$

$g$  is the Landé factor and  $\mu_N$  the nuclear magneton.  $\gamma$  and  $g$  depend on how spin and orbital angular momentum couple. Therefore, the magnetic moment is not proportional

to the nuclear angular momentum. Instead, for  $^{57}\text{Fe}$  we have  $\mu_g = +0.09 \mu_N$  and  $\mu_e = -0.155 \mu_N$ . In the case of  $^{61}\text{Ni}$ , it is  $\mu_g = -0.75 \mu_N$  and  $\mu_e = +0.48 \mu_N$  [Fir96].

In the presence of a magnetic field, the magnetic moment interacts with it. The interaction energy is

$$E_m = -\vec{\mu} \cdot \vec{B} \quad \text{classical} \quad (2.54)$$

$$E_m = \langle I, m | -\mu_z B_z | I, m \rangle = -\gamma \hbar B_z m \quad \text{quantum mechanics} \quad (2.55)$$

A level of given  $I$  splits thus into  $2I + 1$  sublevels corresponding to the possible values of  $m$ . There is no more degeneracy. We chose the z-axis to be parallel to the magnetic field. The field that the nucleus sees is called the hyperfine magnetic field  $B_z = B_{hf}$ .

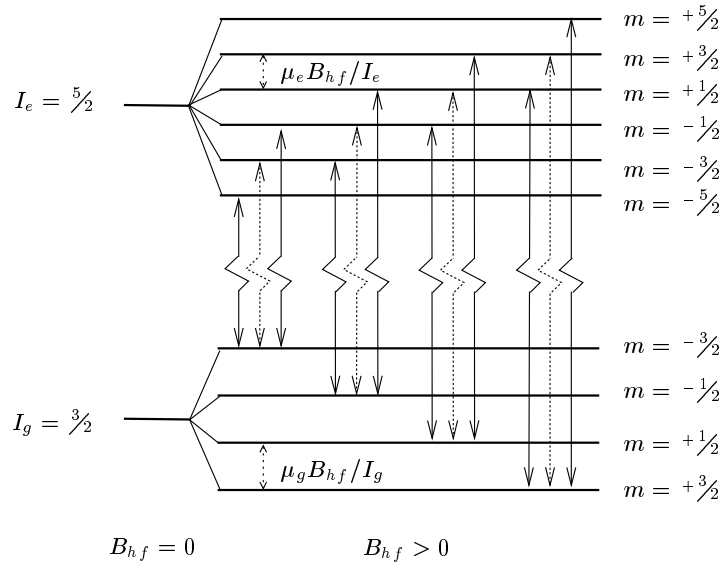


Figure 2.8: Nuclear levels and magnetic hyperfine splitting for  $^{61}\text{Ni}$  in a cubic lattice ( $V_{zz} = 0$ ). The solid transition lines correspond to  $\Delta m = \pm 1$  transitions, the dotted ones to  $\Delta m = 0$ .

Again, the selection rules for possible  $\gamma$ -ray transitions is  $\Delta m = -1, 0, +1$ . In the case of  $^{61}\text{Ni}$ , we end up with 12 allowed transitions and 12 different transition energies, if there is a magnetic hyperfine field at the nucleus. The case for  $^{57}\text{Fe}$  is very similar, but as the nuclear angular moments are  $I_g = \frac{1}{2}$  and  $I_e = \frac{3}{2}$ , the groundstate splits into two levels only and the excited state into four. With the selection rules, 6 transitions of different energy are allowed.

Despite the splitting of the level into  $2I + 1$  sublevels, there is an other result: The nuclear angular momentum precesses around the direction of the magnetic field [Sch92]. This effect is of great importance for SR-PAC, please refer to chapter 7.

The reasons for the hyperfine magnetic field at the nucleus are multiple. The main contributions can be written as [Bar01]:

$$\vec{B}_{hf} = \vec{B}_{core} + \vec{B}_{orb} + \vec{B}_{dip} + \vec{B}_{thf} + \vec{B}_{ext} \quad (2.56)$$

$B_{core}$  is called the core polarisation field or Fermi contact field. It is the interaction of a net spin-up or spin-down density ("unpaired spin density") of s-electrons at the nucleus with the nuclear magnetic moment. Even for a closed s-shell, the net spin density differs from zero, as the spin of the s-electrons interacts with the total spin of the outer electron

shells ( $p$ ,  $d$  and  $f$ ).  $s$ -electrons with a spin anti-parallel to the total spin of the outer shells are stronger repulsed by these shells than  $s$ -electrons with a parallel spin. Therefore, they stay closer to the nucleus and dominate over the other  $s$ -electrons. Also electrons from a conducting band of  $s$ -character contribute to this term. Sometimes their part is designed in an own term  $B_{cep}$ , the conducting electron polarisation field.

$B_{orb}$  is the orbital field. Open, not completely filled shells have an orbital angular momentum  $L$  which interacts with the nuclear magnetic moment. In the case of  $^{57}\text{Fe}$  and  $^{61}\text{Ni}$ , these are the  $3d$ -electrons.  $L$  and  $B_{orb}$  vanish for closed and half-filled shells.

The interaction of the nuclear angular momentum with the spin of the valence electrons is called the spin-dipolar term  $B_{dip}$ . Again, closed or half-filled shells do not contribute. The term is further zero for an atom embedded in a local cubic symmetry.

Finally, the transferred hyperfine field  $B_{thf}$  originates from the influence of distant magnetic ions. Distant magnetic ions can polarise the core electrons (non-metallic systems) or the conduction electrons (metallic systems) of a non magnetic ion via magnetic interaction. This term is in general small, but in cases where the Mössbauer atom has no magnetic moment, it is the only remaining term. A prominent example is  $^{119}\text{Sn}$ .

Off course, an external magnetic field  $B_{ext}$  can be added as well. This is very practical as to obtain the direction of the hyperfine field or to simplify the Mössbauer spectra, see the end of the following chapter 2.2.4.

#### 2.2.4 Mössbauer spectroscopy and line intensities

In chapters 2.2.2 and 2.2.3, we saw that ground state and excited state can split into sublevels. Mössbauer spectroscopy is an excellent tool to investigate these sublevels. In most of the cases, for the Mössbauer source the Mössbauer isotope is embedded in a material that is non-magnetic and shows no electric field gradient. Thus, the nuclear levels do not split into sublevels and only one transition energy is the result. This type of source is called a single line source. The investigated sample contains Mössbauer nuclei embedded in their atomic and nuclear environment. Depending on this environment (resulting charge density at the nucleus, the electric field gradient and the magnetic hyperfine field) the levels of the Mössbauer isotopes in the sample shift with respect to the source or split. As explained in chapter 2.1.4, the energy of the source's radiation is shifted via the Doppler effect. If this energy corresponds to the energy of a possible transition in the sample isotopes, resonant absorption takes place and the transmitted intensity decreases. Changing the incoming energy over a sufficiently large region, all transitions in the sample will be detected and give all valuable information about the hyperfine-splitting, isomer shift or more subtle information like line broadening. In figure 2.9, both for  $^{57}\text{Fe}$  and for  $^{61}\text{Ni}$ , Mössbauer-spectra with electric or magnetic hyperfine splitting are shown as an example.

One point that was not treated so far are the strength of the different observed lines (with "line", one means an energy that corresponds to a transition in the sample). To calculate the strength or intensities, we need to know the multipolarity of the transition and the corresponding transition matrix elements, as well as the radiation characteristic of this multipolarity.

During the transition between the excited state  $I_e, m_e, \pi_e$  and the ground state  $I_g, m_g, \pi_g$ , a photon with quantum numbers  $l = I_e - I_g, m = m_e - m_g, \pi$  is emitted. Conservation of angular momentum and parity  $\pi$  implies the emission of an electromagnetic wave with

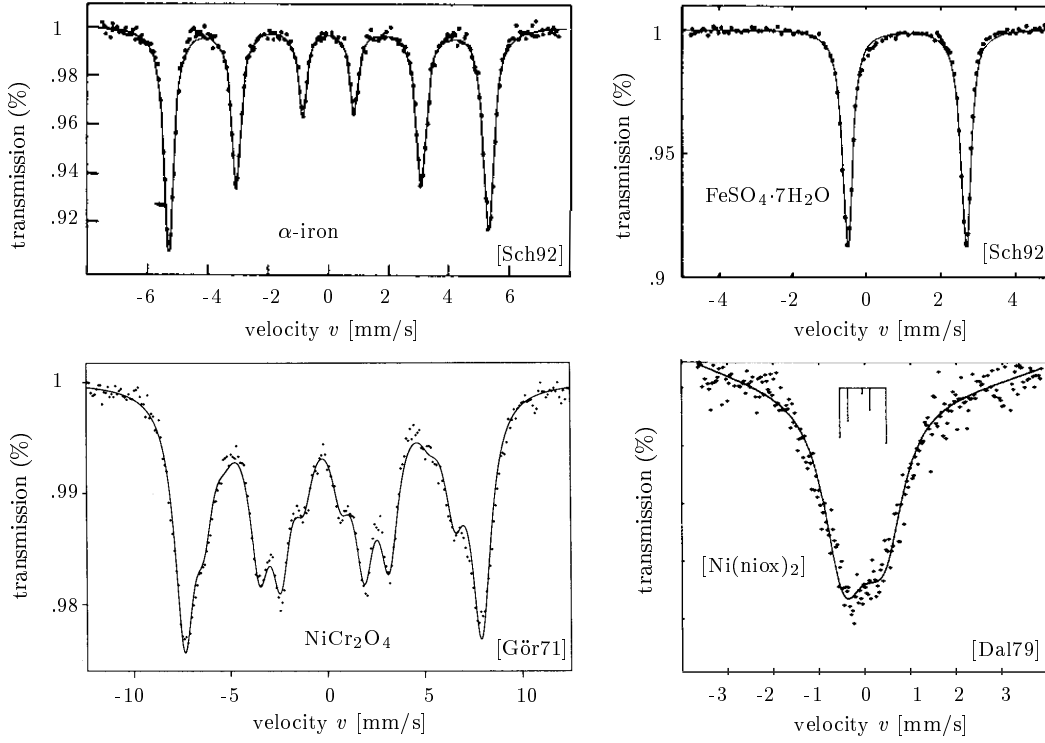


Figure 2.9: Magnetic hyperfine splitting (left) and quadrupole splitting (right) in selected  $^{57}\text{Fe}$  and  $^{61}\text{Ni}$  systems. In the case of  $^{57}\text{Fe}$ , the six lines of a magnetic hyperfine split and the two lines of a quadrupole split spectra are clearly visible. In the case of  $^{61}\text{Ni}$ , the natural linewidth  $\Gamma_o$  is much larger and therefore, the lines are often not completely resolved. A compound with huge  $B_{hf}$  is  $\text{NiCr}_2\text{O}_4$ , and the 12 lines become visible. Electric quadrupole splittings are generally small in  $^{61}\text{Ni}$  compounds. The example shown here shows a rather large quadrupole splitting without simultaneous magnetic interaction. The five lines have been indicated by the author [Dal79]. The energy shift  $\Delta E$  between a particular line and the unshifted value  $E_o$  is given by the Doppler effect and is thus  $\Delta E = \frac{v}{c} E_o$ . (1 mm/s  $\hat{=}$  48,1 neV for  $^{57}\text{Fe}$  and 1 mm/s  $\hat{=}$  225 neV for  $^{61}\text{Ni}$ ).

a well defined characteristic. This is the case for multipole radiation fields. To get their angular radiation characteristic, one calculates the absolute value of the pointing vector  $\vec{S} = \frac{1}{\mu_o}(\vec{E} \times \vec{B})$  with  $\vec{E}$  and  $\vec{B}$  expressed as multipole fields. The normalised angular radiation characteristic is obtained as [Sch92]:

$$F_{lm} = \frac{|\vec{L} \cdot Y_{lm}|^2}{\sum_m |\vec{L} \cdot Y_{lm}|^2} \quad (2.57)$$

$\vec{L}$  is the operator of angular momentum. For  $^{57}\text{Fe}$  and  $^{61}\text{Ni}$ , the multipolarity of the transition is almost of pure M1 character and  $l = 1$ . We obtain:

$$F_{10} = \frac{1}{2} \sin^2 \theta \quad F_{1\pm 1} = \frac{1}{4} (1 + \cos^2 \theta) \quad (2.58)$$

This radiation characteristic is shown in figure 2.10. The z-axis is chosen to be the preferred axis, either of the magnetic hyperfine field  $B_{hf}$  or of the electric field gradient  $V_{zz}$ .  $\theta$  is the angle of observation of the radiation. The second angle  $\phi$  is of no importance, if the other two axes are equivalent, that is  $\eta = 0$  and no combined electric and magnetic splittings.

To get the probability, that a transition between a certain excited state and a certain ground state occurs, as a function of  $I_e, m_e, I_g, M_g$ , we need to calculate the transition



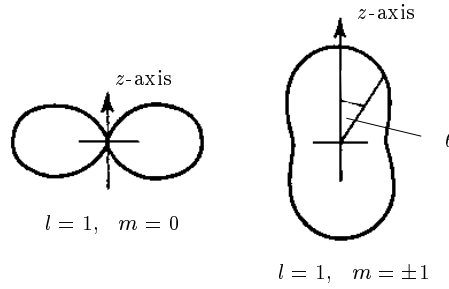


Figure 2.10: Dipole radiation angular characteristic.

matrix element with the concerned multipole transition operator  $\hat{M}(M1)$ . The intensity of a certain transition is given by:

$$I_\gamma \propto \left| \langle I_g, m_g | \hat{M}(M1) | I_e, m_e \rangle \right|^2 F_{1m}(\theta) \quad (2.59)$$

Using the Wigner-Eckart theorem and omitting the reduced matrix elements of  $\hat{M}$  that depend only on  $I_g$  and  $I_e$  and are thus the same for all transitions in one isotope and with the help of 3- $j$ -symbols, this reduces to [Sch92]:

$$I_\gamma \propto \left( \begin{array}{ccc} I_e & 1 & I_g \\ m_e & m & -m_g \end{array} \right)^2 F_{1m}(\theta) \quad (2.60)$$

With this formula, one can calculate the relative line intensities of all possible transitions. In the case of a polycrystalline sample, the values  $F_{1m}(\theta)$  have to be averaged over all directions, due to the arbitrary orientations of the nuclei in the sample.  $\int_\phi \int_\theta F_{1m}(\theta) \sin(\theta) d\theta d\phi = \frac{4\pi}{3}$  in all cases. Then, only the squares of the 3- $j$ -symbols are of importance. In the case of  $^{57}\text{Fe}$  and magnetic hyperfine splitting, we get relative intensities ratios of 3:2:1:1:2:3 for the six transitions, as can be seen also in figure 2.9. For  $^{61}\text{Ni}$ , we obtain 10:4:1:6:3:3:6:6:1:4:10. Still in a polycrystalline sample, but in the case of electric quadrupole splitting, the levels are degenerated and we have to add up intensities of several transitions for one line. For  $^{57}\text{Fe}$ , this leads to a ratio of 1:1 for the two lines, see e.g. figure 2.9. For  $^{61}\text{Ni}$ , the ratios are 9:6:1:4:10, starting with the line of lowest energy.

If the sample is a single crystal or aligned with the help of an external field, the angle  $\theta$  between detector direction and the preferred axis is fixed. The values of  $F_{1m}(\theta)$  play an important role now and may lead to a suppression of some lines ( $\theta = 0^\circ$ ) or to different intensity ratios (e.g.  $\theta = 90^\circ$ ). The different lines correspond also to different polarisations.  $\Delta m = 0$  transitions are linear polarised and  $\Delta m = \pm 1$  transitions are elliptically polarised, reaching in special cases the extrema of circular or linear polarisation [Bar80].

## 2.3 Absorption and scattering

In the previous part of this theory chapter, the Mössbauer effect has been treated as a resonant absorption process. When dealing with SR experiments with a Mössbauer isotope, it can be necessary to treat the subsequent absorption and emission of  $\gamma$  or X-rays as a scattering process of an electromagnetic wavefield.

After the SR excites a nucleus, the nucleus can decay into its ground state using two channels: a radiative decay or the emission of inner shell electron. This electron is called a conversion electron. The electron hole is then filled by an electron of an energetically higher shell, thereby emitting X-ray fluorescence radiation. In case of the radiative decay, it is definitely appropriate to speak about a scattering process. In the second case, the process is sometimes called nuclear absorption [Chu98b]. The conversion electron or the X-ray fluorescence radiation are products of the absorption process. The probability of a radiative decay is given by  $\frac{1}{\alpha+1}$  with  $\alpha$  being the internal conversion coefficient.

The scattering or absorption process can include the participation of phonons and thus a transfer of energy. It is helpful to classify the process with respect of elasticity. The interaction of nuclear matter with the incoming radiation can be described as [Stu04]:

$$|\Psi_i\rangle|\gamma_i\rangle \rightarrow |\Psi_n\rangle \rightarrow |\Psi_f\rangle|\gamma_f\rangle \quad (2.61)$$

Here,  $|\Psi_i\rangle$  and  $|\gamma_i\rangle$  are the initial states of the incoming X-ray wavefield and the nuclear matter. The excited state  $|\Psi_n\rangle$  is a temporary state with the incoming X-ray wavefield being absorbed that finally decays into the final state  $|\Psi_f\rangle$  under the emission of a photon  $|\gamma_f\rangle$  or an other decay product.

If the initial and the final states  $|\gamma_i\rangle$  and  $|\gamma_f\rangle$  are of identical energy, then the interaction process is elastic. If further the decay of the nucleus is radiative, we can speak about nuclear elastic scattering. If phonons participate in the interaction,  $|\gamma_i\rangle$  and  $|\gamma_f\rangle$  are not of identical energy and the process is inelastic. If furthermore the decay channel is the radiative one, the emitted photon can be called  $\gamma$ -ray fluorescence [Chu98b].

To consider coherence, it is necessary to consider a collection of atoms and one can analyse the following expression [Stu04]:

$$|\Psi_i\rangle = |\chi_i\rangle \prod_j |\psi_i^{(j)}\rangle \quad (2.62)$$

$|\chi_i\rangle$  describe the collective state of lattice vibrations and itinerant electrons.  $|\psi_i^{(j)}\rangle$  is the core state of atom  $j$ . In a coherent scattering process, the initial and final core states of all atoms are identical. The scattering process is called incoherent if at least one core state changes.

In nuclear forward scattering and the related nuclear lighthouse effect, the radiative decay is examined under the exclusion of phonon participation. It is an elastic coherent scattering process. The theory to describe this scattering will be sketched in chapter 2.4. Nuclear inelastic absorption [Set95] and nuclear inelastic scattering [Chu98b] are phonon assisted inelastic and incoherent processes. In these processes, coherence is destroyed by the phonon lifetimes on very short time scales, much faster than the nuclear decay and thus practically unobservable in nuclear resonant experiments. Synchrotron radiation based perturbed angular correlation (SR-PAC) is incoherent inelastic, too. It is treated in chapter 7.

Mössbauer spectroscopy is elastic and coherent, though the coherent properties are not easily visible in a standard absorption experiment. Conversion electron Mössbauer spectroscopy (CEMS) is an elastic incoherent process. The coherence vanishes when the conversion electron is emitted.

## 2.4 Nuclear forward scattering

### 2.4.1 Coherent elastic scattering and the nuclear exciton

Mössbauer spectroscopy was introduced in chapter 2.2.4 as a valuable tool to investigate hyperfine interactions. To obtain similar results in a SR scattering experiment, nuclear forward scattering is employed. When the radioactive source used in Mössbauer spectroscopy is replaced by the SR, several experimental facts imply and allow for a different approach. In Mössbauer spectroscopy, the energy of the incoming radiation emitted by the radioactive mother isotope is changed in energy with respect to the investigated sample via the Doppler shift. The energetic width of the emitted radiation is extremely narrow. It was stated in chapter 2.1.1, that in the case of  $^{57}\text{Fe}$  for example, this width is 4.7 neV. Even with best monochromators, as will be seen in chapter 4.2.4, the energy resolution of SR is in the meV range. This is much broader than the energetic splitting due to hyperfine interactions, which is in the order of several tens to hundreds of neV in general. Specific split sublevels can not be excited individually, instead all possible transitions between the sublevels of the ground and excited state are excited simultaneously.

However, as nuclear forward scattering is an elastic coherent scattering process, it is possible to examine the interference between the decaying sublevels. This can easily be done if the SR is of pulsed nature. A flash of SR excites all sublevels of the excited state, and in the following time (when no further excitation happens), the delayed decay of the involved sublevels is observed on the time scale. With the nuclear lighthouse effect, a method was found that is independent from the pulsed behaviour of the synchrotron radiation [Röh00c]. Still, the scattering process can be treated with the same formalism as needed for NFS.

An important consequence of the coherent nature of NFS is the fact, that it is not possible to know which nucleus was involved in the scattering process. No nucleus has been tagged via the emission of a conversion electron or a change in its oscillatory behaviour. An illustrative picture to describe this fact is the nuclear exciton. The nuclear exciton can be expressed as a coherent superposition of all realisations, in which one nucleus is excited and the others remain in their ground states, [Röh04a]:

$$|\Psi_n(\vec{k}_o)\rangle = \frac{1}{\sqrt{N}} \sum_i e^{i\vec{k}_o \cdot \vec{r}_i} |g\rangle |e_i\rangle \quad (2.63)$$

Here,  $|g\rangle$  denotes the ground states of all but one nuclei and  $|e_i\rangle$  the excited state of the remaining nuclei being at the position  $\vec{r}_i$ . The factor  $e^{i\vec{k}_o \cdot \vec{r}_i}$  is needed to preserve the phase relation between the different nuclei at different positions with respect to the incoming radiation  $\vec{k}_o$ . Only in the forward direction, all individual phases add up constructively, unless the arrangement of the nuclei in the sample allows for a Bragg reflection.

To treat nuclear forward scattering with synchrotron radiation, several theoretical concepts can be used. It is possible to treat the scattering in the energy domain, as the Mössbauer effect itself, and examine the response of a collection of individual, energetically different plane waves incident on the nuclear scatterer. The response of the broad-band incoming SR is obtained after integration of all plane waves [Smi99]. The outgoing wave is the sum of the incident plus the scattered wave.

A second possibility is to assume a locally homogeneous scatterer that is represented by its anisotropic and polarisation dependent refractive index [Han99, Bür99, Röh04a].

This approach is used here. As the refractive index is frequency dependent as well, also here a Fourier transform into the time domain is necessary. The outgoing wave is refracted incident wave.

In a third approach, the response function technique, the scattering is solved directly in the time domain, without using the detour of the previous energy dependent plane waves [Shv99]. First order integro-differential equations are used. Their kernel  $K(t, \hat{t})$  represents the coherent single scattering response of the nuclear scatterer at time  $t$  when the excitation happened at time  $\hat{t}$ . This approach has been implemented in the data fitting program Motif which is arguably the most user-friendly fitting program for NFS. However, the complicated theory does not suggest any presentation of it here.

### 2.4.2 Jones matrices and the refractive index of a scattering process

Polarised light travelling along the z-axis can be expressed as

$$\vec{E} = A_\sigma e^{i(\omega t + k z + \phi_\sigma)} \vec{e}_\sigma + A_\pi e^{i(\omega t + k z + \phi_\pi)} \vec{e}_\pi \quad \text{or} \quad \vec{A} = \begin{pmatrix} A_\sigma e^{i\phi_\sigma} \\ A_\pi e^{i\phi_\pi} \end{pmatrix} \quad (2.64)$$

in the Jones matrix formalism, if we restrict us in the following to coherent elastic forward scattering processes. Synchrotron radiation is polarised in the horizontal  $\sigma$ -plane and contains, compared to the width of a nuclear resonance, a broad frequency spectrum monochromatised to a width  $\Delta\omega$ . We can represent it as

$$\vec{A}_0(\omega) = \sqrt{I_0/\Delta\omega} \begin{pmatrix} 1 \\ 0 \end{pmatrix} \quad (2.65)$$

In the following, we will assume  $\sqrt{I_0/\Delta\omega} = 1$ .

The propagation of an electromagnetic wave through a homogeneous material of thickness  $d$  can be described with the transformation of its Jones vector as:

$$\vec{A}'(\omega) = \mathbf{T}_d(\omega) \vec{A}_0(\omega) \quad (2.66)$$

The properties of the propagation matrix  $\mathbf{T}_d(\omega)$  depend on the scattering process and thus on the scattering amplitude. It can be shown [Blu68] that

$$\vec{A}'(\omega) = e^{iknd} \vec{A}_0(\omega) \quad (2.67)$$

is a solution of the wave equation for electromagnetic radiation passing through a medium of refractive index  $\mathbf{n}$ . We use the refractive index in matrix form  $\mathbf{n}$ . In anisotropic media, as is the case for nuclear scatterers with a preferred spin orientation, the index of refraction is not a scalar, but different for orthogonal polarisations. It needs to be represented by the Jones matrices for birefringent material. Polarisation mixing can occur. We use the basis of horizontal and vertical polarised light:

$$\mathbf{n} = \begin{pmatrix} n_{\sigma\sigma} & n_{\sigma\pi} \\ n_{\pi\sigma} & n_{\pi\pi} \end{pmatrix} \quad (2.68)$$

In the case of forward scattering, the refractive index  $\mathbf{n}$  depends on the forward scattering amplitude  $\mathbf{f}$  via, [Lax51]:

$$\mathbf{n} = \mathbf{1} - \frac{2\pi}{k^2} \rho \mathbf{f} \quad (2.69)$$

where  $\varrho$  is the density of scatterers. A simple derivation of this equation can also be found in [Als93].  $\mathbf{1}$  is the diagonal unit matrix and  $\mathbf{f}$  is the polarisation dependent forward scattering matrix. It is convenient for the following treatment to use  $\mathbf{n} = \mathbf{1} + \mathbf{f}/k$  and thus to include the factor  $\frac{2\pi\varrho}{k}$  into the expression of  $\mathbf{f}$ . We further introduce  $\mathbf{k} = k\mathbf{1}$ . Equation 2.67 transforms thus to:

$$\vec{A}'(\omega) = e^{i\mathbf{F}d} \vec{A}_0(\omega) \quad \text{with} \quad \mathbf{F} = \mathbf{k} + \mathbf{f} \quad \text{and} \quad e^{i\mathbf{F}d} = \mathbf{T}_d(\omega) \quad (2.70)$$

However, the factor  $e^{i\mathbf{k}d}$  only accounts for a phase shift of all components of the travelling wave which is neglected again in the Jones vector formalism. Thus in practice, it is sufficient to calculate  $\vec{A}'(\omega) = e^{ifd} \vec{A}_0(\omega)$ .

### 2.4.3 The nuclear scattering amplitude

The scattering amplitude  $\mathbf{f}$  represents the properties of the scatterer, in particular of electronic and of nuclear nature:  $\mathbf{f} = \frac{2\pi\varrho}{k}(\mathbf{f}_e + \mathbf{f}_n)$ . It is a complex amplitude, thus treating both phase shifts and absorption. In usual electronic X-ray scattering experiments that neglect the nuclear contribution, it is common to write

$$f_e = -r_o Z + f' + if'' \quad \text{in cases treated here:} \quad f_e = -r_o Z + i\frac{k}{4\pi}\sigma_{tot} \quad (2.71)$$

where  $r_o Z$  is the Thomson scattering amplitude of  $Z$  electrons,  $r_o = \frac{e^2}{m_e c^2}$  is the classical electron radius and  $f' + if''$  is the complex anomalous dispersion correction term. Far from absorption edges, it is sufficient to consider only the imaginary term  $i\frac{k}{4\pi}\sigma_{tot}$  which comprises the total absorption cross section due to Compton scattering and the photo effect. The magnetic scattering amplitude  $f_m$  has been excluded in this equation. Then, the electronic scattering amplitude is a scalar and  $\mathbf{f}_e = f_e \mathbf{1}$ .

If the nuclear transition occurs between two unsplit nuclear levels, its contribution to the scattering amplitude can be written as:

$$f_n(\omega) = -\frac{Ze^2}{m_p c^2} + \frac{f_o}{2(E_o - \hbar\omega)/\Gamma - i} \approx \frac{f_o}{2(E_o - \hbar\omega)/\Gamma - i} \quad (2.72)$$

The first term corresponds to Thomson scattering on the nucleus and is negligible, since the proton mass  $m_p$  is much larger than the electron mass. The second part is the resonant contribution that has its maximum if the incident photon has the energy  $E_o$  of the nuclear transition.  $f_o$  is given as [Röh04a]:

$$f_o = \frac{1}{2k} \frac{2I_e + 1}{2I_g + 1} \frac{1}{1 + \alpha} f_{LM} \beta \quad (2.73)$$

where  $\beta$  is the isotopic abundance. The nuclear scattering amplitude is connected to the nuclear absorption coefficient  $\sigma_n(\omega)$  of equation 2.30 via the optical theorem  $\sigma_n(\omega) = \frac{4\pi}{k} \text{Im}\{f_n(\omega)\}$ , and thus  $\sigma_o = \frac{4\pi}{k} f_o$ .

If the involved nuclear levels are at least partially split by hyperfine interactions, different transitions between the split levels can only be excited by light of a certain polarisation state, see also chapter 2.2.4. Therefore, the nuclear scattering matrix  $\mathbf{f}_n$  has to include the polarisation information. We will restrict ourselves to a M1 transition as in the case of  $^{61}\text{Ni}$  and  $^{57}\text{Fe}$ . The selection rules require  $\Delta m = -1, 0, 1 =: M$  for the

transition between ground state and excited state. This leads to 6 transitions in the case of a magnetically split iron sample or 12 lines in the similar case for  $^{61}\text{Ni}$ . The nuclear scattering amplitude is given as [Röh04a]:

$$[\mathbf{f}_n]_{\mu\nu} = \frac{4\pi}{k} \sum_{M=-1}^1 [(\boldsymbol{\epsilon}_\nu \times \boldsymbol{\kappa}) \cdot \mathbf{Y}_{1M}(\boldsymbol{\kappa}, \mathbf{b})][\mathbf{Y}_{1M}^*(\boldsymbol{\kappa}, \mathbf{b}) \cdot (\boldsymbol{\epsilon}_\mu \times \boldsymbol{\kappa})] F_M(\omega) \quad (2.74)$$

where  $\nu$  and  $\mu$  run over the two orthogonal directions of the chosen polarisation basis. Using the  $\sigma$  and  $\pi$  directions as polarisation basis, one obtains the matrix form:

$$\mathbf{f}_n = \frac{4\pi}{k} \sum_{M=-1}^1 \left\{ F_M(\omega) \begin{pmatrix} \boldsymbol{\pi} \cdot \mathbf{Y}_{1M}(\boldsymbol{\kappa}, \mathbf{b}) \mathbf{Y}_{1M}^*(\boldsymbol{\kappa}, \mathbf{b}) \cdot \boldsymbol{\pi} & -\boldsymbol{\pi} \cdot \mathbf{Y}_{1M}(\boldsymbol{\kappa}, \mathbf{b}) \mathbf{Y}_{1M}^*(\boldsymbol{\kappa}, \mathbf{b}) \cdot \boldsymbol{\sigma} \\ -\boldsymbol{\sigma} \cdot \mathbf{Y}_{1M}(\boldsymbol{\kappa}, \mathbf{b}) \mathbf{Y}_{1M}^*(\boldsymbol{\kappa}, \mathbf{b}) \cdot \boldsymbol{\pi} & \boldsymbol{\sigma} \cdot \mathbf{Y}_{1M}(\boldsymbol{\kappa}, \mathbf{b}) \mathbf{Y}_{1M}^*(\boldsymbol{\kappa}, \mathbf{b}) \cdot \boldsymbol{\sigma} \end{pmatrix} \right\} \quad (2.75)$$

The energy dependent part is presented by the factor  $F_M$  that is specified later. The polarisation properties are expressed via the term  $[(\boldsymbol{\epsilon}_\nu \times \boldsymbol{\kappa}) \cdot \mathbf{Y}_{1M}(\boldsymbol{\kappa}, \mathbf{b})][\mathbf{Y}_{1M}^*(\boldsymbol{\kappa}, \mathbf{b}) \cdot (\boldsymbol{\epsilon}_\mu \times \boldsymbol{\kappa})]$ .  $\boldsymbol{\sigma}$ ,  $\boldsymbol{\pi}$  and  $\boldsymbol{\kappa}$  are the unit vectors that span the co-ordinate system attached to the incoming SR. The vector spherical harmonics  $\mathbf{Y}_{1M}$  describe the emission or absorption characteristics of a M1 transition. They depend on the direction  $\boldsymbol{\kappa}$  of the examined photon and the quantisation axis of the nuclear scatterer, i.e. the direction  $\mathbf{b}$  of the magnetic quantisation axis or the symmetry axis of an axially symmetric electric field gradient. For a detailed view of these spherical harmonics, see for example [Stu04, page S520] or the appendix of [Han99, Röh99c]. The energy dependent part can be expressed as:

$$F_M(\omega) = 2 \frac{1}{1 + \alpha} \frac{1}{2I_g + 1} f_{LM} \beta \sum_{m_g} \frac{C^2(I_g \ 1 \ I_e; m_g \ M)}{2(E_{(m_g, m_e=m_g+M)} - \hbar\omega)/\Gamma - i} \quad (2.76)$$

The explicit form for  $F_{-1}$ ,  $F_0$  and  $F_1$  for the case of a magnetically split  $^{57}\text{Fe}$  scatterer can be found in [Sid99, page 691]. Equation 2.75 can be transformed with some trigonometrical calculations into:

$$\mathbf{f}_n = \frac{3}{8k} \begin{pmatrix} F_1 + F_{-1} + (\boldsymbol{\pi} \cdot \mathbf{b})^2 (2F_0 - F_1 - F_{-1}) & -i(\boldsymbol{\kappa} \cdot \mathbf{b})(F_1 - F_{-1}) - (\boldsymbol{\sigma} \cdot \mathbf{b})(\boldsymbol{\pi} \cdot \mathbf{b})(2F_0 - F_1 - F_{-1}) \\ i(\boldsymbol{\kappa} \cdot \mathbf{b})(F_1 - F_{-1}) - (\boldsymbol{\sigma} \cdot \mathbf{b})(\boldsymbol{\pi} \cdot \mathbf{b})(2F_0 - F_1 - F_{-1}) & F_1 + F_{-1} + (\boldsymbol{\sigma} \cdot \mathbf{b})^2 (2F_0 - F_1 - F_{-1}) \end{pmatrix} \quad (2.77)$$

Equation 2.77 simplifies drastically, if the preferred quantisation axis is parallel to one of the directions  $\boldsymbol{\sigma}$ ,  $\boldsymbol{\pi}$  or  $\boldsymbol{\kappa}$ . Examples will be seen later together with the time evolution of a decaying ensemble of excited states. If the quantisation axis is distributed isotropically or in a certain plane, the polarisation dependent part  $[(\boldsymbol{\epsilon}_\nu \times \boldsymbol{\kappa}) \cdot \mathbf{Y}_{1M}(\boldsymbol{\kappa}, \mathbf{b})][\mathbf{Y}_{1M}^*(\boldsymbol{\kappa}, \mathbf{b}) \cdot (\boldsymbol{\epsilon}_\mu \times \boldsymbol{\kappa})]$  has to be integrated over all Euler angles  $\alpha$ ,  $\beta$  and  $\gamma$  between  $\boldsymbol{\kappa}$  and  $\mathbf{b}$  [Röh94].

With the use of equations 2.69, 2.77 and 2.76, the transmission matrix  $\mathbf{T}_d(\omega) = e^{i\mathbf{nk}d}$  can be calculated. The matrix exponential can be calculated analytically for certain special cases only and numerically in general. To describe a SR experiment with linearly  $\sigma$ -polarised incoming radiation and a detector that is insensitive to the polarisation, the measured intensity is given by

$$I(t) = |\vec{A}'(t)|^2 = \left| \frac{1}{2\pi} \int_0^\infty \vec{A}'(\omega) e^{-i\omega t} d\omega \right|^2 \quad (2.78)$$

with

$$\vec{A}'(\omega) = \begin{pmatrix} T_{\sigma\sigma}(\omega) \\ T_{\sigma\pi}(\omega) \end{pmatrix} = \begin{pmatrix} T_{\sigma\sigma}(\omega) & T_{\sigma\pi}(\omega) \\ T_{\pi\sigma}(\omega) & T_{\pi\pi}(\omega) \end{pmatrix} \begin{pmatrix} 1 \\ 0 \end{pmatrix} \quad (2.79)$$

and thus

$$I(t) = I_{\sigma\sigma}(t) + I_{\pi\sigma}(t) = \left| \frac{1}{2\pi} \int_0^\infty T_{\sigma\sigma}(\omega) e^{-i\omega t} d\omega \right|^2 + \left| \frac{1}{2\pi} \int_0^\infty T_{\pi\sigma}(\omega) e^{-i\omega t} d\omega \right|^2 \quad (2.80)$$

Here, the inverse Fourier transform was used to obtain the time response  $\mathbf{A}'(t)$  of the scattering amplitude  $\mathbf{A}'(\omega)$ . Causality demands that the integral starts only at  $t=0$ , the arrival time of the SR flash, that is taken to be a delta function in time.

Using this result, some properties of nuclear forward scattering and examples are treated in the following chapters 2.4.4 to 2.4.6.

#### 2.4.4 Dynamical beats and speed-up

The first example to be considered is the case of absent hyperfine interactions. In this case, equation 2.77 reduces to  $\mathbf{f}_n = f_n \mathbf{1}$  with  $f_n$  given by equation 2.72 where the nuclear Thomson scattering term can be neglected. This can be understood as the denominator of 2.76 is equal for all terms and the sum of the nominators is proportional to  $2I_e + 1$ . This leads to  $F_{-1} = F_0 = F_1$  and thus  $F_1 - F_{-1} = 2F_0 - F_1 - F_{-1} = 0$ . The matrix of equation 2.77 is then of diagonal form and proportional to the unit matrix  $\mathbf{1}$ . Accordingly, the matrix exponential  $e^{\mathbf{i}nk d}$  can be determined analytically and the transmission matrix is given as [Sid99]

$$\mathbf{T}(\omega) = e^{-\frac{1}{2}\mu_e d} e^{i \frac{\Gamma_c}{(E_o - \hbar\omega) - i\Gamma/2}} \begin{pmatrix} 1 & 0 \\ 0 & 1 \end{pmatrix} \quad (2.81)$$

The first factor  $e^{-\mu_e d/2}$  is due to the electronic scattering amplitude and  $\mu_e = \varrho \sigma_{tot}$ .  $\Gamma_c$  is the enhanced resonance width given by

$$\Gamma_c = \pi \varrho \beta f_{LM} d \frac{1}{2k^2} \frac{1}{1 + \alpha} \frac{2I_e + 1}{2I_g + 1} \cdot \Gamma = \frac{1}{4} \varrho \sigma_o \beta f_{LM} d \cdot \Gamma \quad (2.82)$$

In the time evolution of the transmitted radiation, this leads to a speed up of the exponential decay. As  $\mathbf{T}(\omega)$  is diagonal, the scattering process does not change the polarisation of the incoming radiation.  $\vec{A}'(\omega)$  is a scalar and given by

$$A'(\omega) = e^{-\frac{1}{2}\mu_e d} e^{i \frac{\Gamma_c}{(E_o - \hbar\omega) - i\Gamma/2}} \quad (2.83)$$

The inverse Fourier transform leads to [Kag79]:

$$I(t) = e^{-\mu_e d} e^{-\frac{t}{\tau}} \frac{\chi}{t\tau} J_1^2 \left( \sqrt{\frac{4\chi t}{\tau}} \right) \quad (2.84)$$

where  $\chi = \frac{\Gamma_c}{\Gamma} = \frac{1}{4} \varrho \sigma_o \beta f_{LM} d$  is the so-called effective thickness and  $J_1$  is the first-order Bessel function.

Equation 2.84 can be approximated at early times by

$$I(t) \propto \chi^2 e^{-(1+\chi)\frac{t}{\tau}} \quad (2.85)$$

which shows that the initial decay is accelerated. This behaviour was termed speed-up. At later times, the Bessel function has repeated minima with decreasing time delay between two adjacent minima. The resulting beat structure was termed dynamical beats, as it appears in thick samples. In the limit of extremely thin samples, the time behaviour of  $I(t)$  approaches the simple decay behaviour of an isolated nucleus  $I(t) = e^{-t/\tau}$ . For  $^{61}\text{Ni}$  samples of varying thickness, the equation 2.84 is sketched in figure 2.11.

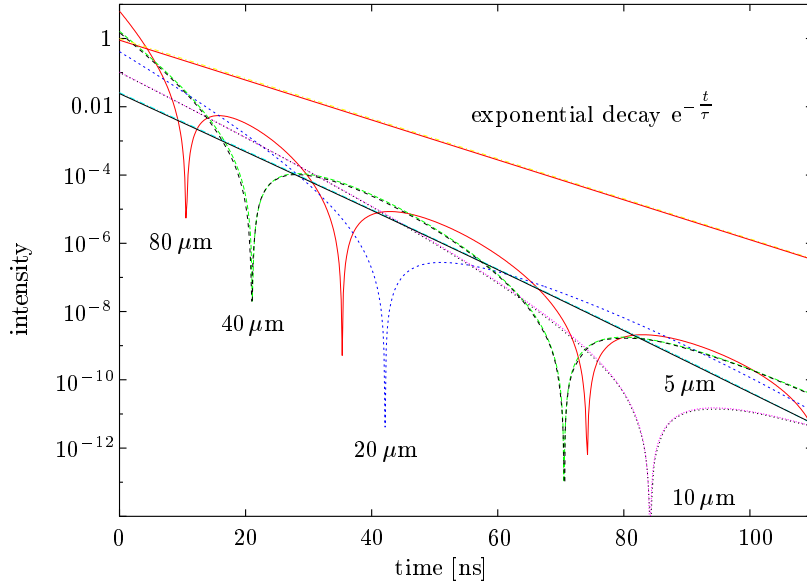


Figure 2.11: The influence of the thickness on NFS with absent hyperfine interactions. A fictive  $^{61}\text{Ni}$ -foil at 180 K without hyperfine splitting is considered. The Lamb-Mössbauer factor is 0.0246. For comparison, the exponential decay with the natural lifetime of 7.4 ns is also given. The decay for real samples is accelerated, this is called the speed-up. The oscillations in the spectra are called dynamical beats.

### 2.4.5 Quantum beats

Now, a nuclear resonant sample will be investigated under the presence of a magnetic hyperfine field. In particular, the magnetic hyperfine field is taken to be aligned in the vertical direction by an external magnetic field. This means  $\boldsymbol{\pi} = \mathbf{b}$ . In this case, equation 2.77 simplifies to

$$\mathbf{f}_n = \frac{3}{8k} \begin{pmatrix} 2F_0 & 0 \\ 0 & F_1 + F_{-1} \end{pmatrix} \quad (2.86)$$

The matrix exponential can be calculated easily, because the scattering amplitude is of diagonal form. As the incident radiation is  $\sigma$ -polarised, only the matrix element  $F_0$  has to be taken into account. The Jones vector for the transmitted radiation is given by

$$\vec{A}'(\omega) = e^{-\frac{1}{2}\mu_e d} e^{i3\chi \frac{1}{2I_e+1} \sum_{m_g} \frac{C^2(I_g 1 I_e; m_g 0)}{2(E_{m_g, m_e=m_g} - \hbar\omega)/\Gamma - i}} \begin{pmatrix} 1 \\ 0 \end{pmatrix} \quad (2.87)$$

The sum runs over the possible transitions between the ground state and the excited state which satisfy  $m_e = m_g$ , i.e.  $M = 0$ . In the case of  $^{61}\text{Ni}$ , these are four transitions, as can be seen in figure 2.8, each having a different energy. To illustrate the interference caused by several possible transitions in nuclear forward scattering, it is more simple to treat the case of  $^{57}\text{Fe}$ , where only two possible transitions exist ( $I_g = \frac{1}{2}$  instead of  $I_g = \frac{3}{2}$  in the case of  $^{61}\text{Ni}$ ). The two transition energies are  $E_a$  and  $E_b$ . Writing  $\vec{A}'(\omega)$  as a scalar now for the  $^{57}\text{Fe}$  case, it is:

$$A'(\omega) = e^{-\frac{1}{2}\mu_e d} e^{i\frac{\chi}{2} \left( \frac{1}{2(E_b - \hbar\omega)/\Gamma - i} + \frac{1}{2(E_a - \hbar\omega)/\Gamma - i} \right)} \quad (2.88)$$

The Fourier transform can easily be performed numerically, although an analytical solution in this case is not at all evident. Still, if the splitting of the two transitions



$\Delta E = |E_b - E_a|$  is larger than the natural line width  $\Gamma$ , a good approximation can be found as [Han99, page 218-219]:

$$A'(t) = -i e^{-\frac{1}{2}\mu_e d} e^{-\frac{t}{2\tau}} \sqrt{\frac{\chi}{2t\tau}} (e^{-iE_a t} + e^{-iE_b t}) J_1\left(\sqrt{\frac{2\chi t}{\tau}}\right) \quad (2.89)$$

This leads to the measured intensity of

$$I(t) = e^{-\mu_e d} e^{-\frac{t}{\tau}} \frac{\chi}{2t\tau} J_1^2\left(\sqrt{\frac{2\chi t}{\tau}}\right) \cos^2 \frac{\Delta E}{2} t \quad (2.90)$$

The cos-term leads to a distinct beat structure. This effect is known as quantum beats. A similar equation as 2.90 can be derived for  $^{57}\text{Fe}$ -nuclei under the influence of an electric field gradient. However, to get the two transitions with equal intensity, an isotropic distribution of the electric field gradient direction is necessary.

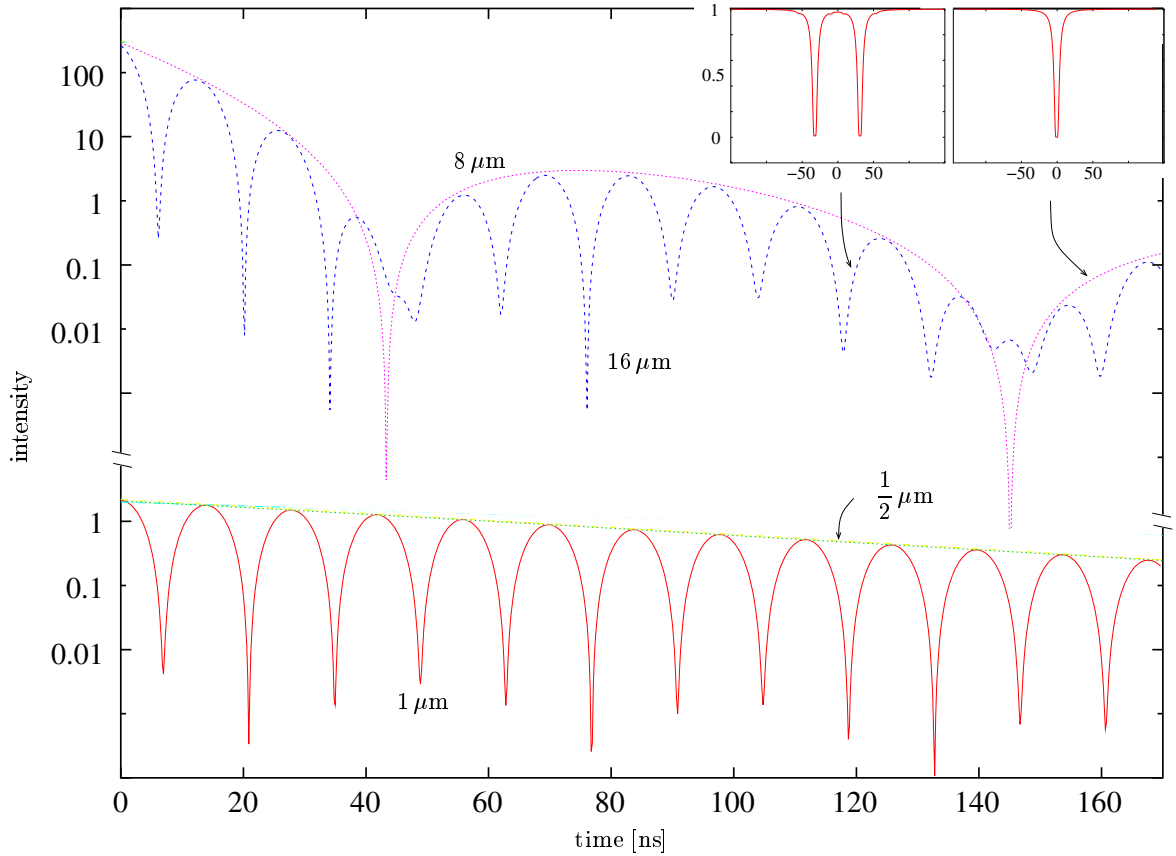


Figure 2.12: Quantum beats for  $\alpha$ - $^{57}\text{Fe}$ -iron at 300 K. The nuclear spins are aligned along the  $\pi$ -direction, e.g. by a small external alignment field. The envelope is a hypothetical non-magnetic  $^{57}\text{Fe}$ -foil of half the thickness. The inset shows the corresponding Mössbauer absorption spectrum where the horizontal axis is the energy in units of the natural linewidth  $\Gamma = 4.65 \text{ neV}$  for  $^{57}\text{Fe}$ . The vertical axis is the transmitted intensity. The splitting is much larger than the natural line width.

Figure 2.12 shows quantum beats in the time spectrum of  $\alpha$ - $^{57}\text{Fe}$  at 300 K. The hyperfine field of  $^{57}\text{Fe}$  is 33 T. The nuclear spins are aligned in the  $\pi$ -direction, which experimentally can be achieved with a small external alignment field. The calculations are performed with the program Motif [Stu94] and not following equation 2.90 as to avoid the approximation used in calculating the Fourier transform of equation 2.88. The result shows that for both thin and thick samples, the time spectrum of NFS is very close

to the modulated cosine function of equation 2.90. As shown in the inset of the figure, the energy difference of the two transitions, given in units of  $\Gamma$ , is much larger than the natural line width. It was stated above that this is a necessary condition to obtain the simple equation 2.90. The overlaying envelope was calculated assuming a hypothetical sample with vanishing hyperfine field of half the thickness as used in the original curve. The envelope only shows dynamical beats.

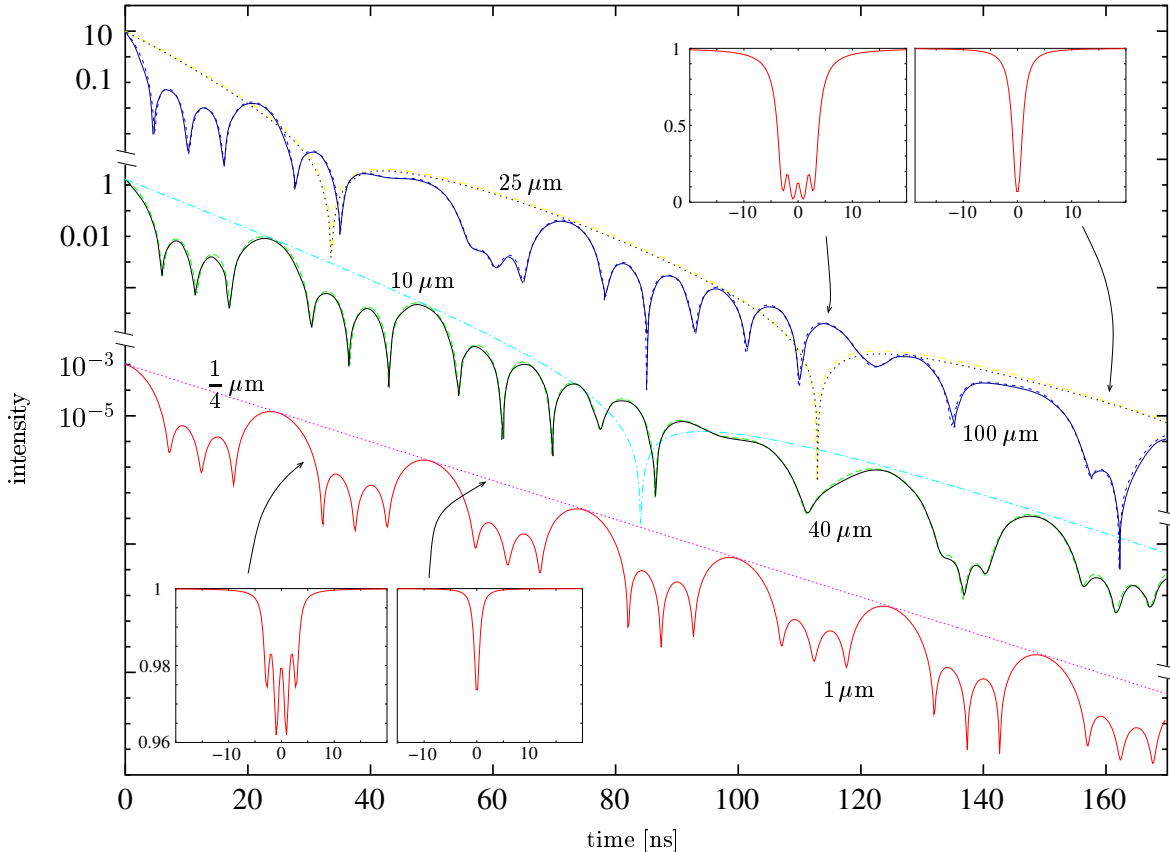


Figure 2.13: Quantum beats for metallic  $^{61}\text{Ni}$  at 180 K. The nuclear spins are aligned along the  $\pi$ -direction, e.g. by a small external field. As the splitting is not much larger than the natural linewidth, the envelope of a hypothetical non-magnetic  $^{61}\text{Ni}$ -foil of a quarter of the thickness does not match perfectly. The inset shows the corresponding Mössbauer absorption spectrum for the thinnest and the thickest foil.

In the case of  $^{61}\text{Ni}$ , where four transitions are allowed with the nuclei being aligned in the  $\pi$ -direction, the simple cosine term of equation 2.90 does not hold. As the energies of the four transitions are equally spaced, three distinct energy differences exist, giving rise to three frequencies in the NFS time spectrum.

For a thin sample of  $1\ \mu\text{m}$  at 180 K, the time spectrum is shown at the bottom of figure 2.13. The magnetic hyperfine field was taken to be 7.3 T. The envelope assuming a fictive identical non-magnetic sample of one fourth of the thickness is shown for comparison. The corresponding Mössbauer absorption spectra are shown in the lower left inset. It is seen that the splitting is only slightly larger than the line width. Therefore, the time spectra with  $40\ \mu\text{m}$  and  $100\ \mu\text{m}$  thick samples are not equivalent to the curve of the magnetic  $1\ \mu\text{m}$  thick  $^{61}\text{Ni}$ -foil modulated by the simple dynamical beat behaviour. The Mössbauer absorption spectra for the  $100\ \mu\text{m}$  thick magnetic foil and the  $50\ \mu\text{m}$  non-magnetic foil are shown in the top right inset.

### 2.4.6 Distributions of magnetic quantisation axis

If the quantisation axis of the nuclei varies inside the sample, this has to be taken into account in nuclear scattering matrix as given by equation 2.77. It was already stated that the polarisation dependent part  $[(\boldsymbol{\epsilon}_\nu \times \boldsymbol{\kappa}) \cdot \mathbf{Y}_{1M}(\boldsymbol{\kappa}, \mathbf{b})][\mathbf{Y}_{1M}^*(\boldsymbol{\kappa}, \mathbf{b}) \cdot (\boldsymbol{\epsilon}_\mu \times \boldsymbol{\kappa})]$  has to be integrated over all Euler angles  $\alpha$ ,  $\beta$  and  $\gamma$  between  $\boldsymbol{\kappa}$  and  $\mathbf{b}$ . If the distribution is completely isotropic, the integration has to be done as given by [Röh94]:

$$\frac{1}{8\pi^2} \int_0^{2\pi} \int_0^\pi \int_0^{2\pi} [(\boldsymbol{\epsilon}_\nu \times \boldsymbol{\kappa}) \cdot \mathbf{Y}_{1M}(\boldsymbol{\kappa}, \mathbf{b})][\mathbf{Y}_{1M}^*(\boldsymbol{\kappa}, \mathbf{b}) \cdot (\boldsymbol{\epsilon}_\mu \times \boldsymbol{\kappa})] d\alpha \sin\beta d\beta d\gamma \quad (2.91)$$

However, in thin films the magnetisation is often restricted to lie in the film plane. Then the integral has to be taken with  $\frac{1}{4\pi^2} \int_0^{2\pi} \int_0^{2\pi} \dots d\alpha d\gamma$  with  $\beta = 90^\circ$ . The resulting nuclear scattering matrices are given by [Röh04a]

$$\mathbf{f}_n^{3d} = \frac{3}{8k} \begin{pmatrix} F_1 + F_{-1} + F_0 & 0 \\ 0 & F_1 + F_{-1} + F_0 \end{pmatrix} \quad \mathbf{f}_n^{2d} = \frac{1}{4k} \begin{pmatrix} F_1 + F_{-1} & 0 \\ 0 & \frac{1}{2}F_1 + \frac{1}{2}F_{-1} + F_0 \end{pmatrix} \quad (2.92)$$

In most experiments with SR, the incident radiation is  $\sigma$ -polarised and the scattered radiation is detected by a polarisation insensitive detector. If the scattering matrix is of diagonal form, only  $F_{\sigma\sigma}$  will contribute. The scattering matrix is also diagonal for  $\mathbf{b} \parallel \boldsymbol{\sigma}$  and  $\mathbf{b} \parallel \boldsymbol{\pi}$ . For  $\mathbf{b} \parallel \boldsymbol{\kappa}$ , this is not the case and polarisation mixing occurs. Polarisation mixing is often referred to as a generalised kind of Faraday-effect.

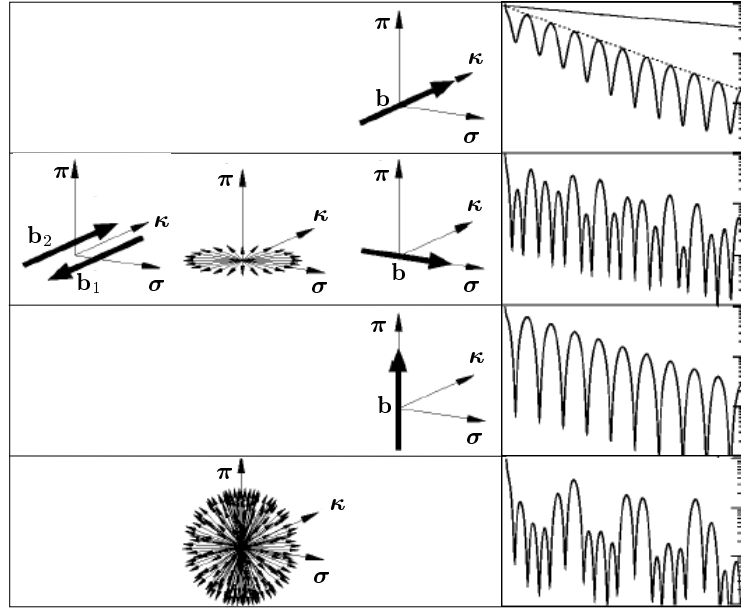


Figure 2.14: The time spectra of nuclear forward scattering on a thin  $^{57}\text{Fe}$  sample with the magnetic quantisation axis aligned or distributed as depicted to the left [Röh04a]. The quantum beats are more or less complex, depending on the number of interfering transitions with different energy.

For  $\alpha$ -iron, the NFS spectra under the conditions stated above are depicted in figure 2.14 for a very thin sample, i.e. no dynamical beats appear. If one has to distinguish between the three cases of row two, additional measurements with a tilted sample can tell the difference, as a different scattering geometry will change  $F_{\sigma\sigma}$ .

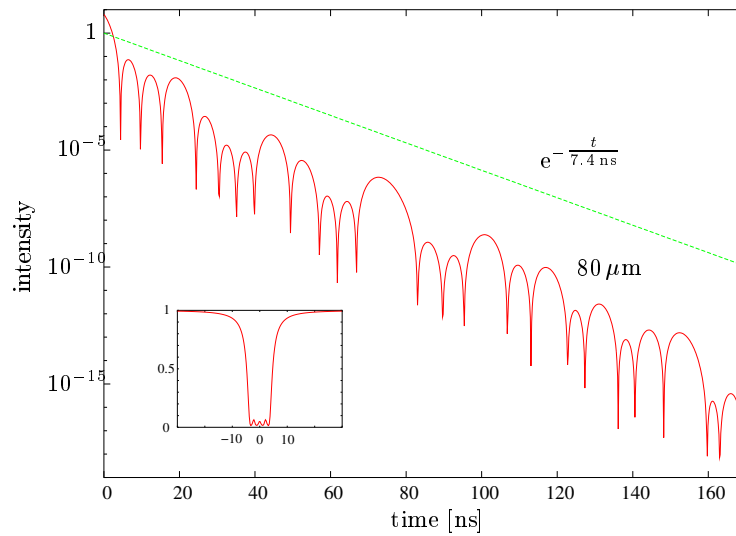


Figure 2.15: The time spectrum of nuclear forward scattering on a polycrystalline  $^{61}\text{Ni}$  sample of  $80\ \mu\text{m}$  thickness at  $180\ \text{K}$ .

Again, the time spectrum of  $^{61}\text{Ni}$  is more complex, due to the maximal 12 possible transitions. The case of a polycrystalline metallic  $^{61}\text{Ni}$ -foil, thus the  $3d$ -case, is calculated with Motif for a  $80\ \mu\text{m}$  thick foil at  $180\ \text{K}$  and with a magnetic hyperfine field of  $7.3\ \text{T}$ , see figure 2.15. For comparison, also  $e^{-t/7.4\ \text{ns}}$  is depicted, i.e. the decay corresponding to the natural lifetime.

The inset of figure 2.15 shows the corresponding Mössbauer absorption spectrum. The magnetic hyperfine splitting in metallic  $^{61}\text{Ni}$  is very small. As the splitting of the excited state  $\Delta E_e = \mu_e B_{hf}/I_e = 44\ \text{neV}$  is much smaller than the splitting of the ground state  $\Delta E_g = \mu_g B_{hf}/I_g = 115\ \text{neV}$ , the twelve transitions are not resolved in the Mössbauer absorption spectrum. Remember that the natural line width is  $85.4\ \text{neV}$ . As can be seen in figure 2.8, the twelve lines can be approximated by 4 triplets which are still resolved in the Mössbauer absorption spectrum. This case is thus not too different from the case of an aligned  $^{61}\text{Ni}$  sample as discussed and depicted in chapter 2.4.5. However, the time spectra of NFS differ quite a lot. The resolution of NFS does not suffer from thick samples.

### 2.4.7 Principal experimental setup of NFS

A brief sketch of the experimental setup used in nuclear forward scattering is shown in figure 2.16. The detector is placed in the direct beam to detect the forward scattered radiation. Coherently scattered radiation of non-crystalline samples only exists in the forward direction or in specular reflections. Unfortunately, non-interacting radiation or electronically scattered radiation is present in the forward direction, too. In fact, it dominates by far the nuclear signal, as the incident radiation is much broader in energy than the nuclear line width. Sophisticated monochromatisation schemes have to be used too limit the detector charge as much as possible without reducing the nuclear signal. The nuclear signal is "filtered" out of the huge total signal by timing electronics. Non-interacting radiation or electronically scattered radiation basically arrives without delay at the detector, whereas the nuclear scattered radiation is delayed in time ranging from  $0\ \text{ns}$  up to several lifetimes of the excited nuclear level. The delayed arrival time with respect

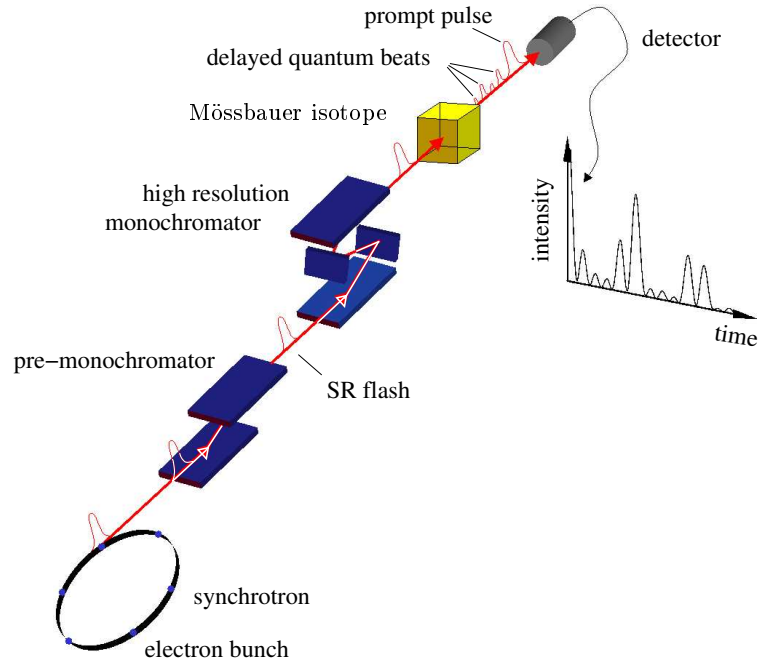


Figure 2.16: View of the experimental setup used for nuclear forward scattering.

to the prompt flash is analysed and a time spectrum acquired. This implies a pulsed time structure of the electrons in the storage ring with sufficiently large gaps between adjacent electron bunches. Furthermore, each electron bunch needs to be short in time. These filling modes are called timing modes. Figure 2.16 indicates quantum beats travelling towards the detector after the nuclear scatterer as one example of a nuclear response.

## 2.5 Grazing incidence scattering

If an electromagnetic wavefield impinges on a surface under a small angle, i.e. in grazing incidence, it gives rise to a reflected and a transmitted wavefield. Reflected and transmitted beam represent two open scattering channels and form the case of a 2-beam diffraction. It is possible to extend the theory developed in chapter 2.4.3 for the case of two (or more) open scattering channels [Röh99b].

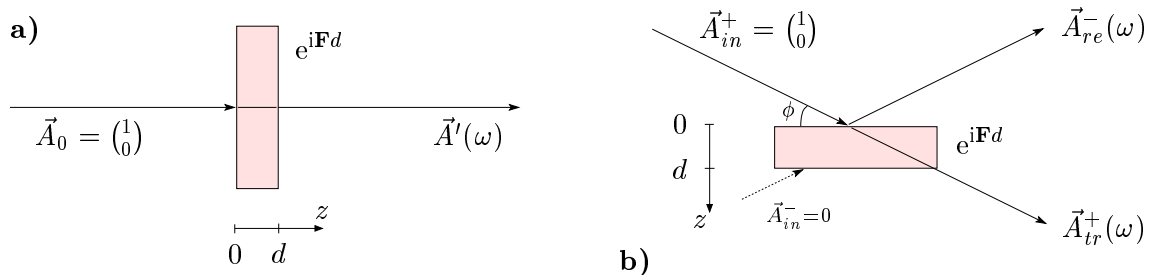


Figure 2.17: Geometry in nuclear forward scattering experiments, panel a), and for grazing incidence reflections, panel b).

Similar to equation 2.70 for forward scattering, the 2-beam case of grazing incidence can

be expressed by the following 4 dimensional equation:

$$\underline{A}(d) = e^{i\mathbf{F}d} \underline{A}(0) \quad (2.93)$$

with the 4 dimensional matrix  $\mathbf{F}$  given in grazing incidence as [Röh99b]:

$$\mathbf{F} = \begin{pmatrix} \mathbf{f} + \mathbf{k}_{0z} & \mathbf{f} \\ -\mathbf{f} & -\mathbf{f} - \mathbf{k}_{0z} \end{pmatrix} \quad (2.94)$$

Here,  $\mathbf{f}$  and  $\mathbf{k}_z = k_z \mathbf{1} \approx \mathbf{k}\phi \cdot \mathbf{1}$  are again the  $2 \times 2$  matrices as described in chapter 2.4.3. Only if the incident angle  $\phi$  is very small, all four  $\mathbf{f}$  matrices that appear in equation 2.94 are identical. The wavevectors  $\underline{A}(0)$  and  $\underline{A}(d)$  are supervectors combining both open scattering channels, designed + for the incident direction and – for the reflected direction:

$$\underline{A}(d) = \begin{pmatrix} \vec{A}_{tr}^+(\omega) \\ \vec{0} \end{pmatrix} \quad \text{and} \quad \underline{A}(0) = \begin{pmatrix} \vec{A}_{in}^+ \\ \vec{A}_{re}^- \end{pmatrix} \quad (2.95)$$

It is helpful to introduce a matrix  $\mathbf{T}$  as defined by

$$e^{i\mathbf{F}d} =: \mathbf{T}(\mathbf{F}) = \begin{pmatrix} \mathbf{T}_{++}(\mathbf{F}) & \mathbf{T}_{+-}(\mathbf{F}) \\ \mathbf{T}_{-+}(\mathbf{F}) & \mathbf{T}_{--}(\mathbf{F}) \end{pmatrix} \quad (2.96)$$

With this notation, the reflected wavefield can be calculated as

$$\vec{A}_{re}^-(\omega) = \underbrace{-[\mathbf{T}_{--}(\mathbf{F})]^{-1} \mathbf{T}_{-+}(\mathbf{F})}_{=: \mathbf{R}} \vec{A}_{in}^+ = -[\mathbf{T}_{--}(\mathbf{F})]^{-1} \mathbf{T}_{-+}(\mathbf{F}) \begin{pmatrix} 1 \\ 0 \end{pmatrix} \quad (2.97)$$

If the scattering matrix  $\mathbf{F}$  is not constant over the thickness  $z$ , like in a layer system of  $N$  layers, the matrix  $\mathbf{T}$  is a product of the matrix exponentials of the individual layers:

$$\mathbf{T} = e^{i\mathbf{F}_N d_N} \dots e^{i\mathbf{F}_2 d_2} e^{i\mathbf{F}_1 d_1} \quad (2.98)$$

The scattering matrices  $\mathbf{F}_i$  account for the electronic and nuclear scattering properties of each individual layer and depend on the incident angle  $\phi$  via the  $\mathbf{k}_z \approx k\phi \cdot \mathbf{1}$  contribution.

Numerically, the matrix exponential  $\mathbf{T} = \prod_i e^{i\mathbf{F}_i d}$  can be derived without further assumptions. Then, equation 2.97 allows to calculate the reflected amplitude and properties important in grazing incident scattering: This is first the reflected intensity as a function of the incident angle  $\phi$  solely due to electronic scattering. It can be calculated if  $\omega$  is chosen close to, but not on the nuclear resonance energy. This is equivalent to neglecting the nuclear scattering amplitude  $\mathbf{f}_n$ . Second, the nuclear contribution can be included and  $\vec{A}_{re}^-(\omega)$  calculated as a function of  $\omega$ , keeping  $\phi$  fixed. The delayed intensity as a function of time is again obtained with the Fourier transform

$$I_{re}(t) = \left| \frac{1}{2\pi} \int_0^\infty \vec{A}_{re}^-(\omega) e^{i\omega t} d\omega \right|^2 \quad (2.99)$$

This time dependent intensity can be integrated over times ranging from  $t_0$  to  $t_1$ . If this procedure is repeated for varying incident angles  $\phi$ , the nuclear reflectivity curve is obtained.

To reduce computing time and to obtain further physical insight of the reflection matrix  $\mathbf{R}$ , the scattering matrix  $\mathbf{F}$  can be diagonalised. An important step of this procedure

is the diagonalisation of  $\mathbf{f}$ . At the end, the matrix exponential  $\prod_i e^{i\mathbf{F}d}$  is expressed as a multiplication of several matrices describing individual processes. For a single freestanding layer, the following expression is derived [Röh99b]:

$$\mathbf{T} = e^{i\mathbf{F}d} = \mathbf{G}_1 \mathcal{T}_{01}^{-1} \mathbf{R}_{01} \mathbf{E}_1 \mathbf{R}_{10} \mathcal{T}_{10}^{-1} \mathbf{G}_1^{-1} \quad (2.100)$$

where all matrices are  $4 \times 4$  matrices as to describe the 2 open scattering channels and two orthogonal polarisations.  $\mathbf{G}_1$  is a coordinate transformation between the chosen set of polarisations and the one in which  $\mathcal{F}$  is of diagonal form.  $\mathcal{T}$  is the transmission of the eigenpolarisations through the interface of vacuum and layer 1.  $\mathbf{R}$  is the reflectivity matrix at the interface vacuum and layer 1 and  $\mathbf{E}$  describes the propagation of the eigenpolarisations through the layer 1. This formalism can be extended to multiple layers easily.

If the layer containing the Mössbauer isotope is ultrathin, it is possible to approximate its scattering matrix  $\mathbf{T} = e^{i\mathbf{F}d}$  by  $\mathbf{T} \approx 1 + id\mathbf{F}$ . It can be shown [Röh99a, Röh04b], that the frequency dependent contribution to the reflectivity matrix  $\mathbf{R}$  as introduced in equation 2.97 is then given by

$$\mathbf{R}(\omega) = ida^2(d_{\text{utl}})\mathbf{f}(\omega) \quad (2.101)$$

with  $a^2(d_{\text{utl}})$  being the normalised wave field intensity at the depth  $d_{\text{utl}}$  of the ultrathin layer of thickness  $d$ . This wave field intensity depends on the electronic scattering properties of the whole layer system and can be increased by an appropriate waveguide structure with the ultrathin layer placed in an anti-node, see chapter 3.4.2. As the layer containing the Mössbauer isotope is ultrathin, the wave field intensity does not depend on the nuclear scattering amplitude in first order. Equation 2.101 is valid as long as  $(k_z d)^2 < 0.1$ , corresponding to nm thickness at typical incident angles at the resonant energy of  $^{57}\text{Fe}$ . This ultrathin limit corresponds to nuclear forward scattering by the ultrathin layer with an effective thickness of  $a^2(d_{\text{utl}})d$ . This case is referred to as the kinematical approximation.

## 2.6 The nuclear lighthouse effect

In nuclear forward scattering, the signal originating from the interaction of the incident photons with the nuclei is delayed with respect to the electronically scattered radiation. This allows to distinguish between them. However, to do so, the exciting radiation has to provide a well defined time structure with quiet time periods that allow to detect the delayed quanta in the absence of electronically scattered radiation. Furthermore, as the detector is placed in the direct beam and the lifetime of the nuclear levels is very short, i.e. typically 1 to 100 ns, the detector needs to recover rapidly after the electronically scattered radiation. This is only possible if the electronically scattered intensity is reduced drastically with the use of high resolution monochromators. A method that achieves a separation of electronic and nuclear scattered photons not only in time, but also in space, is the nuclear lighthouse effect [Röh99c, Röh00c]. This name is used to describe a coherent nuclear resonant scattering experiment on a rapidly rotating sample. High resolution monochromators and a certain time structure of the incident radiation are not essential for this effect.

### 2.6.1 Phase shift upon rotation

Formally, the nuclear lighthouse effect can be explained using angular momentum conservation of a system. Linear translations of spatial coordinates involve a phase shift of the eigenstates of the system that are proportional to the invariants of motion  $\vec{p}$ , the linear momentum, and  $\vec{J}$ , the angular momentum [Röh98]. Here, we are concerned with rotations:

$$\vec{A}(\vec{\psi}_o + \vec{\psi}) = e^{-\frac{i}{\hbar} \vec{J} \cdot \vec{\psi}} \vec{A}(\vec{\psi}_o) \quad (2.102)$$

During a coherent scattering process, the phase difference between the participating scatterers excited by the incident radiation of wavevector  $\vec{k}_o$  stays constant. In nuclear resonant scattering, this coherent excited state is called the nuclear exciton. For a sample at rest, the decay of the exciton follows in the direction of  $\vec{k}_o$ , unless the arrangement of the nuclei allows for Bragg scattering, too. Now suppose the sample spinning with constant angular velocity  $\vec{\Omega}$  and  $\vec{\phi}(t) = \vec{\Omega}t$ . This situation is sketched in figure 2.18.

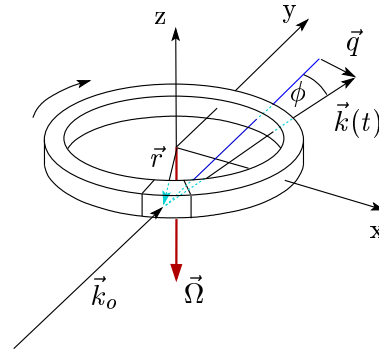


Figure 2.18: Nuclear resonant scattering on a rotating sample element.

Similar to equation 2.102, the nuclear exciton as described via the time-dependent wavefield  $\vec{A}_o(\vec{r}, t)$  that it emits at rest, acquires an additional phase:

$$\vec{A}(\vec{r}, t) = e^{-\frac{i}{\hbar} \vec{J} \cdot \vec{\Omega}t} \vec{A}_o(\vec{r}, t) = e^{-\frac{i}{\hbar} \vec{J} \cdot \vec{\Omega}t} e^{i\vec{k}_o \cdot \vec{r}} \vec{A}_o(t) \quad (2.103)$$

where  $\vec{A}_o(t)$  is the Jones vector of the scattered radiation as given in equation 2.78. The angular momentum  $\vec{J}$  is the sum of orbital angular momentum  $\vec{L}$  and of the spin  $\vec{S}$ :

$$\vec{J} = \vec{L} + \vec{S} = \hbar \vec{r} \times \vec{k}_o + \vec{S} \quad (2.104)$$

Inserting this into equation 2.103, we obtain the exponentials  $\exp(i(\vec{r} \times \vec{k}_o) \cdot \vec{\Omega}t) \cdot \exp(\frac{i}{\hbar} \vec{S} \cdot \vec{\Omega}t)$ . The second factor containing the spin  $\vec{S}$  does not change the  $\vec{r}$  dependence of  $\vec{A}(\vec{r}, t)$ . It changes the polarisation state of  $\vec{A}(\vec{r}, t)$  and may introduce an energy shift of the nuclear level by an amount of  $\hbar\Omega$  which is negligible as compared to the natural linewidth of the nuclear levels [Röh00c]. As the detectors used in nuclear resonant scattering experiments do not depend on the polarisation of the detected radiation, we can neglect this term here.

Using basic vector algebra one can rewrite

$$\frac{1}{\hbar} \vec{J} \cdot \vec{\Omega}t \Rightarrow \frac{1}{\hbar} \vec{L} \cdot \vec{\Omega}t = (\vec{r} \times \vec{k}_o) \cdot \vec{\Omega}t = (\vec{k}_o \times \vec{\Omega}t) \cdot \vec{r} \quad (2.105)$$

and finally obtains [Röh00a, Röh00c]

$$\vec{A}(\vec{r}, t) = e^{i(\vec{k}_o - \vec{k}_o \times \vec{\Omega}t) \cdot \vec{r}} \vec{A}_o(t) \quad (2.106)$$



It is visible that equation 2.106 represents a time modulated ( $\vec{A}_o(t)$ ) plane wave in the direction of  $\vec{k}(t) = \vec{k}_o - \vec{k}_o \times \vec{\Omega}t$ . As the scattering vector  $\vec{q} = \vec{k}(t) - \vec{k}_o = -\vec{k}_o \times \vec{\Omega}t$  is linear in the time, the time response is mapped onto an angular scale with  $|\vec{q}(t)| = k_o \Omega t = k_o \phi(t)$ .

However, the incident SR radiation is not a perfect plane wave but a divergent beam. This leads to a reduced degree of transverse coherence at the nuclei. The transverse coherence is described by a mutual coherence function  $W(\vec{r})$ , represented by a Gaussian of standard deviation  $\xi$ . To obtain information about the angular dependence of the scattered radiation under this condition, it is more convenient to treat the scattering amplitude in reciprocal space. This is done with the Fourier transform

$$\vec{A}(\vec{k}, t) = \int \vec{A}(\vec{r}, t) e^{-i\vec{k}\vec{r}} d\vec{r} = \vec{A}_o(t) \int e^{i(\vec{k}_o - \vec{k}_o \times \vec{\Omega}t) \cdot \vec{r}} e^{-i\vec{k}\vec{r}} d\vec{r} \quad (2.107)$$

With  $\vec{q} = \vec{k}(t) - \vec{k}_o$ , this transforms to

$$\vec{A}(\vec{q}, t) = \vec{A}_o(t) \int e^{-i(\vec{q} - \vec{k}_o \times \vec{\Omega}t) \cdot \vec{r}} d\vec{r} \quad (2.108)$$

In equation 2.108, we still have to include the reduced coherence via the function  $W(\vec{r})$ :

$$\vec{A}(\vec{q}, t) = \vec{A}_o(t) \int e^{-i(\vec{q} - \vec{k}_o \times \vec{\Omega}t) \cdot \vec{r}} W(\vec{r}) d\vec{r} \quad (2.109)$$

If the coherence length is assumed as infinite, the coherence function  $W(\vec{r})$  is constant and 1. The integration of  $\int_{-\infty}^{\infty} e^{-i(\vec{q} - \vec{k}_o \times \vec{\Omega}t) \cdot \vec{r}} d\vec{r}$  leads to  $\delta(\vec{q} - \vec{k}_o \times \vec{\Omega}t)$ . Thus:

$$\vec{A}(\vec{q}, t) = \vec{A}_o(t) \delta(\vec{q} - \vec{k}_o \times \vec{\Omega}t) \quad (2.110)$$

It is convenient to use now  $-\vec{k}_o \times \vec{\Omega}t = k_o \Omega t \hat{x} = k_o \phi \hat{x}$ .

If the coherence length is  $\xi$ , equation 2.109 transforms to

$$\vec{A}(\vec{q}, t) = \vec{A}_o(t) \int e^{-i(\vec{q} - \vec{k}_o \times \vec{\Omega}t) \cdot \vec{r}} e^{-\frac{2x^2}{\xi^2}} d\vec{r} \quad (2.111)$$

The integration together with  $|\vec{q}| = k_o \phi$  leads to

$$\vec{A}(\phi, t) = \vec{A}_o(t) e^{-\frac{1}{2}\xi^2(\phi - \Omega t)^2} \quad (2.112)$$

As the intensity measured at a fixed angle is the square of the wavefield amplitude at that angle, one calculates

$$I(\phi) = \int_0^{\infty} |\vec{A}(\vec{q}, t)|^2 dt \quad (2.113)$$

The results derived here are consistent with a more vigorous theoretical approach [Röh00c] directly in the space time formalism derived by Shvyd'ko [Shv99].

### 2.6.2 Nuclear lighthouse effect experimental scheme

The principal experimental realisation of the nuclear lighthouse effect is depicted in figure 2.19. The delayed nuclear signal of the rotating sample is mapped onto an angular scale. Unfortunately, the nuclear signal is not the only deviated signal. Small angle X-ray scattering also leads to photons deviated off beam-axis, see chapter 2.7. Its distribution to the obtained signal by the detector can be as important as the nuclear signal itself. In figure 6.5, the SAXS is included for the case of an  $^{61}\text{Ni}$  measurement. For technical details of the rotor/stator system, refer to chapter 4.3.

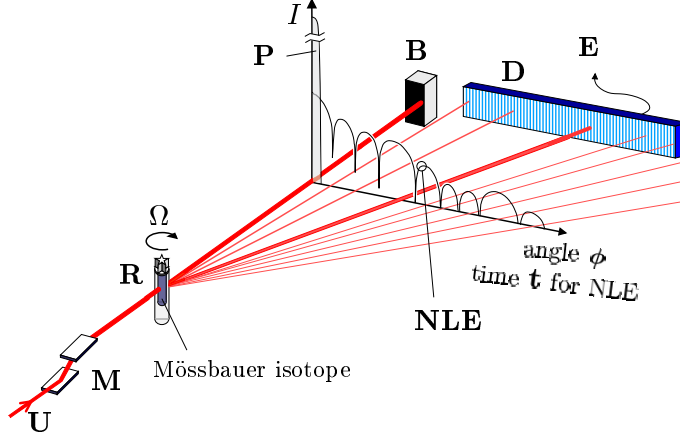


Figure 2.19: Basic experimental setup of the nuclear lighthouse effect. The undulator radiation  $\mathbf{U}$  is monochromatised coarsely by a simple pre-monochromator  $\mathbf{M}$ . The rotor  $\mathbf{R}$  containing a Mössbauer isotope is spinning at high frequencies  $\Omega$ . The non-interacting prompt direct beam (intensity  $\mathbf{P}$ ) hits the beamstop  $\mathbf{B}$ . The delayed nuclear lighthouse effect signal  $\mathbf{NLE}$  is deviated as a function of time and rotor frequency and hits a position sensitive detector  $\mathbf{D}$ . This detector acquires intensity as a function of the deviation angle. In fact, the time spectrum of NFS is mapped to an angular scale. Small angle X-ray scattering, see chapter 2.7 and figure 6.5, has been neglected.

### 2.6.3 Energy shifts

The nuclear lighthouse effect is not only useful as a powerful variation of nuclear forward scattering thanks to the mapping of the decaying radiation onto an angular scale. It further allows to shift the energy of the scattered radiation by small amounts, which is useful in inelastic X-ray scattering [Bur00]. This is explained in detail in [Röh97, Röh98, Röh00b].

To analyse this energy shift, we rewrite the rotational phase of equation 2.105

$$\frac{1}{\hbar} \vec{J} \vec{\Omega} t \Rightarrow (\vec{r} \times \vec{k}_o) \cdot \vec{\Omega} t = (\vec{\Omega} \times \vec{r}) \cdot \vec{k}_o t = \vec{v} \cdot \vec{k}_o t \quad (2.114)$$

Inserting this into equation 2.103:

$$\vec{A}(\vec{r}, t) = e^{i \vec{v} \vec{k}_o t} e^{i \vec{k}_o \vec{r}} \vec{A}_o(t) \quad (2.115)$$

With the Fourier transform, we obtain the scattered amplitude in the energy domain as:

$$\vec{A}(\vec{r}, \omega) = \int e^{i \omega t} e^{i \vec{v} \vec{k}_o t} e^{i \vec{k}_o \vec{r}} \vec{A}_o(t) dt = e^{i \vec{k}_o \vec{r}} \int e^{i(\omega + \vec{v} \vec{k}_o) t} \vec{A}_o(t) dt \quad (2.116)$$

This means that the energy of the scattered radiation is Doppler shifted by the amount  $\Delta\omega = \vec{v} \vec{k}_o$ . For this purpose, it is best to irradiate the nuclear scatterer in the rotor at its edge, so that  $\vec{v} \parallel \vec{k}_o$ . The energy shift will be at maximum. If the rotor is irradiated in its center,  $\vec{v} \perp \vec{k}_o$  and the energy shift is zero. In fact, with the geometry as used in figure 2.18, it is  $\Delta\omega = \vec{v} \vec{k}_o = \Omega k_o x$ .

If a slit after the rotating sample at angle  $\phi_s$  selects a part of the nuclear scattered radiation, the energy of this radiation can be shifted over a few meV when changing the position  $x$  of the impinging beam on the rotor. This has been demonstrated on the  $^{57}\text{Fe}$  resonance [Qua02]. This might allow in future to perform nuclear inelastic scattering

experiments with  $\mu\text{eV}$  resolution [Röh00b, Bur00]. The energetic width of the radiation is only a few  $\mu\text{eV}$  large, depending on the sum of nuclear level width and the lateral beamsizes  $\Delta x$  of the beam at the rotor.

## 2.7 Introduction to small angle X-ray scattering

### 2.7.1 Scattered intensity and correlation function

Small angle X-ray scattering is an elastic scattering process of photons on electron density variations [Wil93]. If the lateral dimensions of these density variations are in the range of 1 to 100 nm, these variations lead to a momentum transfer  $q$  in the angular range within less than 1 degree of the incident beam. This is also the angular range of the expected NLE signal with typical rotor frequencies and nuclear lifetimes. Contrary to the delayed signal originating from an interaction with a Mössbauer nuclei, SAXS happens on a "prompt" time scale of approximately  $10^{-15}$  s.

The volume element  $d^3r$  at the position  $\vec{r}$  contains  $\rho(\vec{r})d^3r$  electrons. The scattering amplitude of this volume element under irradiation is given as [Gla91]:

$$A(q) = A_o \iiint \rho(\vec{r}) e^{-i\vec{q}\cdot\vec{r}} d^3r \quad (2.117)$$

where the scattering vector is given by  $\vec{q} = \vec{k}_{\text{out}} - \vec{k}_{\text{in}}$  and its amplitude in an elastic scattering process with  $|\vec{k}_{\text{in}}| = |\vec{k}_{\text{out}}| = k$  can be expressed as

$$q = 2k \sin \frac{\theta}{2} \approx k\theta \quad (2.118)$$

The last approximation is only valid for small scattering angles  $\theta$  between incident and outgoing wavevector. The scattered intensity as a function of  $q$  is given as

$$I(q) = A(q) \cdot A^*(q) = I_o \iiint d^3r_1 \iiint d^3r_2 \rho(\vec{r}_1) \rho(\vec{r}_2) e^{-i\vec{q}\cdot(\vec{r}_1 - \vec{r}_2)} \quad (2.119)$$

$I_o$  is proportional to the incident intensity and to the square of the classical electron radius  $R_e = \frac{e^2}{m_e c^2}$ . It is useful to introduce an autocorrelation function, also known as Patterson function [Por82], given by

$$\hat{\rho}^2(\vec{r}) = \iiint \rho(\vec{r}') \rho(\vec{r}' + \vec{r}) d^3r' \quad (2.120)$$

which leads to

$$I(q) = I_o \iiint \hat{\rho}^2(\vec{r}) e^{-i\vec{q}\cdot\vec{r}} d^3r \quad (2.121)$$

In many cases, sample is statistically isotropic when averaged over its volume implying  $\hat{\rho}^2(\vec{r}) = \hat{\rho}^2(r)$ . This is also the case for polycrystalline samples. Further, no long range order should exist, leading to  $\hat{\rho}^2(\infty) = \bar{\rho}^2$ . The electron density difference is introduced as  $\Delta\rho(r) = \rho(r) - \hat{\rho}$ . The average of the exponential over all orientations is given by  $\langle e^{-ihr} \rangle = \frac{\sin qr}{qr}$ . With these assumptions and definitions, the scattered intensity gives:

$$I(q) = I_o 4\pi \int_0^\infty r^2 \Delta\rho^2(r) \frac{\sin qr}{qr} dr \quad (2.122)$$

### 2.7.2 Porod's law

Equation 2.122 can be further simplified if the scatterer is a composition of two phases with two distinct electron densities which are different by  $\Delta\rho$ , in particular spherical particles in an environment. One can introduce  $\gamma_o(r) := \frac{\Delta\rho^2(r)}{\Delta\rho}$  where  $\gamma_o(r)$  is only related to the geometry of the sample. If the interfaces of the two samples components are sharp and we consider only the final slope of  $I(q)$ , that is we consider only small distances in real space, namely the interface of the neighbouring two sample components, Porod was able to derive the following approximation of the scattered intensity [Por82]:

$$I(q) = I_o 2\pi S (\Delta\rho)^2 q^{-4} \quad (2.123)$$

where  $S$  is the total interface surface.

Thus, the final slope of  $I(q)$  follows a  $q^{-4}$  behaviour. This power law (power of -4) is known as Porod's law. It is not only valid for single, separated spherical particles, but also for densely packed systems, provided that a well defined internal surface exists [Por82]. If the interface is continuous, the absolute value of the exponent can be even larger than 4, meaning a faster decay of the scattered intensity towards increasing scattering angles. If the interface is sharp, but has a fractal structure, e.g. self-resembling features on several length-scales, the exponent can vary between -2 and -4. A similar power law can be derived also for non-spherical particles: If the particles have a rod-like structure, the exponent is -1, for discs it is -2 [Sch91].

The energy dependence of the scattered intensity can easily be understood when replacing  $q$  by  $k\theta$ . This leads to

$$I(\theta) = I_o 2\pi S (\Delta\rho)^2 k^{-4} \theta^{-4} \quad (2.124)$$

which shows that SAXS is expected to be significantly lower with increasing photon energies.

### 2.7.3 Single crystals

In a NLE experiment in transmission geometry, the material traversed by the beam is the rotor and the sample. As the rotor wall thickness is two times 0.5 mm, but the sample just two times 40  $\mu\text{m}$ , the main SAXS will originate from the rotor material. If the rotor material is polycrystalline, the grain boundaries have a significantly different electron density than the interior of the crystallites. This difference gives rise to a large SAXS and can be treated with Porod's power law for densely packed systems, leading to a  $I(q) \propto q^{-4}$  behaviour. If however, single crystalline rotors are used, e.g. sapphire rotors, these grain boundaries do not exist and this large contribution to the overall SAXS vanishes. The remaining SAXS will be due to the sample itself and the various windows between vacuum sections and ambient pressure sections of the beam path. These windows can be produced out of single crystalline material, like thin silicon wafers in principle.

In a NLE experiment in grazing incident geometry, the main contribution to SAXS is the surface of the top layer, as large electron density variations between the air and the layer material exist. Unfortunately, the interface is not ideally smooth, but characterised by a surface roughness. It is this surface roughness which generates a large SAXS background in the NLE experiments in grazing incidence geometry. Also for surfaces, the final slope of  $I(q)$  can follow a  $q^{-4}$  behaviour, for example with vapour deposited gold films [Lev89].

# Chapter 3

## Investigated samples

### 3.1 $^{61}\text{Ni}$ nuclear parameters

The experiments with the NLE on a thin nickel foil used the nuclear resonance of the  $^{61}\text{Ni}$  isotope. The foil was enriched to 81 % in this isotope. Here are the nuclear parameters of  $^{61}\text{Ni}$ .

property		value	reference
transition energy	$E_o$	67412 eV	
wavelength	$\lambda_o$	0.184 Å	
recoil energy of free nucleus	$E_R$	40.0 meV	
lifetime	$\tau$	7.70 ns	
halfife	$t_{1/2}$	5.34 ns	
natural width	$\Gamma_o$	85.4 neV	
	$2\Gamma_o$	0.76 mm/s	
internal conversion coefficient	$\alpha$	0.12	[Obe73]
nuclear angular momentum	$I_g^{\pi g}$	$\frac{3}{2}^-$	
	$I_e^{\pi e}$	$\frac{5}{2}^-$	
maximum resonance cross section	$\sigma_o$	0.72 Mbarn	[Obe73]
electronic cross section	$\sigma_{el}$	10 barn	[SLAC]
transition multipole character		M1+E2	
mixing	$\delta$	0.0076	
relative change of nuclear radius	$\frac{\delta R}{R}$	-2.6...-0.9 ·10 <sup>-4</sup>	[Obe73]
nuclear quadrupole moment	$Q_g$	+0.162 barn	
	$Q_e$	-0.20 barn	
nuclear magnetic moment	$\mu_g$	-0.750 $\mu_N$	
	$\mu_e$	+0.480 $\mu_N$	
natural abundance	$\beta_{nat}$	1.14 %	

Table 3.1: Nuclear properties of  $^{61}\text{Ni}$ . Unless stated otherwise, values are taken from [Fir96] or derived from it.

Before continuing to the specific  $^{61}\text{Ni}$  sample used in this thesis, the nuclear level diagram of  $^{61}\text{Ni}$  including its possible mother isotopes for traditional Mössbauer spectroscopy should be discussed. It shows the main difficulty in  $^{61}\text{Ni}$  Mössbauer spectroscopy apart from the low Lamb-Mössbauer factor and how much the approach with synchrotron radiation is valuable. About the scientific case for  $^{61}\text{Ni}$  Mössbauer spectroscopy, please refer

to the introduction.

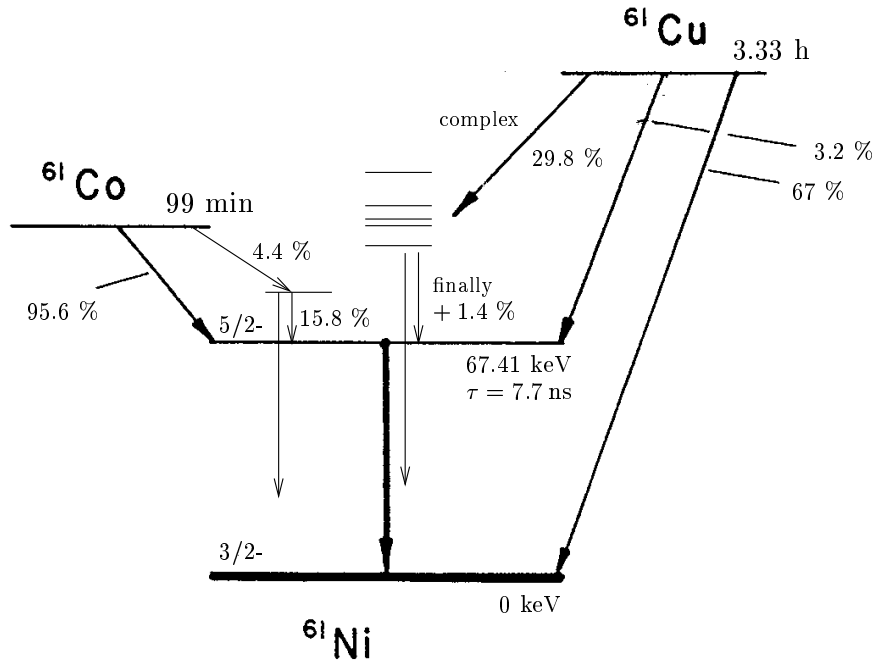


Figure 3.1: Level scheme of  $^{61}\text{Ni}$  and its possible mother isotopes. Values taken from [Fir96]

The two possible mother isotopes of  $^{61}\text{Ni}$  are  $^{61}\text{Co}$  and  $^{61}\text{Cu}$ .  $^{61}\text{Cu}$  has the longer lifetime of 3.33 hours, but only 4.6 % of the decaying copper nuclei populate finally the 67.41 keV level of  $^{61}\text{Ni}$ . Apart from this level, a multitude of other levels are excited and lead to large  $\gamma$ -ray background during measurements.  $^{61}\text{Co}$  decays almost completely into the 67.41 keV level of  $^{61}\text{Ni}$ , but its lifetime is unfortunately even shorter, 99 minutes. As copper is paramagnetic even as pure element, obtaining a single line source is easy. In the case of cobalt, single line sources are NiV(14%), which is non-magnetic at 4.2K and shows almost natural line width, or NiCr(20%) which gives a little broader line [Obe73]. The lifetimes of the mother isotopes are so small, that measurements can only be done in the vicinity of an accelerator, that creates the source activities, partly even in situ. Neither  $^{60}\text{Co}$  nor  $^{60}\text{Cu}$  are stable so that neutron capture of these isotopes is no option. Most common reactions are  $^{64}\text{Ni}(p,\alpha)^{61}\text{Co}$  which requires  $\sim 20$  MeV protons and  $^{62}\text{Ni}(\gamma,p)^{61}\text{Co}$ , which uses bremsstrahlung from a  $\sim 25$  MeV electron beam [Obe73]. Other options are  $^{61}\text{Ni}(p,n)^{61}\text{Co}$  [Nas93],  $^{58}\text{Fe}(\alpha,p)^{61}\text{Co}$  [Sch73] for  $^{61}\text{Co}$  and  $^{58}\text{Ni}(\alpha,p)^{61}\text{Co}$ ,  $^{58}\text{Ni}(\alpha,n)^{61}\text{Zn} \rightarrow ^{61}\text{Cu}$  [Oka95] or  $^{63}\text{Cu}(\gamma,2n)^{61}\text{Cu}$  [Eri69] for  $^{61}\text{Cu}$ . Finally, the 67.41 keV can be populated via Coulomb excitation, that means irradiating  $^{61}\text{Ni}$  nuclei with an oxygen  $\text{O}^{4+}$  ion beam [Sey65].

### 3.2 $^{61}\text{Ni}$ -metal

The  $^{61}\text{Ni}$  sample we used to perform the first hyperfine spectroscopy measurements with synchrotron radiation was an enriched nickel metal foil (85 % enrichment). The foil thickness was 20  $\mu\text{m}$ , thick enough to neglect surface effects. Bulk nickel crystallises in the face centred cubic (fcc) structure. The lattice constant of natural nickel at room temperature

is  $3.52 \text{ \AA}$  and the density is  $8.91 \text{ g/cm}^3$  [Kit96]. The Debye temperature is approximately 390 K above 80 K temperature and increases slightly below [Bir64].

In the temperature range of our experiments, e.g. 100-300 K, nickel is ferromagnetic. The Curie temperature of nickel metal is  $T_c = 632.7 \text{ K}$  [Sha80], above which nickel is paramagnetic. The atomic magnetic moment of nickel is due to the eight electrons in the partly filled  $3d$  shell. As this is the outer shell of valence electrons, the magnetic moments are not localised at the atoms, but of itinerant character. As common for  $3d$  transition metals, the orbital angular momentum of the nickel atom is "frozen", i.e.  $L = 0$ , as opposed to  $L = 3$  following Hund's rule. The reason for this are the strong electrical crystal fields acting on the nickel atoms. Below the Curie temperature, exchange interaction between the atomic spins,  $S = 1$ , leads to a spontaneous ferromagnetic ordering of the magnetic moments in nickel.

The behaviour of the spontaneous magnetisation as a function of temperature,  $M(T)$ , was measured using several techniques, see for example [Sha80].  $M(T)$  can be described with the following equation:

$$M(T) = M(0 \text{ K}) \cdot B \left( \frac{T_c - T}{T_c} \right)^\beta \quad (3.1)$$

[Sha80] derive  $B = 1.3$  and  $\beta = 0.355$  as the critical parameters for nickel close to the Curie temperature.  $B$  is actually temperature dependant and drops to  $B = 1$  at zero temperatures.

The magnetic hyperfine field as measured with NMR follows nearly the same behaviour, as the hyperfine coupling constant is nearly constant independent of temperature [Rie77]. There are no Mössbauer measurements covering this huge temperature range, as a matter of low Lamb-Mössbauer factor. The magnetic hyperfine field at the nickel nuclei was measured close to zero temperature by several groups. For  $B_{hf}$  they obtained  $7.6 \pm 0.1 \text{ T}$  for bulk nickel [Lov71],  $7.50 \pm 0.02 \text{ T}$  for a  $250 \mu\text{m}$  thick nickel foil [Sta87] and  $\nu_{\text{NMR}} = 28.46 \text{ MHz} \rightarrow B_{hf} = \frac{\nu_{\text{NMR}} \hbar}{g \mu_N} = 7.47 \text{ T}$  [Str63, Rie77].

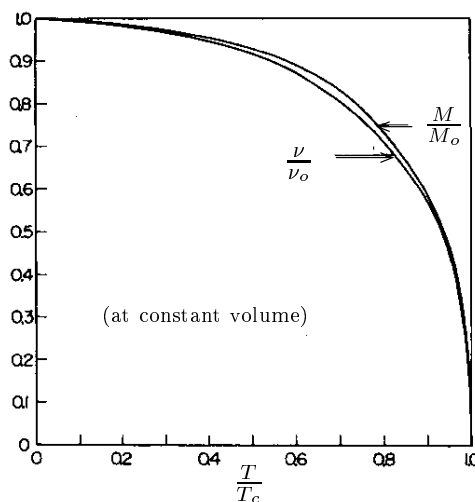


Figure 3.2:  $^{61}\text{Ni}$  NMR ( $\frac{\nu}{\nu_0}$ ) and magnetisation ( $\frac{M}{M_0}$ ) measurements with nickel [Sha80]

The Lamb-Mössbauer factor for nickel metal was measured in 1961 [Obe61] and can be calculated assuming the Debye model of phonon states or knowing the phonon density

of states experimentally. At room temperature,  $f_{\text{LM}} = 0.004$ . Our measurements have been performed at 180 K with  $f_{\text{LM}} = 0.025$  and at 115 K with  $f_{\text{LM}} = 0.066$ . At 4.2 K, the Lamb-Mössbauer factor has been measured to be 0.164 [Obe73]. The temperature dependence of the Lamb-Mössbauer factor is shown in figure 2.3.

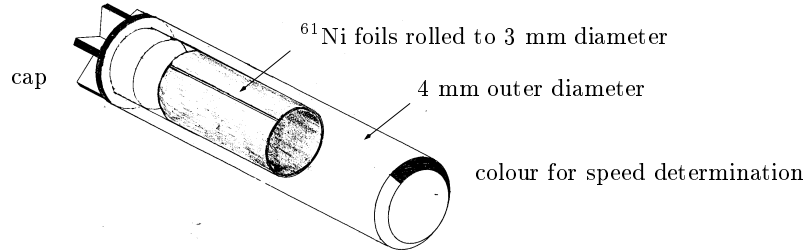


Figure 3.3:  $^{61}\text{Ni}$ -foil in rotor for transmission NLE measurements

Rotors of the 4 mm stator-rotor system have been filled with 2 foils of  $20\ \mu\text{m}$  thickness, each covering once the internal cylinder circumference of  $\pi d = 3\pi\ \text{mm}$ . The height of the foils was 7 mm. As the beam traverses the rotor, it passes through  $80\ \mu\text{m}$  of foil.

### 3.3 $^{57}\text{Fe}$ nuclear parameters

The samples of the grazing incidence NLE measurements contained  $^{57}\text{Fe}$  as nuclear resonant scatterers. It is therefore of interest to review its most important properties here, also to facilitate comparison  $^{57}\text{Fe}$  to  $^{61}\text{Ni}$ .

Note especially the long lifetime, the small natural width and the high maximum resonance cross section of  $^{57}\text{Fe}$ . This, but also the high Lamb-Mössbauer factor for iron or iron compounds is among the main reasons, why Mössbauer spectroscopy with  $^{57}\text{Fe}$  is so widely used. The small natural width is very favourable to detect small hyperfine interactions, the long lifetime practical for time-resolved examinations. The Lamb-Mössbauer factor of  $\alpha$ -iron at room temperature is  $f_{\text{LM}} = 0.77$  [Ber94b]. See also figure 2.3.

### 3.4 Magnetic thin films

Magnetic thin films and multilayers are extremely interesting materials first for fundamental physics with respect to magnetism and second for industrial applications such as magnetic data storage [Gra93]. A multitude of experimental techniques to manufacture and examine magnetic thin films have been developed during the last decades [Bla94, for a nice overview]. As it is sensitive to magnetism on a local scale, nuclear resonant scattering with  $^{57}\text{Fe}$  contributes significantly to advances in thin film and multilayer research [Röh99a, Chu99]. These measurements are performed in grazing incidence geometry [Röh99b].  $^{57}\text{Fe}$  probe layers allow for highest depth selectivity in these kinds of experiments [Nie98, Röh02b, for example]. Alternatively, conversion electron Mössbauer spectroscopy can be used [Wal94], although the brilliance of synchrotron radiation is by no means reached with a conventional radioactive source. Especially in grazing incidence geometry and with small probe layers, count rates favour nuclear resonant scattering with synchrotron radiation. Furthermore, recently the method of using waveguides to enhance



property		value	reference
transition energy	$E_o$	14412.5 eV	[Shv00]
wavelength	$\lambda_o$	0.860 Å	
recoil energy of free nucleus	$E_R$	1.96 meV	
lifetime	$\tau$	141.5 ns	
half-life	$t_{1/2}$	98.1 ns	
natural width	$\Gamma_o$	4.65 neV	
	$2\Gamma_o$	0.194 mm/s	
internal conversion coefficient	$\alpha$	8.18	[Bar80]
nuclear angular momentum	$I_g^{\pi g}$	$\frac{1}{2}^-$	
	$I_e^{\pi e}$	$\frac{3}{2}^-$	
maximum resonance cross section	$\sigma_o$	2.57 Mbarn	[Bar80]
electronic cross section	$\sigma_{el}$	6.0 kbarn	[SLAC]
transition multipole character		M1(+E2)	
mixing	$\delta$	0.0022	
relative change of nuclear radius	$\frac{\delta R}{R}$	$-0.9 \pm 0.05 \cdot 10^{-3}$	[Gol68]
nuclear quadrupole moment	$Q_g$	0 barn	
	$Q_e$	0.15 barn	[Mar01]
nuclear magnetic moment	$\mu_g$	+0.0904 $\mu_N$	
	$\mu_e$	-0.1549 $\mu_N$	
natural abundance	$\beta_{nat}$	2.2 %	

Table 3.2: Nuclear properties of  $^{57}\text{Fe}$ . Unless stated otherwise, values are taken from [Fir96] or derived from it.

the intensity of nuclear scattered signal was developed, decreasing the acquisition time of nuclear time spectra [Röh04b] significantly.

Apart from the scientific motivation, other aspects pushed us to extend the nuclear lighthouse effect to investigations of thin films in grazing incidence: First, small angle scattering from the rotor material would be at a minimum, as no rotor material has to be passed. Second, as the sample is a surface, it has to be at the end of a rotor cylinder which would provide a less critical "top" cooling approach, where only the end part of a massive rotor would be cooled at the outside of the stator block, see figure 4.14. Finally and most interesting from the physical point of view, grazing incidence investigations with the nuclear lighthouse effect have to treat the two beam case. Although signs of the nuclear lighthouse effect were first observed on a rotating disc [Röh97], no further investigations of its angular properties and its time evolution has been done so far.

To demonstrate the possibility to obtain time spectra of the nuclear decay of a rotating sample in the two beam case of grazing incidence, we used three different layer systems, that were measured both with the nuclear lighthouse effect and in standard grazing incidence geometry using a high resolution monochromator with standard timing.

### 3.4.1 $^{57}\text{Fe}$ layer systems

The three different layer systems studied in grazing incidence geometry with the NLE are sketched in figure 3.4. The different layers have been deposited with the sputtering technique: solid targets of the material to be deposited onto a substrate are bombarded with  $\text{Ar}^+$  ions. In collisions with that target material, atoms are ejected from its surface

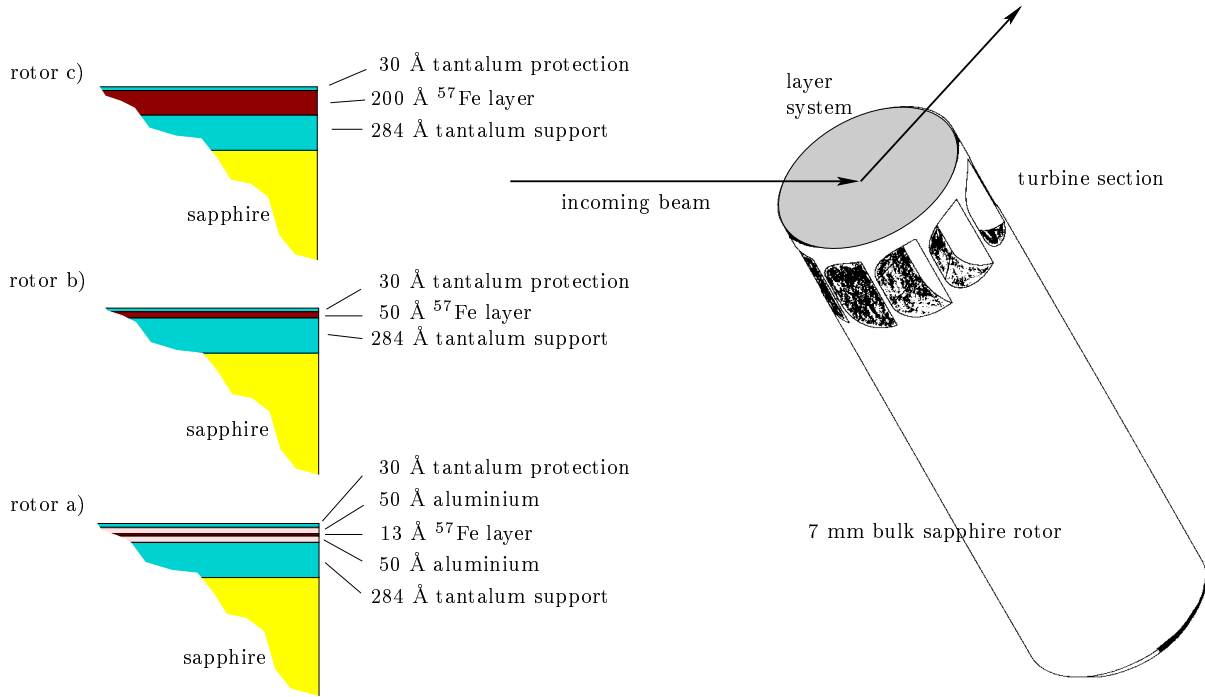


Figure 3.4: 7mm rotors for grazing incidence NLE measurements

and recondense in its surroundings, e.g. on the substrate to be covered. The substrate used here is sapphire, as it is one of the few rotor materials that stand high rotational frequencies and can be polished to yield very smooth surfaces. Target materials were high purity tantalum, aluminium and enriched  $^{57}\text{Fe}$ . The sputtering was performed in dc mode. Sputtering is known to give smoother layer surfaces as compared to evaporation techniques. On the other hand, this technique is less appropriate for epitaxial growth of the layers.

The crystal structure of sapphire,  $\text{Al}_2\text{O}_3$ , is hexagonal-trigonal with  $a = 4.8 \text{ \AA}$  and  $c = 13 \text{ \AA}$ . The c-axis is tilted by  $30^\circ$  with respect to the cylinder axis [BRUK]. The rotor top surface was polished and finally had a mean quadratic surface roughness of 0.13 to 0.14 nm rms [Zeiss]. On top of this surface, an tantalum buffer layer was sputtered. Sputtered tantalum layers generally are tetragonal  $\beta$ -tantalum if oxygen or nitrogen impurities are present, the crystallite size being sometimes extremely small, which has led to the expression of X-ray amorphous tantalum [Sta92]. The sputtered layer here was amorphous [Kle04]. Tantalum is often used as a buffer or protective layer due to the following properties: it forms passivating oxide layers that prevent oxidation of underneath layers. Under special conditions, sputtered tantalum layers might smoothen with increasing layer thickness which improves surface roughness. Self-diffusion is very small and they are often used as diffusion barriers in layered structures. In particular, iron-tantalum interdiffusion is not at all expected [Gra93].

For layer systems b) and c), the following iron layer grows polycrystalline in body centred cubic structure, with  $a = 2.87 \text{ \AA}$ . The size of one crystallite is in the order of several tens of nm. 200  $\text{\AA}$  and 50  $\text{\AA}$  thick  $^{57}\text{Fe}$ -layers have been applied. In magnetic samples, there will be multiple domains, their size is in general in the  $\mu\text{m}$  range [Kle04]. Domain walls in iron are in the order of 40 nm in width [Zab04]. In the case of rotor a),

a 13 Å thick iron layer is sandwiched inside a 100 Å thick aluminium buffer. Aluminium is expected to grow polycrystalline in the ccp structure. Iron and aluminium will not have a sharp interface, due to inter-diffusion. This might have large consequences, as the sputtered iron layer is very thin.

layer	$\delta$	$\beta$	$\phi_c$
tantalum	$13.1 \cdot 10^{-6}$	$1.64 \cdot 10^{-6}$	$0.29^\circ$
iron	$7.4 \cdot 10^{-6}$	$3.39 \cdot 10^{-7}$	$0.22^\circ$
aluminium	$2.6 \cdot 10^{-6}$	$1.53 \cdot 10^{-8}$	$0.13^\circ$
sapphire	$3.9 \cdot 10^{-6}$	$1.45 \cdot 10^{-8}$	$0.16^\circ$

Table 3.3: The complex index of refraction and the critical angle of total reflection of the used layer materials at 14.41 keV.

The complex refractive index for an isotropic medium is given by  $n = 1 - \delta - i\beta$ .  $\delta$  is proportional to the electron density of the material and can be approximated with  $\delta = \frac{1}{2\pi} r_e n_e \lambda^2$  and  $\beta$  is related to the linear absorption coefficient  $\mu$  via  $\beta = \frac{1}{4\pi} \mu \lambda$  [Spi74]. The critical angle of total reflection  $\phi_c$  for radiation incident on a vacuum-matter interface in grazing geometry is given by  $\phi_c = \sqrt{2\delta}$ . We consider X-rays of 14.41 keV energy. Table 3.3 summarises the values of  $\delta$ ,  $\beta$  and  $\phi_c$  for the materials of the layer systems.

### 3.4.2 Waveguides

In the case of nuclear resonant scattering from thin films, count rate considerations play an important role, the thinner the resonant layer gets. Scattered intensities can be enhanced if the resonant layer is incorporated into a waveguide [Spi74, Fen93, Röh04b]. A waveguide is a sandwich of a low electron density layer between two high electron density layers, e.g. tantalum (check for instant table 3.3). Inside a waveguide, multiple reflections of the incident beam lead to the formation of standing waves, as depicted in figure 3.5. Anti-nodes form where the field amplitude of the incident and reflected wavefields add up coherently. If the sample is placed at the depth of such a anti-node, the scattered intensity from this region is enhanced.

The cover layer should be not too thick, as to allow a certain intensity of the incoming beam to traverse this layer. The bottom layer can have quasi-infinite thickness. For tantalum for example, 300 Å are sufficient.

The coupling into a guided mode via the thin cover layer can be observed as a dip in the reflectivity curve ("θ - 2θ scan") of the X-rays incident at a specific angle  $\phi$  below the critical angle  $\phi_c$ . At such an angle, the evanescent field of the incoming radiation inside the waveguide excites a guided mode, characterised by a standing wave. The z-component of the wavevector  $k$  of the incoming radiation (z-axis is normal to the layer plane),  $k_{zi} = \frac{2\pi \sin \theta_i}{\lambda}$  needs to match that of the guided mode. Then, a part of the incident radiation is not reflected, but tunnels into the waveguide [Fen93]. The intensity distribution of the guided mode in the waveguide structure can be calculated [Röh04b].

The layer systems employed here use a waveguide structure with a tantalum substrate and cover layer. Tantalum has a very high electron density, needed for this purpose. Especially layer system c) with the 13 Å of  $^{57}\text{Fe}$  embedded in a thick aluminium sandwich showed the typical behaviour of a waveguide, see chapter 5.1. At proper chosen incident

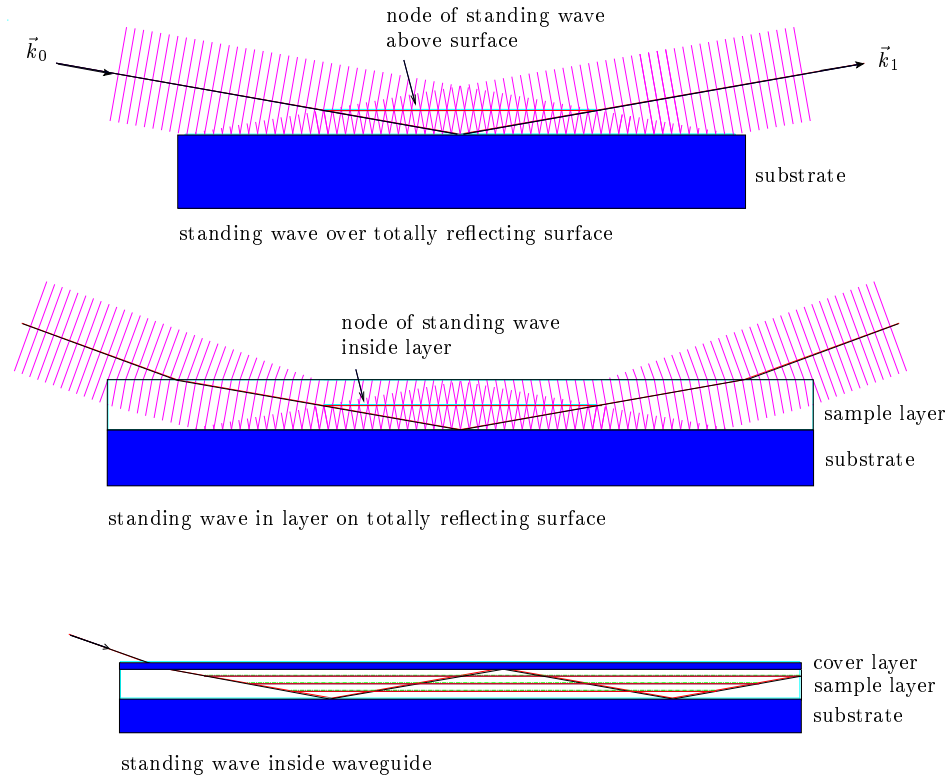


Figure 3.5: Creation of a standing wave in grazing incidence geometry. This method is used to increase scattered intensity, especially in the waveguide [Röh01a, modified].

angle, a node of the standing wave sits at the depth of the small  $^{57}\text{Fe}$  layer, allowing for sufficient count rates for the experiment.

### 3.4.3 Magnetic and electric behaviour of the $^{57}\text{Fe}$ thin films

The only magnetic layer in the simple layered systems shown in figure 3.4 is the  $^{57}\text{Fe}$  layer. Bulk bcc iron, also called  $\alpha$ -iron, is ferromagnetic. The magnetic moment of iron originates from the  $3d$  valence electrons and is described by the itinerant electron model. Below the Curie temperature of 1043 K, the spins of the iron atoms ( $S = 2$ ) order ferromagnetically due to exchange coupling. As common for  $3d$  transition metals, the orbital angular moments of the iron atoms are "frozen", i.e.  $L = 0$  as opposed to  $L = 2$  following Hund's rules. The total angular momentum is thus given by the spin:  $J = S$ . The ferromagnetic state can be expressed with the Hamiltonian describing Heisenberg exchange coupling:  $\hat{H} = -\sum_{ij} J_{ij} \mathbf{S}_i \cdot \mathbf{S}_j$ . For iron and nickel,  $J_{ij} > 0$ , resulting in ferromagnetic order.

It is well known, that magnetic properties of thin films can vary significantly from bulk properties. The reason for this lies in the combined effect of a multitude of influences. The main effects are the crystal, shape and surface anisotropy.

The magnetisation state of a film is the state of minimal total energy  $E = E_{mag} + E_{ex} + E_{ai} + E_{me}$  [Mül03].  $E_{mag}$  is the magnetostatic energy, principally the energy stored in the stray fields.  $E_{ex}$  is the exchange energy, e.g. at domain walls, where regions of differently aligned magnetic moments meet. If there is stress or deformation in the film,

this gives rise to magnetoelastic energy  $E_{me}$ .  $E_{ai}$  is the anisotropy energy. If the internal energy of a magnetic material depends on the direction of its magnetisation, it is called magnetically anisotropic. Different effects contribute to it:

The crystal anisotropy considers a bulk crystal and describes, which direction in the crystal is easy or hard to magnetise. This is also the axis along which the magnetic moments prefer to align in the absence of an external field. In cubic iron, the easy axis of magnetisation are the  $\{100\}$  directions, that are the edges of the cube. The axes  $\{110\}$ , the surface diagonals, are hard. The  $\{111\}$  directions, the volume diagonals, are the hardest to magnetise. The origin of crystal anisotropy is the spin-orbit coupling. As said, in  $3d$  transition metals, the orbital component is strongly suppressed by strong crystal fields. As a consequence, crystal anisotropy is rather small in  $3d$  transition metals. In ferromagnets like iron, stray magnetic fields outside a macroscopic crystal would be important, if the spins of the whole crystal would direct all into the same direction. To reduce the stray field energy, magnetic domains form. Each domain has its spins oriented in one of the easy axis directions. In thin magnetic films, the same stray fields are responsible for the shape anisotropy. Thin films can be more easily magnetised in the plane than perpendicular to the plane. Thus, the shape anisotropy lifts the degeneracy of the easy axis along the cube edges in iron. If the plane normal is the  $z$ -direction, than the  $[001]$  direction is harder than  $[100]$  and  $[010]$ . At surfaces and interfaces, the broken symmetry leads to an additional anisotropy, the surface and interface anisotropy. The strength of this anisotropy is reflected by a parameter, that can be positive or negative, resulting in preferred perpendicular magnetisation or preferred in-plane magnetisation. The surface anisotropy scales with the area  $A$ . However, one has to consider all anisotropy contributions together. With varying film thickness, especially the shape anisotropy contribution varies. Therefore, for iron thin films, perpendicular magnetisation occurs only for very thin films, typically below a few Å. This depends of course strongly on the layer system in which the iron film is embedded, defects and impurities. For the iron film thicknesses of the three layers investigated here, out-of-plane magnetisation can be excluded.

Layer system a) with the thickest iron layer,  $200 \text{ \AA}$ , is expected to show in-plane magnetisation. Due to the polycrystalline structure, many domains with various magnetic orientations will form. This might not necessarily be the case of for example of epitaxial grown iron layers. In principal, the same behaviour of ferromagnetic iron with many domains is to be expected with rotor b) and its  $50 \text{ \AA}$  of iron. However, problems during the sputtering of this layer occurred and a smaller layer thickness can not be ruled out. If the layer thickness is much smaller, the growth of the iron layer might have caused separated islands that did not start to join. In this case, superparamagnetism might be a possible scenario, [Stü63].

Concerning the electric hyperfine interaction of the  $^{57}\text{Fe}$  nuclei, the electric field gradient at the  $^{57}\text{Fe}$  nucleus has to be investigated. Whereas inside cubic bulk bcc iron, do to the symmetric surroundings of any iron atom, no electric field gradient is present,  $^{57}\text{Fe}$  nuclei at surfaces or interfaces will experience electric quadrupole splitting. With decreasing layer thickness, the amount of  $^{57}\text{Fe}$  atoms at the interfaces becomes more important. In the case of aluminium iron interfaces, interdiffusion will lead to a rather thick interface region, where electric field gradients will act on the  $^{57}\text{Fe}$  nucleus. The electric field gradients will vary in amplitude and direction. Furthermore, if the interdiffusion between aluminium and iron is so strong that iron and aluminium atoms mix to ratios around 1:1. Bulk disordered aluminium iron alloys at these mixing ratios become paramagnetic and, correspondingly, the magnetic hyperfine fields drop to zero, [Për87].



## Chapter 4

# Experimental aspects

### 4.1 Synchrotron radiation

One of the motivations of this thesis was to establish nuclear resonant scattering with synchrotron radiation for the Mössbauer isotope  $^{61}\text{Ni}$ , or more general for Mössbauer isotopes of higher energy. Obvious benefits are not only the advantage of avoiding the use of a short lived mother isotope like in the case of  $^{61}\text{Ni}$  Mössbauer spectroscopy, but also collimation, polarisation and intensity of the synchrotron radiation. Therefore the principal properties of this radiation should be briefly reviewed in the following.

#### 4.1.1 History of synchrotron radiation

The theoretical fundamentals needed for synchrotron radiation have been established as early as the end of the 19th, beginning of the 20th century [Bro91, for a nice review]. Starting from the Maxwell's equation in 1891 and the discovery of the electron by Thomson in 1897, the classical theory of the radiation emitted by an accelerated charged particle was established between 1898 and 1912. Though, no verifications of this theory for charged particles on a circular trajectory have been reported until the mid 40's, when the electron synchrotron and other particle accelerators were invented and the radiation emitted by an accelerated relativistic electron was a concern upon the maximum energy an electron could reach with them [Iwa44]. In 1948, the first synchrotron radiation was observed [Eld48] at General Electric in the U.S. and one year later, J. Schwinger re-examined the theory of synchrotron radiation to final detail [Sch49]. Experimentally, its spectral properties have been examined thoroughly in the 50's [Tom56] and its value for solid state spectroscopy was recognised. In 1961, the first synchrotron was build fully dedicated to research with synchrotron radiation. However, its synchrotron radiation originated from one single bunch of electrons that was accelerated (its energy  $E$  rises), accompanied with a synchronous increase of the magnetic field keeping these electrons on the fixed radius of the accelerating structure. Stable beam conditions for multiple bunches in a dedicated storage ring were realised only in the mid 60's and gave a big gain in flux. The first storage ring designed exclusively for synchrotron radiation, and not dedicated for high energy physics, was operational in 1976. Although the first "undulator" radiation was produced in 1951 with electrons from a linear accelerator passing through a periodic magnetic structure [Mot51], it was only much later that their use in a storage ring gained huge interest. The first time that a straight section of a storage ring has been equipped with such

an insertion device was in 1978. Storage rings optimised for the use of undulators and wigglers, called third-generation sources, followed. The European Synchrotron Radiation Facility in Grenoble was the first of this kind in the hard X-ray regime and became operational for users in 1994 [ESRFb]. The Advanced Photon Source [APS] in the United States and Spring-8 in Japan followed [Spr-8].

#### 4.1.2 An accelerated electron

A charged accelerated particle emits radiation. In the case of a relativistic electron, the emitted radiation can be understood as that of an emitting dipole subjected to the Lorentz transformation. It follows that the emitted intensity is strongly directed into a narrow cone in the instantaneous direction of motion of the electron, see figure 4.1.

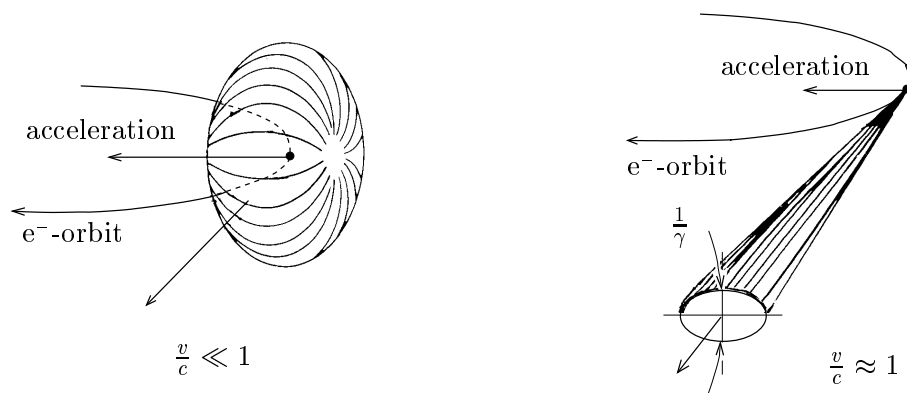


Figure 4.1: Angular emission pattern of an accelerated electron [Koc83, modified]

The opening angle in the laboratory system is approximately  $\Psi = 1/\gamma$  with  $\gamma = \frac{E}{m_e c^2}$ . At the ESRF, electrons are accelerated to  $E=6.04$  GeV, thus resulting in a vertical opening angle of about  $80 \mu\text{rad}$ . The horizontal opening depends on the trajectory the electron takes over time. At a given instant in time, it is the same angle  $\Psi$ .

The energy lost by a charged particle on a circular orbit of radius  $R$  is related to the total radiated power given by

$$P = \frac{1}{4\pi\epsilon_0} \frac{e^2 c}{R^2} \left( \frac{E}{m_e c^2} \right)^4 \quad (4.1)$$

with  $m$  being the particle's mass. To maximise the radiated power, electrons or positrons are used for the purpose of synchrotron radiation, and not the heavier protons. Electrons can be easily produced by heating a cathode, while the production of positrons needs a supplementary step. Though, the use of positrons is believed to be beneficial for the lifetime of the beam current in the storage ring. For example, the APS works with positrons [APS].

The emitted radiation is completely linearly polarised in the plane of the orbit, with the electric field of the radiation being parallel to that plane. The radiation emitted into directions above and below the orbit is elliptically polarised, getting more and more circularly polarised with increasing angle between the orbital plane and the direction of observation [Duk00].



### 4.1.3 Bending magnets, wigglers and undulators

Obviously, a static homogeneous perpendicular magnetic dipole field of a bending magnet accelerates a charged particle centripetally, thereby forcing it to follow a circular orbit. Bending magnets were the first sources of synchrotron radiation and are still in use nowadays, with for example 14 bending magnet beamlines at the ESRF. Anyhow, they are needed to create the closed orbit of the electrons in the storage ring. A more sophisticated method is the use of periodic magnetic structures. Here, the magnets force the electrons on a sinusoidal trajectory around the straight forward direction. These structures are inserted into straight sections between bending magnets and are the main synchrotron radiation sources in third generation facilities. At the ESRF, 29 of these insertion device beamlines operate. One distinguishes between wigglers and undulators, depending on the angle of maximum deviation from the forward direction,  $\alpha$ . If  $\alpha$  is smaller than the instantaneous opening angle  $\frac{1}{\gamma}$ , that is  $K = \alpha\gamma < 1$ , the device is called a undulator.  $K$  is called the deflection parameter. For  $K \gg 1$  the device is a wiggler. The distinction between the two cases is not sharp.

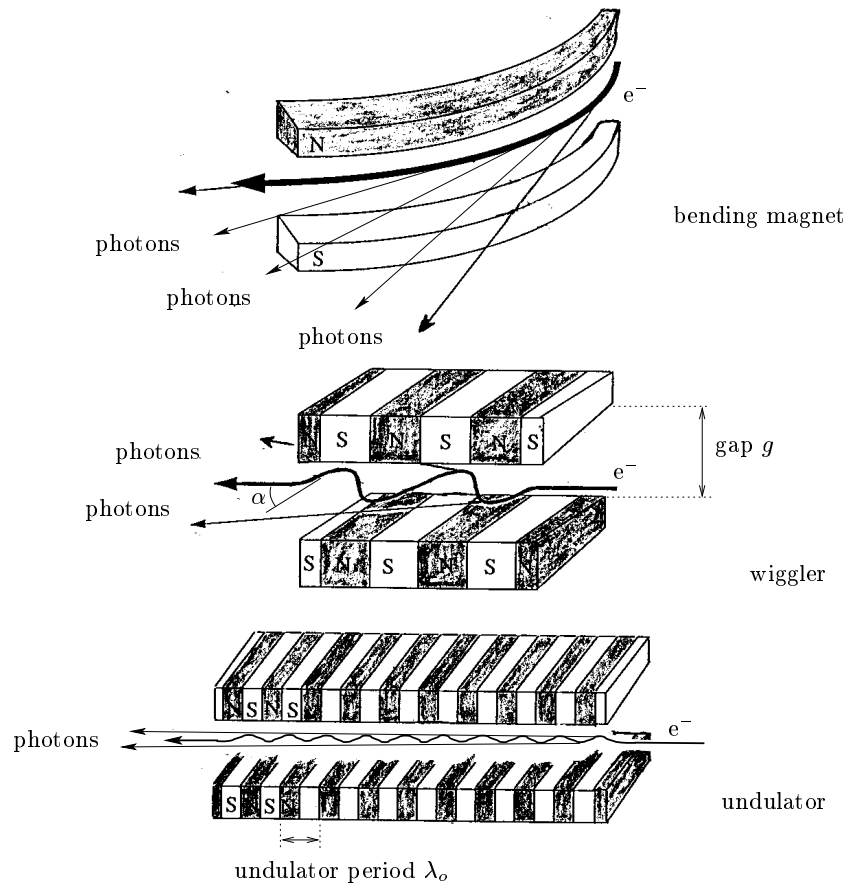


Figure 4.2: Sources of synchrotron radiation: Bending magnet, wiggler and undulator [Duk00, modified]

In a bending magnet, the radiation is distributed over a wide fan, as the trajectory in the bending magnet is a long arc and radiation is emitted from each position on this arc. An observer at a fixed position in this fan is illuminated by one electron during the time, when the cone of opening angle  $\frac{1}{\gamma}$  passes over this position. The duration of the flash is

then [Rao93]

$$\Delta t \approx \frac{2}{3} \frac{R}{\gamma^3 c} \quad (4.2)$$

Frequency components up to  $\omega_c \approx \frac{1}{\Delta t} \approx \frac{3c\gamma^3}{2R}$  can be expected. In fact, a broad range of wavelengths is emitted with a maximum near the characteristic wavelength, defined as the wavelength that splits the spectral radiated power in equal parts:

$$\lambda_c = \frac{2\pi c}{\omega_c} = \frac{4\pi}{3} \frac{R}{\gamma^3} \quad (4.3)$$

At the ESRF, for a bending magnet with  $R = 25.2$  m and with  $E = 6.04$  GeV, this leads to  $\lambda_c = 0.64$  Å or  $E_c = \hbar\omega_c = 19.4$  keV. The duration of the flash from one electron at a fixed point is  $\Delta t = 3.4 \cdot 10^{-20}$  s. The spectral flux distribution can be seen in figure 4.3. Two values describe the intensity of synchrotron radiation. The spectral flux or brightness is defined as the number of photons into a given angle (or through a certain surface), per second, in an energetic bandwidth of 0.1% around a specified energy, and for a given electron beam current. The shorter term "flux" is commonly used for it. The brilliance is the brightness normalised to a source area of 1 mm<sup>2</sup>. The source area is the lateral size of the electron cloud in the bending magnet, wiggler or undulator. The smaller the electron cloud is in this region, the more brilliant is the source. The source size plays an important role for focusing or collimation of the photon beam with optical elements in the beamline. The smaller the source is, the better it is for these purposes.

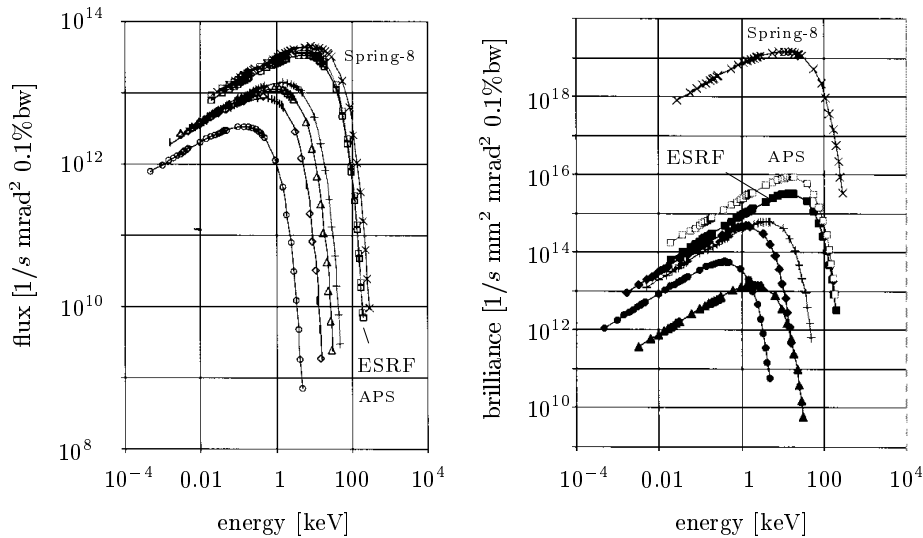


Figure 4.3: Flux and brilliance of bending magnets in different synchrotrons normalised to 250 mA electron beam current [Duk00]

The bending magnets gap or its strength cannot be varied, as it would change the trajectory of the electron beam in the storage ring. On the contrary, for an undulator or a wiggler, the overall straight trajectory of the electron does not change when the gap  $g$  is modified. However, the spectral distribution of the radiation characteristics changes upon variation of the gap. It is therefore possible to adapt these devices to the needs of the experiment. The minimum gap of an insertion device at the ESRF is 11 mm, if the magnetic array is outside the vacuum pipe of the electron beam, like at ID 18, or 6 mm, if the device is incorporated into the vacuum system. The second important parameter of an undulator or wiggler is the period  $\lambda_o$ , which is shown in figure 4.2. It can not

be modified, unless one replaces the whole array by another one. This starts to become possible now thanks to "revolver" undulators. These consist of two individual arrays, that can be interchanged depending on the experimental needs.

In an insertion device, the electrons radiate during each of their turns. The resulting brilliance depends on the deflection parameter  $K$ . The angles  $\alpha$  and  $\frac{1}{\gamma}$  depend on electron beam parameters and the magnetic field properties of the device and  $K$  can be expressed as [Rao93]:

$$K = \alpha\gamma = \frac{e}{2\pi m_e c} \lambda_o B_o \quad (4.4)$$

$B_o$  is the peak magnetic field between the upper and lower array of magnets of the insertion device and depends on the gap  $g$ . If the deviations from the forward direction characterised by  $\alpha$  become bigger than the instantaneous opening angle  $\frac{1}{\gamma}$ , the radiation of each individual turn has to be summed incoherently over the number of turns  $2N$ ; with  $N$  being the number of periods of length  $\lambda_o$ . The insertion device is called a multipole wiggler.

In the contrary case,  $\alpha < \frac{1}{\gamma}$ , the amplitudes of radiation of each turn superpose coherently with the radiation emitted by a different turn. The intensity of this radiation increases with  $N^2$ , as a consequence. Constructive superposition is possible only at certain frequencies of radiation, a fundamental frequency and higher harmonics. Thus, the radiation is monochromatic in the energy region of a particular harmonic. The energy of the  $k^{\text{th}}$  odd harmonic is given by

$$E_k(\theta) = k \cdot E_{\text{fund.}} = k \frac{2c\gamma^2}{\lambda_o} \frac{1}{1 + \frac{1}{2}K^2 + \gamma^2\theta^2} \quad (4.5)$$

It depends on the observation angle  $\theta$  between observer and straight forward direction. The angular distribution of the even harmonics is zero in the straight forward direction, which are therefore irrelevant in experiments. An insertion device with these characteristics is called an undulator. Obvious advantages are a flux increased by  $N^2$  and concentrated in a narrow energy range, as compared to a bending magnet.

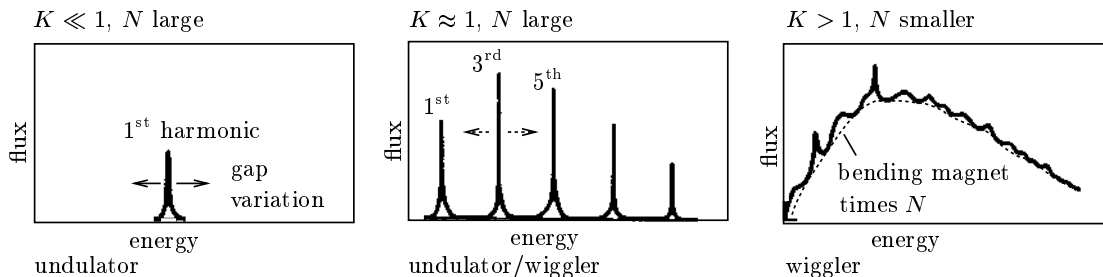


Figure 4.4: Comparison of undulator, wiggler and bending magnet radiation as a function of energy [Mar88, modified]

If the gap of an insertion device is decreased, the peak magnetic field inside the device rises and  $K$  increases as a consequence. The energy of the first harmonic, as well as the others, decreases, following equation 4.5.

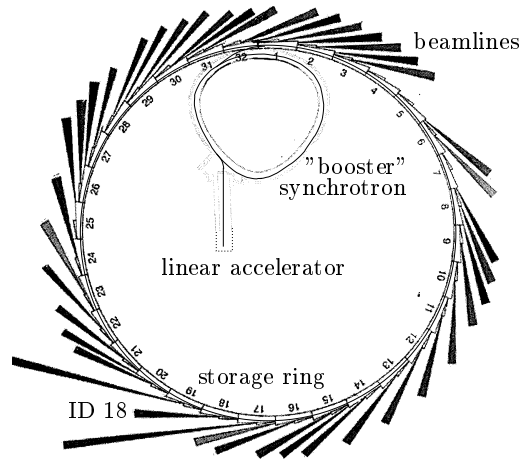


Figure 4.5: Linear accelerator, booster synchrotron, storage ring and the beamlines at the ESRF

#### 4.1.4 The ESRF storage ring

At the ESRF, the electrons are accelerated in two steps before they are stored in the storage ring to supply finally the radiation. A "triode gun" emits electrons with an energy of 100 keV, that enter a linear accelerator pushing them to 200 MeV. After a transfer line, the electrons enter the booster synchrotron. Here, after passing several turns, the electrons are accelerated to the nominal energy of  $6.04 \text{ GeV} \pm 0.1\%$ , before they are injected into the storage ring. In the 844.4m long storage ring, 3 radio frequency cavities provide the electric field that accelerates the electrons permanently to compensate for their radiation losses, which are about 6 MeV at the ESRF per electron and turn [Duk00]. The radio frequency works at 352.24 MHz and thus allows 992 buckets of stable phase for the electrons ( $\frac{c}{844.4 \text{ m}} = 355.08 \text{ kHz}$ ,  $\nu_{RF} = 352.24 \text{ MHz} = 992 \cdot 355.08 \text{ kHz}$ ).

The 992 buckets are spaced by 2.839 ns. If the filling procedure from the booster is carefully done, single buckets can be filled to a high degree of accuracy, leaving the neighbouring buckets empty. A filled bucket is called a bunch. The bunch length is only 50-120 ps. The purity is the charge ratio between filled and empty buckets and is better than  $10^{-7}$  [ESRFc] for the so-called timing modes, see figure 4.6, which are four bunch, 16-bunch and hybrid mode. The transition from filled buckets to completely empty buckets is much less sharp in  $2 \cdot \frac{1}{3}$  mode, where the intensity drops down continuously over approx. 5 to 10 buckets.

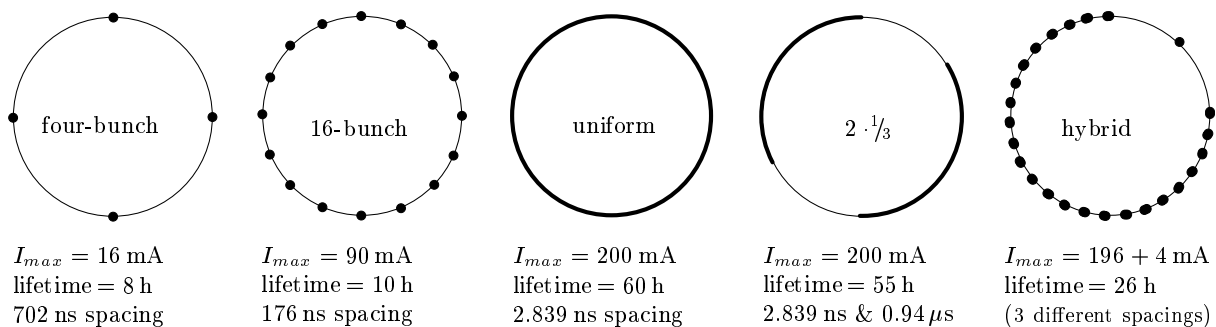


Figure 4.6: Filling modes at the ESRF

In the chapters 4.1.2 and 4.1.3, we examined the radiation characteristics of a single

electron. Fortunately, in a bucket, there is a cloud of electrons. Most of them do not travel on the ideal orbit, but oscillate around it, deviating both in position and in angle. The mean position deviations are  $\sigma_h$  and  $\sigma_v$ , horizontally and vertically. The angular spreads are characterised by  $\sigma'_h$  and  $\sigma'_v$ . An important figure for the quality of the electron beam in a storage ring is the emittance  $\epsilon$ , which is the area of the ellipse occupied by the cloud of electrons in the phase space of position and angle. The emittance is fixed by the design of the storage ring's bending magnets and focusing devices and stays constant over the whole ring. At any position on the storage ring orbit it can be factorised as  $\epsilon_v = \sigma_v \cdot \sigma'_v$  vertically and  $\epsilon_h = \sigma_h \cdot \sigma'_h$  horizontally [Kri83]. It is possible to build a storage ring that has an electron beam of small divergence but a big size in one place, and in different places a small size, but a bigger divergence. The ESRF is build in such a way, providing in half of the straight section (odd IDs) small beam size  $\sigma_h$  with big divergence  $\sigma'_h$  and in the other half (even IDs) small  $\sigma'_h$  with big  $\sigma_h$ . Vertically, the differences between odd and even IDs are small. Using the betatron function  $\beta_h = \frac{\sigma_h^2}{\epsilon_h}$ , the odd IDs are called low-beta beamlines, the even ones high-beta beamlines.

energy		horizontal size		vertical size		rms-divergence	
$E_{e^-}$	$\Delta E_{e^-}$	$\sigma_h$	$d_h$	$\sigma_v$	$d_v$	$\sigma'_h$	$\sigma'_v$
6.04 GeV	0.1 %	395 $\mu\text{m}$	930 $\mu\text{m}$	9.9 $\mu\text{m}$	23.3 $\mu\text{m}$	10.5 $\mu\text{rad}$	3.9 $\mu\text{rad}$

Table 4.1: ESRF high-beta insertion device's electron beam properties. In the beamsizes columns, the first value is rms, the second FWHM, with  $d_{h,v} = 2\sqrt{2\ln 2}\sigma_{h,v}$ .

At the ESRF storage ring,  $\epsilon_h = 3.9 \text{ nm}\cdot\text{rad}$  and  $\epsilon_v = 0.039 \text{ nm}\cdot\text{rad}$ . ID18, the beamline where all measurements concerning this thesis have been performed, is a high-beta beamline. Table 4.1 gives a list of its electron beam properties.

## 4.2 The beamline ID18

ID18 is the ESRF beamline dedicated to nuclear resonant scattering. A second beamline, ID22N, is used as well for nuclear resonant experiments during 16-bunch mode, the most efficient timing mode operation for this kind of research. The timing modes allow the discrimination between delayed photons emitted by the nucleus and the less interesting prompt signal, as explained in chapter 2.

### 4.2.1 Flux at high energies

ID18 is an undulator beamline. The straight section is occupied by three undulators with  $\lambda_o = 32 \text{ mm}$ . Recently, one of the undulators became a "revolver" undulator which allows to change to a second magnet array structure with a period of 20 mm, delivering even higher flux at the 14.413 keV transition of  $^{57}\text{Fe}$ . The 32mm undulators are much more flexible and provide high flux in more than one harmonic, see figure 4.4: On the left the approximate case of the 20 mm undulator, in the middle roughly the case of the 32 mm undulator. The 32 mm undulator allows to cover reasonably all energies between 8 keV and 80 keV, see figure 4.7 for details. Each of the undulators is about 1.6 m long. The vacuum beam pipe is 10 mm high and thus allows a minimum gap of 11 mm between the two magnet arrays of the undulators.

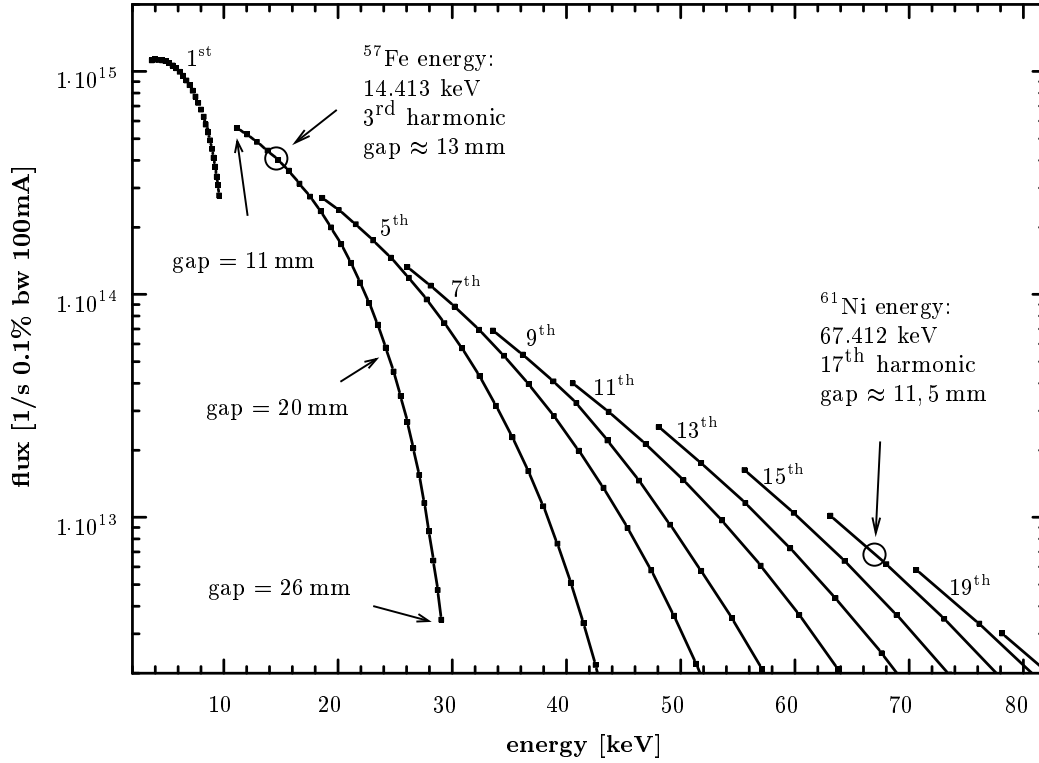


Figure 4.7: Flux at ID18. The values correspond to the flux of three 32 mm undulators through a 2 mm · 1 mm large pinhole (horizontal · vertical) placed 32 m downstream of the middle undulator and considering 100 mA of beam current [Cha04].

In the framework of this thesis, spectroscopic work has been done with two resonances: the  $^{61}\text{Ni}$  resonance at 67.412 keV and the  $^{57}\text{Fe}$  resonance at 14.413 keV. It is interesting to compare the available flux and to understand the performance of the following monochromatisation process, i.e. to know the energetic and angular width  $\Delta E$  and  $\sigma_\theta$  of the undulator radiation at each of these energies. The theory of the undulator radiation of a single electron leads to, [Duk00]:

$$\Delta E_k^{1e^-} = E_k \frac{1}{kN} \quad \sigma_\theta^{1e^-} = \sqrt{\frac{hc}{E_k} \frac{1}{N\lambda_o}} = \sqrt{\frac{hc}{E_k L}} \quad (4.6)$$

Here,  $k$  is the  $k^{\text{th}}$  harmonic,  $N$  is the number of periods in an undulator of period length  $\lambda_o$  with  $L = N\lambda_o$ . The 32 mm undulator has  $N = 51$  periods. The divergence  $\sigma_\theta^{1e^-}$  of an undulator radiation is about  $\frac{1}{\sqrt{kN}}$  that of a dipole bending magnet [Duk00]. If the electron beam has a certain energy spread and a certain divergence at the undulator position, the values have to be corrected for this. This can be done with certain programs for  $\Delta E_k$  [Cha04, using the program code SRW [Chu98a]] and in a simple way for  $\sigma_\theta^{h,v} = \sqrt{(\sigma_\theta^{1e^-})^2 + (\sigma'_{h,v})^2}$  with  $\sigma'_{h,v}$  for the electron beam from table 4.1.

A downstream bending magnet separates the electron beam and the synchrotron radiation produced by the 3 undulators. The photons leave the vacuum system of the storage ring towards the front end beam shutter while passing a 500  $\mu\text{m}$  thick diamond window. At 14.413 keV, 86 % of the photons are transmitted, at 67.41 keV even 97 %.

nuclei	energy	flux in 0.1%bw @ 100mA	$\Delta E_k^{1e^-}$	$\sigma_\theta^{1e^-}$	$\Delta E_k$	$\sigma_\theta^h$	$\sigma_\theta^v$
$^{57}\text{Fe}$	14.413 keV	$4.16 \cdot 10^{14} \text{ 1/s}$	94 eV	$7.26 \mu\text{rad}$	290 eV	$12.7 \mu\text{rad}$	$8.2 \mu\text{rad}$
$^{61}\text{Ni}$	67.41 keV	$6.69 \cdot 10^{12} \text{ 1/s}$	78 eV	$3.36 \mu\text{rad}$	1.6 keV	$11.0 \mu\text{rad}$	$5.1 \mu\text{rad}$

Table 4.2: ID18 photon beam parameters at the  $^{57}\text{Fe}$  and  $^{61}\text{Ni}$  resonance energies. The beam divergences are given as rms values.

### 4.2.2 Monochromatisation

After passing the front end beam shutter and entering the actual beam line, the radiation contains photons of different energy: First, all the different energies corresponding to all the harmonics of the undulator, and second, the broad bending magnet spectrum. However, the natural width of Mössbauer transitions is in the order of a few to a hundred neV. Due to detector limitations, it is necessary to get a much more monochromatic beam. This is done with the high heat load monochromator, often called only the pre-monochromator, since other monochromatisation steps might become still necessary afterwards. If the three undulators are closed down to 11 mm ( $K \approx 1.86$ ), the electron beam current is 200 mA and a slit of 2 mm·1 mm is in front of the monochromator, the power absorbed by the first of these two crystals is about 500 W [San98]. This might lead to important distortions on the crystal, if the crystals were not cooled to about 123 K, where silicon has almost negligible temperature expansion.

The monochromatisation is done by Bragg reflections at two parallel silicon crystals, thereby keeping the outgoing beam parallel to the incoming one. Bragg's law says

$$2d \sin \theta_B = n\lambda \quad (4.7)$$

with  $\theta_B$  being the Bragg angle between the incident beam and the crystal's lattice planes.  $d$  is the lattice plane spacing,  $\lambda$  the wavelength of transmitted radiation and  $n$  the order of reflection, in general equal to 1. As the incoming synchrotron radiation is less divergent in the vertical plane than in the horizontal plane, the crystals reflect the beam in the vertical plane (the crystal plane normal is in the vertical plane). In order to keep the vertical offset constant despite a tuneable energy, the second crystal has to travel laterally, see figure 4.8.

Important for a monochromator is the energetic width of the transmitted radiation as a function of the divergence  $\Delta\theta_\gamma = 2 \cdot \sqrt{2 \ln 2} \sigma_\theta^v$  of the incoming beam. The energy resolution can easily be obtained differentiating equation 4.7:

$$\left| \frac{\Delta E}{E} \right| = \left| \frac{\Delta \lambda}{\lambda} \right| = \left| \frac{\Delta d}{d} \right| + |\Delta\theta_\gamma \cot \theta_B| \quad (4.8)$$

Silicon crystals can be produced with very high purity and values of  $\frac{\Delta d}{d} \lesssim 10^{-8}$  can be reached [Fre93]. Actually, in the case of our silicon crystals, this error can be neglected in most cases.

For a perfect monochromatic, divergent beam, the intrinsic angular acceptance of a Bragg reflection of a symmetrically cut perfect crystal is given by its Darwin width  $\Delta\theta_{sym}$ . The dynamical theory gives the following result for the Darwin width for  $\sigma$ -polarised radiation (like synchrotron radiation, the electric field is in the plane of the storage ring) [Dar14, Toe00]:

$$\Delta\theta_{sym} = \frac{2}{\sin(2\theta_B)} \frac{r_e \lambda^2}{\pi V} |F_H| e^{-M} \quad (4.9)$$

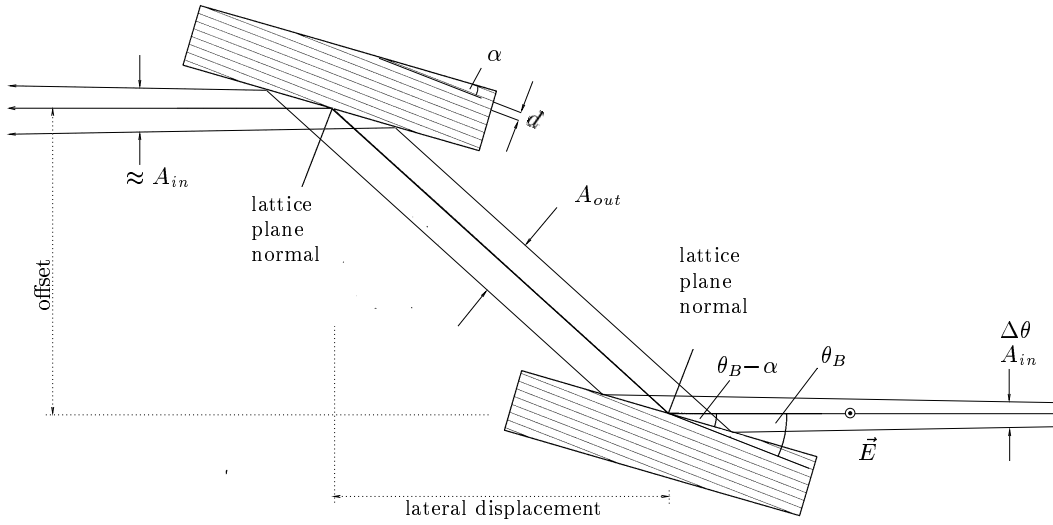


Figure 4.8: Bragg reflection with two asymmetrically cut crystals, as used in the high heat load monochromator at ID18, not to scale.

$r_e$  is the classical electron radius,  $V$  the volume of the silicon unit cell,  $|F_H|$  the product of form-factor and structure factor for the momentum transfer of the reflection.  $e^{-M}$  is the Debye-Waller factor. The Darwin width decreases with increasing Bragg angle up to  $\theta_B \approx 80^\circ$ , then it increases again towards a maximum at  $\theta_B = 90^\circ$ . This is the reason why in some cases back-scattering reflections are used - in this case though, equation 4.9 has to be replaced, as it does not allow  $\theta_B = 90^\circ$ . There are several programs to calculate Darwin widths [San98, Stu94]. The Darwin width should not be smaller than the divergence of the incoming beam, if all photons of the right energy should be transmitted despite their angular spread. Table 4.3 (column  $\alpha = 0$ ) illustrates the problem of monochromatization at high energies, comparing Bragg reflections of a silicon crystal at the energies of the  $^{61}\text{Ni}$  and the  $^{57}\text{Fe}$  Mössbauer transition.

If the crystal is cut asymmetrically, that means the surface is tilted by an angle  $\alpha$  with respect to the reflecting lattice planes, the angular acceptance can be significantly increased. The consequence is an increased beamsize  $A_{out}$ . In particular, with the use of the asymmetry parameter  $b$ :

$$\begin{aligned}
 b &= \frac{\sin(\theta_B - \alpha)}{\sin(\theta_B + \alpha)} \\
 \Delta\theta_{as,in} &= \Delta\theta_{sym} \frac{1}{\sqrt{b}} \\
 \Delta\theta_{as,out} &= \Delta\theta_{sym} \sqrt{b} \\
 A_{out} &= A_{in} \frac{1}{b}
 \end{aligned} \tag{4.10}$$

With two subsequent asymmetrically cut crystals, the effect of beamsize increase can be compensated, and the beam divergence of the part that was transmitted by the two reflections does not change neither. Only the angular acceptance is improved as compared to a symmetric crystal.

The high heat load monochromator at ID18 is slightly asymmetric with  $\alpha = 1^\circ$ . The lateral displacement necessary to lead to the necessary fixed offset of 25mm increases with decreasing Bragg angle. Above 60 keV, the lateral displacement with the



energy [keV]	$hkl$	T [K]	$\theta_B$ [°]	$\alpha = 0^\circ$	$\alpha = 1^\circ$	
				$\Delta\theta_{sym}$	$\Delta\theta_{as,in}$	$\Delta\theta_{as,out}$
14.413	111	80	7.889	18.6 $\mu\text{rad}$	21.1 $\mu\text{rad}$	16.4 $\mu\text{rad}$
	333	80	24.315	3.9 $\mu\text{rad}$	4.1 $\mu\text{rad}$	3.8 $\mu\text{rad}$
67.412	333	80	5.051	0.75 $\mu\text{rad}$	0.92 $\mu\text{rad}$	0.62 $\mu\text{rad}$

Table 4.3: Darwin width of the Bragg reflections used in the high heat load monochromator at ID18.

(111) reflection becomes bigger than the possible maximum value and one has to switch to the (333) reflection. Comparing the angular acceptance of the (333) reflection at 67.41 keV,  $\Delta\theta_{as,in}=0.92 \mu\text{rad}$  with the angular beam divergence of table 4.2,  $\Delta\theta=2\sqrt{2\ln 2} \cdot 5.1 \mu\text{rad}=12 \mu\text{rad}$ , we see that the misfit still remains for the slightly asymmetric high heat load monochromator crystals. For  $^{57}\text{Fe}$ , there is no problem.

A possibility to decrease the divergence of the beam is the use of compound refractive lenses to collimate the beam. This will be explained in the next chapter.

### 4.2.3 Focussing and collimation with compound refractive lenses

Focussing of X-rays can be achieved with bent crystals [Spa80], curved mirrors [Kir48] or the use of compound refractive lenses (CRL) [Sni96]. In the latter case, use is made of the refractive index  $n$ , which is different between air and solid material, like in optics of visible radiation, but with a much smaller variations of  $n$  in the case of hard X-rays. For the refractive index, we have

$$n = 1 - \delta + i\beta \quad (4.11)$$

$\delta$  expresses the refraction and  $\beta$  the absorption. In the X-ray region, the real part of  $n$  is smaller than one. Focussing lenses are therefore of concave shape and not convex like optical focussing lenses. Unfortunately, in the X-ray regime as opposed to the visible range,  $\delta$  is very small. Table 3.3 gives some values for  $\delta$  and  $\beta$  at 14.41 keV. The two parameters can be expressed as [Ell98]

$$\delta \approx \frac{r_o \lambda^2 N_A}{2\pi A} Z \rho \quad \beta = \frac{\lambda \rho}{4\pi \mu} \quad (4.12)$$

The cross section for photo-absorption  $\sigma_{ph}$  scales with  $Z^4$  to  $Z^5$  for the photo-effect and with  $Z$  for the Compton effect. Therefore,  $\beta$  scales with  $Z^\kappa$   $\kappa > 1$  at the  $^{61}\text{Ni}$  energy whereas  $\delta$  varies only with  $Z$ . It is therefore recommended to use low- $Z$  material like beryllium or aluminium.

The focal length of a one bi-concave lens is given by  $F = \frac{R}{2\delta}$ ,  $R$  being the radius of the spherical lens. As  $\delta$  is very small, e.g.  $\delta = 1.19 \cdot 10^{-7}$  for aluminium at 67.41 keV, a stack of a large number  $N$  of these single lenses have to be used in order to reach useful focal distances, see figure 4.9. Then:

$$F = \frac{R}{2\delta N} \quad (4.13)$$

Two lenses for experiments at high X-ray energies used to be installed at ID18. The first one has  $N = 140$  spherical holes of  $R = 1 \text{ mm}$  and a hole distance of  $d = 50 \mu\text{m}$ . The material is  $\text{AlMg}_3$  with  $\delta \approx 9 \cdot 10^{-9}$ . The focal distance is thus  $F = 40.3 \text{ m}$ . The second lens is a pure aluminium parabolic lens with  $R = 0.5 \text{ mm}$ , an aperture of  $2R_o = 2 \text{ mm}$

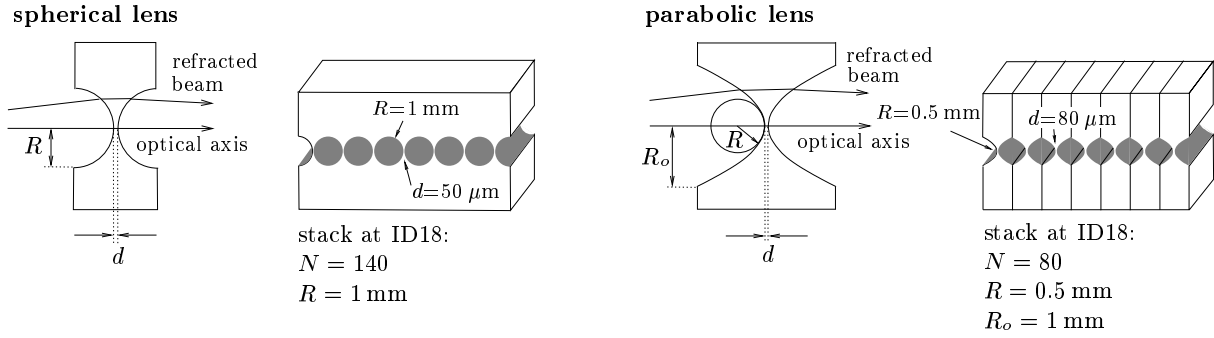


Figure 4.9: X-ray focussing with compound refractive lenses

and  $N = 80$  elements with  $d \approx 80 \mu\text{m}$ . For the aluminium lens at 67.41 keV, we have  $\delta = 1.19 \cdot 10^{-7}$  and thus  $F = 26.3 \text{ m}$ . Both lenses absorb some of the 67.41 keV photons. The transmittance of the pure aluminium lens is 83% [San98].

If a CRL is used at a distance  $f$  from the undulator, i.e. the focal spot of the lens is at the source, the lens collimates and the beam divergence can be greatly reduced. Due to the finite size of the source  $d_v = 2\sqrt{2\ln 2} \sigma_v$  and the effect of an effective aperture  $D_{\text{eff}}$  of a CRL, it is not possible to reduce the divergence to zero. The beam divergence after the CRL can be expressed as [Len99]:

$$\Delta\theta_{\text{CRL}}^v = \sqrt{\left(\frac{d_v}{f}\right)^2 + \left(\frac{1.029\lambda}{D_{\text{eff}}}\right)^2} \quad (4.14)$$

If the CRL would be placed just before the monochromator, 29 m after the undulators,  $f$  should be 29 m. The vertical electron beams size at the source is  $d_v = 23.3 \mu\text{m}$ . If we neglect the second term in the root of equation 4.14, the divergence of the photon beam would reduce to  $0.8 \mu\text{rad}$ . Using the 2 lenses available at ID18, we can calculate the effective aperture [San98, CRL] and obtain  $D_{\text{eff}} \approx 1.1 \text{ mm}$  for the spherical 140-hole lens and  $D_{\text{eff}} \approx 0.87 \text{ mm}$  for the parabolic 80-element lens. This gives us for  $\frac{1.029\lambda}{D_{\text{eff}}}$  approximately  $0.02 \mu\text{rad}$ , which justifies its disregard.

At ID18, the position of the CRL used to be 27.5 m after the undulators, very close to the focal length of the parabolic lens. Now, the angular acceptance of the high heat load monochromator and the divergence of the incoming beam after the parabolic CRL are nicely matched. Unfortunately, the heat generated by the complete spectrum of the undulator radiation on the CRL was more than it could bear, first destroying a 2 mm thick aluminium absorber, then starting to burn holes into the first elements of the lens. We could not continue to use the lenses. Improving the cooling scheme of the lens and placing them further downstream after some additional absorber sheets has to be done in future. The total radiated power of an undulator can be calculated as [Duk00]:

$$P = \frac{4\pi^2}{3} r_e M_e c^2 \gamma^2 \frac{I K^2}{e \lambda_0} N \quad (4.15)$$

with  $N$  being the number of periods of the undulator. For the three undulators at ID18 with 11 mm gap ( $K \approx 1.864$ ) and at a beam current of 200 mA, this gives 8.78 kW. Into a virtual slit of  $5 \times 5 \text{ mm}^2$  at 27.5 m, corresponding to the beam pipe size before the CRL, this is slightly reduced to 5 kW [San98]. Most of this power is contained in the lower harmonics of the undulator radiation.

#### 4.2.4 High resolution monochromatisation

As seen in the preceding chapter, it is principally possible to use the whole divergence of the incoming beam with the Si (3 3 3) reflection of the high heat load monochromator, if a proper CRL is used. For further monochromatisation to the meV range, one should examine two possibilities, one based on standard Bragg reflections and a second on Bragg-back-reflections. These considerations will show the difficulties to realise this high monochromatisation and emphasise, that the nuclear lighthouse effect and SR-PAC, which both do not demand this additional setup, are so far the only possible methods at these energies to perform nuclear resonant spectroscopy.

To give a rough idea for the problems using standard Bragg reflections, we present the following monochromatisation scheme: A CRL with  $F = 29m$  before the high heat load monochromator reduces the divergence of the photon beam to  $\Delta\theta_{\text{CRL}}^v = 0.8 \mu\text{rad}$ . The beamsize at the entrance of the CRL is  $\approx 29m \cdot \tan(2\sqrt{2\ln 2} \cdot 5.1 \mu\text{rad}) = 0.35 \text{ mm}$ . The radiation passes the Si 333 high heat load monochromator without problem, as the angular acceptance of the asymmetric cut crystal is  $0.92 \mu\text{rad}$ . The divergence of the beam after the CRL does not lead to a large increase in beamsize while travelling to the place of the high resolution monochromator at 43 m. The beamsize is now 0.36 mm.

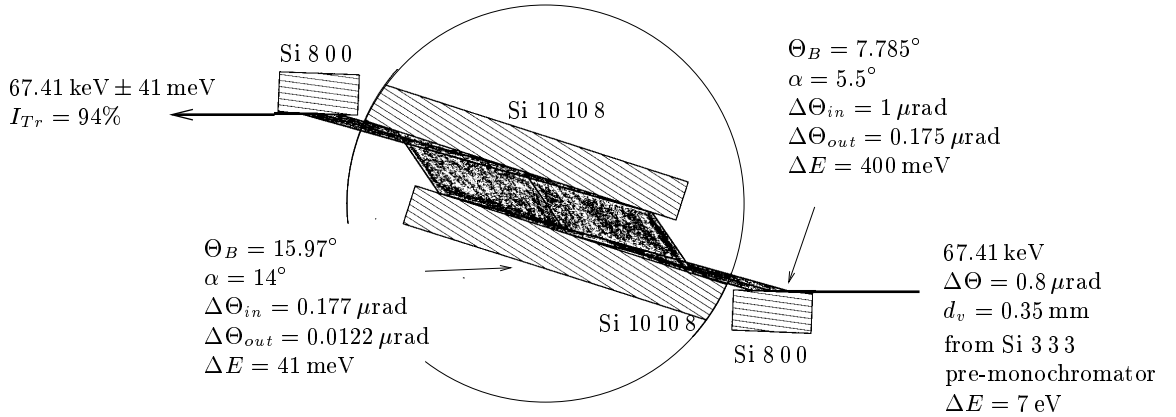


Figure 4.10: Further monochromatisation for  $^{61}\text{Ni}$  NFS

As shown in figure 4.10, a combination of a channel cut Si (10 10 8) monochromator between two Si (8 0 0) crystals would reduce the energetic width of the synchrotron radiation from around 620 meV after the Si (3 3 3) pre-monochromator (using the collimating CRL) down to 41 meV. The transmitted intensity should be 94% [San98, XInpro sub-program]. Important is the stability, that is necessary to reach only a mere 41 meV bandwidth, considering that this is not sufficient for nuclear inelastic scattering anyhow. The angular precision of rotation stages is in the order of 10 nrad. This would be just enough in this case. But between the two Si (10 10 8) reflections of the channel cut crystal, the lattice planes have to be parallel to better than 12 nrad! This seems to be a severe problem even for best single crystals, especially as this accuracy needs to exist on almost 10 cm of lateral dimensions. Less demanding seems the temperature stability, if temperature fluctuations would not tilt different lattice planes with respect to each other. We remember equation 4.8, neglect the angular part of it, and use the linear expansion coefficient  $\beta = \frac{1}{d} \frac{\Delta d}{\Delta T}$ . This leads to

$$\Delta T = \frac{1}{\beta} \frac{\Delta E}{E} \quad (4.16)$$

If the energy of the monochromatic radiation should not shift by more than  $\frac{41 \text{ meV}}{2}$ , which is half the energetic width of our proposed setup, the temperature needs to be stable at around 0.1 K, and this over the whole crystal dimensions. It is of course questionable, if temperature variations in this limit, but at different crystal positions, will not destroy the necessary parallelism. Anyhow, it is evident that this approach faces severe problems.

The second approach that we will elucidate, is Bragg-back-scattering. As we saw in the previous paragraphs, the angular acceptance of higher indexed traditional Bragg reflections decreases too much when the X-ray energy increases and/or the energetic bandwidth should become small. Even asymmetrically cut crystals can not completely help out of this situation. Maybe Bragg-back-reflections can. We remember equation 4.9 for non-backscattering reflections and introduce asymmetry:

$$\Delta\theta = \frac{1}{\sqrt{|b|}} \frac{2}{\sin 2\theta_B} |\chi_H| \quad \chi_H = -\frac{r_e \lambda^2}{\pi V} F_H e^{-M} \quad (4.17)$$

where  $\chi_H$  is the electric susceptibility for this reflection. In the case of  $\theta_B = 90^\circ$  back scattering, dynamic theory yields the following expression for the angular acceptance [Wil03]:

$$\Delta\theta = 2\sqrt{|\chi_H|} \quad (4.18)$$

The electric susceptibility is very small,  $\chi_H \lesssim 10^{-6}$  [Wil03]. As in Bragg-back-scattering, the angular acceptance is proportional to the square root of  $\chi_H$  and not linear to it, the angular acceptance is much increased.

Silicon, though produced with highest quality, is not a suitable crystal for use in Bragg-back-scattering as will be explained now. With  $\theta_B = 90^\circ$ , the Bragg condition of equation 4.7 reduces to

$$n\lambda = 2d_{hkl} \quad (4.19)$$

If the angle is fixed to exact backscattering and a certain energy is demanded, the only variable parameter is  $d_{hkl}$ . An appropriate lattice plane will seldom be found to satisfy this equation, even when temperature adjustments of the crystal are executed to fine-tune  $d_{hkl}$ . In a cubic crystal, several  $hkl$  planes have the same lattice spacing  $d$ . It is therefore beneficial to use non-cubic crystals, e.g. hexagonal sapphire  $\text{Al}_2\text{O}_3$ . It is much more probable to find a certain reflection in an acceptable temperature region.

A possible Bragg-back-reflection at 67.41 keV is the (16 31 54) reflection of  $\text{Al}_2\text{O}_3$  at 100 K [Wil04a]. This reflection has an angular acceptance of  $2.5 \mu\text{rad}$ , which can therefore take the whole beam passing the Si (3 3 3) high heat load monochromator. The energy resolution is 0.03 meV, which is already too narrow for present experiments of nuclear inelastic scattering, giving only minimal countrates, and much too narrow for SR-PAC, which demands a constant countrate covering all phonon energies. For nuclear forward scattering or the nuclear lighthouse effect, we have to compare the  $30 \mu\text{eV}$  to the splitting of the nuclear levels. The largest splitting observed so far with  $^{61}\text{Ni}$  Mössbauer spectroscopy was magnetic hyperfine splitting caused by a magnetic hyperfine field of 80 T in the spinel  $\text{Cu}_{0.9}\text{Ni}_{0.1}\text{Cr}_2\text{O}_4$  [Oka95]. The energies of the possible transitions between the sub-levels, see figure 2.8, cover the range of  $\Delta E_\gamma = 2(|\mu_e| + |\mu_g|)B_{hf} = 6.2 \mu\text{eV}$ , in this example. If now the monochromator drifts slightly, the different possible transitions will no more be excited equally. In the case of  $^{61}\text{Ni}$ -metal, the splitting is about 10 times smaller, and this back-reflection would not be too narrow.

The three big problems of this Bragg-back-reflection are the low reflectivity of the reflection of only 4.5%, the need of large perfect sapphire crystals, as the extinction depth is 3.9 cm and the required temperature stability [Wil04a]. For this reflection,  $\frac{\Delta E}{\Delta T} = -0.048 \frac{eV}{K}$ . As the width is only 0.03 meV, this demands a temperature control of at least 0.2 mK, and this over a crystal which should extend over more than 4 cm.

Thus, also this approach does not promise practical solutions in the near future. A completely other approach might be the development of new detectors, that can cope even higher prompt countrates and would thus not demand such a degree of monochromatisation. Unfortunately, there is no such a detector known yet. Finally, the nuclear lighthouse effect may be employed to separate the prompt background from the delayed nuclear signal.

#### 4.2.5 ID18 layout for the nuclear lighthouse effect and SR-PAC

The layout of ID18, as far as it concerns the measurements on  $^{61}\text{Ni}$  and  $^{57}\text{Fe}$  with the nuclear lighthouse effect, is sketched in figure 4.11. For the lighthouse experiments, of key importance is a large distance between the spinning sample in the lighthouse tower and the detector. This was achieved by putting the lighthouse into the second optics hutch (OH2) and the beamstop as well as the detectors in the third experimental hutch (EH3). The setups for the SR-PAC measurements and the grazing incidence measurements without the lighthouse are not shown explicitly, but they can be easily described. For the SR-PAC measurements and the grazing incidence measurements without lighthouse, the sample and the detectors were in the EH1, with EH2 and EH3 unused. Only for the measurements with  $^{57}\text{Fe}$  in grazing incidence, that were performed for comparison, a high resolution monochromator was used in OH2. In the other cases, the high heat load-monochromator is the only monochromator.

beamline element	distance to source	distance to lighthouse
front end CRL	23.9 m	18.7 m
aluminium CRL	27.1 m	15.5 m
high heat load monochromator	31 m	
slit 3	38.67 m	3.91 m
slit 4	42.14 m	0.44 m
lighthouse	42.58 m	
shutter between EH2 and EH3	54.77 m	12.19 m
detector (slit 5)	56.23 m	13.65 m

Table 4.4: Distances at ID18 beamline

Important distances are given in table 4.4. Especially the lighthouse-to-detector distance  $d$  is important. It is needed for the data analysis of lighthouse experiments, when no time discrimination is used. Then, at a rotational frequency  $\nu$ , the offset  $x$  between the deviated delayed nuclear signal to the direct beam at the distance between lighthouse and detector gives the time  $t$  between excitation of the  $^{61}\text{Ni}$  nuclear level and its decay with the emission of a photon via

$$t = \frac{x}{2\pi d \nu} \quad (4.20)$$

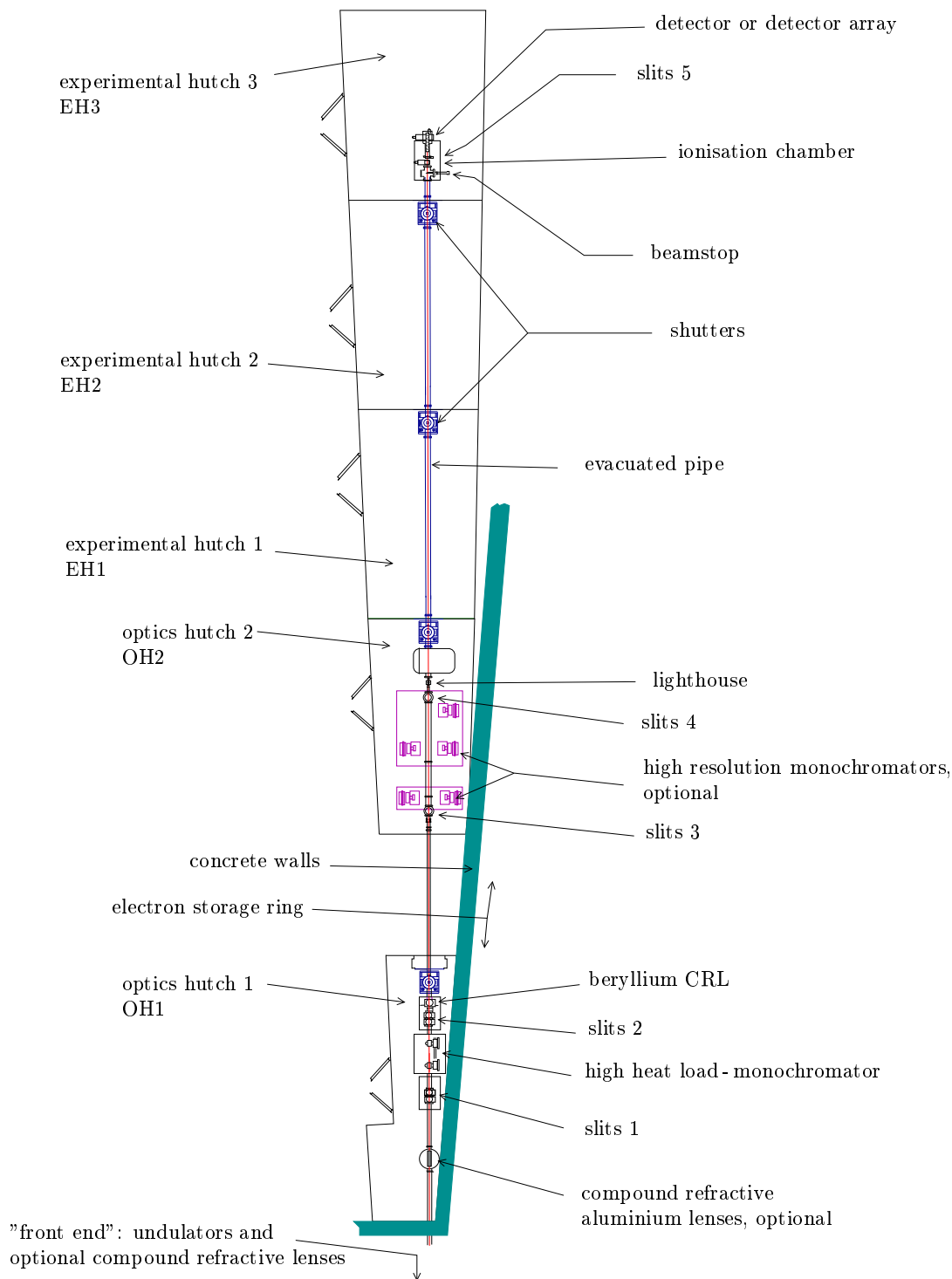
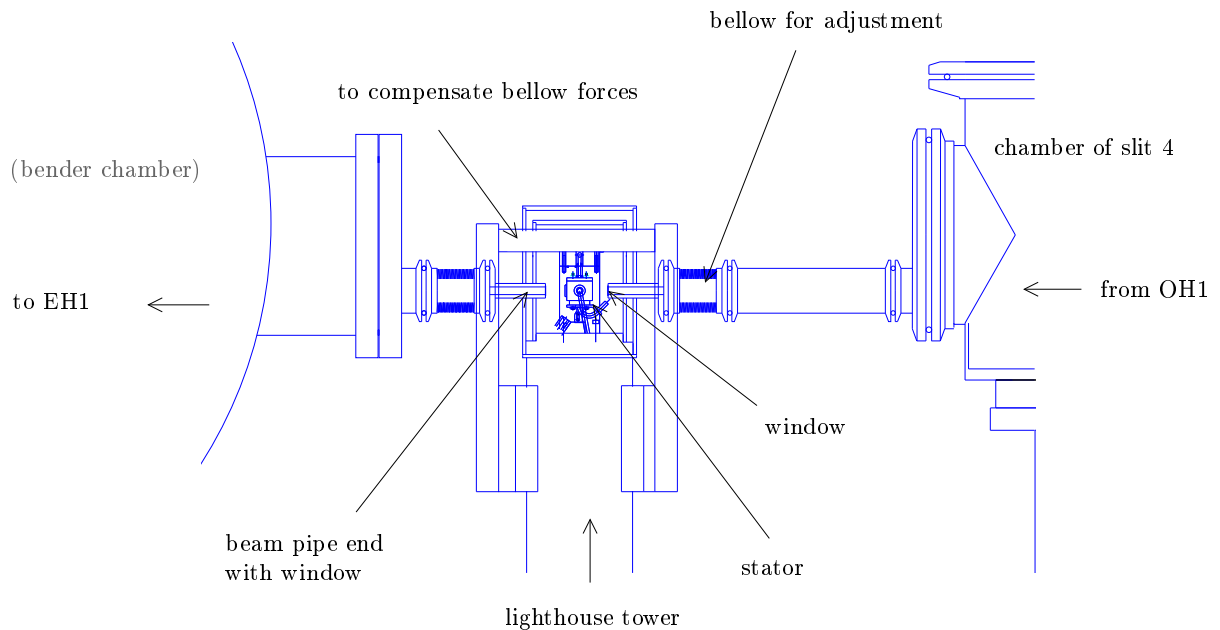


Figure 4.11: ID18 layout for nuclear lighthouse effect measurements. The distance between lighthouse tower and detector is maximised, as to achieve a large displacement of the deviated nuclear signal with respect to the direct beam. Unfortunately, the dimensions of the beam pipes and the beam shutters between the hutches limit this offset. EH1 and EH2 are not used. Different is the setup for traditional grazing incidence nuclear resonance experiments: One of the high resolution monochromators of OH2 has been used, the sample and detector were in EH1. The SR-PAC setup needed no high resolution monochromator and had sample and detector in EH1.

The other shown distances are important when focussing with a compound refractive lens (CRL) or for completeness. The term source signifies the undulators, comparable to a light source in optics. They span over a range of 5 meters. As a good approximation, the centre of the middle undulator is taken as the source point.

To limit absorption and reduce small angle scattering from air, a maximum of the beam path in the beamline is in vacuum. This is done with the help of evacuated beam pipes, having a pressure of approximately  $10^{-2}$  mbar. As a matter of fact, the stator/rotor system cannot be in a vacuum section, as it relies on gas driven acceleration and bearing. Also the detector stays outside the vacuum. Beam exit and entry windows are needed: two windows upstream and downstream of the lighthouse tower, and one large window at the end of the beampipes in EH3, before the detector. These windows can be tailored to one's needs. Additional windows in the beamline are a beryllium window at the entrance of OH2 and further a  $500\ \mu\text{m}$  thick diamond window in the front end, to separate the storage ring vacuum from the beamline. To get the vacuum sections very close to the lighthouse with its gas atmosphere, special beam pipe ends were manufactured, see figure 4.12 for details. The pipe end material is a combination of stainless steel and PEEK (Poly Ether Ether Ketone, a semicrystalline polymer), in order to limit the heat exchange from the part inside the covers to the outside world.



*Figure 4.12: Beam pipe ends upstream and downstream of the lighthouse tower. The windows can either be  $50\ \mu\text{m}$  thick silicon wavers or  $20\ \mu\text{m}$  thick Kapton<sup>®</sup> foils. Whereas the single crystalline wavers produce less SAXS, they are very brittle and do not stand repeated pressure changes do to pumping and flooding of the beam pipes. Therefore, the Kapton<sup>®</sup> windows are preferred. The lighthouse tower itself stands on a combination of a tilt stage, a xyz-stage and a special foot.*

In order to reduce parasitic off-axis radiation, consisting of SAXS from beamline elements upstream of the lighthouse, e.g. windows, absorbers or CRL-lens material, the slit systems "slits 3" and "slits 4" have been installed. Each system has two perpendicular sets of slit blades. Their aim is to cut the outer "halo" of the beam without generating themselves SAXS. Obviously, in-vacuum slits need to be used, as additional windows would compromise the effect of these slits. The slit blades have been fabricated from tungsten monocrystals. As SAXS is scattering on electron density variations, monocrystals

talline material limits these variations to a minimum. The use of two special dedicated slit systems is motivated by the idea that the 4<sup>th</sup> slit will reduce scattering caused by the 3<sup>rd</sup> slit, if the 3<sup>rd</sup> slit blades cut parts of the central beam and not only the halo. The last slit blades should not be orientated in the vertical and the horizontal, but slightly tilted, e.g. 10° as in the case of our setup. As a rectangular slit creates a diffraction pattern, this intensity pattern will be tilted by 10°, too. Instead of giving rise to radiation in the same direction as the delayed nuclear lighthouse signal (horizontal direction), it will be tilted by 10° with respect to this, see figure 4.13. The thickness of the tungsten monocrystals in the beam direction is 2 mm. At 67.41 keV, their transmission is  $2.8 \cdot 10^{-5}$ . The cutting edge has been polished.

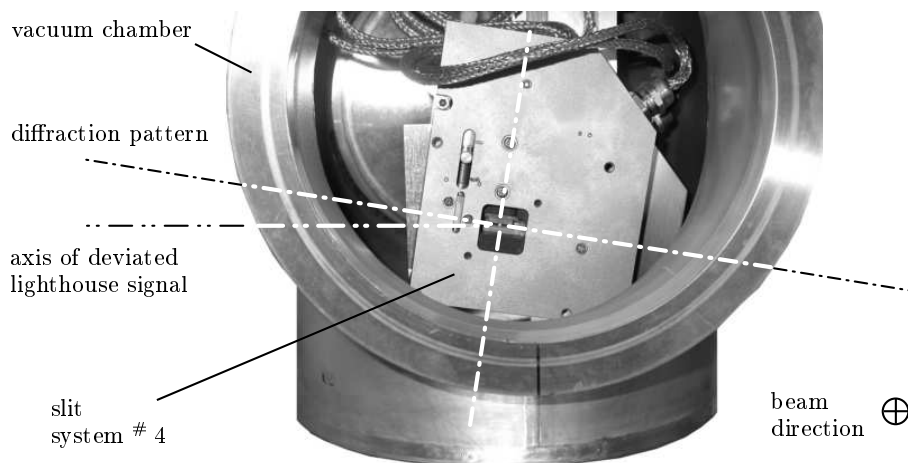


Figure 4.13: The last slit before the lighthouse is tilted by 10°. The benefit of this tilt can easily be seen in the figure. The observer looks upstream and the lighthouse is hidden behind the slit system.

Of course, the considerations concerning the slit system are much less important, if time discrimination of the detector signal is used, thereby blocking out the prompt SAXS intensity anyhow. Nonetheless, detector load is much reduced especially at small angular offsets from the direct beam. This will in most cases allow to access earlier times of the time spectra of the nuclear decay. Therefore, reducing the "SAXS-halo" of the beam should not be neglected in any case, i.e. even when using time discrimination of the detector signal.

## 4.3 Spinning of the sample

The main characteristic of the nuclear lighthouse effect is the fast rotating sample. To achieve highest rotational frequencies, use is made of stator/rotor systems designed for magic angle spinning - NMR [Dot81, Sam02]. The sample is fixed to a cylindrical rotor; either inside it or on its surface. The rotor is gas driven and gas stabilised in a stator block.

### 4.3.1 Stators and rotors

Three different stator/rotor systems are commercially available from Bruker [BRUK], of which two are available at ID18. They differ by the diameter of the rotor: stator/rotor systems exist in diameters of 2.5 mm, 4 mm and 7 mm. The maximum rotational frequencies



possible with such rotors depends on the strain the material can stand, when subjected to huge centripetal forces during rotation. The centripetal force of a pointlike mass is  $F_z = 2\pi m \nu^2 r$ . Therefore, the fastest spinning system is the 2.5 mm system, but it is not available with a cooling gas connection. Further, there do not exist sapphire rotors for this system yet,  $\text{ZrO}_2$  is the only option. This would have compromised intense testing at the  $^{57}\text{Fe}$  resonance in transmission, due to a huge absorption at the  $^{57}\text{Fe}$  transition energy. The 4 mm system and the 7 mm system allow for central cooling, see figure 4.17, and provide a wider choice of rotor materials. For the purpose of the  $^{61}\text{Ni}$  experiments, the 4 mm system has been chosen. It is evident, that cooling is required to increase the Lamb-Mössbauer factor, see figure 2.3. As the lifetime of the excited  $^{61}\text{Ni}$  level is small, high rotational frequencies are needed. The 7 mm system on the other side permits to perform measurements in grazing incidence geometry with  $^{57}\text{Fe}$ . Here, rotational frequencies can be lower, as the lifetime is much larger. The large surface area of the 7 mm rotors is necessary, as the incident angles are very small in grazing incidence (here below  $0.4^\circ$ ). The projection of the surface perpendicular to the beam is much smaller than the vertical beamsizes, even for a 7 mm system.

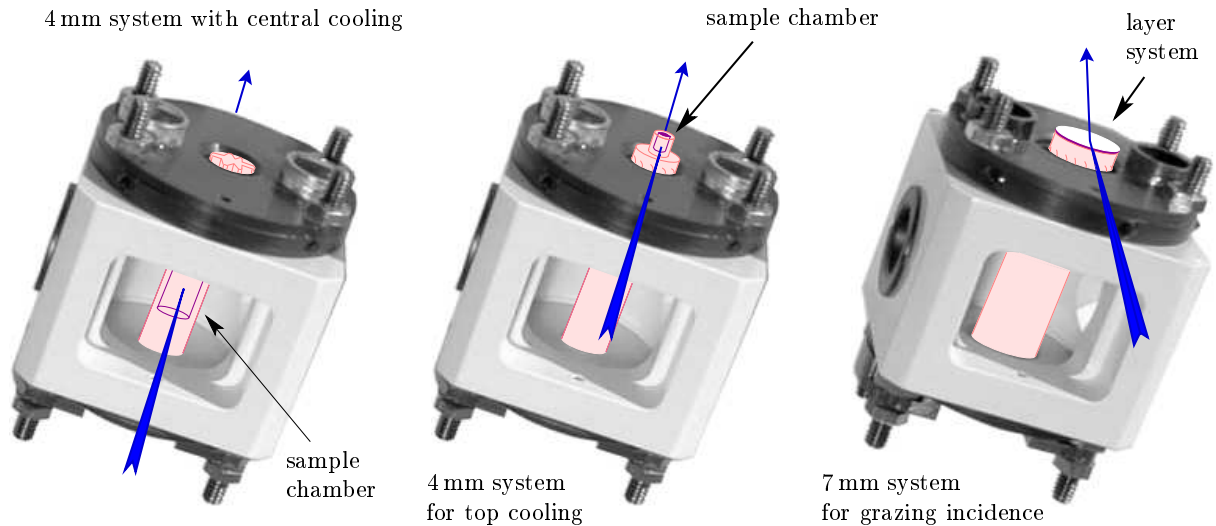


Figure 4.14: The three different experimental configurations. The interior of the stator can be seen, as a cover piece is removed.

In the framework of this thesis, three different configurations have been used. They are depicted in figure 4.14. For the grazing incidence measurements with  $^{57}\text{Fe}$ , the 7 mm stator and a special 7 mm sapphire rotor with several layer systems on a polished flat surface have been used, as shown to the right. The  $^{61}\text{Ni}$  measurements have been done in the geometry as depicted on the left. The sample is in the centre of the rotor and the cooling gas flow has to act there, too. The setup shown in the middle of figure 4.14 was conceived as an alternative to the central cooling 4 mm system. It avoids cooling of the central part, as the sample is placed in an easy accessible region outside the stator block. This is referred to as top cooling. Cooling is treated in detail in chapter 4.4.

### 4.3.2 Stability issues

#### Rotation axis and layer surface normal in grazing incidence geometry

A severe condition that the stator/rotor system has to fulfil for grazing incidence measurements with the lighthouse on layer systems concerns the geometric stability of the layer surface during rotation. This can be expressed by a stationary layer surface normal during rotation. Two influences can compromise this: First a tilt of the rotor surface with respect to the rotor axis, caused by imprecise machining or caused by the surface polishing procedure. Second, a precession of the rotor in the stator during operation. Both influences can not be distinguished during the experiment. It is possible to treat the consequences with the same formalism, analysing the beam after the reflection on a surface that has its surface normal precessing around the fixed stator axis. The angle between the fixed stator axis and the surface normal is  $\epsilon$ , the incident angle is  $\theta$  and the distance to the detector is  $d$ . A screen at the detector positions maps the reflected beam over time. If  $\epsilon = 0$ , there is neither a tilted rotor surface nor a precession. The reflected beam hits the detector always in the same point. If  $\epsilon > 0$ , the beam describes an ellipse on the screen. The size of the ellipse is given by its vertical extend  $A_v$  and its horizontal extent  $A_h$ , see figure 4.15.

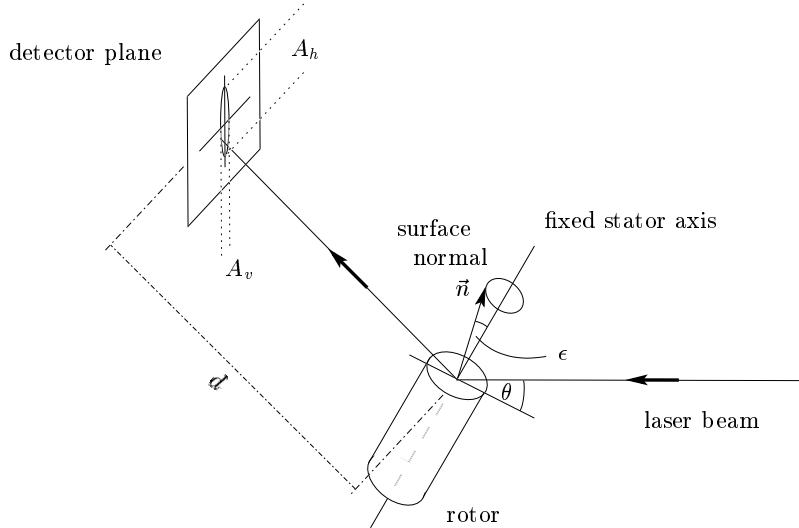


Figure 4.15: Beam imprint at the detector position for inclined rotor surfaces or precession of the rotor in the stator.  $\vec{n}$  is the surface normal of the layer.

$A_v$  and  $A_h$  depend on the angle  $\epsilon$ , the incident angle  $\theta$  and on the distance  $d$ . Tedious calculations lead to the following expressions:

$$A_h = 2d \frac{1}{8} \cos^2 \epsilon \left[ 4 \sin \theta - \cos \theta \left( \tan \theta - \sqrt{\tan^2 \theta + 8 \tan^2 \epsilon} \right) \right] \cdot \sqrt{8 \tan^2 \epsilon - 2 \tan^2 \theta + 2 \tan \theta \sqrt{\tan^2 \theta + 8 \tan^2 \epsilon}} \quad (4.21)$$

$$A_v = 2d \cdot \sin(2\epsilon) \cos(2\theta) \quad (4.22)$$

As  $\epsilon$  is expected to be below  $0.5^\circ$ , and  $\theta$  does not exceed  $1^\circ$  in the grazing incidence geometry, we can approximate the trigonometric functions to first order. This results to:

$$A_v = 4d\epsilon \quad A_h = 2d \frac{1}{8} \left( 3\theta - \sqrt{\theta^2 + 8\epsilon^2} \right) \cdot \sqrt{8\epsilon^2 - 2\theta^2 + 2\theta\sqrt{\theta^2 + 8\epsilon^2}} \quad (4.23)$$

In order to obtain a good separation of the direct beam and the nuclear lighthouse signal, as explained in chapter 4.2.5, the distance  $d$  needs to be big for nuclear lighthouse effect measurements. In particular, the setup as installed at ID18 has the detector at the distance  $d = 13.65$  m. If the rotor turns at 8000 Hz and a time resolution in the order of 1 ns is desired, the lateral detector opening should be  $\Delta x = 0.7$  mm, as a consequence of equation 4.20. In order not to spoil this time resolution, the horizontal extend of the ellipse should be less than half of this, i.e.  $A_h \leq 0.35$  mm. At larger incident angles  $\theta$ , this limitation is more severe, see equation 4.21. An upper limit for  $\theta$  concerning the measurements presented in this thesis is  $0.3^\circ$ . This situation together with equation 4.21 implies  $\epsilon$  to be smaller than  $0.07^\circ$ . However, with  $\epsilon = 0.07^\circ$ , the vertical extend of the ellipse  $A_v$  is 6.7 cm. Either a large detector is necessary, or some nuclear scattered photons will be lost. Although the time resolution is satisfactory with  $\epsilon = 0.07^\circ$ , due to limited detector sizes, a factor of 10 times smaller tolerance is desirable. The error of a tilted rotor surface with respect to the rotor axis can be measured outside the stator. The rotor is to be put into a well machined  $90^\circ$  groove. The reflection of a laser beam at almost normal incidence on the surface is captured on a distant screen. The rotor is turned repeatedly over a small amount in the groove. The laser reflection describes a circle on the distant screen of diameter  $D = d \cdot \sin 2\epsilon$ . Here,  $\epsilon$  is only due to the surface tilt, and the influence from a possible precession in the stator during operation is excluded.

The rotors obtained from Zeiss after a first polishing presented errors of  $0.33(3)^\circ$ ,  $0.36(3)^\circ$ ,  $0.46(3)^\circ$  and  $0.66(3)^\circ$  and had to be repolished. In a second attempt, the angular error was much smaller and measured with the rotation in a fixed groove to be smaller than  $0.03^\circ$ . The machined error could not be determined more precisely due to the experimental error of  $0.03^\circ$ . During the lighthouse effect measurements in grazing incidence, the ellipse of one of the rotors as shown in figure 4.15 has been taken on a photographic paper at the detector position. The ellipse size was measured as  $A_h = 12$  mm and  $A_v = 1.2$  mm. The vertical size is much increased by the normal beamsize at the detector position. Using only  $A_h$  for the calculation of  $\epsilon$ , one obtains  $\epsilon = 0.012^\circ$ . This is the sum of machining error and rotor precession and thus an upper limit for the rotor precession in the stator for the 7 mm system.

### Precessing sample in transmission geometry

Also for the 4 mm stator/rotor system, a precession of the rotor is possible. However, reflectivity measurements as obtained with the 7 mm rotor failed due to the lack of a polished surface with the standard 4 mm rotor. The top part of the special 4 mm rotor (figure 4.14, central panel) could be illuminated by a laser beam. Due to the small curvature of the top part, the reflection travels into all direction of the plane perpendicular to the rotor axis and shows up as a line on a distant screen. At standard operation temperature and at room temperature, no thickness increase of this line could be observed. At very low frequency, especially around 2 kHz, a thickness increase by approximately a factor of two was visible. At low temperatures however, no reflections have been visualised. It is possible that operation at temperatures below 150 K lead to a large precession of the rotor, see chapter 6.4.4. The resulting consequences are explained in that chapter, too.

### 4.3.3 The lighthouse tower

The stator/rotor system is integrated in the lighthouse tower. This tower has been specially designed to direct all gas flows towards the stator and to allow for the two different cooling schemes, top cooling and centre cooling. It further allows for a close approach of the beam pipe ends to the stator. A rigid, but easily removable housing covers the stator in order to prevent heat exchange via convection with the rather humid air of the hutch. The base of the lighthouse tower is evacuated in order to provide a thermal insulation for the transport of the cooling gas to the stator. The details of the lighthouse tower can be seen in figure 4.16.

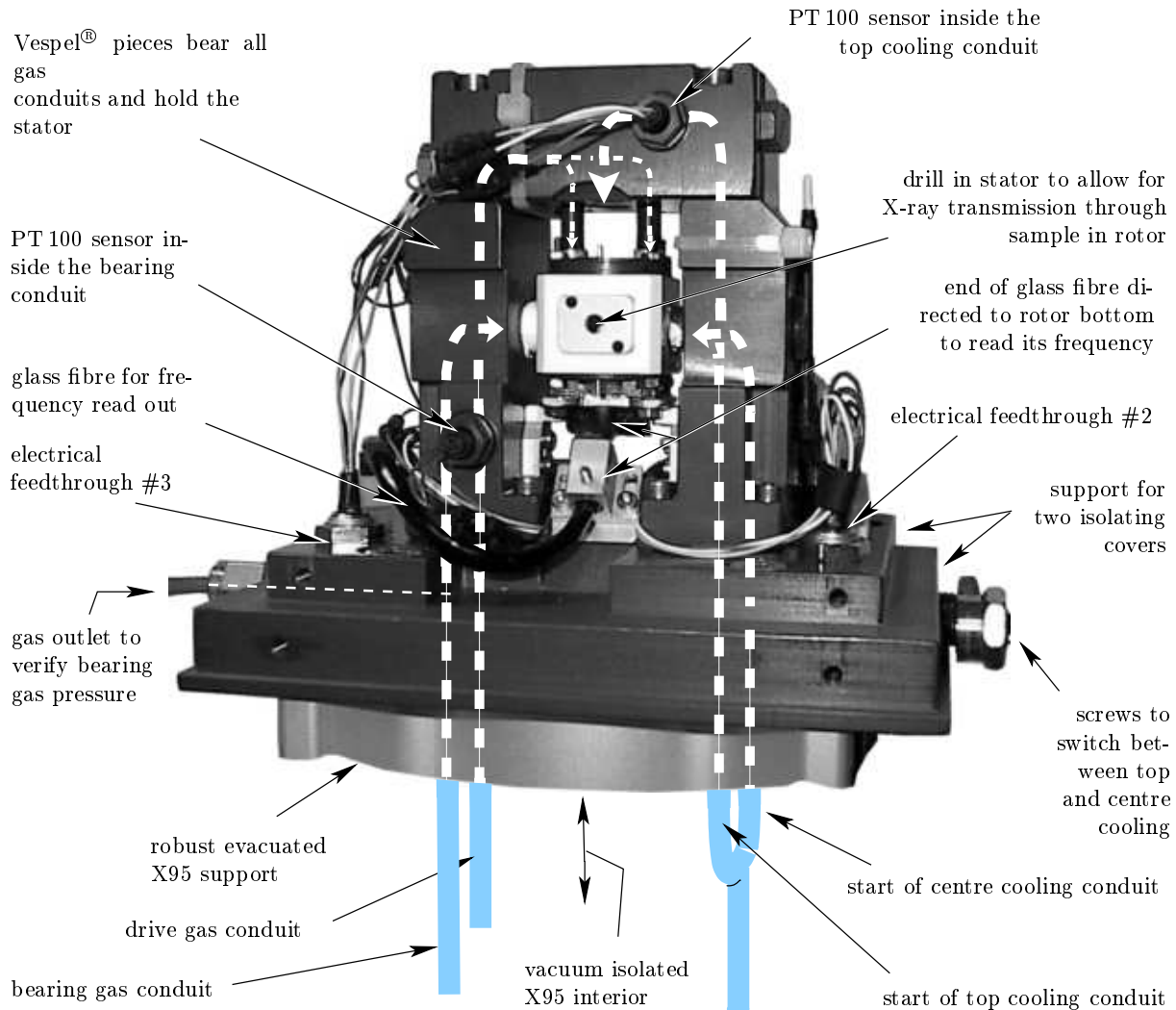


Figure 4.16: The top part of the lighthouse tower. The gas flows inside the main tower parts are indicated by dotted lines.

The rotational frequency is measured via an optical encoder that uses the reflection of a half circumference black and half circumference white paint at the bottom of the rotor. A glass fibre optic system illuminates this area and measures the reflected light. The read out electronics is outside the cooled area, working at room temperature. The accuracy of this equipment is better than 1 Hz. Three electrical feedthroughs with 7 connections each allow the use of several PT 100 resistive thermometers. When the two covers are installed the top part of the lighthouse, the only exhaust is an exhaust pipe, 10 mm large

in diameter. It might be useful to heat it in future to prevent condensation and icing at the outside of the tube and, after long runs, deposits of ice even at the exit of the tube.

The column of the lighthouse tower is a standard X95 bar. It is hollow to take the gas conduits and can be evacuated to minimise heat losses of the cooling gas and in order to prevent condensation of humid air on the X95 outside. All three gas conduits, for bearing, acceleration and cooling, pass through a copper block, thereby decreasing slightly the temperature of the acceleration gas and the bearing gas. This leads to smaller temperature gradients at the rotor and thus a smaller risk of problems due to stress in the rotor. The X95 system further permits attachment of multiple experimental devices if needed. At the lower end of the X95, a huge hollow aluminium cube provides the connection of the feedthroughs for the various gases to the outside of the tower and the connection of a vacuum pump. A baseplate enables the assembly of the lighthouse tower onto a combined tilt and xyz-stage. These stages serve to align the sample in the beam and to tilt it, in order to perform grazing incidence measurements. Unfortunately, the centre of rotation is not at the sample's place, and thus a corrective translation has to be performed at each angular adjustment.

## 4.4 Cooling

### 4.4.1 Cooling method

When addressing Mössbauer isotopes with high transition energies with NFS or the NLE, it is essential to work at low sample temperatures. Only then, the Lamb-Mössbauer factor is significantly different from zero, see for example figure 2.3 for the case of  $^{61}\text{Ni}$ . As the stator/rotor system relies on gas flows, it is not possible to insert the lighthouse into a cryostat. The only cooling option is to cool the sample with the gas flows themselves, either using cooled bearing and drive gas flows, or applying an additional cooling gas flow. The first choice is limited, as cooling and operation are not independent: Increasing the bearing or acceleration gas flows in order to change the rotational speed of the rotor would drastically change the sample's temperature. A further problem would be the Joule-Thomson effect when the bearing and acceleration gas flows leave the tiny drills of the stator block and expand. The temperature could drop so far, that liquid droplets are created, having disastrous consequences on the bearing and the rotor itself. Finally, the sample chamber is not in the immediate vicinity of the bearing and acceleration gas flows, but in the central or the top part of the rotor. As a consequence, we choose to work with an additional cooling gas independent from the bearing and acceleration gas flows to cool the sample.

The independent cooling gas flow emerges from a pressurised liquid nitrogen vessel of 200 l volume. The maximum pressure available is 16 bar. This vessel delivers a sufficient flow of nitrogen gas at room temperature both to the pneumatic control unit for the bearing and the acceleration gas, and for the additional cooling gas. It is important that the gas is completely free of humidity or oil droplets, as these impurities would either freeze and block the gas conduits, or impact on the rotor and cause instability. Highest purity can be obtained when using evaporated nitrogen from a liquid nitrogen reservoir. Using gas from a pressurised bottle is therefore not recommended.

After passing a pressure reducer and a regulation valve, the cooling gas, still at room temperature, enters a heat exchanger. This heat exchanger consists of a 12 turn copper

tube spiral that is immersed into a second liquid nitrogen Dewar. Before leaving the Dewar vessel, the gas directing pipe is isolated by a flexible metal hose that is permanently evacuated. This hose is connected to the lighthouse tower X95 structure, thus allowing a complete insulation between the Dewar and the top of the lighthouse tower. The Dewar vessel can be refilled during cooling operation thanks to a special filling access. In case of problems, the 12 turn spiral can be bypassed and the cooling gas helps heating of the lighthouse tower up to room temperature.

Inside the lighthouse tower, cooling gas, bearing gas and acceleration gas are directed through a copper block. This reduces slightly the temperature of the acceleration and bearing gas flows and prevents the rotor from huge temperature gradients. After this copper block, the cooling gas passes a second copper block with an integrated heater for fine regulation of the gas temperature. Fortunately, already the regulation of the flow of the gas, i.e. its quantity, is sufficient enough to control the temperature with the precision of about 0.5 K as measured with a PT 100 resistor in the gas conduit at 3 cm before hitting the sample. After about one hour of continuous operation with constant frequency and cooling gas flow, the temperature drift at that place is below 0.1 K per minute.

The sample temperature might differ from that measured by the PT 100 due to the influence of the neighbouring bearing gas outlets, see figure 4.17. Fortunately, the mass flow of the cooling gas is by far larger than that of the bearing gas and the acceleration gas. The bearing gas therefore has to exit the stator towards the top and the bottom and not towards the centre. We nevertheless admit that the final uncertainty might reach 5 K.

#### 4.4.2 Stator modifications

After repeated cooling of the stator/rotor system during operation, problems with the stability of the rotational frequencies and even the destruction of a rotor occurred. Although based on limited experience, we believe that the first operation at low temperatures of the stator/rotor system after receiving it from Bruker is free of problems even at high rotational frequencies. The problems appeared only later. We therefore investigated in detail the stator system which is depicted in figure 4.17.

There are several reasons that might lead to the stop of a rotor in the stator during cooling operation. First, droplets might form according to the Joule-Thomson effect at the exit of the tiny drills. This should be a much bigger issue if the bearing and cooling gases are at temperatures close to the dewpoint of nitrogen. In our case, the temperatures seem to be too high for that, but as the gas is at an elevated pressure, this phase transition is already at higher temperatures. It would be interesting to test the operation of the rotor system with helium gas, with its much lower temperature of liquefaction. Second, a different thermal expansion of the stator materials ( $\text{ZrO}_2$  for the bearing parts, BN for the main part, Vespel<sup>®</sup> for the acceleration part) might cause leaks that form at the interfaces, that are only glued by the factory. The different expansion with respect to the rotor's own material and its diameter might change the gap between rotor and stator as much, that it exceeds the tolerances needed for operation. This might be consistent with the observation, that we had only sapphire rotors broken or stopped at low temperature, but no  $\text{ZrO}_2$  rotors, that are of the same material as the bearing disks. On the other hand, sapphire is much more brittle at low temperatures than  $\text{ZrO}_2$ . Whereas the  $\text{ZrO}_2$  rotor might just temporarily slow down during the encounter of a temporary problem, the sapphire rotor could explode immediately on touching any stator part. A third reason

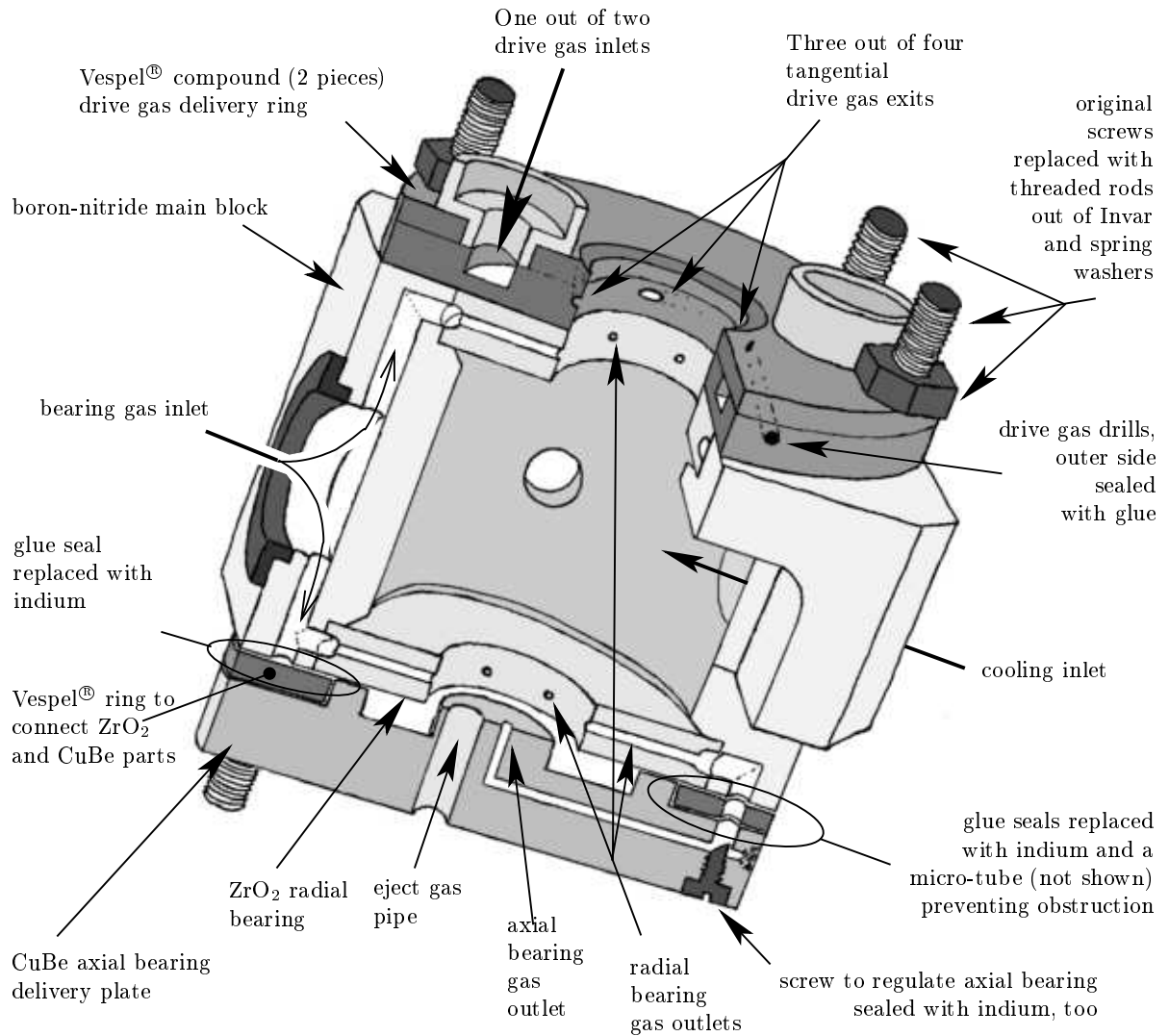
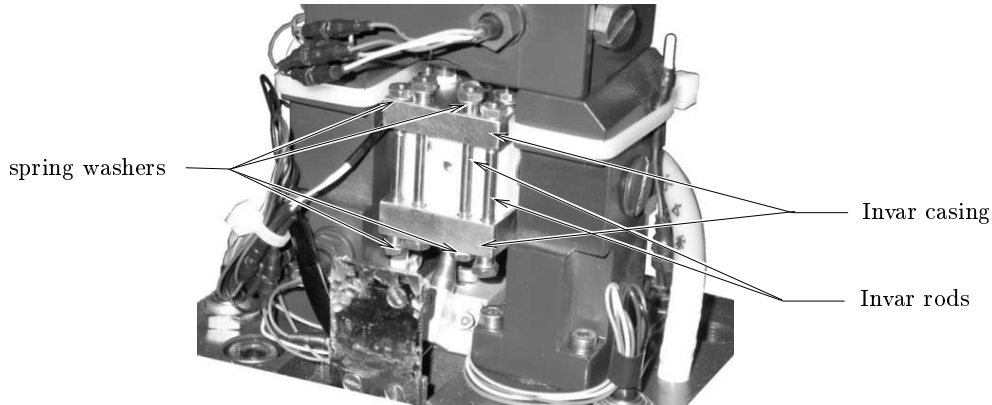


Figure 4.17: The 7mm stator block seen in a cut. All gas flow conduits are illustrated. The configuration as delivered by Bruker [BRUK] has been improved with indium sealings.

are possible leaks that originate from cracks in the glue after repeated cycling. This problem seems very important to us and furthermore could be improved by us with some modifications. A very critical glue connection is the one at the lower part of the bearing gas conduits. It concerns the interfaces between the BN main stator body, a VespeI® ring, and the CuBe bottom plate, see figure 4.17. While removing the four screws assembling the whole stator, the VespeI® ring did not stick to the BN main body anymore, thus fortifying the concern about this interface and the glue. The glue rests have been removed with a scalpel and were replaced by several indium foils, cut especially to cover also the BN to ZrO<sub>2</sub> interface. The connecting hole in the VespeI® ring at the lower right side of figure 4.17 between the BN main body and the CuBe part has been tightened with two indium foils. A micro-tube has been incorporated to prevent obstruction of the conduit by an eventual surplus of indium. The tube has the length of the vertical conduit, but the end parts have been half cut away. When reassembling the stator, the original brass rods (the screws) have been replaced with Invar rods. Invar exhibits almost zero thermal expansion over a wide temperature range.

To strengthen further the interface between the BN main body, the top ZrO<sub>2</sub> bearing



*Figure 4.18: An Invar casing with Invar rods and spring washers replaces the brass screws (compare with figure 4.16). It consists of a top and a bottom plate that fit exactly to the stator surface and thereby hold it tightly. The nuts at the end of the Invar rods act on spring washers, that generate an almost constant pressure on the stator parts independent of the temperature.*

gas disk and the top Vespel<sup>®</sup> compound that assures the drive gas delivery, an Invar casing has been applied. This Invar casing tightly holds the top and the bottom part of the stator and allows the use of spring washers to maintain a constant pressure on the assembly during thermal cycling. The connection between the two plates of that casing is provided by four main Invar rods that replace the original brass rods and eight additional Invar support rods. The nuts have been tightened equally to 6 mN/m. The lower Invar plates further presses an indium foil onto the screw in the CuBe plate, that regulates the axial bearing. This had only been sealed with paint before.

A picture of the Invar casing is shown in figure 4.18, as installed in the lighthouse tower, see chapter 4.3.3. It allows the beam to access both a sample in the centre of a 4 mm rotor or at the top of a 4 mm rotor, if top cooling is desired. The top cooling option is explained in chapter 4.4.4. The success of the modifications has been shown during four consecutive days of beamtime by executing repeated cooling cycles down to 180 K and 115 K for several hours repeatedly. The 4 mm standard ZrO<sub>2</sub> rotors with the sample in the central chamber have been used.

#### 4.4.3 Gas flows and cooling

Without cooling and in automatic mode of the pneumatic control unit, certain drive gas and bearing gas pressures are chosen by the control unit. The quantity of gas thereby provoked is not measured and taken into account. To have a better understanding of this control system and to elucidate cooling operation parameters, we measured the gas flow characteristics of the stator/rotor system. The gas flow measurements have been done at the exit of the pneumatic control unit with the help of standard variable area flow meters [PKP]. Simultaneously, the pressure display of the pneumatic control unit has been read. The measurements are shown in figure 4.19.

As seen in figure 4.19, the bearing gas flow stays below 7 l/min even at high speed. In manual mode, this might be raised to 9 l/min via increasing the bearing gas pressure to about 3600 mbar. During long term cooling operation of several hours, it was repeatedly recognised, that this gas flow decreases slowly down to 6 l/min, where we used to intervene before further problems could occur. By some means, the gas flow seems to be blocked



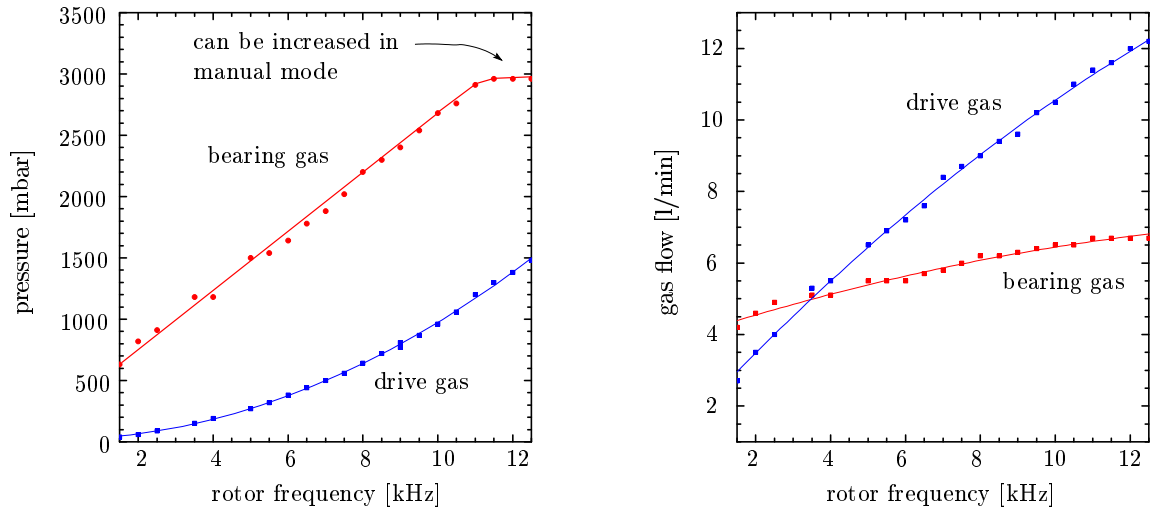


Figure 4.19: Gas pressures (left) and gas flows (right) at room temperature operation in automatic mode of the pneumatic control unit. The bearing and drive gas flows have to be compared to the cooling gas flow, which is much higher, reaching up to 50 l/min.

more and more. Raising the temperature and cooling again usually helps. However, one does not need to heat up to room temperature to achieve this positive behaviour.

The cooling gas flow varies between 20 l/min and 50 l/min, depending on the desired temperature. It is much more important than the bearing gas flow and prevents thereby the bearing gas from entering the central hollow part of the stator and around the sample. The lowest temperatures reached for at least 5 hours of continuous operation has been 90 K, as measured in the gas conduit 3 cm before the sample. The  $\text{ZrO}_2$  rotor turned at 10 kHz, but fluctuating in speed by  $\pm 50$  Hz. The cooling gas flow was 50 l/min. The pneumatic control unit ran in automatic frequency mode, thereby stabilising the frequency on its own. This is not always recommended, especially for the sapphire rotors, as sudden drops in speed at very low temperatures due to stator problems lead to exaggerated response of the acceleration pressure, making things even much worse. Sapphire rotors repeatedly exploded in the old unmodified stator. Frequency variations while cooling are less important at lower speeds. At 8 kHz, typical speed variations are  $\pm 3$  Hz. Due to the copper block heat exchanger inside the evacuated lighthouse tower, that conduits both the cooling and the drive and bearing gas flows, the temperature difference between cooling gas and the other two gas flows is reduced. With the cooling gas having 90 K at 3 cm before reaching the sample, the bearing gas is about 70 K warmer, the drive gas about 110 K warmer, with the rotor turning at 10 kHz. These are the highest temperature differences, as cooling, bearing and drive gas flows are close to their maximum. At lower speed or lower temperatures, these differences are much reduced.

After frequent temperature changes of the rotor during operation, the turbine cap of the standard rotor repeatedly loosened. This is avoided by gluing of the cap to the rotor after the filling of the sample.

#### 4.4.4 Top cooling

To operate the lighthouse at low temperatures, a second cooling scheme has been developed. The first motivation was to avoid the repeated rotor breakdowns with the standard

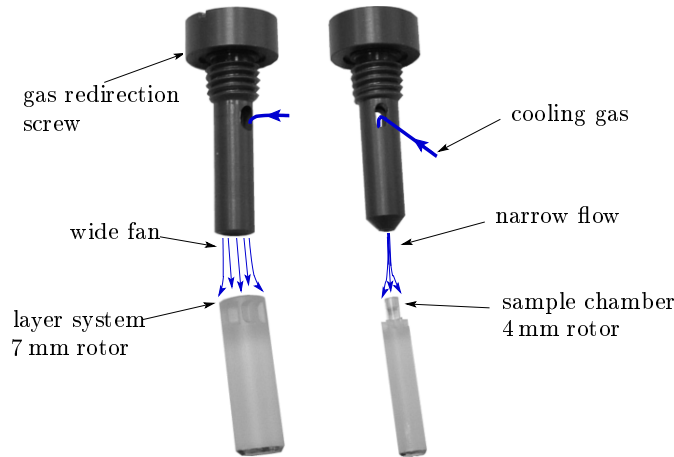


Figure 4.20: The gas redirection screws conceived for top-cooling. On the left the screw providing a wide fan of cool gas for the cooling of the 7 mm rotor. On the right, the gas redirection screw is shown that delivers a narrow cooling gas flow in combination with the 4 mm special sapphire rotors and its top sample chamber.

4 mm system and central cooling while using a standard sapphire rotor. The second motivation was to allow for cooling when investigating layer systems on the top of a 7 mm rotor. In this second cooling scheme the sample is placed outside the stator body at the end of a special rotor. The sample is cooled from the top and thus, large temperature gradients in the region of the bearing gas flow are avoided. To see the cooling gas flow inside the lighthouse tower, see figure 4.16. The special rotors as placed in the stator are depicted in figure 4.14. Two types of a gas redirection screw have been machined, that perform the last part of the cooling gas conduit. They are screwed into the top Vespel® part of the lighthouse tower. The two special rotors accommodate the sample just below this screw. One screw provides a large fan, the other a narrow cooling gas flow, see figure 4.20.

First results with the 4 mm system seem to indicate a lateral force on the top of the rotor, leading to contact of the spinning rotor with the stator. Three of these sapphire rotors broke. The direction of the cooling might need to be better adjusted. The 7 mm system has not been used yet with cooling. Further testing of this cooling scheme has to be performed in the future.

## 4.5 Detectors

### 4.5.1 Photon detection for nuclear resonant scattering

In nuclear forward scattering experiments, including grazing incidence geometry, detectors have to satisfy several criteria. Even when employing high resolution monochromators, the incoming flux is in the order of  $10^7$  to  $10^{10}$  photons per second. Dilute samples or low Lamb-Mössbauer factors on the other hand might limit the nuclear delayed signal to countrates below 1 photon per second. This demands a *huge dynamic range* for the detector and a very *fast recovery time* after the strong "prompt" pulse of non-interacting photons. After the prompt pulse, the detector must soon be ready to count the weak delayed signal. As the nuclear signal might be very low, the detector needs to have a *very low noise*, possibly below 0.01 counts per seconds. The lifetime of the excited state

of typical Mössbauer isotopes varies between 100 and 1 ns, see table 8.2, but the time evolution of their decay can show beats on the ns time scale. The detector needs to have an *excellent time resolution*, around 1 ns seems desirable. Finally, a *high quantum efficiency* is highly appreciated.

A detector that meets many of these criteria is the avalanche photo diode (APD) [Bar00, Bar97]. Although first experiments used a slow Ge diode detector [Ger85] or plastic scintillator coincidence detectors [Met90], APDs became soon the standard detector in nuclear resonant scattering [Kis92, Bar94, concerning pioneering work]. They are based on silicon diodes. The APDs used in our experiments were 120  $\mu\text{m}$  thick and 10 x 10 mm<sup>2</sup> large silicon diodes. The cross section of a diode is shown in figure 4.21. An incident photon will most likely be absorbed in the large depleted region of the diode (100  $\mu\text{m}$  thick). The absorption process will be principally via the photo effect; at photon energies above  $\approx 40$  keV also via the Compton effect. The ejected primary electron will create a huge number of electron hole pairs in its immediate vicinity, about one pair per 3.6 eV. The drift velocity of an electron in the silicon material is about 100  $\mu\text{m}$  per ns. This is the limiting factor for the time resolution. In the gain region close to the p-n-junction, the electric field is maximal and leads to an acceleration of the electrons and the creation of a huge avalanche of secondary electrons. Typical voltages applied to the diodes are between 270 and 450 V.

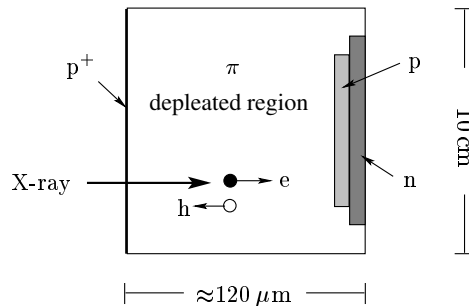


Figure 4.21: Layout of a EG&G reach through APD detector seen in a cut [Bar97]. The large depleted region absorbs X-rays that create thereby electron hole pairs. The depleted region defines the active thickness which is around 100  $\mu\text{m}$  thick. The electrons drift towards the p-n-junction region. Close to that junction, the electric field and the acceleration of the electron are maximal. This is the gain region where avalanches of electrons form.

Immediately after the discovery of the nuclear lighthouse effect, it was believed that detector restrictions known from standard nuclear forward scattering could be drastically released. The direct beam is blocked by a beamstop and the time information is mapped on an angular scale. In fact, demonstration experiments using  $^{57}\text{Fe}$  as the nuclear scatterers worked with simple detectors like wire proportional counters [Röh00b], an image plate [Röh01b] or with lateral scans with avalanche photo diodes *without* the use of time discriminating electronics [Röh00c].

Naturally, demonstration experiments use favourable experimental conditions, here especially the use of  $^{57}\text{Fe}$  as nuclear scatterer and highly enriched samples. Both the delayed nuclear signal and the undesired, but unavoidable SAXS background, are of comparable strength. The discrimination can be done with successive measurements of the angular intensity variation, once at resonance, once slightly detuned, and subtraction [Röh00c]. This is no longer possible in the case of dilute samples and especially for nuclear scatterers with less favourable nuclear parameters, where delayed count rates can drop by

several orders of magnitude. Fast detectors need to be employed to use the time stamp of the detected photon in order to discriminate between the prompt SAXS and the delayed nuclear signal. Finally, APDs, although much less efficient at higher energies like the  $^{61}\text{Ni}$  transition energy, need to be employed.

#### 4.5.2 Avalanche photo diode array

The quantum efficiency of single, thin APD detectors is very poor at energies above 10 to 20 keV, see figure 4.22. Increasing the thickness of the depleted region of a silicon diode to values much higher than 100 to 200  $\mu\text{m}$  would increase the typical drift time of electrons in the material and thereby deteriorate the time resolution to an unacceptable amount. In a first step, the silicon diodes can be inclined, thereby increasing the width as seen by the X-ray while impinging on an angle on it. A second approach is to stack individual thin APDs in a row, an array. If the following electronics is properly adjusted, the total time resolution of the stack approaches the time resolution of an individual APD. A limiting factor is the cost of the APDs and the electronics, or the complexity of the electronics if several APDs are controlled together by the same electronics.

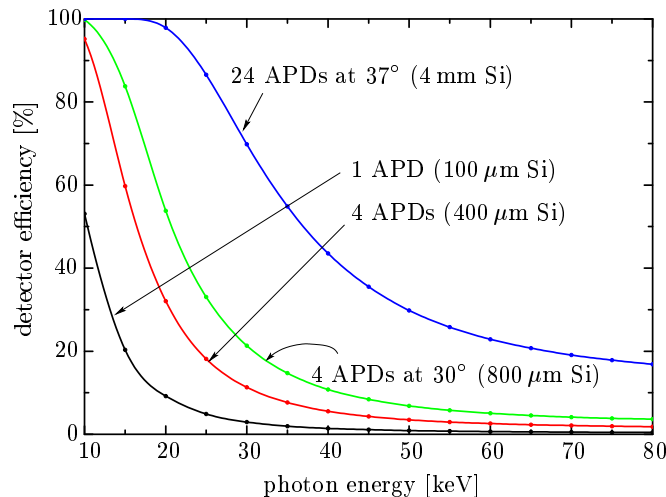


Figure 4.22: Detector efficiency of stacked standard EG&G silicon diodes with an individual active thickness of  $100\ \mu\text{m}$  for photon energies between 10 and 80 keV.

Results presented in this work have been obtained with single APDs (especially nuclear fluorescence signals of  $^{61}\text{Ni}$  and  $^{57}\text{Fe}$ ), a stack of 4 inclined APDs (grazing incidence measurements with  $^{57}\text{Fe}$ ) and in particular with an 24 APD array. This array has been build by the University of Hamburg [Ges04]. 24 individual EG&G silicon diodes, each  $10 \times 10\ \text{mm}^2$  large and  $100\ \mu\text{m}$  thick, are used, each connected to an individual pre-amplifier, see figure 4.23.

Four groups of six detectors have been selected for their almost identical behaviour of break-down voltage and can therefore be connected to the same high voltage power supply. The applied high voltage ranged between 275 and 310 V. The pre-amplified signal outputs of twelve of the detectors are grouped to an analogue sum. Accordingly, two of these sum signals have been directed to the fast electronics, as explained in chapter 4.5.3, which is placed outside the hutch in the control cabin. Using the analogue sum of the pre-amplified signals caused the time resolution to be around 2 ns. The time resolution of an individual APD is twice as good. It is therefore foreseen to convert each individual

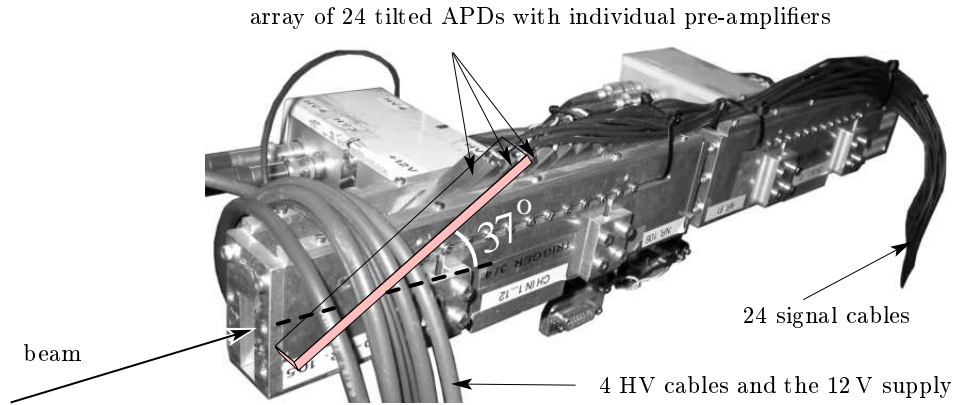


Figure 4.23: Photograph of the 24 APD array. They are inclined to an angle of  $37^\circ$  between the silicon diodes and the beam direction.

pre-amplifier signal to a digital pulse and align these digital signals of individual APDs in time with a digital delay [Ges04] before creating a logical OR afterwards. This process nevertheless demands a bunch clock signal in the hutch itself and further modifications to the standard fast electronics setup of ID18. The time resolution should be close to 1 ns.

### 4.5.3 APD signal electronics

The pre-amplified APD detector signal is fed in general towards two counters and a multi-channel analyser, that acquires the time spectra. The APD signal should be counted in the "prompt" counter, no matter when a photon was detected. If it was detected a reasonable time after the prompt synchrotron radiation flash, it should be counted as a "delayed" photon. To determine, at what time after the prompt flash this "delayed" photon was detected, the delayed signal needs to be further transformed to be analysed by the multi channel analyser. The necessary steps are sketched in figure 4.24.

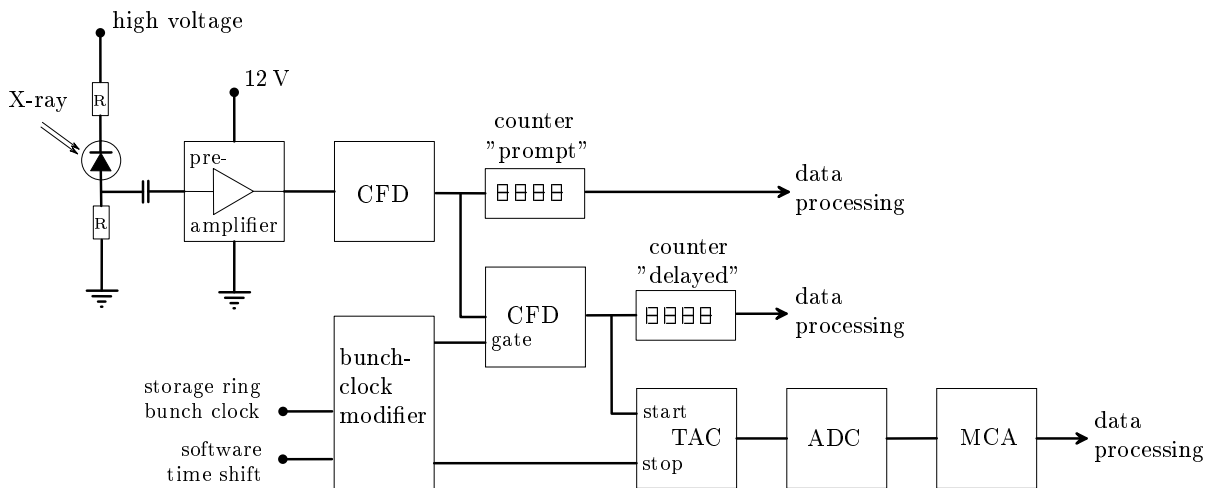


Figure 4.24: Fast electronics at ID18 to deliver counter signals and information for the multi-channel analyser. Constant fraction discriminator CFD, time to amplitude converter TAC, analogue to digital converter ADC and multi channel analyser MCA.

Upon absorption of an incident photon in the APD, the resistivity of the APD drops and a voltage variation is passed via a capacitor into the pre-amplifier. This amplifier is in

the direct vicinity of the silicon diode, as to reduce noise. After the 3 amplification stages of the pre-amplifier, the signal is sufficiently strong to be transferred to a rack outside the experimental hutch. A constant fraction discriminator, CFD, eliminates peaks below a certain threshold (noise or low energy X-rays) and delivers a NIM signal relatively independent of the incoming signal's pulse height (constant fraction). The output is split to be a) counted as a photon event in the "prompt" counter (it does not only count prompt photons, but all photons actually) and b) to be directed to a second CFD. The second CFD is gated by a modified bunch clock signal, that vetoes counting during the arrival of the prompt photon pulse in the detector. If the gate does not block the output of the second CFD, the photon arrived outside the prompt flash and is counted as a delayed photon. It therefore originates likely from the decay of an excited nuclear level or backscattering from the distant experimental hutch walls. The latter can be avoided by proper shielding in the vicinity of the detector, thereby reducing the flight time of backscattered photons. If a photon is detected as delayed, the output of the second CFD further starts a time-to-amplitude converter, TAC. The next signal from the bunchclock modifier delivers the stop pulse. The amplitude of the TAC signal is converted into a digital signal via the analogue to digital converter, ADC, and is fed accordingly into the multi-channel analyser. The delayed photon contributes thus as one event in the time-spectrum. The time axis is inverted due to the cabling of the start and stop signals of the TAC. This cabling choice is deliberate because it avoids to reset the TAC for all bunches that do not show a delayed photon.

#### 4.5.4 Position sensitive APD detectors or scanning detectors

It should be stressed, that the described 24 APD array detector as described in chapter 4.5.2 needs to be scanned over the angular range off the direct beam that is expected to show a measurable nucleary scattered signal. To increase efficiency, the individual APDs are stacked in beam direction, and not lateral to it. The lateral dimensions are finite, 10 mm x 6 mm due to the 37° inclination, housings reduce this further. Due to the finite angular acceptance of the detector, most of the nuclear scattered photons from the lighthouse will pass undetected.

Let us first consider a more general detector that is scanned: Without time discriminating detector electronics, the slit size in front of the detector defines the time resolution and each detector position  $x$  corresponds to a time  $t$  according to  $x = 2\pi d \nu \cdot t$ , with  $d$  being the distance between sample and detector and  $\nu$  the rotational frequency of the rotor.  $x = 0$  is the position of the direct beam. If no slit is used but the detector signal is analysed with time discriminating electronics together with a MCA, the time resolution is given by the detector and its electronics. Then, a large detector is better, provided it still bears the overall incoming flux, especially the SAXS background.

To improve the detection, one could imagine a lateral set of APDs with sufficient individual efficiency. As the nuclear lighthouse effect scatters the delayed photons at different times into different directions, compromises can be done between position resolution and electronic time resolution. No trade-off can be done with the electronic suppression of the prompt SAXS background.

Fast, position sensitive or segmented detectors with high efficiency at photon energies above 40 keV are a huge challenge. There is nonetheless work in progress on position sensitive APD arrays for use at rather low photon energies, [Bar00, Bar03]. For nuclear

lighthouse effect measurements with  $^{57}\text{Fe}$ , such a detector would need to span over at least 40 to 50 mm of lateral dimensions, to cover a wide range of angles and thus times. A standard thickness of  $100\ \mu\text{m}$  would be sufficient. An array of 50 APD, each covering 1 mm horizontally and for example 2 mm in the vertical direction, could be achieved reasonably. For nuclear lighthouse effect measurements with  $^{61}\text{Ni}$ , the thickness of the individual elements should be at least in the mm range. This could be achieved by using the silicon diode sheets stacked like a pile of paper, and the beam impinging from the pile's side. A standard  $10 \times 10\ \text{mm}^2$  diode would be 1 cm thick in this geometry. Unfortunately, to cover about 3 cm at least (due to the short lifetime of  $^{61}\text{Ni}$ , the angular range to be covered is less), one would need to pile more than 200 of these silicon diodes. A more practical solution could consist of thirty diodes inclined to  $6^\circ$ . Each diode covers  $10\ \text{mm} \cdot \sin 6^\circ = 1\ \text{mm}$  in the horizontal direction and would have an effective thickness of  $100\ \mu\text{m} / \sin 6^\circ = 1\ \text{mm}$  in the beam direction.

A further advantage of a fast segmented detector, that spans the whole angular range of interest at once (i.e. without scanning), is its independence from beam intensity variations. Especially the drift of the monochromator leads to fast changes of the intensity of resonant photons, as angular acceptances of Bragg reflections at high energies are particular small. Alternatively, the performance of the monochromator could be checked with a fluorescence signal from an additional  $^{61}\text{Ni}$  sample. This is explained in chapter 4.6.

## 4.6 Beamstop and in-vacuum flux monitor

Among the advantages of the lighthouse effect is the point, that the direct beam does not reach the detector. Thereby, detector overload can be avoided without the use of sophisticated high resolution monochromators. The use of a beamstop does not seem to be necessary at first sight, as one might just not put the detector in the direct beam. However, at small lateral offsets from the direct beam, that beam might create fluorescence radiation in the detector housing and generate undesired background radiation. Further, an in-vacuum beamstop can avoid SAXS scattering that would be generated if the full beam leaves the vacuum pipes via a window. For the design of the beamstop, some points are important, especially at high photon energies or if no time discrimination of the detector signal is performed.

A first point is the position, where to put the beamstop. It needs to be far away from the lighthouse, as to allow wide separation of direct beam and deviated photons that have been nuclearly scattered at early times. The drift tube between lighthouse and detector needs to be evacuated, as to reduce further SAXS or absorption in air to a minimum. Unfortunately, for technical and practical reasons, this detector is in air, thereby requiring a large exit window at the end of the evacuated drift pipe. A large Kapton<sup>®</sup> window,  $200\ \mu\text{m}$  thick, has been used in our case. The detector is placed behind that window. If the direct beam is blocked after the window, a huge amount of additional SAXS would be produced by the window and scatter also towards the close detector. This can be nicely reduced in integrating the detector into the vacuum system, such as to block the direct beam just before the Kapton<sup>®</sup> window. A "4-way-cross" vacuum vessel together with a motorised arm has been installed, the beamstop being attached at the end of the arm. Fine positioning of the beamstop can be achieved with an ion chamber temporarily positioned after the Kapton<sup>®</sup> window.

Apart from absorbing the primary radiation, interaction of photons with material leads

in many cases to excited electronic levels. The ground state is often reached again via the emission of photons of the different K-level emission lines. Resonant processes lead to an increased extinction length for these energies, so care has to be taken to absorb this fluorescence radiation further on. Due to the low energy of the K-level fluorescence radiation, detectors are in general much more efficient for them. Usually, sandwiches of different absorber materials are used.

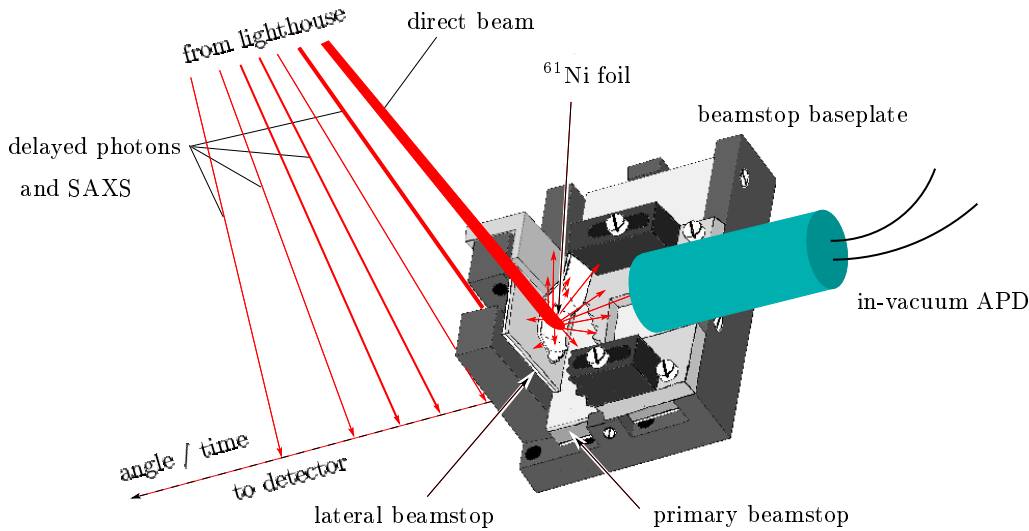


Figure 4.25: Drawing of the beamstop that cuts the direct beam. An enriched  $^{61}\text{Ni}$  foil is incorporated to monitor the energy of the monochromatised beam via detection of the nuclear fluorescence radiation with an in-vacuum APD.

A final point is the integration of a foil of the investigated Mössbauer isotope in front of the beamstop, but shielded to the side. This is depicted in figure 4.25. An in-vacuum APD close to this foil will be able to detect nuclear fluorescence radiation. The intensity of this radiation serves as monitor signal for the energy of the monochromator. If it drifts, this will be seen easily. Especially when the principal "lighthouse" detector is scanning over a wide range of angles, needing a certain time at each position, resonant flux variations can be monitored and be used to calibrate the countrate of the principal detector. The in-vacuum detector needs to be fast of course, as to distinguish between prompt electronic scattering and the delayed nuclear fluorescence signal. Therefore, an APD has been chosen. APDs should work under good vacuum. Unfortunately, without the installation of further powerful pumps, we could not reach  $10^{-4}$  mbar or better. Intermediate pressures ( $10^{-2}$  to  $10^{-3}$  mbar) are critical for the APD, as electric discharge arcs can occur close to the high voltage of the APD. Air at intermediate pressures is less isolating. For efficient pumping, the APD should have a quite open case and especially the diode packaging should not be vacuum tight. With an open casing, noise of the APD tends to increase, so care has to be taken. The APD needs to be fixed to the beamstop and the motorised arm.

The beamstop conceived for our measurements uses a 1 mm hafnium, 2 mm tungsten,  $250\ \mu\text{m}$  silver and  $100\ \mu\text{m}$  iron sandwich as primary beamstop for the direct beam. A small 1 mm hafnium,  $250\ \mu\text{m}$  silver sandwich as lateral beamstop absorbs the fluorescence radiation from the integrated  $^{61}\text{Ni}$ -foil.



## Chapter 5

# $^{57}\text{Fe}$ -layer measurements in grazing incidence

This chapter presents the first angle-resolved measurements with the nuclear lighthouse effect in grazing incidence geometry. This geometry was motivated by the fact, that no rotor material had to be crossed by the beam, avoiding small angle X-ray scattering (SAXS) from the rotor material itself. Furthermore, the conceived rotors for this geometry have their layer system outside the stator block, allowing for a different cooling scheme, top-cooling. Finally, SAXS turned out to be still important, now caused by the surface roughness of the layers. Therefore, 16-bunch mode became necessary for the success of the measurements even for  $^{57}\text{Fe}$  and its favourable nuclear properties, i.e. relatively high countrates as compared to similar systems with other Mössbauer isotope. Due to beam-time limitations, no measurements with the cooling scheme have been performed.

It should be stressed that the primary aim of the measurements presented here has not been to obtain insight in the physical properties of the investigated samples, but to show the feasibility of the grazing incidence geometry with the nuclear lighthouse effect. To understand in detail the structural and magnetic properties of the investigated layers, different additional methods would have been needed. Possible methods for the investigations of thin layers are such diverse techniques as the magneto-optical Kerr effect (MOKE), Auger electron spectroscopy, Conversion electron Mössbauer spectroscopy (CEMS), Low energy electron diffraction (LEED) or atomic force microscopy (AFM), to cite a few. This is outside the scope of this thesis. For a nice overview of these techniques, see for example [Gra93, Bla94].

In order to validate the approach with the nuclear lighthouse effect, measurements with the standard grazing incidence geometry of nuclear resonant scattering have been performed on the same layer systems for comparison. The time spectra of both setups agree to a very high degree, as presented in the following.

The standard method without the lighthouse turned out to be more comfortable. As the detector can be in the same hutch, thus avoiding the passage through three beam shutters, the electronic and nuclear reflectivity curves of the layer systems are obtained much easier and especially over a much wider angular range. With the lighthouse, the  $\theta$ - $2\theta$  scans were limited by the vertical opening or stroke of the shutters between the hutches. Further, in the standard grazing incidence geometry, almost all of the 176 ns time gap between the bunches can be used, whereas with the lighthouse, the angle scans are limited by the horizontal opening of the shutters and the beampipe.

## 5.1 13 Å thin $^{57}\text{Fe}$ layer in an aluminium and tantalum sandwich

Rotor a) of figure 3.4 consists of a very thin  $^{57}\text{Fe}$  layer, around 13 Å nominal thickness. It is embedded in the centre of a buffer or sandwich layer of nominal 100 Å aluminium. This layer system is connected via an approximately 300 Å thick tantalum layer to the sapphire substrate, which is the rotor itself. The whole is covered by 30 Å of tantalum.

### 5.1.1 Electronic and nuclear reflectivity curves

Electronic and nuclear reflectivity curves of rotor a), figure 3.4, have first been taken during the nuclear lighthouse measurements in 16 bunch-mode. With this experimental arrangement unfortunately, three shutters, the detector and the tilt stage of the rotor need to be moved simultaneously to allow for the passage of the reflected beam to the detector, being in the last hutch. The motors are in different hutches and use different control programs (spec sessions). The last shutter has even been displaced manually with screws on the shutter casing, to allow for a larger range of displacements. Even then, the reflectivity curves have been limited to the range between 0 and  $0.28^\circ$ , roughly. Furthermore, the rotor was not held tightly during the scan, but could move within the tolerances given by the stator. It did not turn, as not to average over all surface orientations during rotation, due to a tilted rotor surface or the precession of the rotor. Of no surprise, much better measurements have been done later when using the standard grazing incidence setup. All equipment was in EH1 alone. We therefore solely use reflectivity curves obtained in this setup. This is also valid for rotors b) and c).

As the rotor surface is only 7 mm wide in diameter and inclined to grazing incidence, the beamsize at the rotor position is much larger than the projected rotor surface as seen by the beam. With increasing tilt angle  $\theta$ , a larger part of the incoming beam can be reflected by the layer system on the rotor surface. Therefore, the measured reflectivity curves are to be scaled with a factor  $\frac{1}{\sin \theta}$  when compared to theoretical calculations. The measured electronic and nuclear reflectivity curves without proper  $\frac{1}{\sin \theta}$  scaling can be seen in figure 5.1.

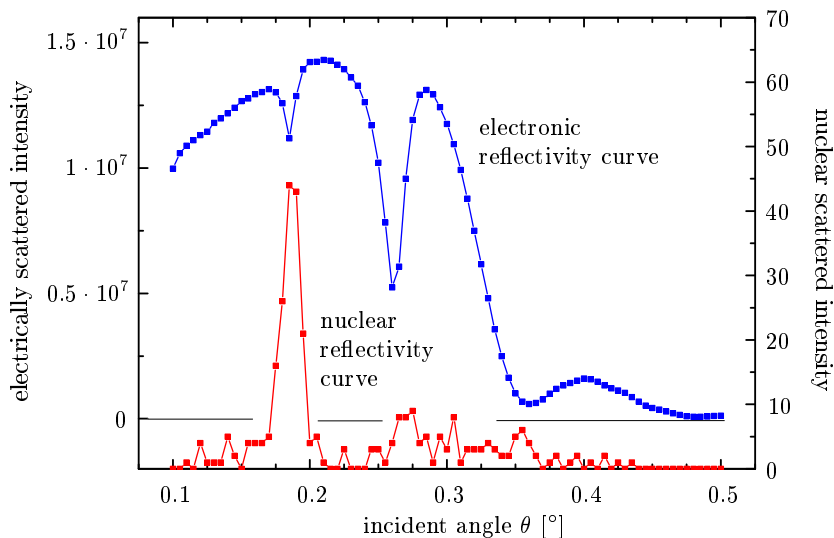


Figure 5.1: The experimental electronic and nuclear reflectivity curves without  $\frac{1}{\sin \theta}$  scaling.

Electronic and nuclear reflectivity curves depend strongly on the composition of the layer system. With the CONUSS module KGIN for grazing incidence [Röh99a, p.465], electronic as well as nuclear reflectivity curves can be simulated and compared with the experimental data. It is favourable to start with the electronic reflectivity curve, as it offers more features. The electronic reflectivity curve as measured is scaled by  $\frac{1}{\sin\theta}$  and normalised to obtain the value of about 1 at angle  $\theta = 0$ . Relatively good agreement for the electronic reflectivity curve is obtained with the simulation shown in figure 5.2.

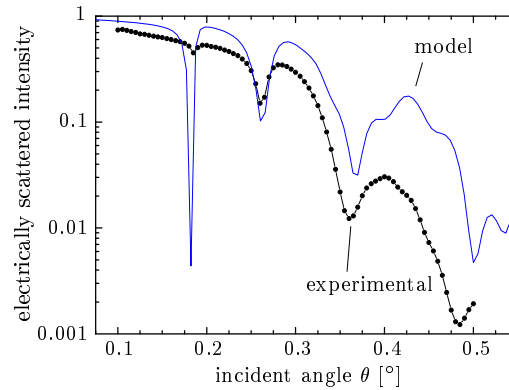


Figure 5.2: The electronic reflectivity curve and the theoretical curve assuming an increased aluminium layer thickness.

It appears that the positions of the minima reproduce nicely with a model, that assumes an increased aluminium layer thickness, in which the 13 Å  $^{57}\text{Fe}$  layer is embedded, although none of the simulations reproduce the depth of the minima and the overall slopes. The reason for different minima and slopes might be due to surface roughness or detector saturation, but is not of big importance in our case. The best fit was observed with 30 Å Ta, 50 Å Al, 13 Å  $^{57}\text{Fe}$ , 90 Å Al and 284 Å Ta on sapphire. The total aluminium layer thickness is 140 Å, but could be decomposed differently around the  $^{57}\text{Fe}$  layer, e.g. 70 Å and 70 Å. However, the nuclear reflectivity curve fits best with a 50 Å and 90 Å repartition. This is shown in figure 5.3.

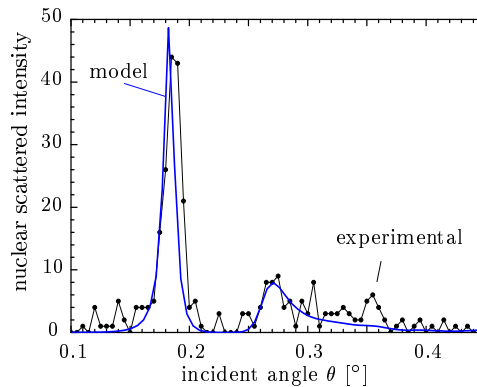


Figure 5.3: The nuclear reflectivity curve and the theoretical curve assuming an increased, and asymmetric, aluminium layer thickness: 50 Å Al, 13 Å  $^{57}\text{Fe}$ , 90 Å Al.

### 5.1.2 Nuclear response

Time spectra of the layer system were measured at the incident angle of  $\theta = 0.27^\circ$  both with the standard grazing incidence technique and with the nuclear lighthouse effect. These two measurements are compared in the lower part of figure 5.4. It can be clearly seen that the two measurements agree perfectly in the range up to 70 ns. At later times, the deviated beam is cut by the beam shutter between EH2 and EH3 or the vacuum pipe itself. With the standard nuclear grazing incidence setup, this is of course not a problem and the measurement continues up to 165 ns. At 176 ns, the next bunch arrives. Using the standard grazing incidence setup, the time spectrum at an additional angle of  $\theta = 0.187^\circ$  was obtained, too. This time spectrum is shown in the upper part of figure 5.4.

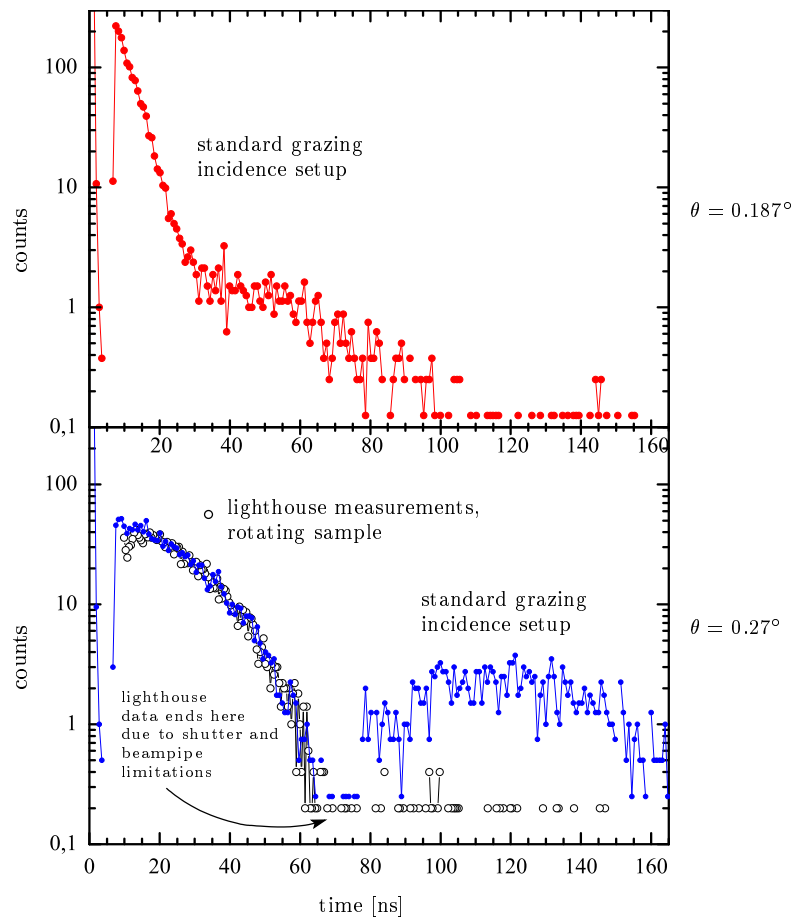


Figure 5.4: The time spectra of the layer system at the incident angles of  $\theta = 0.187^\circ$  in the upper graph and  $\theta = 0.27^\circ$  in the lower graph. In the lower graph, the open circles correspond to lighthouse measurements. Five channels have been summed up. It has been scaled to fit to the underlying curve of full circles, which corresponds to measurements in the standard grazing incidence setup, where eight channels have been summed up.

The agreement between the lighthouse effect measurement on the rotating layer system and the measurement using the standard setup with the rotor at rest is remarkable, as seen in the lower part of figure 5.4.

### 5.1.3 Fitting with NFS theory

In a first approach to analyse the measured data of this layer system a), it will be treated like nuclear forward scattering: Due to the small thickness of the  $^{57}\text{Fe}$  layer (13 Å), the delayed temporal response can be described in the kinematical approximation of NFS. In that case, the amplitude of the resonantly scattered radiation is proportional to the nuclear scattering amplitude  $f(\omega)$  [Röh02a].

We will first consider the time spectrum at the incident angle of  $\theta = 0.27^\circ$ . The structure with maxima and minima in NFS time spectra can be due to thickness effects (dynamical beats) or hyperfine interactions (quantum beats). This has been explained in chapter 2.4. In figure 5.4, only one minimum is visible. It is not immediately evident, whether the time spectrum shows dynamical or quantum beats. If we assume the absence of hyperfine interactions and consider only dynamical beats due to the thickness of the sample, then the beats are described by a Bessel function. The formula for the time spectra of dynamical beats can be reduced to:

$$D(t) = I_o \cdot e^{-c_1 \frac{t}{\tau}} \cdot \frac{J_1 \left( \sqrt{\frac{t}{\tau}} \sigma f_{\text{LM}} \beta n d \right)^2}{t} \quad (5.1)$$

with  $\sigma = 256 \cdot 10^{-18} \text{ cm}^2$  the maximum resonant cross section,  $d$  being the sample thickness,  $n = 8.3 \cdot 10^{22} \frac{1}{\text{cm}^3}$  the density of the Mössbauer element and  $\beta$  the enrichment in the  $^{57}\text{Fe}$  isotope.  $c_1$  should allow for an additional speedup. It cannot be smaller than 1. This function has been used to fit the data, see the dotted line in figure 5.5. In order to have the minimum of  $D(t)$  in coincidence with the minimum of the measured time spectrum,  $d$  has been fixed to  $1.75 \mu\text{m}$ .  $c_1$  is 1. Only smaller values, not being physical, would improve the fit in rising the curve at later times. The only free parameter left is  $I_o$ . As seen, the measured data can not be explained by a simple dynamical beat when using NFS theory.

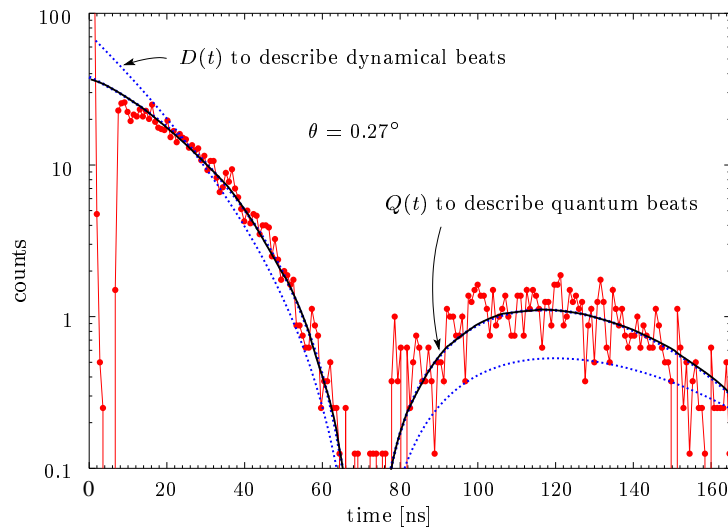


Figure 5.5: The time spectrum at  $\theta = 0.27^\circ$  with two fits assuming nuclear forward scattering theory. It is seen that the data corresponds to quantum beats,  $Q(t)$ , and not to dynamical beats,  $D(t)$ .

Alternatively, the beat structure could represent quantum beats, originating from the interference of split nuclear levels under the influence of hyperfine interactions. As the

$^{57}\text{Fe}$  layer is very thin ( $\approx 13 \text{ \AA}$ ) and probably contaminated with aluminium atoms due to interdiffusion, electric quadrupole splitting seems more probable than magnetic hyperfine splitting. The electric quadrupole interaction in  $^{57}\text{Fe}$  splits the excited state into two sublevels. Then, for a thin sample, the time spectra can be explained by the formula:

$$Q(t) = I_o \cdot e^{-c_2 \frac{t}{\tau}} \cdot (1 + \cos(\Omega \cdot t)) \quad (5.2)$$

$\Omega$  characterises the frequency of the beat structure and is proportional to  $\frac{1}{\Delta E_{eq}}$ , the electric quadrupole splitting.  $c_2$  allows for an additional speed-up. These two parameters have been fitted to match  $Q(t)$  to the data. The result is seen in figure 5.5.

The obtained value for  $\Omega$  is  $0.044 \frac{1}{\text{ns}}$ ,  $c_2 = 3.88$ . The speedup of  $2.88 = 3.88 - 1$  can be explained as an influence of the thickness. In fact, a combination of dynamical and quantum beats can be formulated with [Bür92]:

$$H(t) = I_o \cdot e^{-c_3 \frac{t}{\tau}} \cdot \frac{J_1 \left( \sqrt{\frac{t}{2\tau}} \sigma f_{\text{LM}} \beta n d \right)^2}{t} \cdot \left( 1 + \cos \left( \Omega \cdot t + \frac{\sigma n f_{\text{LM}} \beta d}{8\Omega \tau} \right) \right) \quad (5.3)$$

Given the right parameters, this function  $H(t)$  looks completely similar to  $Q(t)$  in figure 5.5. The reason for this agreement can be understood when approximating the Bessel function at early times by an exponential decay. The necessary parameters are  $d = 1.07 \mu\text{m}$  and  $\Omega = 0.038 \frac{1}{\text{ns}}$ . With  $\Delta E \cdot \Delta t = \hbar$  and  $\frac{1}{\Delta t} = \Omega$ , the value for  $\Omega = 0.038 \frac{1}{\text{ns}}$  translates to an electric quadrupole splitting of  $\Delta E = 25 \text{ neV} = 5.38 \Gamma_o \hat{=} 0.52 \frac{\text{mm}}{\text{s}}$ .

There has been no attempt to fit this spectra with NFS theory and a magnetic hyperfine interaction at this point. However, it will be considered with the theory of grazing incidence in chapter 5.1.4.

#### 5.1.4 Fitting with the grazing incidence extension to CONUSS

As the  $^{57}\text{Fe}$  layer thickness increases or the incident angle varies in such a way, that the incident beam stays longer in the layer, the kinematical approximation used in chapter 5.1.3 might no longer be valid. The correct formalism of nuclear grazing incidence reflection has to be employed. This formalism has been implemented in the extension KGIN [Röh99a, p. 465] of the software package CONUSS [Stu94] and is used in the following. The time spectra of the nuclear response in grazing incidence geometry are simulated as a function of layer thicknesses, layer roughness, incident angle and of course the hyperfine interactions. The result can be scaled automatically to a given data set.

At the two angles  $\theta = 0.27^\circ$  and  $\theta = 0.187^\circ$ , simulations with various electric quadrupole splittings and magnetic hyperfine fields have been performed. The results are shown in figure 5.6.

All four simulations at each of the two angles fail when excluding hyperfine interactions. A thickness effect can be excluded for the  $13 \text{ \AA}$  of  $^{57}\text{Fe}$  for each of the two incident angles. The first thickness beat without hyperfine interactions would be located at  $t = 300 \text{ ns}$  for  $\theta = 0.27^\circ$  and at  $t = 100 \text{ ns}$  for  $\theta = 0.187^\circ$ . However, it is not clear whether magnetic or electric hyperfine interactions cause the minima in the two time spectra. It is possible to fit the time spectra with either a randomly orientated electric field gradient, or with randomly orientated magnetic hyperfine fields  $B_{hf}$ , or with an out-of-plane  $B_{hf}$  field or finally with randomly orientated in-plane  $B_{hf}$  fields. To distinguish between these cases,

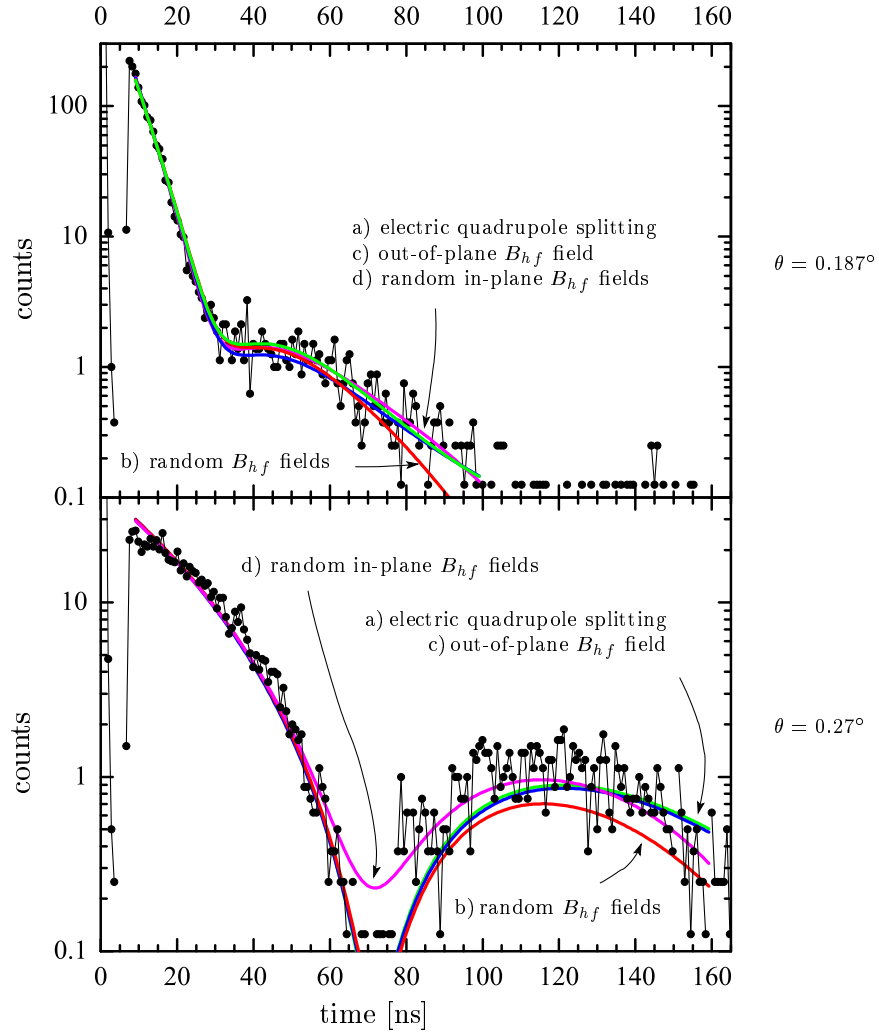


Figure 5.6: The time spectra of the layer system at the incident angles of  $\theta = 0.187^\circ$  in the upper graph and  $\theta = 0.27^\circ$  in the lower graph. For each angle, four simulations have been performed, assuming a) a randomly orientated electric field gradient, b) randomly orientated magnetic hyperfine fields  $B_{hf}$ , c) an out-of-plane  $B_{hf}$  field and d) randomly orientated in-plane  $B_{hf}$  fields.

simulation	$\theta = 0.187^\circ$		$\theta = 0.27^\circ$	
	strength	FWHM of distribution	value	FWHM of distribution
random Efg: $\Delta E_{efg}$	$0.6 \frac{\text{mM}}{\text{s}}$	$0.48 \frac{\text{mM}}{\text{s}}$	$0.45 \frac{\text{mM}}{\text{s}}$	$0.32 \frac{\text{mM}}{\text{s}}$
random $B_{hf}$	2.6 T	0.26 T	1.9 T	0
in-plane $B_{hf}$	2.3 T	0	1.7 T	0.1 T
out-of-plane $B_{hf}$	3.4 T	2.7 T	2.45 T	1.7 T

Table 5.1: Parameters for the hyperfine interactions used to fit the time spectra of figure 5.6.

a better statistic and an extension of the spectra to later times would be needed. The parameters used in the simulations are given in table 5.1.

For the simulations, not a unique sharp value for the hyperfine interaction has been used. Instead, the value in the column "strength" refers to the central peak value of a distribution. The distribution was assumed to be Gaussian and has a FWHM given in

per cent of the peak value. This width is stated in the column "distribution". In the first row, "Efg" stands for "electric field gradient". The strength of the electric quadrupole interaction is given by the splitting of the two sublevels of the excited state, in  $\frac{\text{mm}}{\text{s}}$ . The splitting is a function of the product of the nuclear quadrupole moment of the  $^{57}\text{Fe}$  nuclei with the local electric field gradient  $V_{zz}$ , see chapter 2.2.2.

It seems surprising, that the hyperfine interaction parameters differ between the two examined angles: The hyperfine properties of the sample do not change when tilting the sample. Most probably, the reason for the different measured values originates from the fact, that at the two angles, different depth and positions in the sample are probed.

Comparing the value of  $0.6 \frac{\text{mm}}{\text{s}}$  for the electric quadrupole splitting at  $\theta = 0.27^\circ$  with the value obtained in chapter 5.1.3:  $0.52 \frac{\text{mm}}{\text{s}}$ , we see a pretty nice agreement.

## 5.2 medium thick ( $\approx 75 \text{ \AA}$ ) $^{57}\text{Fe}$ layer

Rotor b) of figure 3.4 carries a more basic layer system. It contains a  $^{57}\text{Fe}$  layer sandwiched between the tantalum support and the tantalum cover layers. The  $^{57}\text{Fe}$  layer thickness is approximately  $75 \text{ \AA}$  as determined by analysis of the electronic reflectivity curve. Due to problems during the production of the layer system, no nominal values are available to compare to this result.

### 5.2.1 Electronic and nuclear reflectivity curves

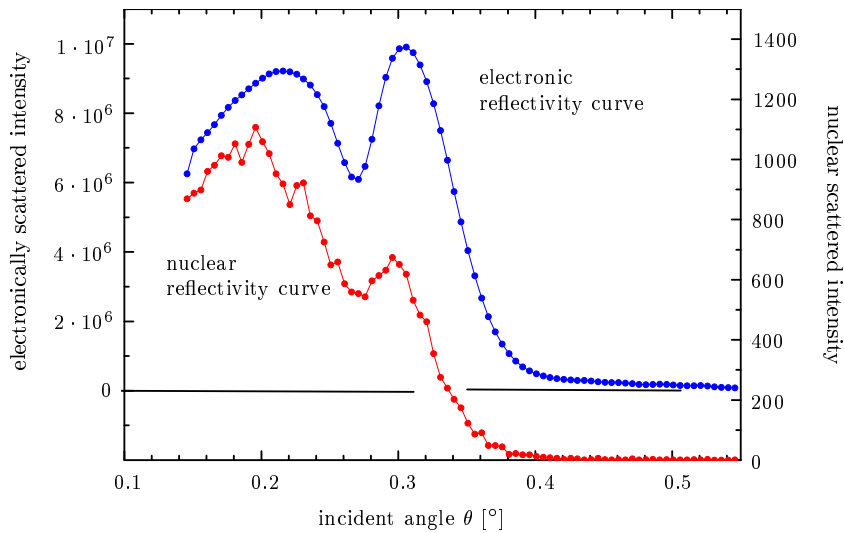


Figure 5.7: The experimental electronic and nuclear reflectivity curves. The puzzling nuclear reflectivity might be spoiled by a insufficient gating of the prompt signal.

Figure 5.7 shows the raw data of the electronic and nuclear reflectivity curves as obtained in a standard setup without the lighthouse. They have not been scaled by  $\frac{1}{\sin \theta}$ . Surprisingly, both electronic and nuclear reflectivity curves follow the same overall slope. This was not the case with the waveguide structure of the thin  $^{57}\text{Fe}$  layer in the aluminium sandwich, see figure 5.1. A possible explication for the nuclear reflectivity curve might be an improper gating of the prompt signal, e.g. by an unnoticed shift of the



time gating module or its control software, or by an increased prompt signal extending slightly to later times then. However, the time spectrum of nuclear resonant scattering obtained with these settings is in nice agreement with the time spectrum obtained using the nuclear lighthouse effect with the rotating layer system, as will be seen in chapter 5.2.2.

The electronic reflectivity curve could be fitted assuming a sophisticated model including an oxidised top tantalum cover layer and varying interface roughnesses. The  $^{57}\text{Fe}$  layer thickness was determined to be  $75 \text{ \AA}$  thick. The cover layer of tantalum has been divided into a  $32 \text{ \AA}$  thick  $\text{Ta}_2\text{O}_5$  layer and only  $6 \text{ \AA}$  of unoxidised tantalum remaining below the oxidised layer. Their density was evaluated as  $12 \frac{\text{g}}{\text{mm}^3}$ . The tantalum layer between the sapphire substrate and the  $^{57}\text{Fe}$  layer is found to be larger than  $300 \text{ \AA}$ . Its actual thickness is not important for the fitting of the nuclear time spectra, but a thickness of  $500 \text{ \AA}$  or larger is necessary to reduce oscillations at higher angles of the electronic reflectivity curve. The surface and interface roughnesses vary between  $5$  and  $10 \text{ \AA}$ . The best fit to the electronic reflectivity curve obtained with these values is shown in figure 5.8

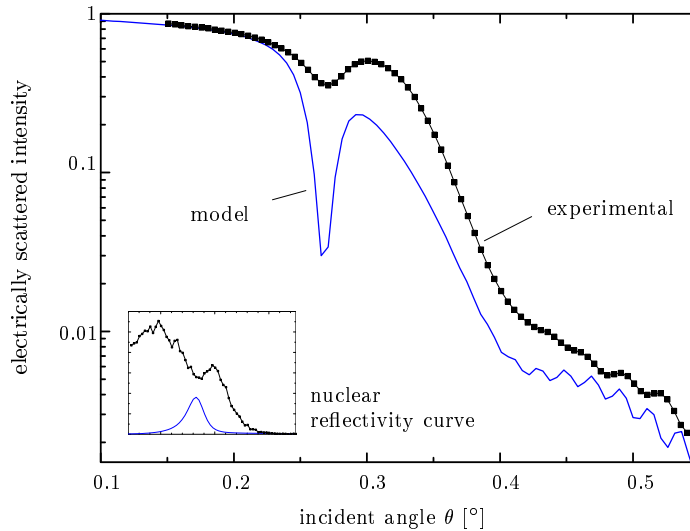


Figure 5.8: The electronic reflectivity curve and the best theoretical model that considers an oxidised tantalum cover layer, increased interface roughnesses and leading to a  $^{57}\text{Fe}$  layer thickness of  $75 \text{ \AA}$ . The inset shows the corresponding nuclear reflectivity curve and the measured one.

The nuclear reflectivity curve obtained with the same values is shown in the inset, showing a maximum at the minimum of the electronic curve. This behaviour is not reflected in the measured curve. However, as the interest of the measurements was to compare the grazing incidence measurements with the NLE and standard measurements without rotating sample, we will not focus on this detail and proceed instead with the time spectra measured with this layer system.

### 5.2.2 Nuclear response

The time response in nuclear resonant scattering at grazing incidence reflection of the layer system on rotor b) is shown in figure 5.9. It compares the measurements using the NLE with those using the standard setup without rotation of the sample. The incident angle was  $\theta = 0.25^\circ$  in both cases.

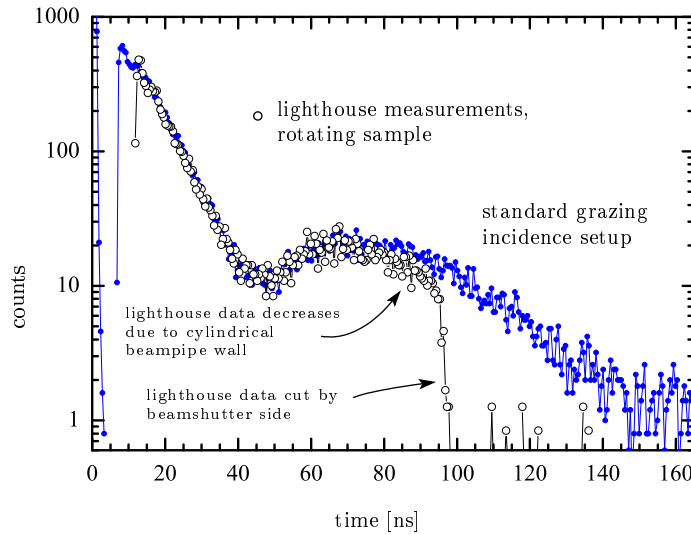


Figure 5.9: The hollow circles correspond to lighthouse measurements. That curve has been scaled to fit to the curve of blue dots, which was measured with the standard grazing incidence setup. In both cases, five channels have been summed up. The incident angle was  $\theta = 0.25^\circ$ .

Again, a perfect agreement between the lighthouse data and the standard method can be observed at times below 70 ns. At 95 ns, the lighthouse data drops to zero as the deviated beam is cut by the beam shutter at the end of the second experimental hutch. Between 70 and 95 ns, the lighthouse data lies below the data as obtained with the standard setup. This drop can be explained with the beam pipe in EH3 starting to cut the deviated beam.

### 5.2.3 Fitting of the nuclear response

The experimental time spectra have been compared to simulations using the grazing incidence extension to CONUSS. With the iron layer thickness of  $75 \text{ \AA}$  as obtained from the electronic reflectivity curve and assuming an isotopic enrichment in  $^{57}\text{Fe}$  of 98%, a first thickness minimum or dip is observed in the simulations already at times earlier than 40 ns. The only possibility to avoid a dip before the experimentally measured one at 40 ns was to reduce the abundance of the  $^{57}\text{Fe}$  isotope in the iron layer. As an alternative, the layer thickness might be decreased, but then the electronic reflectivity curve would change, too.

Finally, the time spectra at  $\theta = 0.25^\circ$  could be fitted with an isotopic enrichment of 28% and an electric field gradient resulting in an electric quadrupole splitting of  $0.62 \frac{\text{m}}{\text{s}}$ . The electric field gradient has thereby to follow a Gaussian distribution around the maximum value with a FWHM of 10 % with respect to its peak value. This simulation is shown in figure 5.10 as fit a).

However, with these hyperfine interactions, the simulation of the time spectrum changes when changing the incident angle  $\theta$  to  $0.15^\circ$ . In fact, the minimum at 40 ns shifts to later times. This has not been observed in reality, as measured with the standard grazing incidence geometry and presented in figure 5.11. The measurements at the two angles do not differ significantly. The first minimum thus needs to be a hyperfine interaction caused minimum.

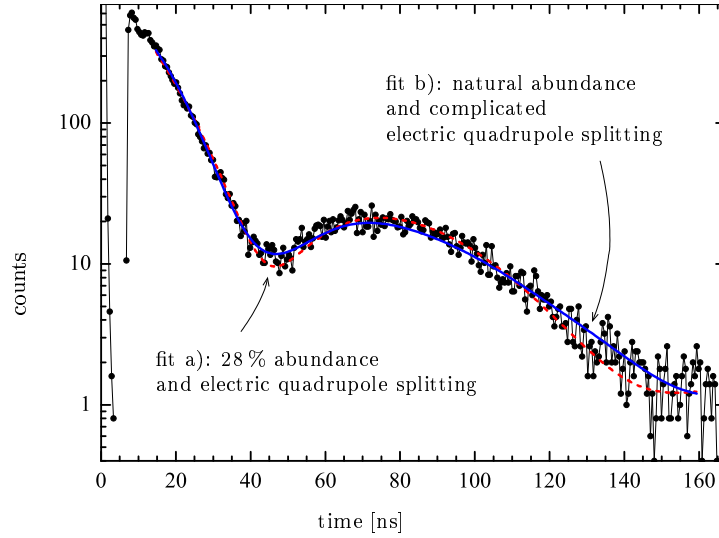


Figure 5.10: Two possibilities to fit the time spectrum of the layer system with the medium thick  $^{57}\text{Fe}$  layer.

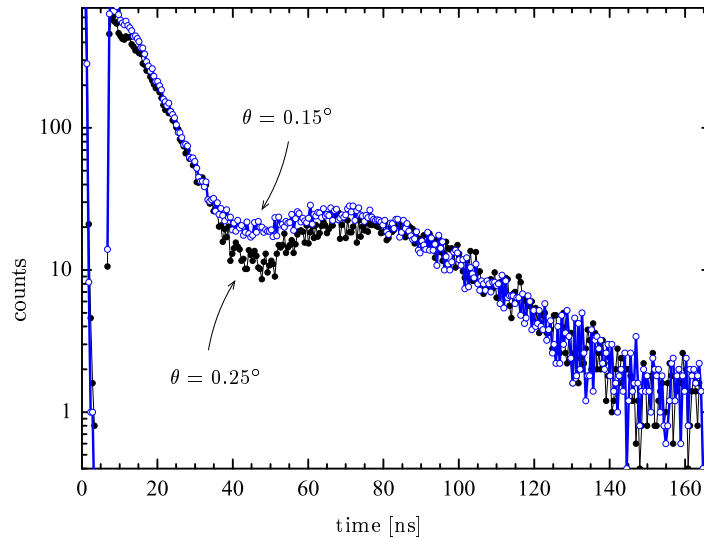


Figure 5.11: Almost identical time spectra at the two angles  $\theta = 0.15^\circ$  and  $\theta = 0.25^\circ$ . This would imply a very thin iron layer or a very small abundance of the  $^{57}\text{Fe}$  isotope like in an unenriched iron layer.

An alternative explanation could be that the iron sputtering target was not enriched iron, but natural iron. Then, the first dynamical thickness minimum is at much later times. In this case, it was possible to simulate the time spectrum with an interplay of two nuclear sites with different electric field gradients. This is equivalent to a distribution of electric field gradients with two different maxima. Fit b) in figure 5.10 was obtained in this way. The electric quadrupole splitting of site 1 is  $1.4 \frac{\text{mm}}{\text{s}}$  with a Gaussian distribution around this value with  $2.2 \frac{\text{mm}}{\text{s}}$  FWHM. The splitting of the second site is  $0.27 \frac{\text{mm}}{\text{s}}$  with a Gaussian distribution around this value with a FWHM of  $0.24 \frac{\text{mm}}{\text{s}}$ .

Normally, an iron layer of a thickness of  $75 \text{ \AA}$  would be expected to order ferromagnetically. The magnetic hyperfine field at the  $^{57}\text{Fe}$  nucleus of ferromagnetic iron is known

to be around 33 T. This is not at all observed in the time spectra presented here. As the nuclear reflectivity curve and the isotopic enrichment needed for a reasonable simulation of the time spectra are puzzling, no further analysis of this layer system has been performed. The main intend was to compare the NLE measurement with the standard one. This agreement is excellent, as seen in figure 5.9.

### 5.3 thick ( $\approx 178 \text{ \AA}$ ) $^{57}\text{Fe}$ layer

Rotor c) of figure 3.4 consists of a  $^{57}\text{Fe}$  layer sandwiched between the tantalum support and the tantalum cover layers. The  $^{57}\text{Fe}$  layer thickness is approximately  $178 \text{ \AA}$  as determined by analysis of the electronic reflectivity curve.

#### 5.3.1 Electronic and nuclear reflectivity curves

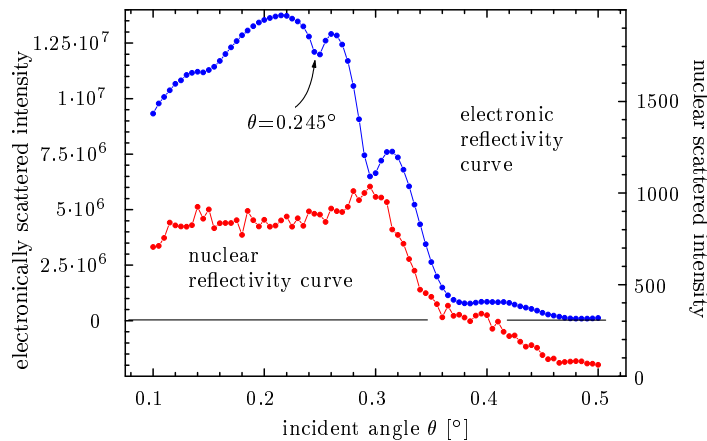


Figure 5.12: The experimental electronic and nuclear reflectivity curves of rotor c).

The electronic and nuclear reflectivity curves of this layer system are shown in figure 5.12 without the proper  $\frac{1}{\sin \theta}$  scaling.

The properly scaled electronic reflectivity curve was used to analyse the thicknesses of the layer system constituents. The electronic reflectivity curve could be fitted assuming a sophisticated model including an oxidised top tantalum cover layer and varying interface roughnesses. The  $^{57}\text{Fe}$  layer thickness was determined to be  $178 \text{ \AA}$  thick. The cover layer of tantalum has been divided into a  $24 \text{ \AA}$  thick  $\text{Ta}_2\text{O}_5$  layer and only  $3 \text{ \AA}$  of unoxidised tantalum remaining below the oxidised layer. Similar to layer system b), the tantalum layer between the sapphire substrate and the  $^{57}\text{Fe}$  layer is definitely larger than the targeted thickness of  $300 \text{ \AA}$ . Its actual thickness is not important for the fitting of the nuclear time spectra, but a thickness of  $500 \text{ \AA}$  or larger is necessary to reduce oscillations at higher angles of the electronic reflectivity curve. The surface and interface roughnesses vary between  $6$  and  $20 \text{ \AA}$ . The best fit to the electronic reflectivity curve obtained with these values is shown in figure 5.13.

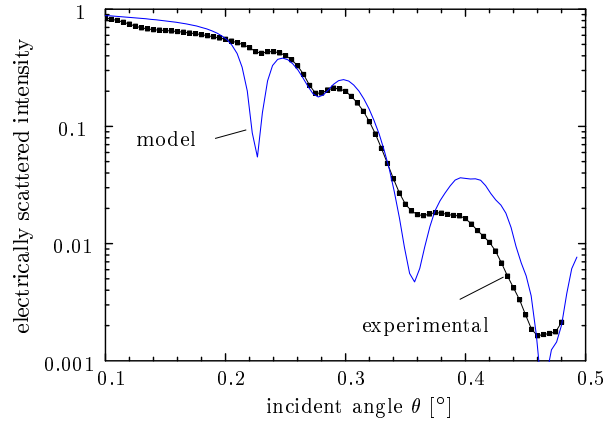


Figure 5.13: The electronic reflectivity curves as measured compared with the best model layer system.

### 5.3.2 Nuclear response

The nuclear response of the layer system on rotor c) of figure 3.4 was investigated thoroughly in different variations with the nuclear lighthouse effect. As the SAXS background was too high to use the nuclear lighthouse effect without additional timing to prevent the counting of small angle scattered photons, an electric veto and a multi channel analyser have been used. The same situation was already presented in chapter 6.4. The electrical gate signal vetoes the detector signal during the first 5 to 10 ns after the excitation of the nuclei by the SR flash. Still, the detector position can provide the time information using the formula  $t = \frac{x}{2\pi d\nu}$ . No further electronically obtained time information is needed to acquire a time spectrum of the investigated sample. The time spectrum obtained in this way from rotor c) at the incident angle of  $0.245^\circ$  is shown as tiny squares in figure 5.14. Only the detector position is used to generate the time axis. The step size of the detector displacement was 0.5 mm. The rotor turned at 6 kHz and the detector-to-sample distance  $d$  is 13.65 m. The detector displacement corresponds thus to a change in time of 0.97 ns. However, it is possible to connect the detector signal not only to a counter, but also to a time-to-amplitude converter and further to a multi channel analyser (MCA). During the lateral displacements of the detector, the MCA keeps acquiring a proper time spectrum. This time spectrum is shown as open circles in figure 5.14. Here, 5 channels have been added. The MCA uses 10 channel to cover 1 ns. The agreement between the two data collection methods is perfect.

As the layout for the NLE measurements was principally intended to access the short lived  $^{61}\text{Ni}$  isotope, measurements with the long lived  $^{57}\text{Fe}$  isotope run into problems when the setup stays unchanged: the larger deviation angles of the delayed photons exceed 50 mm, which is the lateral opening of the beam shutters between the hutches. The deviation angle  $\alpha$  can be decreased when turning the sample at lower frequencies. However, photons scattered into small angles  $\alpha$ , corresponding to early decay times, are getting even closer to the direct beam and are either blocked already by the beamstop or fall in the region where SAXS is the most important. Thus, counts at early decay times are sacrificed for the benefit of photons scattered at later times. The time resolution gets worse with decreasing rotational frequency, if the slit size in front of the detector is kept constant. Identical time resolutions are obtained when the slit is scaled with the rotational frequency.

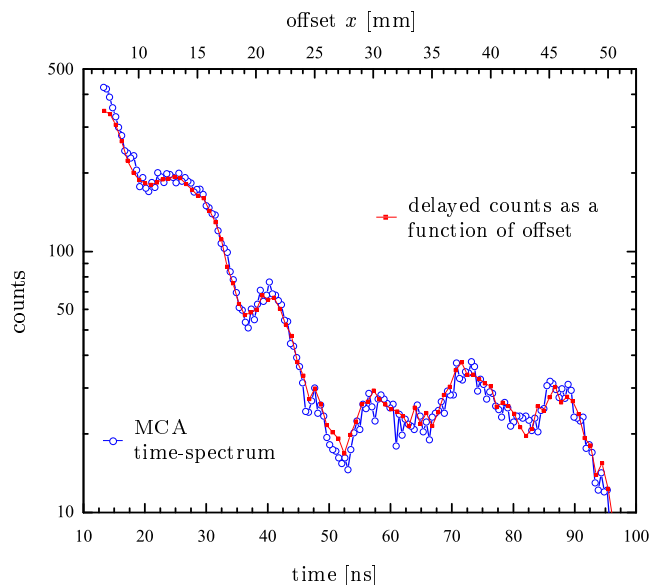


Figure 5.14: Hollow circles represent the time spectrum as obtained with the time-to-amplitude converter and the MCA. 5 channels have been summed. The tiny squares represent the delayed countrate as a function of the offset  $x$ . Here, only an electrical veto is used to prevent counting SAXS scattered photons and no further time information is obtained electronically. The detector position provides the time information via the offset and equation  $t = \frac{x}{2\pi d\nu}$ .

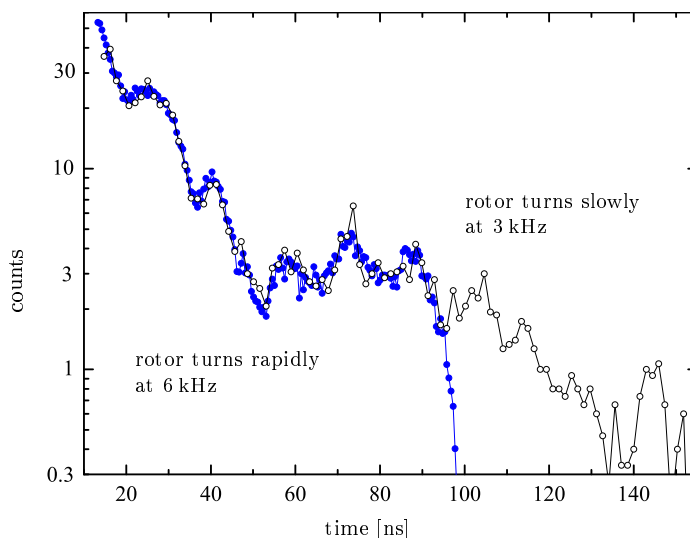


Figure 5.15: The time spectrum of rotor c) obtained at two different rotational frequencies with the nuclear lighthouse effect.

With the layer system on rotor c), the time spectra at two different rotational frequencies have been acquired and are compared. For comparison, it is important to scale the detector size, i.e. the detector horizontal slit size, in accordance with the rotational frequency. The result is shown in figure 5.15. The horizontal axis in this figure is the time and not the offset. On the time scale, the two measurements give the same curve in the area that is covered by both measurements. Only the lower frequency shows data at later times. The 6 kHz data reaches closer to  $t = 0$ .

In figure 5.16, three trials are shown to simulate the measured time spectrum obtained with the NLE. The 3 kHz and the 6 kHz measurements are combined for this purpose. All simulations assume a magnetic hyperfine field at the  $^{57}\text{Fe}$  nuclei of 32 to 34 T. It is nicely visible that the beat frequency of these fits correspond rather well with the actual measured ones. However, the amplitude of the beating are either too big (simulations a) and c)) or dynamical beats change the phase of the beats at inappropriate times (simulation b)). The difference among the fits is the assumed distribution of the directions of the magnetic hyperfine field. Simulations a) and b) assume a uniform magnetic hyperfine field in the direction of the wavevector  $\vec{k}$  of the incoming synchrotron radiation. As the sample turns and no permanent magnet around the rotor was used, this direction is not possible even when having only a single domain. Further details of the fit are an abundance of 15 % (simulation a)) or of 80 % (simulation b)) in the  $^{57}\text{Fe}$  isotope in the iron layer. The magnet field follows a Gaussian distribution around its peak value with a FWHM of 3.4 T in simulation a) and 0.3 T in simulation b). The simulation c) assumes an out-of-plane magnetisation of the sample. The abundance is 25 % and the distribution of the magnetic hyperfine field is 5.8 T FWHM. An out-of-plane magnetisation might occur within extremely thin iron films but certainly not for a film thickness of 178  $\text{\AA}$ . Better fits without assuming complex hyperfine field distribution could not be obtained, especially not for the case of a random in-plane distribution of hyperfine field directions. This case would be expected for thin magnetic films with a domain structure. In this case of a random in-plane orientation, more than one beat frequency should be visible, as sketched in figure 2.14. The same is true for a random orientation in all directions. In the measured data, there is only one major beat frequency. The distance between the minima is always close to 14.8 ns. Much more effort would be needed to obtain better a better simulation. However, this is not in the aim of this thesis.

In the lower right part of figure 5.16, the time spectrum as obtained with the NLE is compared to the time spectrum as obtained with the standard grazing incidence technique. The agreement is not as nice as in the previous cases of rotor a) and c). However, strong similarities are visible at early times and for the frequency of the beating. The reason for the small discrepancy might originate from the domain structure of the layer system. When using the NLE, the sample rotates in the beam and many domain distribution participate in an averaging process. In the setup with the rotor at rest, a specific domain distribution is selected, that leads to a slightly different time spectrum.

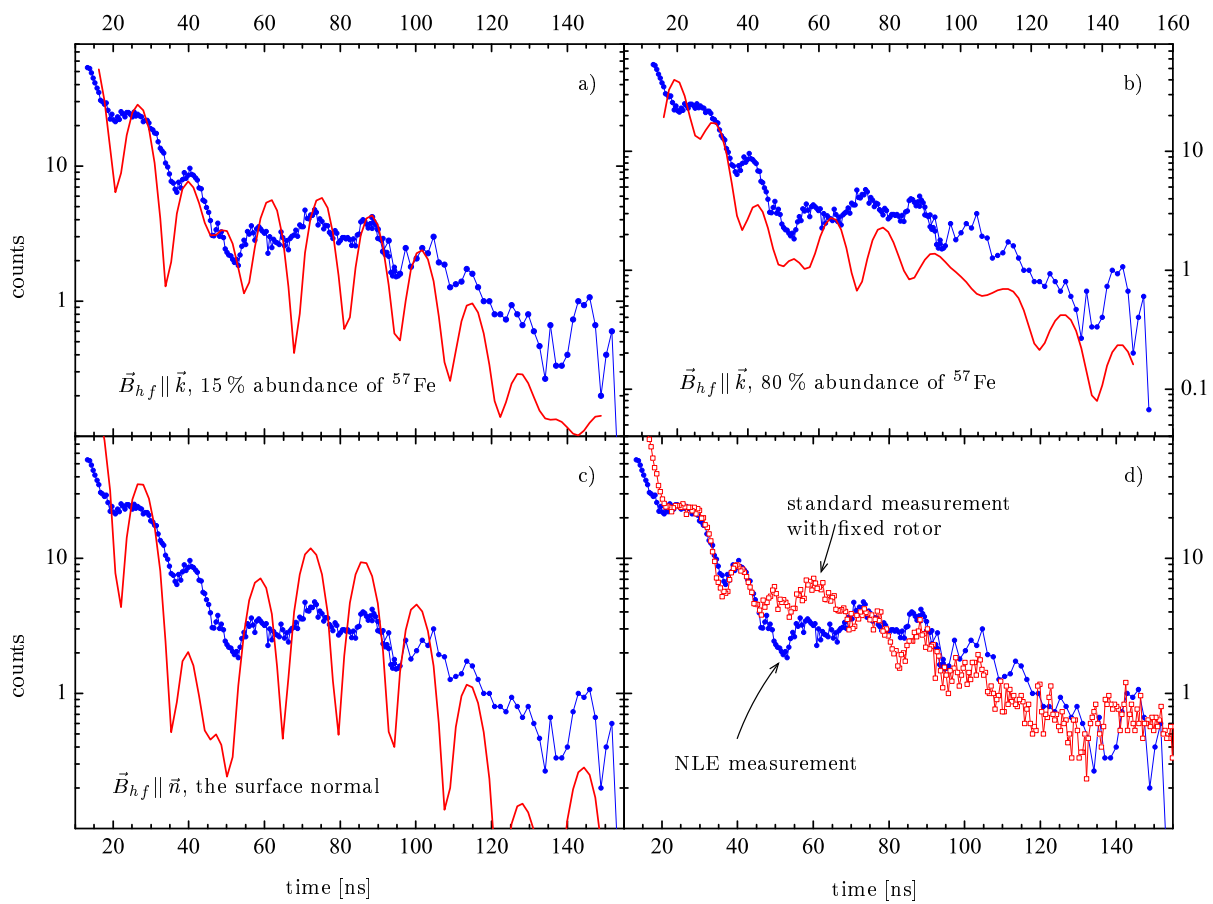


Figure 5.16: The time spectrum of rotor c) obtained with the NLE is compared to various simulations and to a measurement with the standard grazing incidence setup.



## Chapter 6

# Nuclear lighthouse effect with $^{61}\text{Ni}$

The development of coherent nuclear resonant scattering with synchrotron radiation for the Mössbauer isotope  $^{61}\text{Ni}$  was the main task of this thesis. Before, only at DESY in Hamburg, the nuclear level of  $^{61}\text{Ni}$  at 67.41 keV was excited with synchrotron radiation and fluorescence radiation from the following decay was detected [Wil02, Ger02]. In this chapter, the results of the first hyperfine spectroscopic measurements on  $^{61}\text{Ni}$  with synchrotron radiation are presented, using the nuclear lighthouse effect. This was the first time, that the nuclear resonant beamline ID18 at the ESRF was operated at photon energies above 30 keV. Therefore, this chapter starts with flux measurements at the energy of the  $^{61}\text{Ni}$  resonance, before presenting the results of nuclear resonant scattering with  $^{61}\text{Ni}$ .

### 6.1 Flux at ID18 at the $^{61}\text{Ni}$ resonance energy

Different detectors have been employed to measure the flux available at the  $^{61}\text{Ni}$  resonance energy at ID18: an argon filled ionisation chamber, a silicon pin diode and dosimetric films. Whereas the ionisation chamber and the pin diode measure the absorbed energy via the current created from electron ion or electron hole pairs, the dosimetric film measures the energy deposited via a chemical reaction. For a monochromatic beam, all obtained values are proportional to the number of incoming photons.

In an ionisation chamber, an electron is produced by photo absorption or the Compton effect. That electron ionises gas atoms and loses its ionisation energy while slowing down in the ionisation chamber. The created current depends on the absorption coefficient of X-rays in the gas and on parameters of the following ionisation process caused by the electrons. We measured ionisation chamber currents obtained at ID18 with the undulators and the high heat load monochromator adjusted to 67.41 keV and with different absorber foils far in front of the ionisation chamber. With this set of measures, we could determine the different distributions of each energy transmitted by the high heat load monochromator in the (1 1 1), (3 3 3), (4 4 4) and (5 5 5) reflections. The 67.41 keV radiation is best transmitted with the Si (3 3 3) reflection, as the Si (1 1 1) reflection is out of reach due to geometrical limitations of the monochromator mechanics and the Si (4 4 4) or (5 5 5) reflections have an even smaller angular acceptances for the divergent incident beam than the Si (3 3 3) reflection. The highest flux with the 32 mm undulators is obtained if the 17<sup>th</sup> harmonic is used, since in this case, the undulator gap is just slightly above 11 mm, which is the lower limit. Also, 17 is not a multiple of 3 (the Si (3 3 3) reflection is used), which means that no other undulator harmonic matches with an other monochromator reflection. For example, it would be less favourable to use the 15<sup>th</sup> harmonic via

the Si (3 3 3) reflection. Then, the 5<sup>th</sup> harmonic of the undulator radiation would be perfectly transmitted via the Si (1 1 1) reflection at the same time.

Currents as presented in table 6.1 have been measured with a 30 cm long argon filled ionisation chamber using one undulator at a storage ring current of 180 mA through a slit of  $0.05 \times 0.05 \text{ mm}^2$  slit placed closely after the monochromator.

absorber element and thickness	transmission				ionisation chamber current [pA]
	at 22.5 keV via 1 1 1	at 67.4 keV via 3 3 3	at 89.9 keV via 4 4 4	at 112.3 keV via 5 5 5	
no absorber	1	1	1	1	9035
500 $\mu\text{m}$ Pb	0	0.111	0.012 (above K-edge)	0.082	23.5
2 mm Cu	0	0.124	0.35	0.53	35.3
5 mm Al	$3.8 \cdot 10^{-2}$	0.722	0.78	0.81	413
150 $\mu\text{m}$ Ta	$1 \cdot 10^{-5}$	0.0565 (above K-edge)	0.24	0.45	19
400 $\mu\text{m}$ Sn	$1.1 \cdot 10^{-2}$	0.249	0.53	0.70	196
75 $\mu\text{m}$ Au	$2.9 \cdot 10^{-4}$	0.627	0.38	0.57	170
50 $\mu\text{m}$ Au	$4.4 \cdot 10^{-3}$	0.732	0.52	0.69	230
250 $\mu\text{m}$ Ag	$3.2 \cdot 10^{-2}$	0.334	0.60	0.75	334
150 $\mu\text{m}$ Ag	0.126	0.518	0.74	0.84	1144
100 $\mu\text{m}$ Ag	0.25	0.645	0.82	0.89	2366

Table 6.1: Ionisation chamber currents for flux measurements

For each absorber, the angle of the first high heat load monochromator crystal was scanned to insure a parallel crystal alignment of the monochromator during the ion chamber reading. With the aluminium, the thin gold, the tin and the thickest gold absorbers, it was possible to distinguish between a broad Gaussian coming from the Si (1 1 1) reflection and a much more narrow contribution from the narrow higher reflections. We finally obtain the result that a non-absorbed radiation would lead to 8700(200) pA originating from the radiation passing via the Si 1 1 1 reflection, 230(20) pA passing via the (3 3 3) reflection and 20(15) pA via the (4 4 4) reflection. The contribution from the Si (5 5 5) reflection is less than 5 pA. With the tantalum, lead and copper absorber, which transmit almost only the higher energies of the Si (3 3 3), (4 4 4) and (5 5 5) reflections and blocks the lower energy of the Si (1 1 1) reflection, measurements with a  $0.5 \cdot 0.5 \text{ mm}^2$  slit have been done, too. The flux is a factor of 78(2) times higher. We thus have 18(2) nA caused by the 67.41 keV radiation over the Si (3 3 3) reflection into a  $0.5 \cdot 0.5 \text{ mm}^2$  slit. The program "absorb" [SLAC] calculates an absorption of 1.81% for the 67.41 keV radiation in the 30 cm of the argon filled ionisation chamber. The slowing down of a photo-effect created electron of 67.4 keV leads to 2767 ion pairs, as one ion pair needs 24.4 eV to be created for the argon gas. We can thus calculate the flux of incoming photons of

$$I_{in} = \frac{18 \text{ nA}}{e \cdot 2767 \cdot 0.0181} = 2.2(3) \cdot 10^9 \frac{1}{\text{s}} \quad (6.1)$$

Unfortunately, the program "absorb" considers each Compton or Rayleigh scattered photon as absorbed, although only a fraction or none of the photon's energy is absorbed in the argon gas. With the XOP-package [San98], we can calculate the cross sections for photo-effect, Compton and Rayleigh scattering at 67.41 keV in the argon gas. We get 12.7, 8.9 and 2.8 barns per atom, respectively. The total cross section for Compton scattering  $\sigma_c$  can be split into two cross sections, which describe the fractions of energy kept by the scattered photon  $\sigma_c^s$  and the fraction of energy taken by the recoil electron and thus absorbed in the material  $\sigma_c^a$  [Leo94]

$$\sigma_c = \sigma_c^s + \sigma_c^a \quad (6.2)$$

Formulas to calculate  $\sigma_c^s$  and  $\sigma_c^a$  are presented in [Leo94]. At 67.41 keV, the ratio between total Compton cross section and the part describing the energy absorbed by the electrons is  $\frac{\sigma_c}{\sigma_c^a} = 9.74$ . As the absorption is very small (only 1.18% as calculated by "absorb"), we can consider a linear approximation for the exponential absorption and get for the absorption leading to detectable electrons equivalent of 67.41 keV the following value:

$$I_{in}^{corr.} = \frac{\sigma_{photo} + \sigma_c + \sigma_{rayl.}}{\sigma_{photo} + \frac{1}{9.74}\sigma_c} I_{in} = 4.3(5) \cdot 10^9 \frac{1}{s} \quad (6.3)$$

If we consider the whole beam, which is about 2.1 mm horizontal times vertical, we have to multiply the last value by a factor of 4 to 5. With 3 undulators and scaling to a storage ring flux of 100 mA, we finally get a flux of  $3.2(5) \cdot 10^{10}$  at 67.4 keV passing over the Si (3 3 3) monochromator. We can do the same reasoning for the other energies. With no absorbers, at the same time, we get 4.5 times more flux coming over the Si (1 1 1) reflection at 27.47 keV, and about 8 times less flux coming over the Si (4 4 4) reflection at 89.9 keV and about very roughly 60 times less flux coming over the Si (5 5 5) reflection. This ratio could be verified with a lithium doped germanium Ge(Li) detector and a very small slit, see figure 6.1.

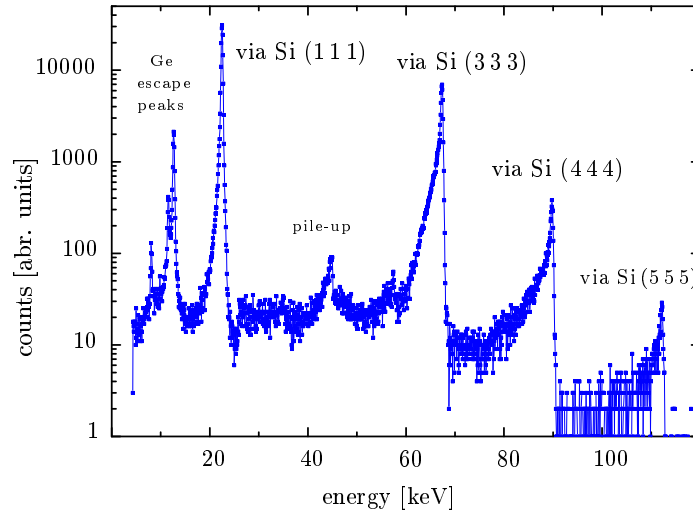


Figure 6.1: Energy spectrum of the transmitted radiation when using the 17<sup>th</sup> harmonic at 67.41 keV via the Si (3 3 3) monochromator, measured with a Ge(Li) detector.

The silicon pin diode is equivalent to a gas-filled ionisation chamber, only it is in a solid state. Here, one electron hole pair needs 3.6 eV to be produced. The measurements with a 300  $\mu\text{m}$  thick silicon pin diode have been performed with 3 undulators and 190 mA storage ring current. Two different absorbers have been employed, see table 6.2.

absorber	transmission				current [pA]
	at 22.5 keV	at 67.4 keV	at 89.9 keV (above K-edge)	at 112.3 keV	
470 $\mu\text{m}$ Pb	$2 \cdot 10^{-15}$	0.143	0.02	0.11	$3.8 \cdot 10^5$
1 mm Cu	$3 \cdot 10^{-10}$	0.359	0.60	0.72	$9.9 \cdot 10^5$
300 $\mu\text{m}$ Si	0.80	0.981	0.986	0.988	

Table 6.2: Relevant transmission for pin diode measurements

To analyse these flux measurements, one result of the measurements with the argon filled ionisation chamber is used, namely that the flux over the Si (1 1 1) reflection is about 4.5 times bigger and the flux via the Si (4 4 4) or (5 5 5) reflections 8 or 60 times smaller than the flux of

interest passing over the Si (3 3 3) reflection. Actually, the only critical value here is the ratio of 8 with respect to the (4 4 4) reflection of the 89.9 keV photons. The other two energies can be completely neglected here. Again, one has to consider only partly absorbed photons, if they were scattered by the Compton effect, like explained for the case of the argon ionisation chamber. In detail this is done when calculating:

$$I_{in} = \frac{I_c}{\sum_{i=1,3,4,5} r_i T_i \cdot \frac{E_i}{3.6 \text{ eV}} e \cdot (1 - T_i^{Si}) \frac{\sigma_{photo} + \sigma_c^a}{\sigma_{photo} + \sigma_c + \sigma_{rayl.}}} \quad (6.4)$$

with  $r_i = \{4.5, 1, \frac{1}{8}, \frac{1}{60}\}$  and  $T_i$  the transmitted intensity in the concerned reflection of energy  $E_i$  through the lead or the copper absorber.  $(1 - T_i^{Si})$  is the calculated absorption for 300  $\mu\text{m}$  of silicon, including photo effect, Compton scattering and Rayleigh scattering.  $I_c$  is the measured pin diode current and  $e$  the electron charge.

We calculate a flux of  $1.08 \cdot 10^{11}$  and  $1.18 \cdot 10^{11}$  photons per second, considering the copper and the lead case, respectively. If we normalise this result to 100 mA storage ring current, we get an average value of  $5.9(6) \cdot 10^{10}$  at 67.41 keV into a  $2 \cdot 1 \text{ mm}^2$  large slit.

The third type of measurement has been performed with dosimetric films. We used again the 470  $\mu\text{m}$  thick lead absorber and the 1 mm thick copper absorber. After the lead absorber, a dose of  $1200 \frac{\text{Gy}}{\text{h}}$  has been measured and after the copper absorber  $3600 \frac{\text{Gy}}{\text{h}}$ , [Brä03]. If this dose would be only due to 67.41 keV photons, neglecting especially the 89.9 keV photons coming over the Si (4 4 4) reflection, one would have the following correspondence:  $1 \frac{\text{photon}}{\text{s mm}^2} \triangleq 1.2 \cdot 10^{-7} \frac{\text{Gy}}{\text{h}}$ . Considering the absorption as stated in table 6.2, normalising to 100 mA storage ring current and averaging over the two measurements, we obtain a flux of  $4.5(5) \cdot 10^{10} \frac{\text{photon}}{\text{s mm}^2}$ . As the beamsize is roughly  $1 \text{ mm}^2$  FWHM, this transforms then to  $4.5(10) \cdot 10^{10}$  photons per second at 67.4 keV into a  $2 \cdot 1 \text{ mm}^2$  large slit and with 100 mA storage ring current. The increased error is the result of this rough extrapolation to the increased slit size.

Averaging over all three measurements (ionisation chamber, pin diode and dosimetric film), it seems that the value of  $4.5(10) \cdot 10^{10}$  photons per second is fairly well. The energetic width of these photons is determined by the intrinsic Darwin width of the high heat load monochromator of  $0.92 \mu\text{rad}$  and the beam divergence of the undulator radiation of  $12 \mu\text{rad}$  FWHM. With equation 4.8, it follows that the energetic width after the high heat load monochromator is 9.1 eV. Within the width of the  $^{61}\text{Ni}$  resonance, there should thus be  $\frac{85.4 \text{ neV}}{9.1 \text{ eV}} 4.5 \cdot 10^{10} \frac{1}{\text{s}} = 422$  photons per second. To obtain the number of photons in this energy range coming from the undulator, one has to multiply the result of 422 photons per second with several factors: With  $\frac{12 \mu\text{rad}}{0.92 \mu\text{rad}} = 13$  for the ratio between incoming angular divergence and crystal Darwin width; with  $1/0.96$  for the reflectivity of the two Si (3 3 3) reflections [KPNR] and with  $1/0.95$  for different absorbers, namely 500  $\mu\text{m}$  of diamond before the "Front End" and 200  $\mu\text{m}$  of Beryllium in OH2. The result of this calculation is  $6 \cdot 10^3$  photons per second coming from the undulator in the energetic width of the  $^{61}\text{Ni}$  resonance. The value calculated for the undulator radiation is  $7 \cdot 10^3$ , see table 8.2. This is an impressive agreement.

For lighthouse experiments without timing, the small angle X-ray scattering (SAXS) has to be suppressed as much as possible. Especially the flux at 22.47 keV and 89.9 keV should be blocked. Different absorbers are possible. If the  $\text{ZrO}_2$  rotor is used, the rotor material itself cuts all low energy photons. If the sapphire rotor is used, an additional absorber becomes necessary. We used the aluminium in the walls of a compound refractive lens or a copper absorber, if the lens was not used. Copper is easily available in the desired thicknesses. Better absorbers would be thin lead or tungsten sheets, as they would also block the 89.9 keV radiation. The tungsten foil might be more convenient, it is much stiffer. To compare the different absorbers, see figure 6.2.

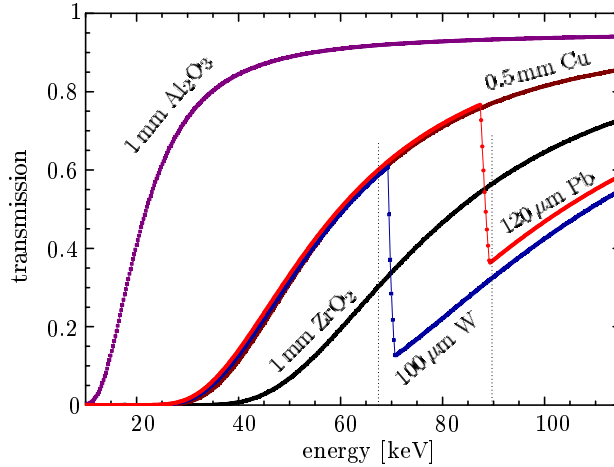


Figure 6.2: Effect of different absorbers to the flux at 22.47 keV, 67.412 keV and 89.9 keV.

## 6.2 The energy of the first excited nuclear level of $^{61}\text{Ni}$

To determine the energy of the excited level of  $^{61}\text{Ni}$ , one can compare the high heat load monochromator angles for the  $^{61}\text{Ni}$  resonance with the absorption curve at the tantalum  $K$ -edge, see figure 6.3. Alternatively, one can compare the Bragg angles of our high heat load monochromator for the  $^{61}\text{Ni}$  and for the  $^{57}\text{Fe}$  resonance. Unfortunately, for this approach, the precise knowledge of the lattice spacing  $d$  of the silicon crystal at 80 K is necessary. This is the temperature of the second crystal of the high heat load monochromator. Our results can not compete with the precision of the literature value, as we did not measure the different angles immediately one after the other. If both the resonance and the  $K$ -edge were measured simultaneously without a delay that allows silicon crystal temperature changes, we could present a more reliable value.

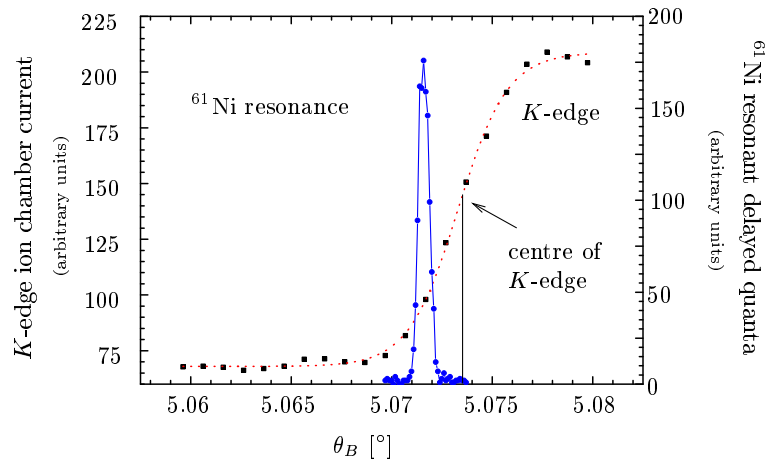


Figure 6.3: Energy of the  $^{61}\text{Ni}$  resonance and Ta  $K$ -edge

The more reliable crystal of the high heat load monochromator is by far the downstream crystal, as it is much less perturbed by the power of the incoming beam. This is the crystal we consider here. We find the  $^{61}\text{Ni}$ -resonance at  $\Delta\theta = \theta_{K\text{-edge}} - \theta_{\text{Ni}} = 0.0016(3)^\circ$  below the tantalum  $K$ -edge. Later, when comparing  $^{61}\text{Ni}$  and  $^{57}\text{Fe}$  resonance positions, dynamical corrections to the Bragg angle given by the kinematic Bragg equation need to be considered. Here, as both

energies are close, these corrections can be omitted. With

$$E_{\text{Ni}} = \frac{hc}{2d \sin \theta_{\text{Ni}}} \quad \text{and} \quad E_{\text{K-edge}} = \frac{hc}{2d \sin \theta_{\text{K-edge}}} \quad (6.5)$$

we can derive the following expression:

$$E_{\text{Ni}} = E_{\text{K-edge}} \frac{\sin \theta_{\text{K-edge}}}{\sin(\theta_{\text{K-edge}} - \Delta\theta)} = \frac{E_{\text{K-edge}}}{\cos \Delta\theta - \sin \Delta\theta \cot \theta_{\text{K-edge}}} \quad (6.6)$$

With equation 6.6 and  $E_{\text{K-edge}}^{\text{Ta}} = 67416 \text{ eV}$  [Fir96, vol. 2 page F-37], we obtain  $E_{\text{Ni}} = 67437(4) \text{ eV}$ . As  $\sin \Delta\theta$  is very small here, the exact angle  $\theta_{\text{K-edge}}$  does not influence the result to a sensible extent. In fact, an angular uncertainty of  $0.1^\circ$  only leads to an energy error of  $0.5 \text{ eV}$ . The biggest problem here is the time delay between the two measurements, which can lead to temperature changes and thus a variation of the crystal lattice spacing and angle. These should nevertheless be small, as the beam current does not vary significantly on moderate time scales. The two curves here have been measured in a 1 hour 15 minutes interval. Principally, it is possible to measure both values simultaneously.

The second possibility is to compare the Bragg angles of the  $^{57}\text{Fe}$  resonance and the  $^{61}\text{Ni}$  resonance. This is not very reliable, as we need to know either the lattice spacing or the correct angle of the  $^{57}\text{Fe}$  resonance. A better option is to compare the Bragg angles of the  $^{61}\text{Ni}$  resonance with different reflection, like Si (3 3 3) with Si (4 4 4) and Si (5 5 5). This has not been done so far. The two resonances have been used repeatedly one after the other in the same filling mode of the synchrotron. The heat load is therefore not too different, although the undulator gap is slightly different. The  $^{57}\text{Fe}$  resonance has been addressed with photons transmitted via the Si (1 1 1) reflection, the  $^{61}\text{Ni}$  resonance via the Si (3 3 3) reflection. Averaging over several of these changes gives a difference between the crystal angle of  $\Delta\theta = 2.8423(5)^\circ$ . Dynamical theory predicts the angular deviation from the kinematic Bragg angle and the experiment, see equation 4.9. In particular  $\Delta\theta_{\text{asym}} = \Delta\theta_{\text{sym}}(1 + \frac{1}{b})$  for the asymmetric cut second monochromator crystal. For the Si (1 1 1) reflection at the  $^{57}\text{Fe}$  resonance this is  $\Delta\theta_{\text{asym}} = 8.8^\circ \cdot 10^{-4}$ . For the Si (3 3 3) reflection at the  $^{61}\text{Ni}$  resonance this is  $\Delta\theta_{\text{asym}} = 5.8^\circ \cdot 10^{-5}$ . We thus correct  $\Delta\theta$  to  $2.8415(5)^\circ$ . We modify equation 6.6 to consider the different reflections (1 1 1) and (3 3 3):

$$E_{\text{Ni}} = \frac{3E_{\text{Fe}}}{\cos \Delta\theta - \sin \Delta\theta \cot \theta_{\text{Fe}}} = \frac{3E_{\text{Fe}}}{\cos \Delta\theta - \sin \Delta\theta \cot \left( \arcsin \frac{hc}{2d_{111} E_{\text{Fe}}} \right)} \quad (6.7)$$

We need to know the exact lattice spacing  $d_{111}$  at 80 K. At 300 K, the lattice constant of silicon is given as  $5.43102088(16) \text{ \AA}$  [Moh00]. We multiply this value with 0.99974 to obtain the lattice constant at 80 K [Wil03] and obtain  $d_{111} = 3.1348(1) \text{ \AA}$ . This value changes only by  $0.0004 \text{ \AA}$  between 70 and 100 K, as the expansion coefficient of silicon is very small in this region [Wil03]. The biggest error comes thus from the error of  $\Delta\theta$ . We finally get  $E_{\text{Ni}} = 67463(15) \text{ eV}$ .

The literature value of  $67412(3) \text{ eV}$  [Fir96] was obtained observing the decay of  $^{61}\text{Cu}$  with a Ge(Li) detector [Mey78]. Three other authors report similar values, although with slightly bigger errors [Bha99]. We believe the discrepancy of our values originate mainly from the different conditions at the second crystal of the high heat load monochromator, as concerning heat load or problems of mechanical stability. Remember that the values for  $\Delta\theta$  have been obtained comparing angles measured at different times. M. Gerken, who succeeded to excite the  $^{61}\text{Ni}$  level with synchrotron radiation for the first time, presents a similar figure like our figure 6.3, but state the energy difference between the  $K$ -edge and the  $^{61}\text{Ni}$  resonance to be only  $3 \text{ eV}$  [Ger02]. In a future beamtime, the energy question could be addressed in more detail.

### 6.3 The lifetime of the 67.41 keV level of $^{61}\text{Ni}$

For the determination of the lifetime of the 67.41 keV level, the temporal evolution of the incoherent scattering of individual  $^{61}\text{Ni}$  nuclei (nuclear fluorescence) was measured. The coherence is destroyed, when phonons intervene and an energy transfer (phonon creation or annihilation) takes place during the nuclear transition. The decay of individual excited nuclei follows an exponential behaviour and the re-emitted photons proceed into  $4\pi$  as opposed to the forward direction in the case of NFS and the NLE. Some precautions have to be taken when realising the setup shown in the inset of figure 6.4. The  $^{61}\text{Ni}$  metal foil was kept at room temperature to obtain a negligibly low Lamb-Mössbauer factor. The Debye model for the Lamb-Mössbauer factor with a Debye temperature of 390 K yields  $f_{\text{LM}} = 0.003$  at room temperature. With higher Lamb-Mössbauer factor, coherent effects like a propagating delayed wavefield through the sample due to NFS [Ber94a] would influence the time behaviour of the fluorescence radiation. Moreover, by covering a large solid angle with the detector, effects from the angular correlation between incident and scattered photons affecting the temporal evolution are averaged out, as opposed to the technique of SR-PAC, see chapter 7.

To excite the 67.41 keV level of  $^{61}\text{Ni}$ , the 17<sup>th</sup> harmonic of the three 32 mm undulators at ID18 was used. The high-heat-load monochromator was set to the (333) reflection. An appropriated absorber, here 0.5 mm of copper, reduced the number of photons passing via the (111) reflection. The delayed, incoherent inelastic nuclear fluorescence radiation from a 16 times folded  $^{61}\text{Ni}$  foil of 20  $\mu\text{m}$  thickness was measured at room temperature with one standard APD detector. Fast electronics was used to select the delayed signal coming from the decay of the excited level of  $^{61}\text{Ni}$ .

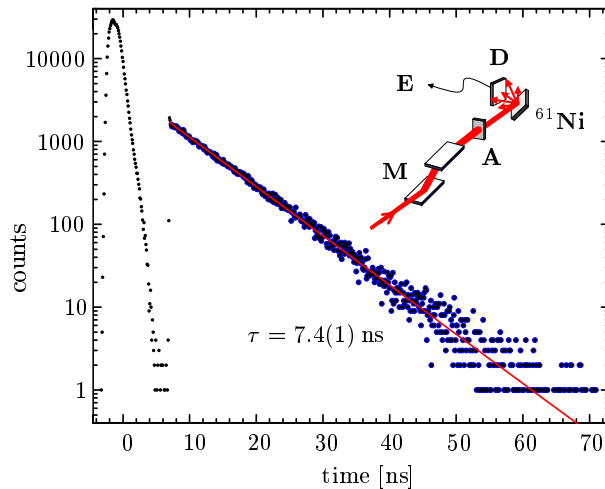


Figure 6.4: Time evolution of the fluorescence radiation of the 67.41 keV  $^{61}\text{Ni}$  level. The setup consists of the two Si high heat load monochromator crystals **M** on the (333) reflection, an absorber **A** to reduce photon intensity transmitted via the Si (111) reflection, the  $^{61}\text{Ni}$  foil and a fast detector **D** with time discriminating electronics **E**. An electronic gate blocks data acquisition during the first 7 ns, i.e. especially the prompt photons, that are shown on the left, when deactivating the gate temporarily.

This type of measurement was repeated several times within two years. Averaging over the set of results leads to the following lifetime of the excited level of  $^{61}\text{Ni}$ :  $\tau = 7.4(1)$  ns and  $t_{\frac{1}{2}} = 5.13(7)$  ns. The error is about 5 times bigger as the statistical error of the single measurements. Nuclear data sheets like [Fir96] and [Bha99] present a half-life of 5.34(16) ns. They base this value on four sources:  $t_{\frac{1}{2}} = 5.27(23)$  ns [Roo75],  $\tau = 7.3(3)$  ns [Shi69],  $\tau = 7.5(3)$  ns [Mey78] and  $t_{\frac{1}{2}} = 5.41$  ns [Azi71]. The previous measurements using synchrotron radiation to excite the  $^{61}\text{Ni}$

resonance suggest a lifetime of 7.16(20) ns [Ger02] and 7.6(4) ns [Wil02]. The last measurement suffered from impurity bunches in the storage ring and needs thus to be considered with care. Nevertheless, all values are in principle in agreement with our measurements, considering their relatively large errors. We achieved a more precise result, which will be used in the treatment of the NLE.

## 6.4 Nuclear lighthouse effect in transmission with $^{61}\text{Ni}$

### 6.4.1 Brief experimental review

The experiments were performed in the 16-bunch filling mode at the nuclear resonance beamline ID18 at the ESRF. Although the NLE does principally not depend on the type of filling mode [Röh00c], additional time discrimination was preferable in the case of  $^{61}\text{Ni}$ : The nuclear signal of  $^{61}\text{Ni}$  is quite small as compared to the electronic scattering background mainly caused by small angle X-ray scattering (SAXS). As the latter is scattering on a "prompt" timescale of  $10^{-15}$  s, 16-bunch mode together with a fast detector permits a time discrimination between the two processes. The reason for the small ratio of the nuclear signal to the electronic scattering is the low Lamb-Mössbauer factor  $f_{\text{LM}}$  for high-energy nuclear transitions, see figure 2.3. However, evidence of the NLE without timing mode is presented in chapter 6.4.5.

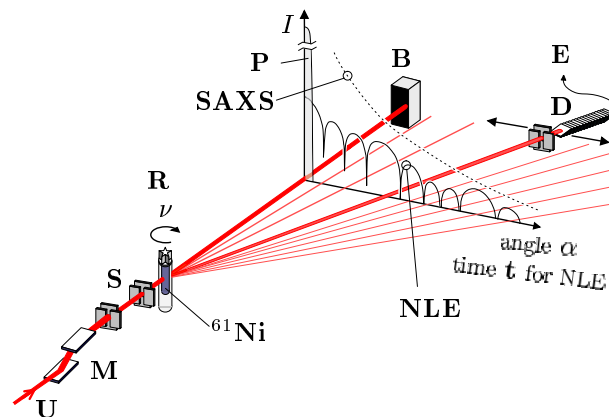


Figure 6.5: The undulator radiation  $U$  is monochromatised coarsely ( $\delta E = 9$  eV) by two Si (333) reflections  $M$  and shaped by a slit system  $S$ . The rotor  $R$  containing  $^{61}\text{Ni}$  is spinning at  $\nu = 8$  kHz. The non-interacting prompt direct beam (intensity  $P$ ) hits the beamstop  $B$ . The prompt small angle X-ray scattering  $\text{SAXS}$  is in competition with the delayed nuclear lighthouse effect signal  $\text{NLE}$ , thus demanding fast detection with an array of avalanche photo diodes  $D$  and time discriminating electronics  $E$ . The detector scans over a range of angles. Only for the nuclear delayed signal, angles are resolved proportional to the interaction time.

The setup of the experiment is shown in figure 6.5 together with an illustration of the photon intensities from three different processes. The huge peak  $P$  to the left corresponds to non-interacting undeviated photons and thus defines the time  $t = 0$ . Compton scattering and SAXS contribute to deviated photons, but their interaction time with the electrons of the sample and the rotor walls is on a prompt timescale of around  $10^{-15}$  s. This part is sketched by a dotted line following an angular dependence of  $\alpha^{-4}$  according to Porod's law for SAXS from randomly oriented particles, see chapter 2.7. The third category are the photons that are scattered via excitation of the 67.41 keV nuclear level in  $^{61}\text{Ni}$ . They are both delayed and deviated to the side according to the time spent in the foil before de-excitation. In favourable cases such as at the  $^{57}\text{Fe}$  resonance in transmission geometry, both SAXS and NRS signals are of comparable



strength. The discrimination can be done with successive measurements of the angular intensity variation, once at resonance, once slightly detuned, and subtraction [Röh00c]. In the case of  $^{61}\text{Ni}$  this is not possible and fast detectors are employed to use the time information to discriminate between SAXS and the nuclear signal. Without discriminating detector electronics, the slit size in front of the detector defines the time resolution and each detector position  $x = d\alpha$  corresponds to a time  $t$  according to  $x = 2\pi d\nu \cdot t$ , with  $d$  being the distance between sample and detector and  $\nu$  the rotational frequency of the rotor.  $x = 0$  is the position of the direct beam. If instead time discrimination is applied, the time resolution is given by the detector and its electronics. Then, a large detector is best if it can bear the overall incoming flux. With small detectors as in our setup, that do not cover the whole angular region of interest, one needs to scan uniformly over the whole angular region, see also chapter 4.5.4.

The sample consisted of two isotopically enriched  $^{61}\text{Ni}$  foils (85% enrichment), each  $20\ \mu\text{m}$  thick. Each foil was rolled to a tube that fitted tightly into a hollow  $\text{ZrO}_2$  rotor of 3 mm inner diameter, see figure 3.3. The  $\text{ZrO}_2$  rotor absorbs 70% of the 67.41 keV photons and gives rise to some SAXS. Undulator radiation having 1/3 of that energy (22.47 keV) is transmitted by the Si (1 1 1) reflection of the monochromator, but it is completely absorbed by the  $\text{ZrO}_2$  rotor walls. Therefore, it does not contribute to the SAXS background. Single crystalline sapphire rotors that absorb less and give less SAXS broke repeatedly and have not been employed in 16-bunch mode operation presented. However, some results are presented in 6.4.5.

We used the stack of 24 silicon avalanche photo diodes, each  $100\ \mu\text{m}$  thick and  $10 \times 10\ \text{mm}^2$  large, and inclined to an angle of  $37^\circ$  between the silicon surface and the beam direction, see chapter 4.5.2. A detector slit limited the sensitive area to  $6 \times 4\ \text{mm}^2$ , horizontal  $\times$  vertical. At 67.41 keV, the calculated efficiency of the total assembly is 20%. The electronic time resolution was 2 ns. The detector array was scanned repeatedly over a lateral displacement  $x$  ranging from 0 (behind the beamstop) to 50 mm. With  $\nu = 8\ \text{kHz}$  and  $d = 13.9\ \text{m}$ , the corresponding times are 0 to 72 ns. Between two scans, the monochromator energy was checked using a setup as depicted in the inset of figure 6.4. The time discrimination in order to block the prompt signal of the SAXS background is done with an electronic gate that opens 7 ns after the arriving SR pulse. A multi-channel analyser (MCA) records the time spectrum (10 channels per ns; 400 channels are displayed in figure 6.7). The detector is 6 mm wide laterally, corresponding to a temporal width of 8.6 ns. This defines the time window where photon counting is possible at each detector position. The precise time information within this window is obtained with the timing electronics and the MCA. The time resolution is thus given by the detector with its electronics and not by the detector slit size.

### 6.4.2 NLE time/angle spectra of $^{61}\text{Ni}$ and background evaluation

Three time spectra have been acquired during the experiment. At the  $^{61}\text{Ni}$  resonance energy time spectra have been acquired at temperatures of 180 K and 115 K. These raw spectra are presented in figure 6.6 at the left and in the middle. To estimate the influence of electronic noise and cosmic background radiation, a third time spectrum has been acquired under the same experimental conditions, but with an empty  $\text{ZrO}_2$  rotor. It turned at 8 kHz as in the other two cases to deliver the same SAXS background. The presence of the  $^{61}\text{Ni}$  sample is negligible for the size of the SAXS background, as compared to the SAXS of the rotor itself. The background measurement was done with the stator/rotor system operating at room temperature. It is shown on the right side of figure 6.6.

The countrates at late times in all three spectra are solely due to electronic noise and cosmic background radiation. The height of this background level scales with the time needed to acquire the spectra. In the background time spectrum, a slightly increased countrate in the region

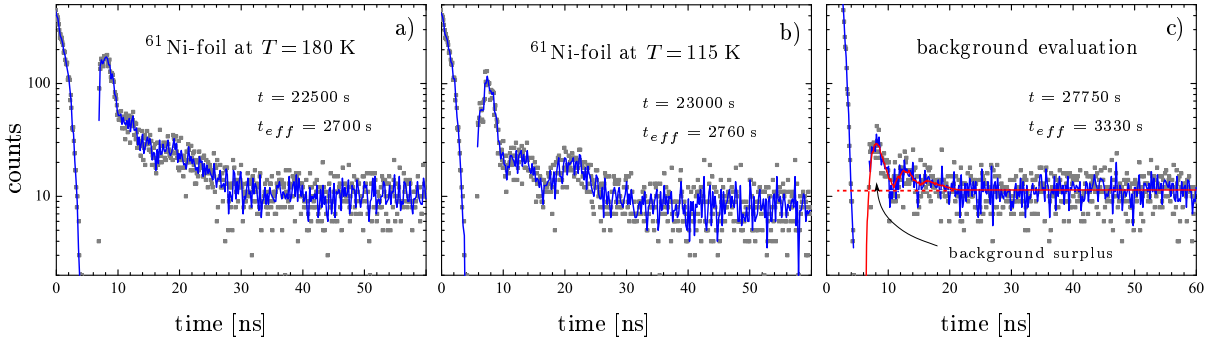


Figure 6.6: The raw data of the  $^{61}\text{Ni}$  NLE measurements in 16-bunch mode and with timing electronics in order to suppress the SAXS background. Time spectra of nuclear resonant scattering by  $^{61}\text{Ni}$  have been obtained at 115 and 180 K. To evaluate electronic noise and background radiation, a time spectrum without the  $^{61}\text{Ni}$ -foil in the  $\text{ZrO}_2$  rotor was acquired.

between 7 and 22 ns is observed. The reason for this might be sporadic electronic overshooting after the detection of a prompt photon, that triggers an additional counting event in this time region. However, this additional "overshooting" background is rather small and can be easily subtracted from the time spectra at 115 and 180 K. Therefore, the time spectra of the background measurement is smoothed over 30 MCA channels, and the surplus of counts in the region between 7 and 22 ns with respect to the average countrate at times above 22 ns is calculated. Properly scaled to the acquisition time of each spectrum, this surplus is subtracted from the time spectra at 115 K and 180 K.

### 6.4.3 Results at 180 K

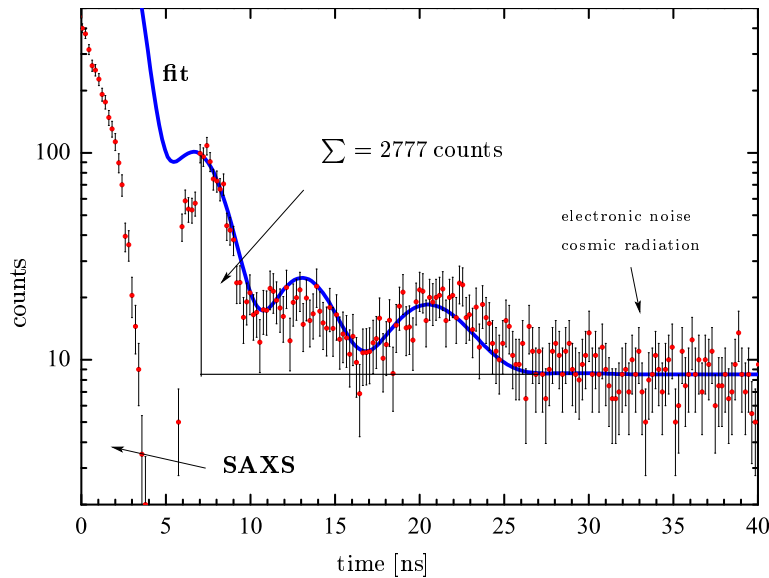


Figure 6.7: The nuclear lighthouse effect with  $^{61}\text{Ni}$  at 180 K. The detector signal was gated off during the first 7 ns to discriminate the prompt SAXS background ( $\sim 10$  kHz summed over the angular range covered by the detector). The SAXS is seen at early times when removing the gate temporary for a short instant. The NLE data could be fitted by the theory of nuclear forward scattering using the program Motif [Shv99]. The beat structure originates from the interference of the 12 transitions between the hyperfine-split ground and 67.41 keV excited states in the presence of a magnetic hyperfine field  $B_{hf}$ , see figure 2.8.

The measurement at 180 K is presented in figure 6.7. The overall time the detector was

in place to acquire delayed photons for a particular data point in figure 6.7 was 45 minutes. The average beam current in the storage ring was 70 mA. We detected 2770 photons being scattered by the  $^{61}\text{Ni}$  nuclei, after subtracting the background solely due to cosmic radiation or electronic noise. This corresponds to a countrate of  $1\text{ s}^{-1}$ , if a large detector would cover the whole interesting angular range at once. The rate of incoming photons in the energetic width of the resonance is  $300\text{ s}^{-1}$  at the stated electron beam current, obtained by rescaling the result of chapter 6.1.

The data was fitted using the program Motif [Shv99] and a magnetic hyperfine field of  $6.7(2)\text{ T}$  was obtained together with an additional line broadening of  $0.45$  natural line widths  $\Gamma_0$ . As input parameters, we use  $\mu_g = -0.75\ \mu_N$  and  $\mu_e = 0.48\ \mu_N$  for the nuclear magnetic moments of  $^{61}\text{Ni}$  [Fir96] and  $f_{\text{LM}} = 0.025$  according to the Debye model with a Debye temperature of  $390\text{ K}$  [Bir64]. The lifetime of the excited level was taken to be  $7.4\text{ ns}$ , as determined by the detection of the incoherently emitted photon, see chapter 6.3. The thickness was taken to be  $80\ \mu\text{m}$ . Both thickness and hyperfine field were kept fixed without assuming any distribution.

The magnetic hyperfine field at this temperature as measured with NMR is  $7.2\text{ T}$  [Str63]. This slight discrepancy might be due to a small relative movement between the two sides of the cylindrical foils as seen by the beam, see chapter 6.4.4. This lateral movement can be due to a precession of the rotor and might cause a Doppler shift acting on the transition energies [Qua02]. An inhomogeneous line broadening was also observed in the NMR measurements [Str63] and attributed to impurities and strain.

#### 6.4.4 Results at 115 K

Thanks to the improved stator and the applied Invar corset, a NLE measurement at  $115\text{ K}$  could be performed. The result at  $115\text{ K}$  is presented in figure 6.8, together with the measurement at  $180\text{ K}$ .

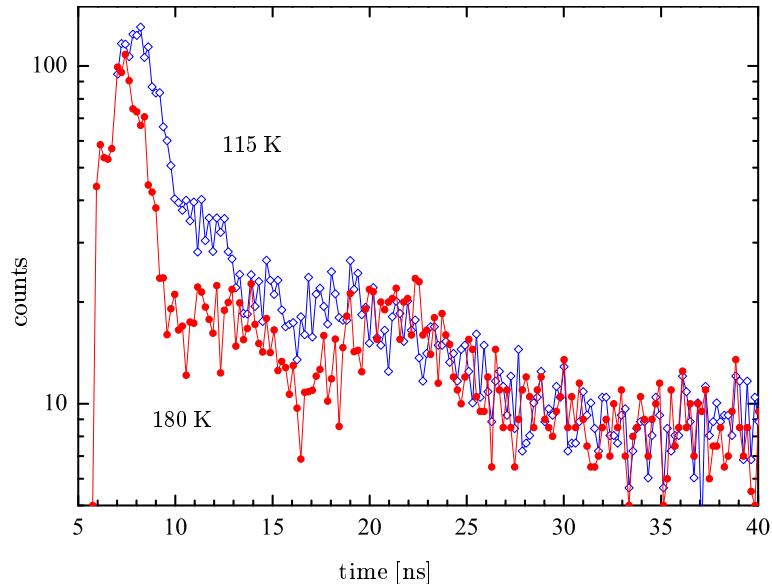


Figure 6.8: Comparison of the NLE results at  $180\text{ K}$  shown by full circles with the measurement at  $115\text{ K}$  shown as hollow diamonds.

At first glance, it is very surprising that the time spectrum changes significantly. Metallic nickel is not expected to show a phase transition in the temperature range covered. On the contrary, the magnetic hyperfine field is known to change only slightly in this region, as the Curie

temperature is at 632.7 K [Sha80]. In fact, NMR measurements of the magnetic hyperfine field are available and presented in figure 7.6. They show only 2% of change in the magnetic hyperfine field between 180 and 115 K. However, the Lamb-Mössbauer factor of nickel changes from 0.0246 to 0.066 when decreasing the temperature from 180 to 115 K. This change is significant. Using the fit result for the magnetic hyperfine field as obtained with motif, but increased by 2% and changing the Lamb-Mössbauer factor, we simulated the time spectrum to be expected at 115 K. This simulation together with the fit at 180 K is shown on the left side of figure 6.9. In this comparison, no background is considered and the time resolution of the detector is considered to be ideal. The simulation at 115 K scaled and background corrected as done with the 180 K fit is shown on the right side, together with the actual measurement.

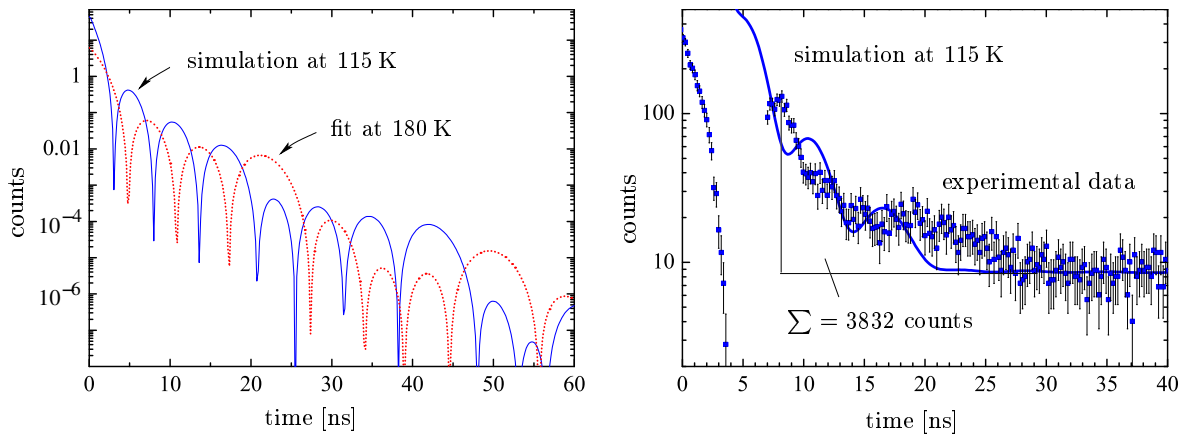


Figure 6.9: On the left side, the time spectrum of metallic  $^{61}\text{Ni}$  at 115 K is simulated using the parameters obtained for the fit at 180 K. Only the Lamb-Mössbauer factor and the magnetic hyperfine field have been adjusted to the expected value at 115 K. On the right side, this simulation is compared to the actual measurement.

It is evident, that this fit does not reproduce the obtained data. Even when allowing the magnetic hyperfine field, the Lamb-Mössbauer factor and the sample thickness to vary without restrictions, no reasonable fit for this data set could be obtained. This significant discrepancy might be explained with the influence of a precession and nutation of the rotor on the sample geometry. Figure 6.10 illustrates this influence.

The rotor used in this experiment was filled with two foils that both covered completely the inside wall of the rotor, see figure 6.10, top left. The thickness of one foil was  $20\ \mu\text{m}$ . NFS on this rotor at rest would show the time spectrum of a  $80\ \mu\text{m}$  thick sample. The same is true for an ideally turning rotor, that means a rotation without precession and nutation. If on the contrary the rotor is subject to a precession and nutation, the two parts of the foil illuminated by the beam are in a relative moment of one with respect to the other. Two foils of individual thickness of  $40\ \mu\text{m}$  have to be considered with a relative motion and thus a Doppler shift of the transition energies of one illuminated part with respect to the other. For the measurements at 180 K, this behaviour might be less important and stays thus unperceived because of two reasons, one is that the higher temperature allowed for better operation of the stator/rotor system, the other one is the much smaller Lamb-Mössbauer factor. Multiple nuclear scattering is therefore negligible. At 115 K, the operation of the stator/rotor system might create perturbations on the rotor, i.e. droplets of liquid nitrogen that tip the rotor, causing permanent or damped precession and nutation. Further, the Lamb-Mössbauer factor is much higher and multiple nuclear scattering can play a stronger role.

The problem caused by this sample geometry can be completely overcome in using only a 1/3 filled rotor, as depicted in the lower row of figure 6.10. In this case, the beam illuminates

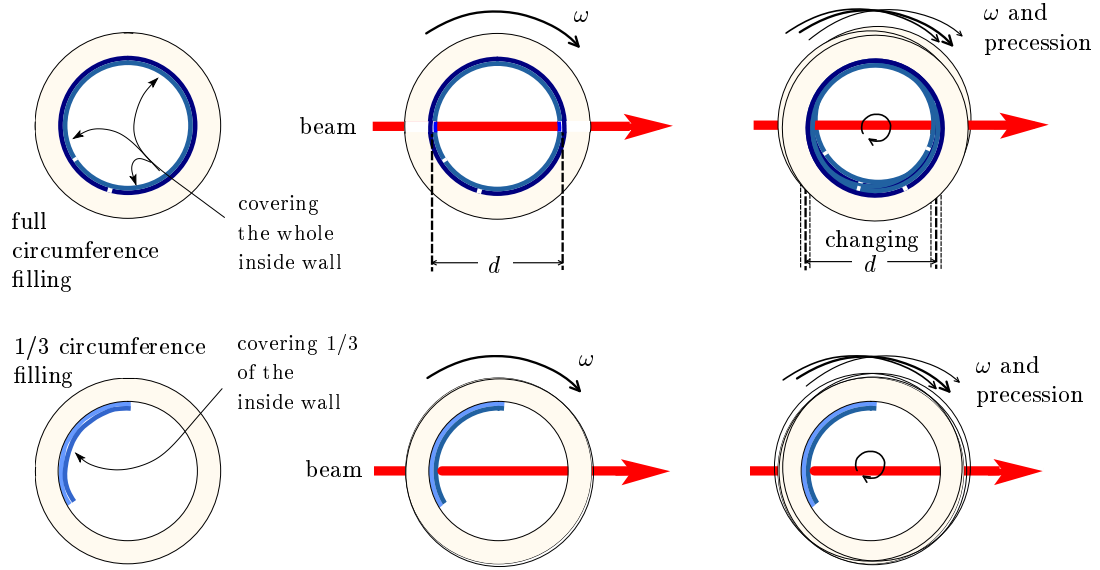


Figure 6.10: The interplay of the sample geometry with the precession of the rotor. In the top row, a fully filled rotor is used. If the rotor turns perfectly, the beam crosses the sample twice and no relative movement between the two sample parts illuminated is observed. If the rotor precesses, there is a relative movement between the two irradiated parts. A rotor filled only on 1/3 of the circumference avoids the problem.

only once the sample, if the transverse beamsize is less than 1/6 of the rotor inner circumference. Now, a precession or notation of the rotor does not change the time spectrum, as NFS and the NLE are not sensitive to a Doppler shift without an incorporated reference sample.

A positive result of the 115 K measurement is the increase in the delayed countrate by a factor of 1.4 as compared to the 180 K measurement. This is not surprising, due to the increase of the Lamb-Mössbauer factor. In fact, the simulation at 115 K and the fit at 180 K as shown on the left side of figure 6.10 can be analysed and their integral in the range between 7 and 40 ns can be calculated. The increase in delayed countrate calculated this way is a factor of 1.6, not too far away from the value obtained in the experiment.

#### 6.4.5 Measurements without timing electronics for the lighthouse signal

To conclude this chapter on the results of the NLE measurements with  $^{61}\text{Ni}$ , the question whether this type of experiment could be performed also in non-timing filling modes of the synchrotron should be raised. The use of the timing mode to obtain the results as presented above is not satisfying, knowing that the NLE principally does not depend on the timing mode. Prior measurements on the  $^{61}\text{Ni}$  resonance with the NLE without the use of timing electronics have been performed in fact and showed some positive results. These will be sketched briefly now.

The synchrotron was filled in  $2\cdot\frac{1}{3}$ -filling mode. This allowed at least to verify the energy of the incoming photons and to adjust the high heat-load monochromator if necessary. Therefore, the same incoherent scattering setup as depicted in the inset of figure 6.4 was used. Unfortunately, in  $2\cdot\frac{1}{3}$ -filling mode, the end of the  $\frac{1}{3}$  bunch trains is not at all sharp, instead the intensity drops slowly to zero over the last 10 to 12 buckets. To measure the delayed photons from the decaying individual nuclei, the end of the bunch-train had to be completely gone, thereby limiting the obtained countrates of the  $^{61}\text{Ni}$  decay. With the electronic gate opening roughly 25 ns after the end of the bunch trains, the  $^{61}\text{Ni}$  resonance energy scan as depicted in panel a) of figure 6.11

was obtained.

To optimise the ratio of photons lying energetically within the bandwidth of the resonance to overall photons, the spherical compound refractive lens as depicted in figure 4.9 was used. However, even the intensity of one undulator was enough to damage the lens during this experiment. The two other undulators have been left open therefore.

The measurements were performed on the same sample as reported on in chapter 6.4.3, i.e. 2 foils of  $20\ \mu\text{m}$  thickness covering each the full circumference. However, the rotor material was single-crystalline sapphire and not  $\text{ZrO}_2$ . Otherwise, SAXS and absorption are much too high to perform measurements without timing electronics. The detector was a lithium doped germanium detector with the efficiency for  $67.41\ \text{keV}$  photons being close to 100 %. The sensitive area of the detector was limited with a slit system to 2 mm horizontal opening and 1 mm vertical opening. The rotor turned at 7.5 kHz. With this slit size and rotor speed, the time resolution of the NLE time/angle scans is 3 ns at the detector distance of 13.9 m. The temperature of the  $^{61}\text{Ni}$  sample was 145 K.

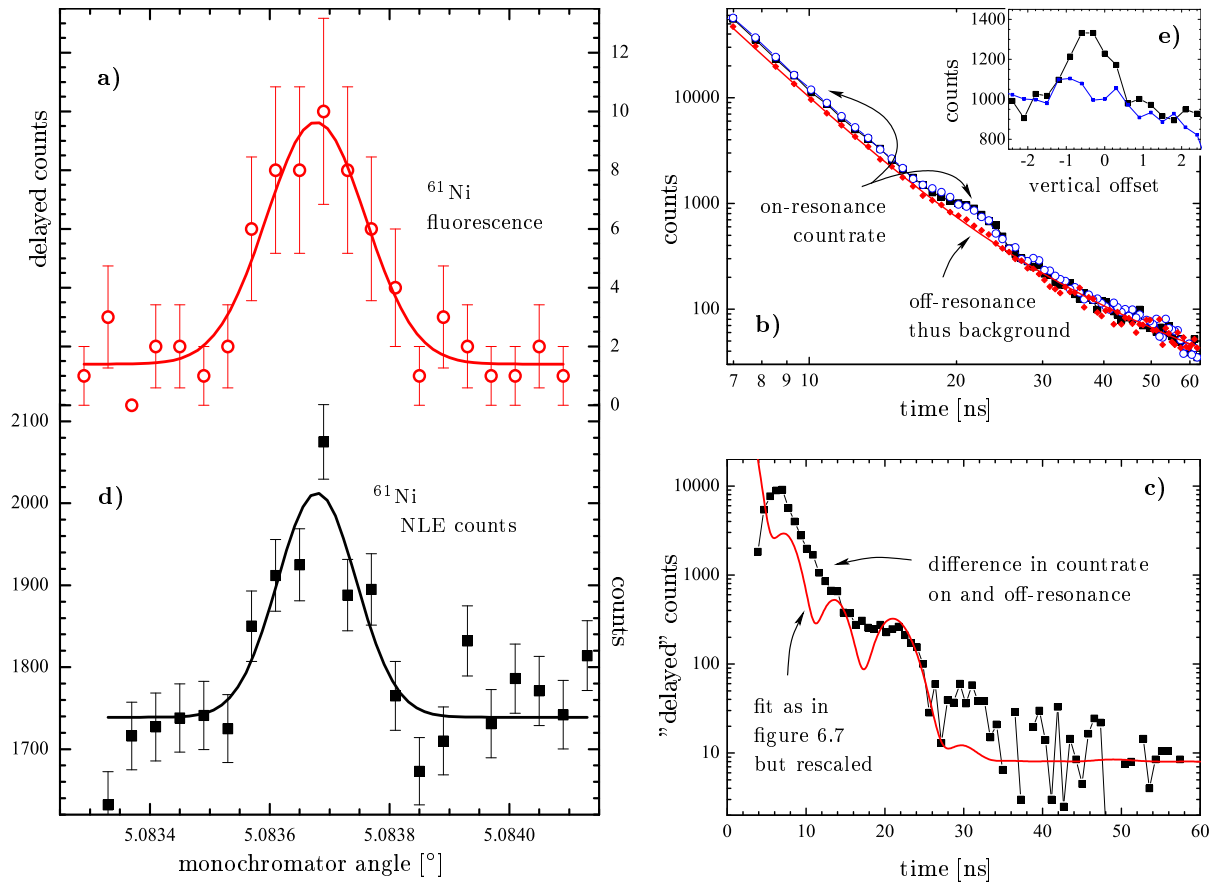


Figure 6.11: NLE measurements on the  $^{61}\text{Ni}$  resonance in  $2\cdot\frac{1}{3}$ -filling mode. The  $^{61}\text{Ni}$  resonance energy was checked with an inelastic scattering setup, panel a). At this energy and with the  $^{61}\text{Ni}$  sample turning at 7.5 kHz at 145 K, the deviated photons have been measured and compared to same scan off resonance energy, panel b). The difference is shown in panel c) and compared to the fit of chapter 6.4.3. At  $t = 20\ \text{ns}$  or the offset  $x = 13\ \text{mm}$ , the same energy scan as shown in a) has been repeated, see panel d). Further, at the same horizontal offset  $x$ , the vertical scan e) was obtained.

With these experimental conditions, NLE angle scans have been performed, both on and off resonance energy. The corresponding offset at the detector position ranged between 0 mm (behind the beamstop) to 40 mm, equivalent to 61 ns. The step size was 0.5 mm and the ac-

quisition time per data point was 20 s. To drop off the resonance energy for the off-resonance scans, the monochromator angle was changed by 0.0005 dg or 7 eV. As seen in figure 6.11, panel c), a significant difference between the two scans at 20 ns (or an offset  $x = 13$  mm) is clearly seen. The on-resonance scan was performed twice. The off-resonance scan consists of the SAXS background and follows a smooth decay that could be fitted by  $I_{\text{SAXS}} = a_1 \cdot x^{-4.45} + a_2 \cdot x^{-1.7}$ .

The difference between the on and off-resonance scans is shown in figure 6.11, panel c), together with the fit obtained in chapter 6.4.3 during timing mode experiments. The fit was rescaled and the background adjusted. Although the quality is rather poor, the overall behaviour is matched.

Nevertheless, to proof definitely that the difference is due to resonantly scattered photons from the  $^{61}\text{Ni}$  sample, two further test have been performed. In both cases the detector offset from the direct beam was chosen as  $x = 13$  mm as measured from the centre of the detector slit, corresponding to  $t = 20$  ns. This is the region of high contrast between on and off-resonance scan in panel b) of figure 6.11. At this point, the photon energy was varied with the high heat-load monochromator and the countrate obtained as a function of the monochromator angle, see panel d). As expected, the behaviour is identical to the inelastic version of this energy scan seen in panel a), giving clear proof that the surplus of data obtained at  $x = 13$  mm or  $t = 20$  ns consist of resonantly scattered photons.

Further, still at the horizontal offset of 13 mm from the direct beam, the vertical detector position was scanned over  $\pm 2.5$  mm. In leaving the horizontal plane, the NLE photons have to disappear, as the rotor turns around a vertical axis. This is clearly seen in panel e) of figure 6.11. This measurement has been performed on resonance and results in a distinct peak at the vertical offset  $z = 0$  (large squares). If the experiment is repeated off-resonance, this peak disappears of course (small squares). The acquisition time per data point was 50 s.

It is of interest to compare the countrates in both experiments. In the experiment with the APD-stack in timing mode, a countrate of 1 Hz was derived, if the detector could cover the whole angular range of interest simultaneously, i.e. the times between 7 and 40 ns. With the lithium doped germanium detector, the same problem exists, the different angles cannot be measured at the same time. The sum of the delayed counts between 7 and 40 ns in panel c) of figure 6.11 is 32 000. The detector spent 2200 seconds to acquire photons in this range, e.g. 50 seconds per point and 44 data points in this range (covering 22 mm). As the horizontal detector opening was 2 mm, just  $\frac{1}{11}$  of the time range under consideration was covered at once. The effective time is thus 200 seconds only, as a large position sensitive detector with the same characteristics could have been covering all this at once in principle. 32 000 counts in 200 seconds leads to a countrate of 160 Hz.

Still, the countrate obtained in 16-bunch mode has to be adjusted by the following factors:  $\times 5$  for the ratio of detector efficiencies, namely 100 % for the lithium doped germanium detector and only 20 % for the APD stack.  $\times 2.2$  for the ratio of storage ring beam current ( $\approx 70$  mA in 16-bunch mode and  $\approx 170$  mA in 2/3 filling mode).  $\times 10$  as the increase in spectral flux passing via the Si (3 3 3) monochromator when using the compound refractive lens.  $\times 4.4$  for the change in rotor material absorption (92 % transmission for 1 mm of sapphire, only 21 % transmission for the  $\text{ZrO}_2$  rotor).  $\times \frac{1}{3}$  as all three undulators have been used in the 16-bunch mode experiment. The product of these factors is roughly 160. This agreement is amazing. However, the temperature in the non-timing measurement was 145 K instead of 180 K.





# Chapter 7

## SR-PAC with $^{61}\text{Ni}$

Synchrotron radiation based perturbed angular correlation (SR-PAC) is the scattering analogue of time-differential perturbed angular correlation (TD-PAC), well established in nuclear solid state physics [But96].

The idea of performing TD-PAC measurements with synchrotron radiation instead of using a radioactive source and without involving a three level nuclear energy scheme was evoked a long time ago by Trammel and Hannon [Tra78]. The first experimental observation of the resulting "single nucleus quantum beats" was in 1995, [Bar96], using the  $^{57}\text{Fe}$  isotope. However, further investigations with this method have not been reported until recently, when it was revitalised and named SR-PAC, [Ser03, Ser04, Set03].

SR-PAC is an incoherent single nucleus resonant scattering process that reveals hyperfine interactions without depending on the size of the Lamb-Mössbauer factor. It is therefore perfectly suited for the investigations of high transition energy Mössbauer isotopes with SR, where the Lamb-Mössbauer factor is vanishing at room temperature and rather small even at very low temperatures. This is demonstrated here for the 67.41 keV transition of  $^{61}\text{Ni}$ .

### 7.1 Nuclear levels important for TD-PAC and SR-PAC

In TD-PAC, an intermediate nuclear level is populated by a gamma decay of a higher nuclear level that itself is populated by the decay of a radioactive mother isotope. This first gamma decay is detected by a first detector. The following decay of the intermediate level into the ground state is detected by a second detector. If the intermediate level is split by hyperfine interactions, the interference of indistinguishable paths of the  $\gamma$ - $\gamma$  cascade via the split intermediate level leads to modulations in the detected intensity of detector 2 when the time between the two gamma emissions is used as time axis. These modulations reveal the strength or type of the hyperfine interactions. Typical isotopes used in TD-PAC are  $^{111}\text{Cd}$  with its mother isotope  $^{111}\text{In}$ , further  $^{100}\text{Rh}$  (with  $^{100}\text{Pd}$ ),  $^{140}\text{Ce}$  (using  $^{140}\text{La}$ ) and  $^{181}\text{Ta}$  (with  $^{181}\text{Hf}$ ).

In SR-PAC measurements, the intermediate state is populated from the ground state with the help of a SR pulse. No higher excited state is involved. The direction and timing of the first detector is replaced by the direction of the incident photon and its time. The direction of the emitted photon as a function of time is recorded by a detector. If the intermediate state (in fact, this "intermediate" state is the only excited state) is split due to hyperfine interactions, the interference between the decay of the sublevels leads to the same kind of modulations as in the TD-PAC case. Figure 7.1 illustrates both methods.

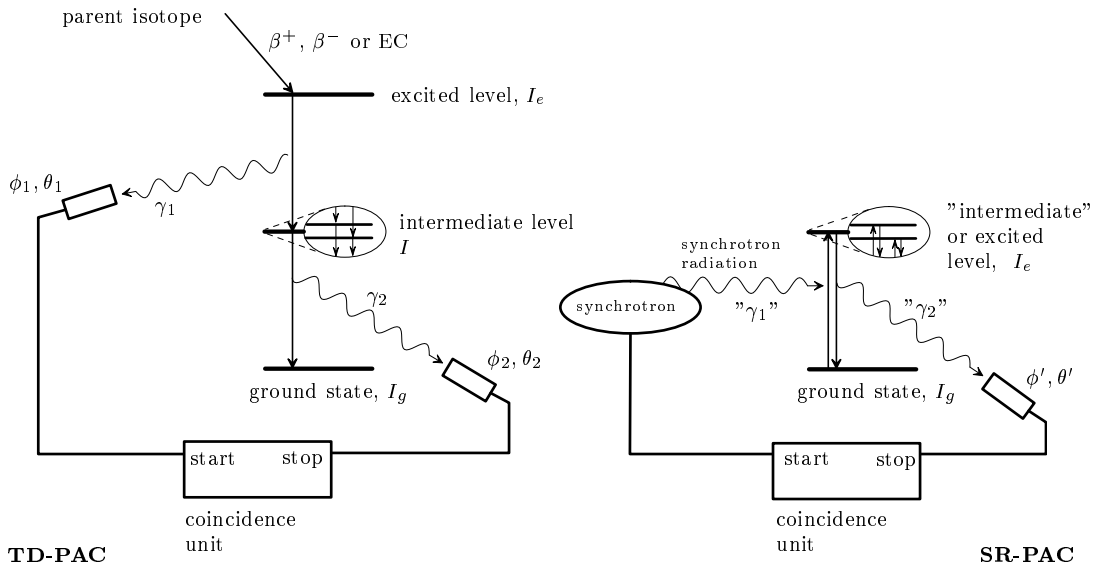


Figure 7.1: A combined picture of involved nuclear levels and detection scheme for TD-PAC (left) and SR-PAC (right).

It is important to block X-ray fluorescence radiation originating from the possible internal conversion process in the decay of the excited nuclear level. In this process, the directional information is not at all easily accessible. The decay detected only with X-ray fluorescence is solely exponential and shows no angular or time differential modulations. As the energy of the X-ray fluorescence is always lower than the nuclear level, suitable absorbers can be found in most cases.

## 7.2 Theory of synchrotron radiation based perturbed angular correlation

We will limit our theoretical considerations to the case of a vanishing Lamb-Mössbauer factor. This is the case where SR-PAC is particularly valuable, as the alternative method of nuclear forward scattering can not be applied then. With a vanishing Lamb-Mössbauer factor, the time behaviour of the incoherent inelastic decay of the nuclei is not perturbed by the propagation of the delayed wavefield through the sample in the forward direction [Ber94b, Bar96], thereby insuring that the excitation of each nucleus happens at the arrival of the SR pulse only. With an appreciable Lamb-Mössbauer factor, the propagation of the delayed wavefield in the sample in the forward direction will excite nuclei in the downstream part of the sample also at much later times.

### 7.2.1 Differential angular probability of scattering

The basic principle of perturbed angular correlation measurements is the fact, that particles with an oriented spin emit radiation with an angular distribution or anisotropy. The orientation of the spins can be achieved by detecting the radiation of the first step in a  $\gamma$ - $\gamma$  cascade (TD-PAC). Due to angular momentum conservation, the remaining sub-ensemble remains aligned or anisotropic, as the first detected  $\gamma$ -ray itself has a certain angular momentum. Alternatively, the orientation of the spins can be achieved after the excitation of a level with SR from a defined

direction (SR-PAC). In both cases, the hyperfine interactions can change the spin orientation and affect thereby the emission pattern as well. A comprehensive treatment of perturbed angular correlations can be found in [Fra68, Ste75]. Here, the special case of SR-PAC with a Mössbauer isotope showing a M1 transition, like the  $^{61}\text{Ni}$  isotope, in the presence of an external magnetic field  $\vec{B}_{ext}$  will be treated. The presence of  $\vec{B}_{ext}$  is valuable, as it selects a subset of possible nuclear transitions between the ground state and the excited state, if the direction of  $\vec{B}_{ext}$  with respect to the incoming synchrotron radiation is properly chosen. This simplifies the modulations on the exponential decay.

If a randomly orientated system of spins decays or the detector can cover the full solid angle of  $4\pi$ , the decay will follow a simple exponential:

$$I(t) = I_o e^{-\frac{t}{\tau_o}} \quad (7.1)$$

However, if the decay originates from an aligned set of spins and the detection does not cover the full solid angle, a more detailed analysis including the angular emission probability  $W$  has to be considered:

$$I(t) = I_o e^{-\frac{t}{\tau_o}} \cdot \int_{\Delta\Omega} \frac{dW(\vec{k}_1, \vec{\sigma}_1, \vec{k}_2, \vec{\sigma}_2, t)}{d\Omega} d\Omega \quad (7.2)$$

In the last equation 7.2, the function  $W(\vec{k}_1, \vec{\sigma}_1, \vec{k}_2, \vec{\sigma}_2, t)$  depends on the direction and polarisation of the two involved photons. The most general expression for the differential angular emission probability  $dW$  for a  $\gamma$ - $\gamma$ -cascade and a TD-PAC measurement is [Ste75]:

$$dW(\vec{k}_1, \vec{\sigma}_1, \vec{k}_2, \vec{\sigma}_2, t) = \frac{d\Omega_1 d\Omega_2}{16\pi^2} \sum_{\substack{\lambda, \hat{\lambda} \\ q, q', \hat{q}, \hat{q}'}} B_{\lambda, q'}^* \cdot D_{q'q}^{(\lambda)}(\mathbf{s}_1 \rightarrow \mathbf{s}_{hf}) \cdot G_{\lambda\hat{\lambda}}^{qq'}(t) \cdot D_{\hat{q}'\hat{q}}^{(\hat{\lambda})}(\mathbf{s}_{hf} \rightarrow \mathbf{s}_2) \cdot A_{\hat{\lambda}, \hat{q}'} \quad (7.3)$$

$B_{\lambda, q'}^*$  is an angular distribution coefficient that concerns the decay of the excited to the intermediate level in TD-PAC, or alternatively the excitation of the only excited level in SR-PAC. It depends on the polarisation of the involved radiation and the kind of the transition. It is most conveniently expressed in a co-ordinate system  $\mathbf{S}_1$  (or  $\mathbf{S}_{in}$  with SR-PAC) reflecting properties of the incoming radiation, e.g.  $\vec{k}_1 \parallel \vec{z}$ .

$D_{q'q}^{(\lambda)}(\mathbf{s}_1 \rightarrow \mathbf{s}_{hf})$  is a rotation matrix as introduced by Wigner that changes from the co-ordinate system  $\mathbf{S}_1$ , or  $\mathbf{S}_{in}$ , to a co-ordinate system  $\mathbf{S}_{hf}$  which reflects the direction or symmetry of the hyperfine interactions acting on the nucleus.

$G_{\lambda\hat{\lambda}}^{qq'}(t)$  describes the evolution of the excited state under the influence of the hyperfine interactions, e.g. its precession in a magnetic field. It can be treated as a rotation matrix

$D_{\hat{q}'\hat{q}}^{(\hat{\lambda})}(\mathbf{s}_{hf} \rightarrow \mathbf{s}_2)$  is again a co-ordinate transformation allowing to use the co-ordinate system  $\mathbf{S}_2$ , or  $\mathbf{S}_{out}$ , adapted to describe the outgoing photon.

$A_{\hat{\lambda}, \hat{q}'}$  describes the transition from the excited state to the ground state, similar to the angular distribution coefficient  $B_{\lambda, q'}^*$ .

The sum in equation 7.3 runs over the indices  $\lambda$  and  $\hat{\lambda}$  from 0, 1, 2, ... and over the indices  $q$  from  $-\lambda$  to  $\lambda$  and similar for  $q', \hat{q}, \hat{q}'$ .

Equation 7.3 can be reduced to concern only SR-PAC, following [Ser05]. In particular, the incoming radiation is linearly polarised in the plane of the storage ring, i.e. the  $\sigma$ -polarisation. The detector is not sensitive to the polarisation of the scattered radiation. Further, one can limit the treatment to M1 transitions, like is the case for  $^{61}\text{Ni}$ ,  $^{57}\text{Fe}$  and many other isotopes. Any admixture of E2 components is excluded. The incoming SR is very collimated and  $\frac{d\Omega_{in}}{4\pi} = 1$ . These assumptions lead to  $L = 1$  and certain restrictions in the indices of the sum:

$$dW(\vec{k}_{out}, t) = \frac{d\Omega_{out}}{4\pi} \sum_{\substack{\lambda, \hat{\lambda}=0,2 \\ q'=0, \pm 2 \\ q, \hat{q}}} B_{\lambda, q'}^* \cdot D_{q'q}^{(\lambda)}(\mathbf{s}_{in} \rightarrow \mathbf{s}_{hf}) \cdot G_{\lambda\hat{\lambda}}^{qq'}(t) \cdot D_{\hat{q}'0}^{(\hat{\lambda})}(\mathbf{s}_{hf} \rightarrow \mathbf{s}_{out}) \cdot A_{\hat{\lambda}} \quad (7.4)$$

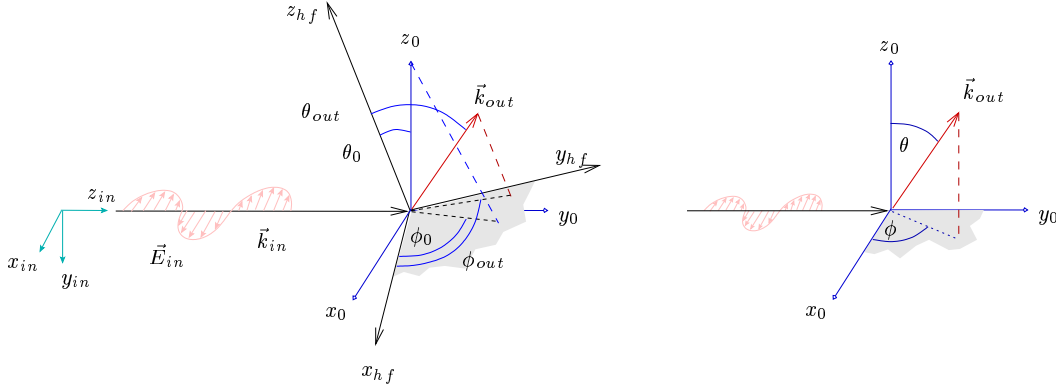


Figure 7.2: The angles and co-ordinate systems used to present the SR-PAC theory.

The transition amplitudes  $B_{\lambda,q'}$  and  $A_{\hat{\lambda}} \equiv A_{\hat{\lambda},q'=0}$  are given by [Ser05]

$$B_{\lambda 0}^* = A_{\lambda} \quad (7.5)$$

$$B_{\lambda \pm 2}^* = \frac{1}{4} \sqrt{\frac{(\lambda+2)!}{(\lambda-2)!}} A_{\lambda} \quad (7.6)$$

$$A_{\lambda} = (-1)^{I_g + I_e - 1} (2L + 1) \sqrt{(2\lambda + 1)(2I_e + 1)} \begin{pmatrix} L & L & \lambda \\ 1 & -1 & 0 \end{pmatrix} \begin{Bmatrix} L & L & \lambda \\ I_e - I_e & I_g \end{Bmatrix} \quad (7.7)$$

where Wigner 3j-symbols and 6j-symbols are employed, see [Var88] for example.

The summation over  $q'$  can be executed, using a co-ordinate transformation for  $D_{q'q}^{(\lambda)}(\mathbf{s}_{in} \rightarrow \mathbf{s}_{hf})$  that is split into two rotations [Ser05]. The first transformation rotates into a co-ordinate system with the  $z$ -axis vertical. The second one rotates from this new intermediate co-ordinate system to the co-ordinate system of the hyperfine interaction  $\mathbf{s}_{hf}$ . Then, the summation over  $q'$  simplifies to:

$$\sum_{q'} B_{\lambda q'}^* \cdot D_{q'q}^{(\lambda)}(\mathbf{s}_{in} \rightarrow \mathbf{s}_{hf}) = p_{\lambda} A_{\lambda} \cdot D_{0q}^{(\lambda)}(\mathbf{s}_0 \rightarrow \mathbf{s}_{hf}) \quad (7.8)$$

where  $p_{\lambda} = 1$  and  $-2$  for  $\lambda = 0$  and  $2$ , respectively. This leads to:

$$dW(\vec{k}_{out}, t) = \frac{d\Omega_{out}}{4\pi} \sum_{\substack{\lambda, \hat{\lambda}=0,2 \\ q, \hat{q}}} p_{\lambda} A_{\lambda} A_{\hat{\lambda}} \cdot G_{\lambda \hat{\lambda}}^{q \hat{q}}(t) \cdot D_{0q}^{(\lambda)}(\mathbf{s}_0 \rightarrow \mathbf{s}_{hf}) \cdot D_{\hat{q}0}^{(\hat{\lambda})}(\mathbf{s}_{hf} \rightarrow \mathbf{s}_{out}) \quad (7.9)$$

The factors  $G_{\lambda \hat{\lambda}}^{q \hat{q}}(t)$  which describe the hyperfine interactions are diagonal in their indices for many experimental conditions. This is true in particular for magnetic dipole and axially symmetric electric quadrupole interactions [Ste75] and even for powder samples regardless of axial symmetry [But96]. Using this restriction, one obtains

$$dW(\vec{k}_{out}, t) = \frac{d\Omega_{out}}{4\pi} \sum_{\lambda=0,2} p_{\lambda} A_{\lambda} A_{\lambda} \sum_{q=-\lambda}^{\lambda} G_{\lambda \lambda}^{qq}(t) \cdot D_{0q}^{(\lambda)}(\mathbf{s}_0 \rightarrow \mathbf{s}_{hf}) \cdot D_{q0}^{(\lambda)}(\mathbf{s}_{hf} \rightarrow \mathbf{s}_{out}) \quad (7.10)$$

We introduce the anisotropy coefficient  $A_{\lambda \lambda} \equiv A_{\lambda} A_{\lambda}$  and can execute the first sum easily:

$$dW(\vec{k}_{out}, t) = \frac{d\Omega_{out}}{4\pi} \left[ 1 - 2A_{22} \sum_{q=-2}^2 G_{22}^{qq}(t) \cdot D_{0q}^{(2)}(\mathbf{s}_0 \rightarrow \mathbf{s}_{hf}) \cdot D_{q0}^{(2)}(\mathbf{s}_{hf} \rightarrow \mathbf{s}_{out}) \right] \quad (7.11)$$

where the fact was used that  $A_{00} = 1$ ,  $G_{00}^{00}(t) = G_{00}(t) = 1$  and that  $D_{00}^{(\lambda)}(\alpha, \beta, \gamma) = P_\lambda(\cos \beta)$  and thus  $D_{00}^{(0)}(\mathbf{s}_0 \rightarrow \mathbf{s}_{hf}) D_{00}^{(0)}(\mathbf{s}_{hf} \rightarrow \mathbf{s}_{out}) = 1$ .  $P_\lambda(x)$  are the Legendre polynomials. To evaluate equation 7.11 further, more details have to be known about the hyperfine interaction. The two cases of isotropic hyperfine interactions and of an external magnetic field will be treated separately.

### 7.2.2 Isotropic hyperfine interactions

It can be shown [Win83], that in the case of isotropic hyperfine interactions (electric or magnetic) and averaging over all intermediate co-ordinate systems, equation 7.11 further reduces to

$$dW(\vec{k}_{out}, t) = \frac{d\Omega_{out}}{4\pi} [1 - 2A_{22} G_{22}(t) P_2(\cos \theta)] \quad (7.12)$$

where  $\theta$  is the angle between the incoming SR and the detector direction. The Legendre polynomial is  $P_2(\cos \theta) = \frac{1}{4}(1 + 3 \cos 2\theta)$ . For axially symmetric hyperfine interactions,  $G_{kk}(t)$  is given by [But96]

$$G_{kk}(t) = \frac{1}{2k+1} + \sum_{m \neq m'} \begin{pmatrix} I_e & I_e & k \\ m' & -m & m-m' \end{pmatrix} \cos \frac{(E_m - E_{m'}) t}{\hbar} \quad (7.13)$$

As transitions with  $\Delta m = 0, \pm 1$  are allowed, this leads to two different possible frequencies in equation 7.12; see figure 2.8. As the lifetime of  $^{61}\text{Ni}$  is quite short as compared to the frequencies appearing in equation 7.13, this interplay of two different frequencies is not very convenient.

However, investigations of relaxation effects in glasses that show only electric quadrupole interactions can be studied with great success using this approach and  $^{57}\text{Fe}$  as the nuclear probe [Ser03, Ser04, Ser05]. The influence of relaxation modifies the functions  $G_{kk}$ .

### 7.2.3 External magnetic field $\vec{B}_{ext}$

In applying an external field perpendicular to the wavevector  $\vec{k}_{in}$  of the incident SR, transitions with  $\Delta m = 0$  are not allowed. Unfortunately, the case of isotropic hyperfine interactions of the preceding chapter 7.2.2 can not be applied.

The perturbation factors for a static magnetic hyperfine interaction which is axially symmetric around the direction of an external magnetic field is given by [Ste75] as:

$$G_{\lambda\lambda}^{qq}(t) = e^{-iq\omega_B t} \equiv D_{qq}^{(\lambda)}(q\omega_B t, 0, 0) \quad (7.14)$$

Thereby, the direction of the external field defines the z-axis of the co-ordinate system  $\mathbf{S}_{hf}$ . The Larmor frequency  $\omega_B$  is given by  $\omega_B = -\frac{q\mu_N}{\hbar} B_{hf}$ , if  $B_{ext} \ll B_{hf}$ . In equation 7.11, this leads to the following sum over  $q$  [Ste75]:

$$\sum_{q=-2}^2 D_{0q}^{(2)}(\mathbf{s}_0 \rightarrow \mathbf{s}_{hf}) D_{qq}^{(2)}(q\omega_B t, 0, 0) D_{q0}^{(2)}(\mathbf{s}_{hf} \rightarrow \mathbf{s}_{out}) = D_{00}^{(2)}(\mathbf{s}_0 \rightarrow \mathbf{s}(-\omega_B t) \rightarrow \mathbf{s}_{out}) = P_2(\cos \eta(t)) \quad (7.15)$$

where  $\cos \eta(t)$  is given by:

$$\cos \eta(t) = \cos \theta_0 \cos \theta_{out} + \sin \theta_0 \sin \theta_{out} \cdot \cos(\phi_{out} - \phi_0 - \omega_B t) \quad (7.16)$$

The result of equation 7.15 together with equation 7.11 leads to:

$$dW(\vec{k}_{out}, t) = \frac{d\Omega_{out}}{4\pi} [1 - 2A_{22} \cdot P_2(\cos \eta(t))] \quad (7.17)$$

### 7.2.4 Special orientations of the external magnetic field $\vec{B}_{ext}$

If the magnetic field is parallel to the vertical axis  $z_0$  or parallel to  $\vec{k}_{out}$ , then either  $\theta_0 = 0$  or  $\theta_{out} = 0$  and the second term containing the sine-functions is zero. Thus, no time dependence remains and  $\cos \eta(t) = \cos \theta$ , with  $\theta$  being the angle between the vertical  $z_0$ -axis and  $\vec{k}_{out}$ . This arrangement is depicted in on the right side of figure 7.3. It is not suited to measure the magnetic hyperfine field  $B_{hf}$ . The measured intensity is given via

$$dW(\vec{k}_{out}, t) = \frac{d\Omega_{out}}{4\pi} [1 - 2A_{22} \cdot \frac{1}{4}(1 + 3 \cos \theta)] = \text{const.} \quad (7.18)$$

and accordingly

$$I(t) = I_0 e^{-\frac{t}{\tau_0}} \cdot \text{const.} \quad (7.19)$$

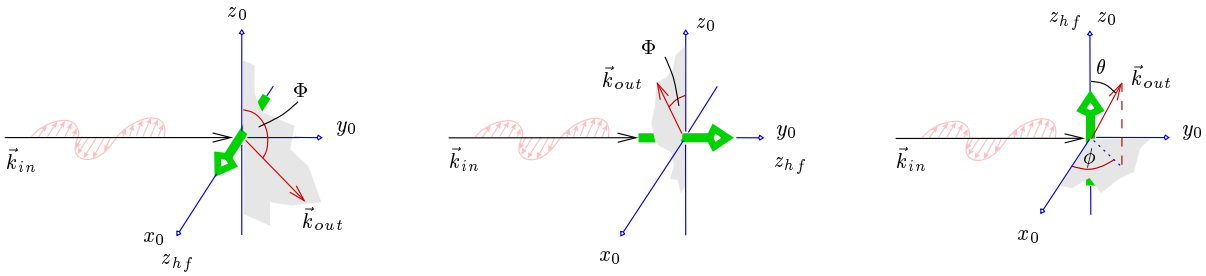


Figure 7.3: The experimental arrangement when applying an external field. To the left and in the middle,  $\vec{B}_{ext} \perp z_0$  and  $\vec{B}_{ext} \perp \vec{k}_{out}$ . To the right,  $\vec{B}_{ext} \parallel z_0$ .

If the magnetic field  $\vec{B}_{ext}$  is set perpendicular to the vertical axis  $z_0$  and perpendicular to  $\vec{k}_{out}$ , then  $\theta_0 = \theta_{out} = 90^\circ$  and  $\eta(t)$  simplifies to

$$\eta(t) = \phi_{out} - \phi_0 - \omega_B t = \Phi - \omega_B t \quad (7.20)$$

where  $\Phi$  is the angle between  $z_0$  and  $\vec{k}_{out}$ . This situation is depicted on the left side and in the middle of figure 7.3. The Legendre polynomial with this conditions can be calculated to be

$$P_2(\cos \eta(t)) = \frac{1}{4}(1 + 3 \cos(2\Phi - 2\omega_B t)) \quad (7.21)$$

and

$$dW(\vec{k}_{out}, t) = \frac{d\Omega_{out}}{4\pi} [1 - 2A_{22} \cdot \frac{1}{4}(1 + 3 \cos(2\Phi - 2\omega_B t))] \quad (7.22)$$

If the detector size is sufficiently small, we can consider  $dW$  to be constant over the spatial range of the detector and the integral in equation 7.2 can be evaluated immediately.

$$I(t) = I_0 e^{-\frac{t}{\tau_0}} \cdot \frac{\Delta\Omega_{out}}{4\pi} [1 - 2A_{22} \cdot \frac{1}{4}(1 + 3 \cos(2\Phi - 2\omega_B t))] \quad (7.23)$$

This equation can be rewritten as

$$I(t) \propto e^{-\frac{t}{\tau_0}} [1 - K \cos(2\Phi - 2\omega_B t)] \quad (7.24)$$

with  $K = \frac{3A_{22}}{2-A_{22}}$  being the experimentally observable contrast. The last equation is exact only for an infinitesimal small detector.

In fact, an optimum distance and size for the detector has to be found to maximise countrate without loosing the contrast of the modulations. The modulations average to zero, if the whole solid angle of  $4\pi$  is detected.

## 7.3 Measurements

For  $^{61}\text{Ni}$ , the transition takes place between a ground state of angular momentum  $I_g = \frac{3}{2}$  and the excited state with  $I_e = \frac{5}{2}$ . The resulting anisotropy coefficient is  $A_{22} = \frac{7}{50} = 0.14$ . Equation 7.24 reduces thus to

$$I(t) \propto e^{-\frac{t}{\tau_0}} \left[ 1 - \frac{7}{31} \cos(2\Phi - 2\omega_B t) \right] \quad (7.25)$$

To verify this behaviour and to obtain an alternative measure for the magnetic hyperfine field of  $^{61}\text{Ni}$ , different experimental arrangements have been realised, using the ID18 beamline at the ESRF in 16-bunch mode.

A 20 times fold 85 % enriched  $^{61}\text{Ni}$ -foil of  $20 \mu\text{m}$  thickness was irradiated at an incidence angle of around  $10^\circ$ . Its temperature was 300 K. The Lamb-Mössbauer factor of  $^{61}\text{Ni}$  at this temperature using the Debye model and a Debye temperature of  $\Theta_D = 390 \text{ K}$  is  $f_{\text{LM}} = 0.003$ , see chapter 2.1.2. NFS is completely negligible in this case and will not perturb the time evolution of the decay. At elevated temperatures like room temperature, SR-PAC is thus the only nuclear resonant scattering method that can be applied for  $^{61}\text{Ni}$ .

The monochromatisation of the SR was performed using the high heat load monochromator in the Si (333) reflection. A copper sheet of 1 mm thickness blocked the radiation transmitted via the Si (111) reflection of the high heat load monochromator, for details see chapter 6.3 and figure 6.2. A standard  $10 \times 10 \text{ mm}^2$  large APD detector was used together with fast timing electronics that prevented counting during the first 7 ns after the prompt signal. The detector was placed at a distance of approximately 15 mm from the sample as a compromise between a reduction of solid angle and a high countrate. A sheet of 1 mm aluminium protected the detector from X-ray fluorescence radiation consisting of the 7.5 keV and 8.3 keV  $K_\alpha$  and  $K_\beta$  electronic emission lines of  $^{61}\text{Ni}$ . This X-ray fluorescence radiation follows the decay of the excited nuclear level if the decay channel of electronic conversion is taken, i.e. a K-level electron is ejected. The probability for this process is  $\frac{\alpha}{1+\alpha} = 0.12$ . Thus, 88 % of the excited  $^{61}\text{Ni}$  nuclei emit 67.41 keV photons. However, see figure 4.22, the detector efficiency at 8 keV ( $\approx 77\%$ ) is much higher than at 67.41 keV ( $\approx 1\%$ ) and the detection of the X-ray fluorescence radiation would reduce significantly the observed contrast. The aluminium sheet transmits only  $1.7 \cdot 10^{-4} \%$  of photons having the energy of 8 keV and 94 % of photons at 67.41 keV.

The results for three different geometric arrangements are shown in figure 7.4. The left column shows the total counts as a function of time, the right column shows the part  $\cos(2\Phi - \omega_B t)$  describing the modulation. In the top timespectrum, the geometry shown in the left panel of figure 7.3 is realised with the magnetic field applied in the horizontal plane and perpendicular to the incoming beam. Under this condition,  $\Delta m = 0$  transitions can not be excited. Only one frequency is measured in the time evolution of the spectrum. In the middle timespectrum, the setup shown in the middle panel of figure 7.3 is realised with the magnetic field parallel to  $\vec{k}_{in}$  and the detector in the plane perpendicular to the magnetic field at the sample. Transitions with  $\Delta m = 0$  do not emit radiation into this plane with this external magnetic field. Again, one frequency is visible in the time spectrum. In the bottom timespectrum, the external magnetic field was applied vertically as seen on the right side of figure 7.3. In accordance with equation 7.19, no modulations on top of the exponential decay are visible in this case.

The typical counting time per spectrum was about three hours. In each spectrum, 30 MCA channels have been added, leading to one data point per 3 seconds. The bottom time spectrum of figure 7.4 was fitted to an exponential decay plus a background and without the oscillatory term. The other spectra have then be fitted with the function  $I(t) = e^{-\frac{t}{\tau}} (1 - K \cos(2\Phi - 2\omega_B t)) + c$  with  $\tau$ ,  $K$ ,  $\Phi$ ,  $\omega_B$  and  $c$  as free parameters. The fits covered the time range from 15 to 160 ns.

The results for the contrast ranged between  $K = 0.121$  and  $K = 0.129$ , significantly lower

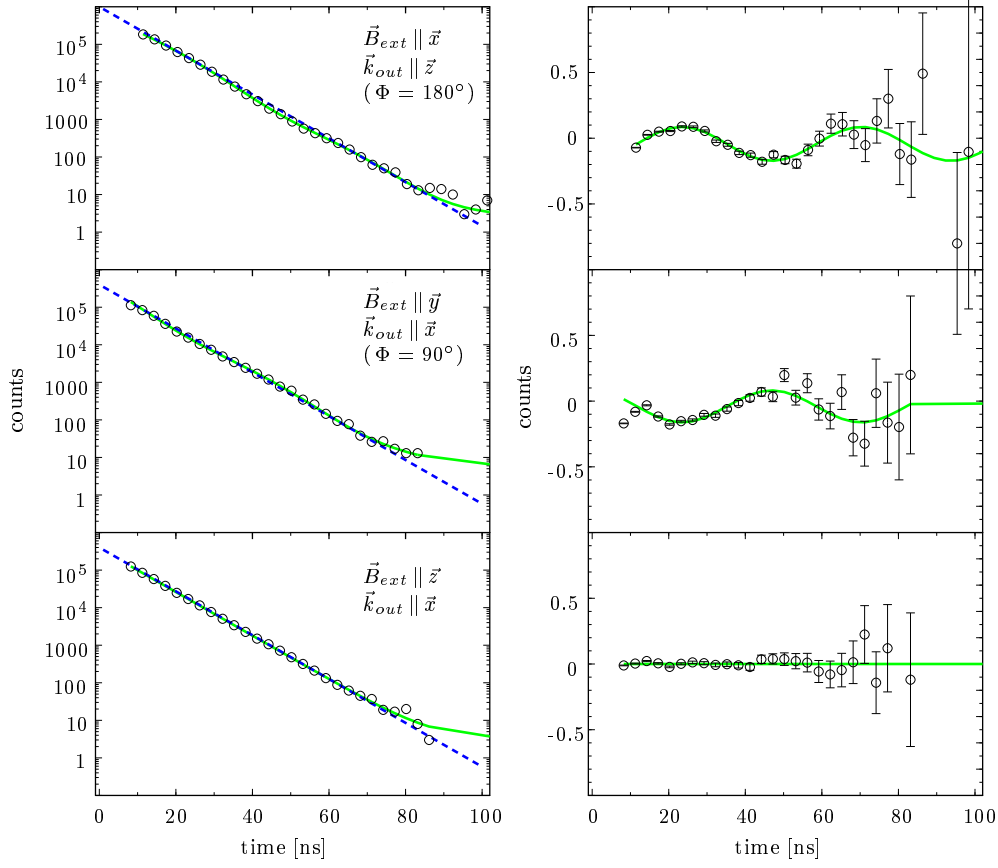


Figure 7.4: SR-PAC measurements with  $^{61}\text{Ni}$  and an external magnetic field applied in various directions. The detector is placed perpendicular to both the incoming beam and the magnetic field.

as the optimum case of  $K = \frac{7}{31} = 0.226$ . This is understandable, as the finite detector size,  $10 \times 10 \text{ mm}^2$ , together with the rather small distance to the sample, 15 mm, causes an averaging over several angles. The results for  $\tau$  have been in perfect agreement with the value 7.4(1) ns as obtained in chapter 6.3.

The external magnetic field has been only a small alignment field of some tens of mT. We can neglect it in the calculation of  $\omega_B$ . The obtained fit parameters for  $\omega_B$  ranged between 65 and 67 MHz with the average value being  $\omega_B = 66(1) \text{ MHz}$ . The period of the cosine modulation as seen in the timespectra is related to  $\omega_B$  via  $T_{exp} = 2\pi/\omega_{exp} = \pi/\omega_B = 47.6 \text{ ns}$ . The relation between the Larmor-frequency measured with SR-PAC and the magnetic hyperfine field is given by

$$B_{hf} = \frac{\hbar \omega_B}{g_e \mu_N} = \frac{\hbar \omega_B I_e}{\mu_e} \quad \text{with} \quad g_e = \frac{\mu_e}{\mu_N I_e} \quad (7.26)$$

The values for the nuclear parameters can be found in table 3.1. One obtains  $B_{hf} = 7.18(11) \text{ T}$ . This result is in fair agreement with the value of  $B_{hf} = 6.87(2) \text{ T}$  obtained at room temperature as the average of two solid state NMR measurements [Str63, Rie77]. When comparing the frequencies as measured by NMR with those obtained with SR-PAC, one has to be careful that NMR measurements reveal the splitting of the ground state, and SR-PAC measurements the splitting of the excited state. Evidently, the Landé  $g$ -factor is different for the excited and the ground state.

In figure 7.5, different angles  $\Phi$  have been arranged with the experimental setup as shown on



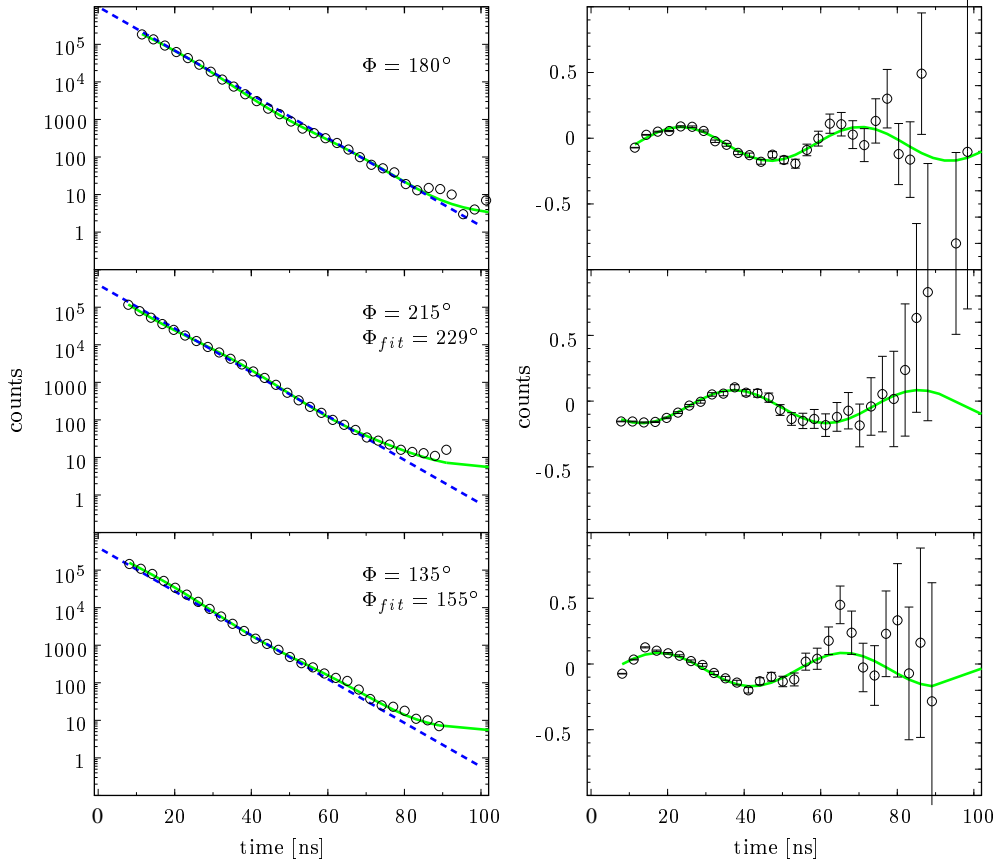


Figure 7.5: SR-PAC measurements with  $^{61}\text{Ni}$  and an external magnetic field in the horizontal direction perpendicular to  $\vec{k}_{in}$ . The detector is in the plane spanned by  $\vec{k}_{in}$  and the vertical axis, see figure 7.3. Equation 7.25 applies.

the left of figure 7.3, i.e. in all cases, the magnetic field was in the horizontal plane perpendicular to the incoming SR. The detector was in the plane perpendicular to the magnetic field. In the top timespectrum, the detector was below the sample, i.e.  $\Phi = 180^\circ$ . The other two time spectra have been measured at the same time with two detectors forming a  $90^\circ$  angle. Thereby, one detector was placed at  $\Phi = 180^\circ - 45^\circ = 135^\circ$  below the vertical axis, the other one at  $\Phi = 180^\circ + 45^\circ = 215^\circ$ . The spectra could be fitted with  $\Phi_{fit} = 155^\circ$  and  $\Phi_{fit} = 229^\circ$ . As the difference is only  $74^\circ$ , probably the whole detector set was placed too far below the sample. Also, it seems to be shifted to higher angles. These alignment problems can explain the small deviations of  $\Phi_{fit}$ .

## 7.4 Discussion

The results presented in figures 7.4 and 7.5 are clearly in accord with the formulas of SR-PAC for magnetically ordered samples presented in chapter 7.2. The magnetic hyperfine field of  $^{61}\text{Ni}$  could be measured with this method at room temperature, where the Lamb-Mössbauer factor is vanishing and nuclear forward scattering is not feasible.

However, the magnetic hyperfine fields  $B_{hf}$  as obtained with the NLE at 180 K and with the method of SR-PAC at 300 K differ by more than the temperature dependence of spontaneous magnetisation or hyperfine splitting predict, and the SR-PAC value at 300 K is even larger than

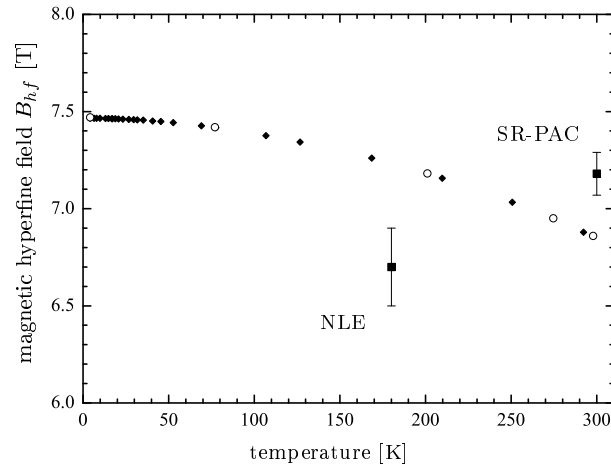


Figure 7.6: Comparison of NLE and SR-PAC data with literature values. Black diamonds [Rie77] and open circles [Str63] are NMR measurements.

the NLE value at 115 K, contrary to common sense. A comparison of the results presented here obtained with the NLE and with SR-PAC together with literature values is given in figure 7.6.

The fact that one measurement (SR-PAC) lies above and the other measurement (NLE) below the line of literature values following the typical temperature variation given by equation 3.2 could indicate remaining problems with the precision of the measurements presented here. In both cases, SR-PAC and NLE, the sample was build from the same foil, so impurities or stress effects would likely act similar at both temperatures, having both our data above or below the curve given by [Str63] and [Rie77]. If however the literature values of the nuclear magnetic moments  $\mu_g$  of the ground state and  $\mu_e$  of the excited state are slightly wrong, this will change the different obtained values, too. The NMR values lead to the magnetic hyperfine field using  $B_{hf} = \hbar \omega_B I_e / \mu_g$  and require knowledge of  $\mu_g$ . The SR-PAC measurements lead to a value for the magnetic hyperfine field via  $B_{hf} = \hbar \omega_B I_e / \mu_e$  and require knowledge of  $\mu_e$ . The adopted literature values are  $\mu_g = -0.75002(4) \mu_N$  [Fir96, Bha99] and  $\mu_e = 0.480(6) \mu_N$  [Fir96], based on Mössbauer effect measurements [Lov71, Gör71]. In the analysis of the NLE time-spectrum, both values intervene. An increase of  $\mu_e$  to  $\mu'_e = 0.503 \mu_N$  would achieve coincidence between the SR-PAC measurements presented here and the NMR values. However, this is outside the error of the Mössbauer effect measurements by [Lov71] and [Gör71]. Furthermore, this value for  $\mu_e$  used in the fit of the NLE times spectrum shown in figure 6.7 would decrease the obtained value for the magnetic hyperfine field instead of raising it. Thus,  $\mu_g$  would need to take the value of  $-0.64 \mu_N$ , definitely wrong and affecting the NMR result, loosing the desired coincidence between the SR-PAC and NMR results. To assume an error in  $\mu_e$  or  $\mu_g$  is thus not helpful.

Nevertheless, the discrepancies between the literature value of  $B_{hf}$  and the results presented here are still small, i.e. less than 10%.

## Chapter 8

# Nuclear resonant scattering with high energy Mössbauer transitions

### 8.1 Experimental milestones

So far, a variety of Mössbauer isotopes has been addressed with synchrotron radiation. Table 8.1 summarises them together with the used method.

nuclei	$E_0$ [eV]	$\tau$ [ns]	NFS	NBS	NLE	N-Fluo	NIS	SR-PAC
<sup>181</sup> Ta	6214	6800	[Chu95]					
<sup>169</sup> Tm	8410	5.8		[Stu91]				
<sup>83</sup> Kr	9403	212	[Joh95]			[Bar95]	[Zha02]	
<sup>57</sup> Fe	14413	141.1	[Has91]	[Ger85]	[Röh00c]	[Ber94a]	[Set95, Stu95]	[Bar96, Ser04]
<sup>151</sup> Eu	21541	14.0	[Leu96]			[Koy96]	[Leu97, Bar04a]	
<sup>149</sup> Sm	22496	10.7	[Bar04b]		[Röh01c]	[Kit00]		
<sup>119</sup> Sn	23880	25.7	[Alp93]		[Röh01d]	[Kik94]	[Chu98b]	
<sup>161</sup> Dy	25651	42.0	[Shv01]			[Koy96]	[Chu01, Shv01]	
<sup>129</sup> I	27750	23.1	[Kit03]			[Kit03]		
<sup>40</sup> K	29834	5.9	[Set02]			[Set00]	[Set02]	
<sup>121</sup> Sb	37147	5.0	[Wil04b]			[Kit00]		
<sup>127</sup> I	57610	2.8				[Yod02]		
<sup>61</sup> Ni	67415	7.4			this thesis	[Wil02]		this thesis
<sup>197</sup> Au	77351	2.7				[Kis00]		

Table 8.1: NFS = nuclear forward scattering. NBS = nuclear Bragg scattering. NLE = nuclear lighthouse effect. “N-Fluo” stands for nuclear fluorescence and means the detection of the inelastic, incoherent decay channel without pushing the setup to observe the phonon density of states or hyperfine interactions via SR-PAC. NIS stands for nuclear inelastic scattering and means in particular energy resolved measurements of the density of phonon states. SR-PAC = synchrotron radiation based perturbed angular correlation

### 8.2 Overview of Mössbauer isotopes

The following figure 8.1 displays the family of Mössbauer isotopes with transition energies between 5 and 95 keV and half-lives between 1 ns and 10  $\mu$ s. Small grey circles represent the isotopes examined with the standard Mössbauer effect. Empty large circles are isotopes that have been excited with synchrotron radiation and the nuclear fluorescence was detected. Full large circles are isotopes investigated further with synchrotron radiation, e.g. NBS, NFS, NLE, NIS and SR-PAC. Radioactive isotopes are marked by a star or an empty circle.

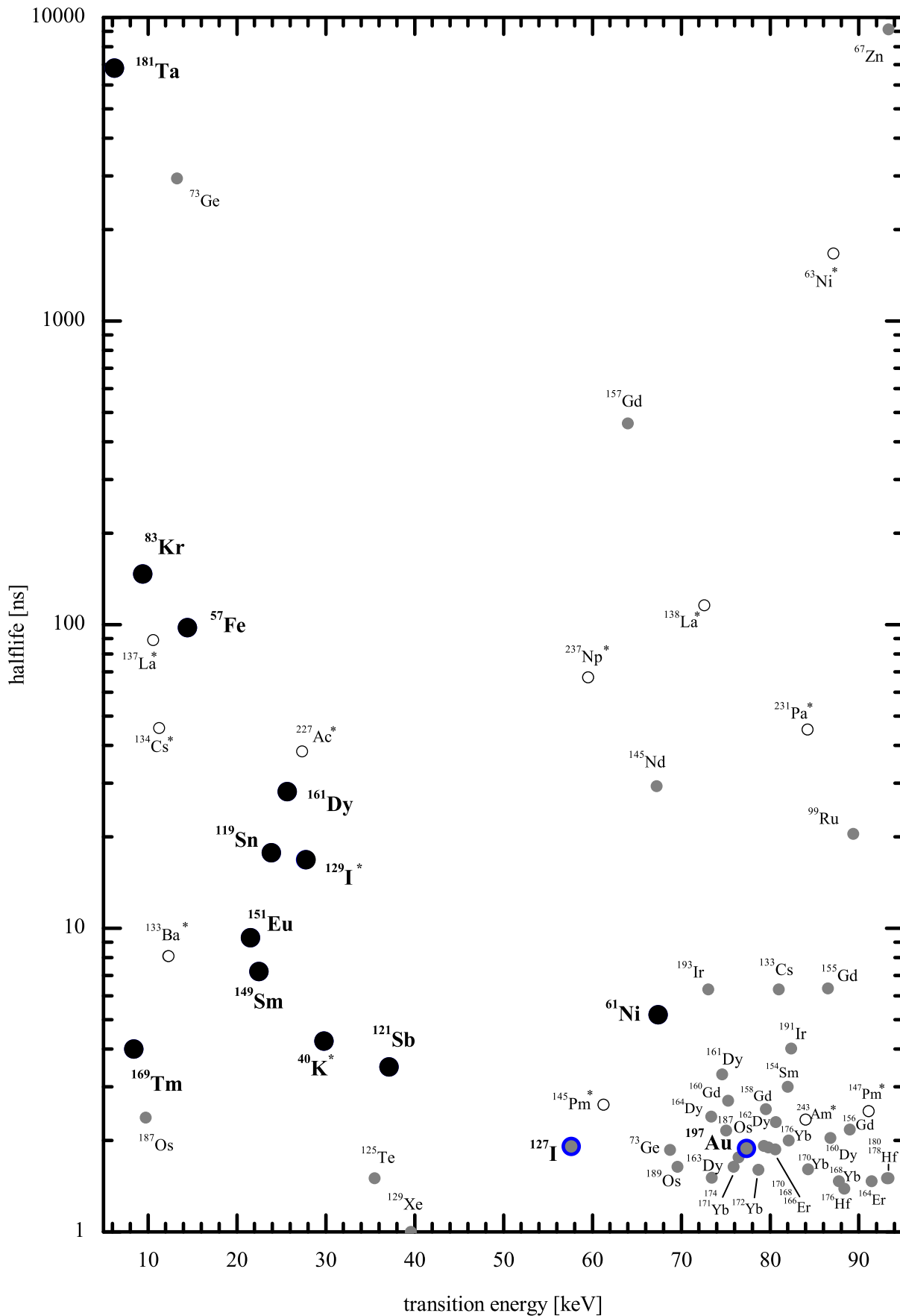


Figure 8.1: Mössbauer isotopes having a transition energy between 5 and 95 keV and half-lives between 1 ns and 10  $\mu\text{s}$ . Radioactive isotopes have a half-life above one year.

nuclei	$E_0$ [keV]	$\tau$ [ns]	$\beta_{nat}$ [%]	$\alpha$	$I_g$	$I_e$	$\sigma_0$ [ $10^{-24}\text{m}^2$ ]	$\Theta_D$	$f_{LM}^{100\text{K}}$	$\Phi_{\Gamma}^{\text{ID18}}$ [ $\text{s}^{-1}$ ]	$I^{\text{N-Fluo}}$ [ $\text{s}^{-1}$ ]	$I^{\text{SR-PAC}}$ [ $\text{s}^{-1}$ ]	$\hat{I}_{100\text{K}}^{\text{NLE}}$ [ $10^{-48}\text{m}^4\text{s}^{-1}$ ]
<sup>57</sup> Fe	14.413	141.5	2.2	8.2	$\frac{1}{2}$	$\frac{3}{2}$	256.0	420	0.896	$1.08 \cdot 10^5$	$1.0 \cdot 10^5$	2823.	$5.47 \cdot 10^9$
<sup>169</sup> Tm	8.410	5.9	100.	268.	$\frac{1}{2}$	$\frac{3}{2}$	25.78	167	0.942	$6.23 \cdot 10^6$	$2.7 \cdot 10^6$	2476.	$1.57 \cdot 10^9$
<sup>119</sup> Sn	23.871	25.6	8.6	5.12	$\frac{1}{2}$	$\frac{3}{2}$	140.3	170	0.513	$1.37 \cdot 10^5$	$1.1 \cdot 10^5$	4609.	$5.85 \cdot 10^8$
<sup>133</sup> Ba*	12.29	11.7	0.	110.	$\frac{1}{2}$	$\frac{3}{2}$	29.19	110	0.696	$2.17 \cdot 10^6$	$1.3 \cdot 10^6$	2980.	$5.46 \cdot 10^8$
<sup>187</sup> Os	9.75	3.4	1.6	264.	$\frac{1}{2}$	$\frac{3}{2}$	19.44	375	0.982	$3.82 \cdot 10^6$	$8.9 \cdot 10^5$	840.	$3.25 \cdot 10^8$
<sup>83</sup> Kr	9.40	212.	11.5	19.6	$\frac{9}{2}$	$\frac{7}{2}$	107.5	72	0.459	$8.78 \cdot 10^4$	$8.6 \cdot 10^4$	95.8	$2.09 \cdot 10^8$
<sup>161</sup> Dy	25.652	42.0	18.9	2.9	$\frac{5}{2}$	$\frac{5}{2}$	95.33	186	0.617	$6.30 \cdot 10^4$	$5.6 \cdot 10^4$	2624.	$1.94 \cdot 10^8$
<sup>181</sup> Ta	6.24	8728.	99.99	70.5	$\frac{7}{2}$	$\frac{9}{2}$	109.9	225	0.982	$9.51 \cdot 10^3$	$9.5 \cdot 10^3$	12.2	$1.11 \cdot 10^8$
<sup>151</sup> Eu	21.531	13.8	47.8	28.6	$\frac{5}{2}$	$\frac{7}{2}$	23.75	115	0.407	$3.65 \cdot 10^5$	$2.6 \cdot 10^5$	921.	$2.38 \cdot 10^7$
<sup>227</sup> Ac*	27.37	55.3	0.	4.5	$\frac{3}{2}$	$\frac{3}{2}$	59.39	100	0.283	$4.00 \cdot 10^4$	$3.7 \cdot 10^4$	1064.	$1.03 \cdot 10^7$
<sup>149</sup> Sm	22.496	10.4	13.8	50.	$\frac{7}{2}$	$\frac{5}{2}$	7.11	166	0.610	$4.28 \cdot 10^5$	$2.6 \cdot 10^5$	92.9	$4.95 \cdot 10^6$
<sup>121</sup> Sb	37.15	5.0	57.2	11.1	$\frac{5}{2}$	$\frac{7}{2}$	19.54	211	0.343	$1.40 \cdot 10^5$	$5.1 \cdot 10^4$	455.	$2.31 \cdot 10^6$
<sup>129</sup> I*	27.75	23.1	0.	5.1	$\frac{7}{2}$	$\frac{5}{2}$	39.07	106	0.129	$8.93 \cdot 10^4$	$7.3 \cdot 10^4$	214.	$1.85 \cdot 10^6$
<sup>137</sup> La*	10.56	128.4	0.	122.	$\frac{7}{2}$	$\frac{5}{2}$	13.35	142	0.853	$1.23 \cdot 10^4$	$1.2 \cdot 10^4$	1.73	$1.53 \cdot 10^6$
<sup>125</sup> Te	35.5	2.2	7.1	13.6	$\frac{1}{2}$	$\frac{3}{2}$	26.60	153	0.181	$4.02 \cdot 10^5$	$3.9 \cdot 10^4$	662.	$8.92 \cdot 10^5$
<sup>134</sup> Cs*	11.23	65.9	0.	90.6	4	5	25.89	33	0.0392	$3.95 \cdot 10^5$	$3.7 \cdot 10^5$	347.	$3.78 \cdot 10^5$
<sup>61</sup> Ni	67.412	7.4	1.14	0.135	$\frac{3}{2}$	$\frac{5}{2}$	71.16	400	0.0894	$6.80 \cdot 10^3$	$3.6 \cdot 10^3$	438.	$1.44 \cdot 10^5$
<sup>237</sup> Np*	59.54	96.7	0.	1.1	$\frac{5}{2}$	$\frac{5}{2}$	30.94	187	0.174	$1.01 \cdot 10^3$	963	78.6	$2.81 \cdot 10^4$
<sup>189</sup> Os	69.53	2.3	16.1	8.0	$\frac{3}{2}$	$\frac{5}{2}$	8.42	375	0.400	$1.74 \cdot 10^4$	$2.1 \cdot 10^3$	31.9	$2.33 \cdot 10^4$
<sup>73</sup> Ge	68.75	2.5	7.7	0.8	$\frac{9}{2}$	$\frac{7}{2}$	23.01	360	0.0848	$1.77 \cdot 10^4$	$2.4 \cdot 10^3$	30.9	$9.23 \cdot 10^3$
<sup>193</sup> Ir	73.04	8.8	62.7	6.5	$\frac{3}{2}$	$\frac{1}{2}$	3.06	420	0.435	$3.92 \cdot 10^3$	$2.2 \cdot 10^3$	0.	$3.92 \cdot 10^3$
<sup>187</sup> Os	75.04	3.1	1.6	14.8	$\frac{1}{2}$	$\frac{5}{2}$	3.77	375	0.341	$8.72 \cdot 10^3$	$1.8 \cdot 10^3$	14.5	$2.90 \cdot 10^3$
<sup>73</sup> Ge	13.27	4260.	7.7	1095.	$\frac{9}{2}$	$\frac{5}{2}$	0.76	360	0.912	$4.38 \cdot 10^3$	$4.4 \cdot 10^3$	0.14	$2.11 \cdot 10^3$
<sup>243</sup> Am*	84.0	3.4	0.	0.3	$\frac{5}{2}$	$\frac{5}{2}$	25.88	200	0.0497	$3.13 \cdot 10^3$	712	97.0	$1.18 \cdot 10^3$
<sup>164</sup> Dy	73.39	3.4	28.2	9.3	0	2	22.05	186	0.0207	$9.60 \cdot 10^3$	$2.3 \cdot 10^3$	78.0	469
<sup>191</sup> Ir	82.40	5.9	37.3	10.7	$\frac{3}{2}$	$\frac{1}{2}$	1.54	420	0.343	$2.25 \cdot 10^3$	961	0.	267
<sup>145</sup> Pm*	61.25	3.8	0.	6.4	$\frac{3}{2}$	$\frac{7}{2}$	11.75	160	0.0176	$2.12 \cdot 10^4$	$5.7 \cdot 10^3$	81.6	242
<sup>170</sup> Er	78.68	2.7	14.9	7.3	0	2	23.44	195	0.0182	$6.74 \cdot 10^3$	$1.1 \cdot 10^3$	46.3	197
<sup>168</sup> Er	79.80	2.7	26.8	7.1	0	2	23.72	195	0.0165	$6.47 \cdot 10^3$	$1.0 \cdot 10^3$	45.1	157
<sup>99</sup> Ru	89.36	29.6	12.8	1.5	$\frac{5}{2}$	$\frac{7}{2}$	8.12	430	0.0955	232	196	0.78	118
<sup>160</sup> Gd	75.26	3.9	21.9	7.4	0	2	25.69	176	0.00974	$6.74 \cdot 10^3$	$1.9 \cdot 10^3$	78.9	116
<sup>176</sup> Hf	88.34	2.1	5.2	5.9	0	2	22.71	227	0.0259	$3.72 \cdot 10^3$	329	17.0	114
<sup>166</sup> Er	80.57	2.6	33.6	6.9	0	2	23.86	195	0.0145	$6.20 \cdot 10^3$	924	41.7	111
<sup>231</sup> Pa*	84.22	65.1	100.	1.8	$\frac{3}{2}$	$\frac{5}{2}$	4.80	275	0.163	157	145	2.21	88.6
<sup>157</sup> Gd	63.93	664.	15.7	0.97	$\frac{3}{2}$	$\frac{5}{2}$	23.20	176	0.0331	118	117	4.24	68.8
<sup>180</sup> Hf	93.33	2.2	35.1	4.7	0	2	24.64	227	0.0185	$2.45 \cdot 10^3$	243	15.2	50.7
<sup>162</sup> Dy	80.66	3.2	25.5	6.55	0	2	24.91	186	0.00874	$5.08 \cdot 10^3$	$1.1 \cdot 10^3$	49.7	49.9
<sup>178</sup> Hf	93.18	2.1	27.3	4.6	0	2	25.17	227	0.0180	$2.50 \cdot 10^3$	240	15.3	49.2
<sup>158</sup> Gd	79.51	3.6	24.8	6.0	0	2	27.65	176	0.00536	$4.96 \cdot 10^3$	$1.3 \cdot 10^3$	64.0	27.6
<sup>161</sup> Dy	74.57	4.5	18.9	0.65	$\frac{5}{2}$	$\frac{3}{2}$	6.75	186	0.0169	$6.34 \cdot 10^3$	$2.1 \cdot 10^3$	4.78	27.4
<sup>163</sup> Dy	73.44	2.2	24.9	8.4	$\frac{5}{2}$	$\frac{7}{2}$	6.44	186	0.0201	$1.52 \cdot 10^4$	$1.5 \cdot 10^3$	17.4	25.6
<sup>160</sup> Dy	86.79	2.9	2.3	4.5	0	2	29.53	186	0.00386	$3.06 \cdot 10^3$	550	35.7	7.13
<sup>63</sup> Ni*	87.13	2409.	0.	0.99	$\frac{1}{2}$	$\frac{5}{2}$	48.40	400	0.0201	3.61	3.61	0.52	3.41
<sup>164</sup> Er	91.40	2.1	1.6	4.2	0	2	28.16	195	0.00403	$2.47 \cdot 10^3$	234	16.0	3.00
<sup>154</sup> Sm	81.99	4.4	22.7	5.05	0	2	30.08	166	0.00173	$3.19 \cdot 10^3$	$1.0 \cdot 10^3$	59.8	2.74
<sup>197</sup> Au	77.35	2.8	100.	4.3	$\frac{3}{2}$	$\frac{1}{2}$	3.86	165	0.0114	$7.49 \cdot 10^3$	$1.2 \cdot 10^5$	0.	2.36
<sup>155</sup> Gd	86.55	9.4	14.8	0.43	$\frac{3}{2}$	$\frac{5}{2}$	33.96	176	0.00182	976	573	55.5	2.19
<sup>156</sup> Gd	88.97	3.1	20.5	3.9	0	2	31.54	176	0.00132	$2.35 \cdot 10^3$	458	33.3	0.791
<sup>145</sup> Nd	67.25	42.4	8.3	6.1	$\frac{7}{2}$	$\frac{3}{2}$	3.81	157	0.00645	$1.26 \cdot 10^3$	$1.1 \cdot 10^3$	3.16	0.678
<sup>40</sup> K*	29.83	6.1	0.01	6.6	4	3	28.97	91	$4.7 \cdot 10^{-5}$	$2.84 \cdot 10^5$	$1.3 \cdot 10^3$	330.	0.230
<sup>127</sup> I	57.6	2.8	100.	3.8	$\frac{5}{2}$	$\frac{7}{2}$	20.49	106	$1.3 \cdot 10^{-4}$	$4.46 \cdot 10^4$	$7.6 \cdot 10^3$	168.	0.0527
<sup>174</sup> Yb	76.47	2.6	31.8	9.4	0	2	20.12	118	$8.6 \cdot 10^{-5}$	$8.68 \cdot 10^3$	$1.3 \cdot 10^3$	43.0	0.00374
<sup>171</sup> Yb	75.88	2.4	14.3	7.8	$\frac{1}{2}$	$\frac{5}{2}$	14.49	118	$8.5 \cdot 10^{-5}$	$1.02 \cdot 10^4$	$1.2 \cdot 10^3$	39.9	0.00185
<sup>138</sup> La*	72.57	167.4	0.09	6.41	5	3	3.99	142	$5.8 \cdot 10^{-4}$	211	204	1.17	0.00108
<sup>129</sup> Xe	39.6	1.4	26.4	12.3	$\frac{1}{2}$	$\frac{3}{2}$	23.47	64	$1.4 \cdot 10^{-5}$	$3.60 \cdot 10^5$	$1.0 \cdot 10^4$	190.	0.00101
<sup>172</sup> Yb	78.7	2.4	21.9	8.5	0	2	20.79	118	$4.4 \cdot 10^{-5}$	$8.14 \cdot 10^3$	996	37.4	$8.3 \cdot 10^{-4}$
<sup>147</sup> Pm*	91.0	3.7	0.	2.2	$\frac{7}{2}$	$\frac{5}{2}$	6.93	160	$1.5 \cdot 10^{-4}$	$1.55 \cdot 10^3$	385	2.17	$4.3 \cdot 10^{-4}$
<sup>176</sup> Yb	82.13	2.5	12.7	7.1	0	2	22.41	118	$2.3 \cdot 10^{-5}$	$5.40 \cdot 10^3$	754	33.2	$2.1 \cdot 10^{-4}$
<sup>67</sup> Zn	93.31	13200.	4.1	0.89	$\frac{5}{2}$	$\frac{1}{2}$	4.96	305	0.00157	0.401	0.40	0.	$2.4 \cdot 10^{-5}$
<sup>170</sup> Yb	84.26	2.3	3.1	8.1	0	2	18.94	118	$8.9 \cdot 10^{-6}$	$4.41 \cdot 10^3$	505	19.8	$1.4 \cdot 10^{-5}$
<sup>168</sup> Yb	87.73	2.1	0.13	5.43	0	2	24.72	118	$2.9 \cdot 10^{-6}$	$3.87 \cdot 10^3$	367	20.4	$1.8 \cdot 10^{-6}$
<sup>133</sup> Cs	81.0	9.1	100.	1.7	$\frac{7}{2}$	$\frac{5}{2}$	10.36	33	$2 \cdot 10^{-74}$	$1.72 \cdot 10^3$	989	6.59	$4 \cdot 10^{-143}$

Table 8.2: Properties and accessibility of Mössbauer isotopes shown in figure 8.1

The information of the preceding table 8.2 has to be explained: The \* character indicates a radioactive isotope having a half-life of more than one year at least. Energy  $E_0$ , lifetime  $\tau$  of the excited state, natural abundance of the isotope  $\beta_{nat}$ , conversion factor  $\alpha$ , nuclear angular momentum of the ground state  $I_g$  and the excited state  $I_e$  do not need further explanations. The data of these columns is based on [Fir96] apart of the values for  $\alpha$  [Ste73, NDS]. The maximum nuclear cross section  $\sigma_0$  is given by equation 2.31. It has further been multiplied with the branching ratio concerning the decay of the excited level, if there is the possibility of a radiative decay into an intermediate level. This ratio is less than one only in a few isolated cases ( $^{157}\text{Gd}$ ,  $^{161}\text{Dy}$ ,  $^{187}\text{Os}$ ,  $^{231}\text{Pa}$ ,  $^{237}\text{Np}$  and  $^{243}\text{Am}$ ).

For an estimation of the feasibility of NFS and NLE experiments, the Lamb-Mössbauer factor plays a crucial role. It depends on the energy of the transition and the Debye temperature  $\Theta_D$ , 2.21. The latter can vary over a huge range depending on the sample where the nuclei are embedded in. However, as the aim is only to get an estimation, a pure sample is considered. Thus,  $\Theta_D$  is the Debye temperature for a solid containing only the corresponding element [Kit96] or if possible at 100 K if data was available for that temperature. 100 K is the actual low temperature limit of the lighthouse operation and was chosen therefore. With the Debye temperature and using equation 2.21, we get the value of column  $f_{LM}^{100\text{K}}$  for the Lamb-Mössbauer factor. In compounds, such as oxides, the Debye temperature and thus the Lamb-Mössbauer-factor might deviate significantly from this value.  $^{133}\text{Cs}$  suffers most from this simple calculation, having a Debye temperature in the pure metal of only 33 K, far below the lighthouse operation temperature of 100 K. Taking different compounds into account was nevertheless omitted, due to the huge number of possible compounds. Further, the dilution of the nuclei in a compound leading to a more rigid solid might also decrease the obtained NFS or NLE intensity.

The next column is again unambiguous.  $\Phi_{\Gamma}^{\text{ID18}}$  is the spectral flux at the ESRF beamline ID18 obtained with the three 32 mm undulators, a storage ring current of 80 mA, passing through a slit of 2 mm horizontally times 1 mm vertical placed at a distance of 31 m, which is the place of the high heat load monochromator [Cha04, for flux over 0.1% bandwidth]. Spectral flux, because it designates the flux in a certain energy band, which is here the natural width  $\Gamma_0 = \frac{\hbar}{\tau}$  of the excited nuclear level.

The column  $I^{\text{N-Fluo}}$  stands for nuclear fluorescence and considers the detection of decaying nuclei emitting radiation in  $4\pi$  containing photons having the resonance energy and fluorescence radiation. It is simply the spectral flux  $\Phi_{\Gamma}^{\text{ID18}}$  times a factor  $e^{-5\text{ns}/\tau}$ . This factor considers an exponential decay of intensity and a detector that is available only 5 ns after the excitation of the nuclear levels by the synchrotron flash. Just the part  $e^{-5\text{ns}/\tau}$  is seen after 5 ns. Thus:

$$I^{\text{N-Fluo}} \sim \Phi_{\Gamma}^{\text{ID18}} \cdot e^{-5\text{ns}/\tau} \quad (8.1)$$

If the sample is thick enough, and we neglect electronic absorption in that sample,  $\sigma_0$  is of no importance. In other words, we assume the nuclear cross section to be much bigger than the electronic absorption cross section. In a few cases, like  $^{73}\text{Ge}$  at 13.26 keV, this might be wrong, but in general it seems ok. The collection of all delayed quanta after 5 ns is considered, neglecting detector efficiencies and the solid angle that this detector covers. The solid angle is independent of the considered isotope. The detector efficiency could of course be taken into account, but would restrict us to a certain detector choice. Therefore, it was omitted.

The next two columns are meant as an indicator to estimate the accessibility of a certain isotope with nuclear resonance investigations, in particular SR-PAC and the NLE. They are by no means more than an estimation! They are based on many approximations, but must contain some truth nevertheless, as isotopes already addressed in nuclear resonant scattering are found in the top places. The column  $I^{\text{SR-PAC}}$  concerns the feasibility of SR-PAC. It uses a similar

evaluation as used in column  $I^{\text{N-Fluo}}$ . However, photons emitted by the nuclei after internal conversion processes are excluded, see chapter 7.1. This implies a multiplication with  $\frac{1}{\alpha+1}$ . In chapter 7.2, the time spectrum of a decaying ensemble of excited nuclei as measured by a SR-PAC experiment has been calculated for nuclear transitions of multipolarity 1. Both for random hyperfine interactions and magnetically aligned samples, the measured intensity containing the hyperfine interaction information included the factor  $A_{22} = A_2 \cdot A_2$ , the anisotropy. This factor can be easily calculated following equation 7.7 and covers values between 0.357 and 0. Taking all factors together, we have:

$$I^{\text{SR-PAC}} \sim \Phi_{\Gamma}^{\text{ID18}} \cdot e^{-5ns/\tau} \cdot \frac{1}{\alpha+1} \cdot A_{22} \quad (8.2)$$

For M2 and E2 transitions, further anisotropy terms contribute, too. Therefore, the limitation to  $A_{22}$  in these cases is risky. In these cases, the obtained value is displayed in grey colour and slanted in the table. The SR-PAC intensity is independent of the Lamb-Mössbauer factor and therefore to a large degree temperature independent. Of course, SR-PAC investigations are easier to analyse in the case of vanishing  $f_{\text{LM}}$ , which means sometimes higher temperatures.

The last column concerns the nuclear lighthouse effect and might give an idea, which isotopes could be addressed in future. This is the key interest of the table. The value cited is a product of four factors: The spectral flux  $\Phi_{\Gamma}^{\text{ID18}}$  designates the available flux incident on the sample having the right energy. Angular acceptance considerations of the high heat load monochromator or absorbing windows are neglected. A compound reflective lens might be needed. The following two factors concern the nuclear lighthouse effect in particular: the signal is proportional  $\sigma_0^2 \cdot f_{\text{LM}}^2$ . The NLE is a coherent scattering process and quantum beats and dynamical beats have been discussed in detail in chapter 2. To calculate in detail the time behaviour of this complicated decay would have been unfeasible for this table and the many isotopes. A rough approximation of the time integrated intensity seen by the detector starting 5 ns after excitations is again quantified by the factor  $e^{-5ns/\tau}$ . This clearly takes account of the fact, that the decay of an isotope with a small lifetime will lead to larger losses due to detector deadtime (due to gating of the signal) than an isotope with longer lifetime. In the end, one has

$$\hat{I}_{100\text{K}}^{\text{NLE}} \sim \Phi_{\Gamma}^{\text{ID18}} \cdot \sigma_0^2 \cdot f_{\text{LM}}^2 \cdot e^{-5ns/\tau} \quad (8.3)$$

The table is ordered with decreasing  $\hat{I}_{100\text{K}}^{\text{NLE}}$ . No surprise,  $^{57}\text{Fe}$  is in the top position, followed by all other isotopes employed by nuclear resonant spectroscopy with synchrotron radiation (except  $^{40}\text{K}$ ) and some intrusions: the radioactive isotopes  $^{133}\text{Ba}$ ,  $^{227}\text{Ac}$ ,  $^{137}\text{La}$ ,  $^{134}\text{Cs}$  and the short lived isotopes  $^{187}\text{Os}$  and  $^{125}\text{Te}$ . A detailed discussion about the feasibility of applying the NLE or SR-PAC to investigate a certain isotope is found in chapter 8.3.

## 8.3 New Mössbauer isotopes to be addressed with SR

### 8.3.1 NLE isotopes

The last column of table 8.2 was obtained using many assumptions, as mentioned already in the preceding chapter. The point which is the most problematic is the value of the Lamb-Mössbauer factor. It depends both on the energy and the Debye temperature and cannot be easily split into two parts, one containing the energy, the other one the Debye temperature. Therefore, the discussion of the isotopes that can be addressed with the NLE will first consider the final result as obtained with the Lamb-Mössbauer factor of the pure element. However, a few other isotopes that suffered a lot from the low Debye temperature or are otherwise noteworthy will be included, too.

Isotopes with transition energies below 30 keV can be perfectly addressed with NFS and NIS using high resolution monochromators. There is principally no need to use the NLE there. In practice however, there are a few exceptions. The first one is the  $^{57}\text{Fe}$  transition. As the nuclear parameters of  $^{57}\text{Fe}$  (see table 8.2) are so favourable for coherent nuclear scattering, the NLE permits with certain  $^{57}\text{Fe}$  samples to work in any filling modes of the synchrotron, especially  $2 \cdot \frac{1}{3}$  or uniform filling, and this despite the presence of SAXS.

The second exception are isotopes with very long lifetimes. Although fitting programs like Motif and CONUSS take the filling structure of the storage ring into account, if the lifetime is much larger than the SR pulse repetition rate, problems arise. The beat structures at late times can be spoiled by the decay of nuclei excited by a following bunch. This concerns  $^{181}\text{Ta}$  with a lifetime of 8728 ns, which has already been addressed with NFS, and  $^{73}\text{Ge}$  with its 13.23 keV transition and a lifetime of 4260 ns, unused so far. The gap between two filled bunches in 16 bunch mode is 176 ns and 2816 ns in single bunch mode. SAXS is quite high at low energies, but the advantage of long lifetimes is the possibility to deviate the delayed quanta via the NLE far off the beam axis, where SAXS becomes smaller and smaller. The countrate of a NLE experiment with the 13.23 keV transition of  $^{73}\text{Ge}$  could be at the lower limit of feasibility. It is much lower compared to other Mössbauer isotopes in this low energy range as a result of its tremendous internal conversion factor  $\alpha$ . The value  $\hat{I}_{100\text{K}}^{\text{NLE}}$  of  $^{73}\text{Ge}$  calculated according to equation 8.3 is already 50 times smaller than the one of  $^{61}\text{Ni}$ .

The last exception is due to the simple universal implementation of the NLE as compared to the construction of individual high resolution monochromators for NFS. If no high resolution monochromator is yet available for a certain isotope, the NLE might be used. At ID18, this concerns  $^{187}\text{Os}$ ,  $^{169}\text{Tm}$  and  $^{83}\text{Kr}$  as well as the radioactive isotopes  $^{133}\text{Ba}$ ,  $^{134}\text{Cs}$ ,  $^{137}\text{La}$  and  $^{227}\text{Ac}$ . The danger of a rotor breakdown while spinning a radioactive sample will be treated later.  $^{187}\text{Os}$  with its low energy and the high Debye temperature and high Lamb-Mössbauer factor even at room temperature might be a interesting candidate to be used in a 2.5 mm stator/rotor system that allows frequencies up to 35 kHz without cooling. This might allow to address more easily the early times of the decay of this short lived isotope as with the standard NFS experiment.

Traditional NFS becomes more complicated at energies above 30 keV, the reason being the angular acceptance of the Bragg reflections needed for a high resolution monochromator. There is the possibility to extend NFS to energies up to say 50 keV using backscattering reflection in the design of the high resolution monochromator. This needs highly perfect and thick single crystals of silicon, or better sapphire, as it has more possible reflections close to 90 degrees. The crystals need to be thick, because the extinction length at high energies becomes more and more pronounced. This sort of monochromator has recently been applied to  $^{121}\text{Sb}$  [Wil04b] with its transition at 37.15 keV and worked very well. In the same energy range lies the 35.5 keV transition of  $^{125}\text{Te}$ . Unfortunately, its lifetime is very short, 2.2 ns. Still, the countrate to be expected after 5 ns is even higher than in the case of  $^{61}\text{Ni}$ , which has successfully been used with the NLE. It is therefore a future candidate both for investigations with a backscattering high resolution monochromator as well as the NLE.

The next isotopes showing a Mössbauer transition and a lifetime above 1 ns follow only at above 57 keV. At these energies, even backscattering monochromators run into difficulties, as the extinction length increases and perfect crystals in these dimensions are needed. As an example, using a sapphire (16 31 54) backscattering reflection for the 67.41 keV resonance of  $^{61}\text{Ni}$ , a crystal thicker than 4 cm would be needed (the extinction length is 3.9 cm) and still only reflect 4.5 % of the incoming beam [Wil04b]. The NLE is so far the only method to address these transitions, if we exclude SR-PAC for now.  $^{61}\text{Ni}$  was the first isotope to be studied in this range.

Likewise,  $^{237}\text{Np}$ ,  $^{189}\text{Os}$ ,  $^{193}\text{Ir}$  and a second transition in  $^{73}\text{Ge}$  have transition energies between



55 and 75 keV and follow  $^{61}\text{Ni}$  in the placement of table 8.2. None of these elements has been used in NRS experiments with SR yet. Especially the 59.54 keV transition of  $^{237}\text{Np}$  is of interest. Together with  $^{227}\text{Ac}$ , they are the only actinides with reasonable nuclear parameters allowing for NRS with SR. Actinides and actinide-compounds are extremely interesting due to their magnetic properties arising from the unfilled  $5f$  electronic shell. There are several recent works on Mössbauer-spectroscopy with the  $^{237}\text{Np}$  isotope [Col04, for example]. Due to the long lifetime of the excited state, separation from SAXS might be feasible even without timing. On the other hand, exploding rotors have to be excluded, as it would be undesirable to have radioactive sample parts distributed in the experimental hutch after a failure of the stator-rotor system. The half-life of the ground state of  $^{237}\text{Np}$  is  $2.14 \cdot 10^6$  years.  $^{237}\text{Np}$  is part of the plutonium-neptunium decay chain. For  $^{227}\text{Ac}$ , the half-life is only 21.8 years, which means a higher radioactivity of a comparable amount of sample material and thus make handling more dangerous.

The 69.53 keV transition of  $^{189}\text{Os}$  and the 68.75 keV transition of  $^{73}\text{Ge}$  have not only comparable energies, but also lifetimes, 2.3 ns and 2.5 ns respectively. Both seem to be reasonably accessible via the lighthouse effect, but 16 bunch mode and electronic gating of the prompt SAXS is a must, due to the short lifetimes. Both samples have to be isotopically enriched. The 69.53 keV transition of Osmium is very attractive for investigations of electric quadrupole and magnetic hyperfine interactions [Güt78]. It even gives the advantage to kill  $K_\beta$  background radiation of Osmium with time gating, which masks the signal in traditional Mössbauer spectroscopy experiments.

Finally, the 73.04 keV transition of  $^{193}\text{Ir}$  might be addressed, having the advantage of a quite long lifetime of 8.8 ns, a high Debye temperature and high natural abundance. Unfortunately, the maximum resonance cross section of this transition is quite small.

There is a huge number of rare earth Mössbauer transitions in the range around 80 keV. Unfortunately, although the high interest in these elements concerning magnetism, the expected signal after 5 ns is rather poor. The reason lies in the combination of the short lifetime of these isotopes, the high energy of the transition and to a lesser extent in the modest Debye temperature of the pure rare earth metals. Compounds with a much increased Debye temperature could improve the situation slightly.

There are a few more isotopes that catch the eye on figure 8.1. These are  $^{155}\text{Gd}$ ,  $^{157}\text{Gd}$ ,  $^{145}\text{Nd}$ ,  $^{133}\text{Cs}$  and  $^{138}\text{La}$ . Although the lifetimes are quite high, especially  $^{157}\text{Gd}$  with  $\tau = 664$  ns, they might not be addressable easily with the NLE. The longer the lifetime is, the smaller the resonance width and thus the available flux in this energy width. In none of these isotopes, this small spectral flux is compensated by a high Lamb-Mössbauer factor. The Debye temperature is moderate to small, especially for  $^{133}\text{Cs}$  where in the pure state, it is only 33 K. A compound leading to much stronger bonds of the element in the lattice and thus a much higher Debye temperature might class these elements higher in the table. But efforts to use the pure element in coherent nuclear resonant scattering at 100 K will be in vain. For lanthanum and caesium, the low energy isotopes seems more accessible. The half-lives of these radioactive isotopes is 6000 years for  $^{137}\text{La}$  and two years for  $^{134}\text{Cs}$ .

### 8.3.2 SR-PAC isotopes

The analysis of the column  $I^{\text{SR-PAC}}$  is not as ambiguous as the previous discussion, as the Lamb-Mössbauer factor does not play any role anymore. The maximum resonance cross section does not play a role neither, if we assume that nuclear absorption dominates the electronic one and if we have a thick enough sample, that all photons with the right energy will finally interact.

However, high lifetimes and high incoming flux lead again to best conditions for low energy transitions.

Among the most favourable isotopes for SR-PAC are  $^{119}\text{Sn}$ ,  $^{57}\text{Fe}$  and  $^{161}\text{Dy}$ . These isotopes are regularly and easily addressed with NFS, unless the temperatures are high and the Lamb-Mössbauer factor vanishes. Then, SR-PAC might extend investigations to higher temperatures. The anisotropy is 0.25 for  $^{57}\text{Fe}$  and  $^{119}\text{Sn}$  and 0.183 for  $^{161}\text{Dy}$ .

$^{169}\text{Tm}$  and  $^{133}\text{Ba}$  should give high SR-PAC countrates, too. They have not been addressed with NFS, yet, although  $^{169}\text{Tm}$  was used in a NBS experiment. SR-PAC measurements would be easy to realise without needing the conception of high resolution monochromators (which should be easy to implement, though). Their conversion coefficient is quite unfavourable, so the detector should get some proper absorbers to diminish counts arising from decays via electron conversion. For the radioactive  $^{133}\text{Ba}$ , also the radiation following the radioactive decay would have to be filtered. It's half-life is 10.5 years. The anisotropy is 0.25 in both cases.  $^{227}\text{Ac}$  will need filtering, too. It is also rather promising and has an anisotropy of 0.16.

$^{151}\text{Eu}$  is the next practical isotope according to the SR-PAC column of table 8.2. It is again a "standard" NRS isotope, so SR-PAC measurements would focus still at high temperature, probably. The anisotropy is 0.107.  $^{187}\text{Os}$  follows. However, its very small lifetime might be problematic if the expected modulation frequency is much larger. For  $^{61}\text{Ni}$  with its lifetime of 7.4 ns, the cosine like modulation with the period of 47.6 ns could hardly be seen completely. Comparable countrate as for the  $^{61}\text{Ni}$  isotope should come from SR-PAC investigations with  $^{121}\text{Sb}$ . The anisotropy is slightly smaller, namely 0.107. The lifetime is smaller, too, and the same comment to the case of  $^{187}\text{Os}$  apply. Still,  $^{121}\text{Sb}$  is not easily addressed with NFS and was examined only very recently [Wil04b] with a backscattering monochromator.

Following the argumentation as above concerning the modulation frequency compared to the lifetime,  $^{125}\text{Te}$  seems to be out of reach for reasonable applications, despite the rather high value obtained in the SR-PAC column. Its anisotropy is 0.25.

Slightly less countrates are expected from  $^{40}\text{K}$  and  $^{129}\text{I}$ . Both isotopes can still be examined with standard methods, see table 8.1. Both isotopes and  $^{134}\text{Cs}$  with a similar countrate are radioactive and their decay might lead to an increased background radiation, if no proper filters are used. In all cases, the anisotropy is small, e.g. 0.02 for  $^{40}\text{K}$ , 0.018 for  $^{129}\text{I}$  and a slightly better 0.088 for  $^{134}\text{Cs}$ . The small anisotropy implies, that there will be a much higher background of exponentially decaying intensity than in the case of an isotope with high anisotropy having a similar value in column  $I^{\text{SR-PAC}}$ . I do not think that this is a problem for the measurement and the data analysis if the underlying exponential decay is perfect. However, if the Lamb-Mössbauer factor is not completely negligible, the propagation even of a weak delayed wavefield through the sample might perturb the exponential decay by more than the anisotropy term. This problem is similar for  $^{83}\text{Kr}$  and  $^{149}\text{Sm}$  with an anisotropy of 0.023 and 0.018, respectively.

The two isotopes where SR-PAC will be extremely helpful as compared to NFS and NIS are  $^{237}\text{Np}$  and  $^{155}\text{Gd}$ . Both isotopes are far above the range of operating high resolution monochromators. Magnetism in rare earth elements is very interesting and no gadolinium isotopes are accessible with NRS yet. The internal conversion of  $^{155}\text{Gd}$  is very low and the anisotropy high, i.e. 0.14. The lifetime of 9.4 ns should be sufficiently high to observe complete oscillations. Although the transition energy of 86.55 keV is extremely high, the spectral flux within the energetic width of the transition available at ID18 is higher than that for 63.93 keV transition of  $^{157}\text{Gd}$ , which seems attractive due to its longer lifetime.

For  $^{237}\text{Np}$ , the internal conversion is very low and the anisotropy high, i.e. 0.183. The lifetime of  $^{237}\text{Np}$  is a comfortable 96.7 ns. The radioactive background needs to be filtered and a threshold on the detector signal might have to be applied. Using the method of SR-PAC on

$^{237}\text{Np}$  instead of the NLE avoids all security issues concerning the possibility of an exploding rotor due to a gas bearing failure.



## Chapter 9

# Conclusions and outlook

### Nuclear lighthouse measurements with $^{61}\text{Ni}$

For the first time, coherent nuclear resonant scattering with synchrotron radiation was applied to energies well above the 10 to 30 keV region. The only method capable of doing this at present is the nuclear lighthouse effect (NLE). Using this method, we have performed the first coherent nuclear resonant scattering from the 67.41 keV level of  $^{61}\text{Ni}$ . A magnetic hyperfine field of 6.7(2) T at 180 K was found.

Traditional Mössbauer spectroscopy with  $^{61}\text{Ni}$  is very much hampered by the short lifetimes of the radioactive mother isotopes  $^{61}\text{Co}$  and  $^{61}\text{Cu}$ , i.e. 99 and 100 minutes, respectively. Fast detectors and time discriminating electronics alone in standard NFS geometry without a viable high resolution monochromator fails. The prompt flash of non-interacting photons hitting the detector is too intense to detect the smaller nuclear resonant signal shortly afterwards. Even Bragg-backscattering monochromators are not available for the  $^{61}\text{Ni}$  resonance yet and furthermore seem difficult to realise. Thanks to the NLE, the prompt undeviated beam and the delayed nuclear signal are separated in space.

As the Lamb-Mössbauer factor for Mössbauer isotopes having a high transition energy is very small at room temperature, the cooling of the sample is a must. A cooling scheme for the rotor/stator system has been developed, tested and improved. The cooling is realised by a stream of cold gas flowing towards the rotor's centre. This scheme performs down to 90 K. However, rotor instabilities might be important at temperatures below 150 K. In changing the cooling, bearing and acceleration gases to helium, stability problems due to possible liquid nitrogen droplets can be ruled out. Then, an operation at temperatures down to 20 K might be envisaged.

The major obstacle for a general application of the NLE to a large variety of Mössbauer isotopes, whatever their transition energy is, is small angle X-ray scattering (SAXS). SAXS covers the same angular range as the deviated NLE signal. In the case of  $^{61}\text{Ni}$ , it was necessary to use 16 bunch mode, fast detectors and timing electronics to distinguish between the prompt SAXS contribution and the delayed nuclear part and to obtain a reasonable time spectrum. However, also without timing electronics, the nuclear distribution hidden under the strong SAXS background was identified irrevocably.

To increase the signal-to-noise ratio, several improvements are possible. First, a collimating compound refractive lens (CRL) [Len99] can increase the countrate by a factor of 10: The vertical divergence of the photons from the undulator is  $\sigma=12\ \mu\text{rad}$  FWHM. It can be decreased by a 80-hole parabolic aluminium CRL to  $\Delta\theta=0.9\ \mu\text{rad}$  which matches the acceptance of a  $1^\circ$  asymmetrically cut Si (333) reflection. Second, a further improvement of the cooling scheme

to reach standard operation at 100 K without rotor stability problems seems reachable. The lateral rotor movement or a precession of the rotor can be disregarded, if only 1/3 circumference sample foils are used, as the beam passes the sample only once. Lower temperatures increase tremendously the Lamb-Mössbauer factor and operation at 100 K will give about another factor of 10 higher NLE signal. If the stability problems are solved, the use of single-crystalline sapphire rotors would be beneficial in decreasing both the SAXS signal and the absorption of 70% of 67.41 keV photons as compared to the ZrO<sub>2</sub> rotor used here. Rotational frequencies can still increase to 12 kHz, allowing both to reach earlier decay times and a lower SAXS background at a fixed time. Finally, although linear detectors with high efficiency at these energies are missing, detector improvements can give at least a factor of 2, e.g. with two sets of detectors that scan half of the angular range simultaneously. Much higher efficiency would be obtained by an array as described in chapter 4.5.4.

The NLE experiment presented here opens a new field for hyperfine spectroscopy at high transition energies. The method of the nuclear lighthouse effect is extended to lower temperature conditions and might be applied to temperature dependent phase transitions in future.

### Nuclear lighthouse measurements on rotating surfaces

While elaborating a new cooling scheme for NLE measurements in transmission geometry, cooling of a sample at the top of a rotor was examined. From there, it was only one step to develop grazing incidence NLE measurements on rotating surfaces. We examined <sup>57</sup>Fe containing layer systems sputtered onto polished rotor top surfaces. This was the first use of the nuclear lighthouse effect in grazing incidence geometry.

Very important for these measurements is the stability of the rotor's surface normal during operation. A tilting of the rotor surface with respect to its rotation axis or a precession of the rotor in the stator have to fulfil severe limitations. The SAXS originating from the surface roughness is much higher than was hoped and implies that NLE in grazing incidence needs fast timing electronics and timing mode operation of the synchrotron. The beamline layout with individual hutches and shutter between them is very limiting for  $\theta$ - $2\theta$  reflectivity scans. Beam pipes to decrease SAXS from air between the surface and the detector limit the beam path further, the larger  $\theta$  is. This implies a slow speed, which does not favour the time resolution or the SAXS background level. However, the used 7 mm large rotor/stator system does principally not allow for a much faster rotation. There is still a long way to follow before this method could be an alternative to standard grazing incidence measurements on Mössbauer isotope containing layer systems.

### SR-PAC investigations of <sup>61</sup>Ni

For high transition energies as is the case of <sup>61</sup>Ni, the Lamb-Mössbauer factor is comparably small. Incoherent synchrotron radiation based perturbed angular correlation does not depend on this factor and proved to be a valuable alternative for the study of hyperfine interactions. First results with <sup>61</sup>Ni were obtained. The temperature range useful for SR-PAC is much larger than for the NLE, especially to higher temperatures. The simplicity of the SR-PAC setup encourages to address other isotopes in the future, see below. However, SR-PAC with <sup>61</sup>Ni profits from a high anisotropy  $A_{22} = 0.14$ . The lifetime of the 67.41 keV level of <sup>61</sup>Ni is just large enough to observe a full oscillation generated by the magnetic hyperfine field of approximately 7.18 T at room temperature. Although hyperfine field as obtained by NLE and SR-PAC differ, they are still in fair agreement with NMR results. The error is less than 10 %.

## New isotopes with NLE and SR-PAC

As was mentioned in chapter 8.3, traditional nuclear forward scattering offers the great advantage of an unlimited sample environment, e.g. possibilities to apply high pressures or temperatures down to 4 K. If high resolution monochromators are practicable for the desired isotope's transition energy, one would in general not use the nuclear lighthouse effect. This is not the case for isotopes showing a high transition energy. Above 50 keV, even Bragg-backscattering monochromators seem to be severely limited. Then, the NLE or SR-PAC are the only options. First applications were presented in this thesis on the 67.41 keV transition of  $^{61}\text{Ni}$ . In future, other isotopes in this energy region could be addressed as well, especially  $^{237}\text{Np}$  (59.54 keV and  $\tau=97$  ns),  $^{193}\text{Ir}$  (73.04 keV,  $\tau=8.8$  ns), but also  $^{189}\text{Os}$  (69.53 keV,  $\tau=2.3$  ns) and  $^{73}\text{Ge}$  (68.75 keV,  $\tau=2.5$  ns) with NLE experiments. The approach with the NLE is more general, as it can be applied easily to transitions of multipolarity one and two. M2 and E2 transitions can not be analysed with the present SR-PAC theory, yet. The anisotropy term for SR-PAC experiments is very small if the excited state is of smaller spin than the ground state and is even zero if  $I_e = \frac{1}{2}$ , like for  $^{193}\text{Ir}$ . The NLE does not depend that much on these spin considerations. Isotopes where SR-PAC is the preferable method as compared to NLE and NFS are  $^{237}\text{Np}$  and  $^{155}\text{Gd}$ , both having transitions well above of current high resolution monochromators. The problem of a radioactive source that might explode in a rotor accident can be avoided here, but care has to be taken whether the radioactive background close to the detector can be filtered out or not.

## Further future applications of the NLE

Apart from hyperfine spectroscopic studies on Mössbauer isotopes with high transition energies or other particularities, two further applications of the NLE have been proposed: The first one dates back to the "roots" of the NLE and considers  $\mu\text{eV}$ -resolution inelastic scattering [Röh97, Röh99c, Röh00a, Bur00]. At a certain angle  $\alpha$  of the nuclear radiation deviated by the lighthouse, a slit system filters out a small part of the beam, having  $\mu\text{eV}$  bandwidth that can be tuned in energy over a range of several meV. This was discussed in chapter 2.6.3. Finally, the NLE has been proposed for the use in an experiment to distinguish between covariant ether theories and special relativity [Kho04]. In the desired experiment, two samples would be placed at different radii in a rotor and turned at high frequencies. As each sample travels at a different speed relative to an arbitrary reference frame (special relativity) or the distinguished reference frame (ether theory), interference effects between the two sample part arise and principally can lead to a distinction between the two theories. For both of these applications SAXS suppression is very crucial. A special slit system and focussing of the beam to  $\mu\text{m}$  size has been proposed in order to reduce it [Röh04a, page 279]. Nevertheless, countrates need to be improved, possibly with 4<sup>th</sup> generation sources, especially for the experiment as described by [Kho04].





# Bibliography

- [Ach62] A. I. Achieser & W. B. Berestezki. *Quantenelektrodynamik*. Teubner Leipzig, 1962.
- [Alp93] E. E. Alp, T. M. Mooney, T. Toellner, W. Sturhahn, E. Witthoff, R. Röhlberger, E. Gerdau, H. Homma & M. Kentjana. Time Resolved Nuclear Resonant Scattering from  $^{119}\text{Sn}$  Nuclei Using Synchrotron Radiation. *Phys. Rev. Lett.* **70** p. 3351, 1993.
- [Als93] J. Als-Nielsen. Diffraction, refraction and absorption of x-rays and neutrons - A comparative exposition. In Baruchel et al. [Bar93].
- [Amb69] F. Ambe, S. Ambe, M. Takeda, H. H. Wei, K. Ohki & N. Saito. Radiochemical preparation of  $^{61}\text{Cu}$  single line source for the measurement of the Mössbauer effect in  $^{61}\text{Ni}$ . *Radiochem. Radioanal. Lett.* **1** p. 341, 1969.
- [APS] <http://www.aps.anl.gov>. Advanced Photon Source.
- [Ast01] T. Asthalter, I. Sergueev, H. Franz, R. Rüffer, W. Petry, K. Messel, P. Härter & A. Huwe. Quasielastic nuclear forward scattering as a background-free probe of slow glass dynamics in confined geometries. *Eur. Phys. J. B* **22** p. 301, 2001.
- [Azi71] S. A. Azimov, M. Gulyamov, T. Iskhakov & M. M. Khodzhaev. *Proc. 21<sup>st</sup> Ann. Conf. Nucl. Spectr. Struct. At. Nuclei*, Moscow, p. 45, 1971. Not available, but as [Bha99] calculated an average value for the lifetime of  $^{61}\text{Ni}$ , it should state  $\tau = 5.41$  ns.
- [Bar80] D. Barb. *Grundlagen und Anwendungen der Mössbauerspektroskopie*. Akademie-Verlag Berlin, 1980. Romanian original, published in 1972 by Editura Academiei Bucuresti.
- [Bar93] J. Baruchel, J. L. Hodeau, M. S. Lehmann, J. R. Regnard & C. Schlenker, editors. *Neutron and Synchrotron Radiation for Condensed Matter Studies*, vol. I. Editions de Physique, Springer-Verlag, 1993.
- [Bar94] A. Q. R. Baron & S. L. Ruby. Time resolved detection of X-rays using large area avalanche photodiodes. *Nucl. Instr. Meth. Phys. Res. A* **343** p. 517, 1994.
- [Bar95] A. Q. R. Baron, A. I. Chumakov, S. L. Ruby, J. Arthur, G. S. Brown, G. V. Smirnov & U. van Bürck. Nuclear resonant scattering of synchrotron radiation by gaseous krypton. *Phys. Rev. B* **51** p. 16384, 1995.
- [Bar96] A. Q. R. Baron, A. I. Chumakov, R. Rüffer, H. Grünsteudel, H. F. Grünsteudel & O. Leupold. Single-nucleus quantum beats excited by synchrotron radiation. *Europhys. Lett.* **34** p. 331, 1996.
- [Bar97] A. Q. R. Baron, R. Rüffer & J. Metge. A fast, convenient X-ray detector. *Nucl. Instr. Meth. Phys. Res. A* **400** p. 124, 1997.
- [Bar00] A. Q. R. Baron. Detectors for nuclear resonant scattering experiments. *Hyperfine Interact.* **125** p. 29, 2000.
- [Bar01] A. Barla. *Development of  $^{119}\text{Sn}$  Nuclear Resonant Scattering and First Applications*. CGA-Verlag Herdecke, 2001. Dissertation, Universität zu Köln.
- [Bar03] A. Q. R. Baron. Avalanche Photodiodes (APDs) as Fast X-Ray Detectors, 2003. ESRF Detector Workshop, Grenoble France, 13 February 2003.

- [Bar04a] A. Barla, M. Chefki, C. Huhnt, M. Braden, O. Leupold, R. Ruffer, J. P. Sanchez, A. Wurth, A. Mewis & M. M. Abd-Elmeguid. Interplay between structural instability and lattice dynamics in  $\text{EuRh}_2(\text{P}_x\text{As}_{1-x})_2$ . *Phys. Rev. B* **69** p. 100102, 2004.
- [Bar04b] A. Barla, J. P. Sanchez, Y. Haga, G. Lapertot, B. P. Doyle, O. Leupold, R. Ruffer, M. M. Abd-Elmeguid, R. Lengsdorf & J. Flouquet. Pressure-Induced Magnetic Order in Golden  $\text{SmS}$ . *Phys. Rev. Lett.* **92** p. 066401, 2004.
- [Ber94a] U. Bergmann, J. B. Hastings & D. P. Siddons. Time evolution of incoherent nuclear scattering from  $^{57}\text{Fe}$  excited with synchrotron radiation. *Phys. Rev. B* **49** p. 1513, 1994.
- [Ber94b] U. Bergmann, S. D. Shastri, D. P. Siddons, B. W. Batterman & J. B. Hastings. Temperature dependence of nuclear forward scattering of synchrotron radiation in  $\alpha$ - $^{57}\text{Fe}$ . *Phys. Rev. B* **50** p. 5957, 1994.
- [Bha99] M. R. Bhat. Nuclear Data Sheets for A=61. *Nuclear Data Sheets* **88** p. 417, 1999.
- [Bir64] R. J. Birgenau, J. Cordes & A. D. B. Woods. Normal Modes of Vibration on Nickel. *Phys. Rev.* **136** p. A1359, 1964.
- [Bla94] A. C. Bland & B. Heinrich, editors. *Ultrathin Magnetic Structures*, vol. I and II. Springer-Verlag, 1994.
- [Blu68] M. Blume & O. C. Kistner. Resonant Absorption in the Presence of Faraday Rotation. *Phys. Rev.* **171** p. 417, 1968.
- [Brä03] E. Bräuer-Krisch. private communications about analysis of dosimetric films, 2003.
- [Bre36] G. Breit & E. Wigner. Capture of Slow Neutrons. *Phys. Rev.* **49** p. 519, 1936.
- [Bro91] G. Brown & W. Lavender. Synchrotron-radiation spectra. In G. S. Brown & D. E. Moncton, editors, *Handbook on Synchrotron radiation*, vol. 3. Elsevier Science Publishers, 1991.
- [BRUK] Bruker Analytik GmbH, Rheinstetten, Germany.
- [Bür92] U. van Bürck, D. P. Siddons, J. B. Hastings, U. Bergmann & R. Hollatz. Nuclear forward scattering of synchrotron radiation. *Phys. Rev. B* **46** p. 6207, 1992.
- [Bür99] U. van Bürck. Coherent pulse propagation through resonant media. *Hyperfine Interact.* **123/124** p. 483, 1999.
- [Bur00] E. Burkel. Phonon spectroscopy by inelastic x-ray scattering. *Rep. Prog. Phys.* **63** p. 171, 2000.
- [But96] T. Butz. Nuclear Quadrupole Interactions Studied by Time Differential Perturbed Angular Correlations of  $\gamma$ -Rays. *Z. Naturforsch.* **51a** p. 396, 1996.
- [Cha04] J. Chavanne. private communications, 2004. ESRF insertion device group. Calculations using [Chu98a].
- [Chu95] A. I. Chumakov, A. Q. R. Baron, J. Arthur, S. L. Ruby, G. S. Brown, G. V. Smirnov, U. van Bürck & G. Wortmann. Nuclear Scattering of Synchrotron Radiation by  $^{181}\text{Ta}$ . *Phys. Rev. Lett.* **75** p. 549, 1995.
- [Chu98a] O. Chubar & P. Elleaume. Accurate and Efficient Computation of Synchrotron Radiation in the Near Field Region. *Proc. 6<sup>th</sup> Europ. Part. Accel. Conf. Stockholm* p. 1177, 1998.
- [Chu98b] A. I. Chumakov, A. Barla, R. Ruffer, J. Metge, H. F. Grünsteudel, H. Grünsteudel, J. Plessel, H. Winkelmann & M. M. Abd-Elmeguid. Nuclear inelastic scattering of synchrotron radiation by  $^{119}\text{Sn}$ . *Phys. Rev. B* **58** p. 254, 1998.
- [Chu99] A. I. Chumakov, L. Niesen, D. L. Nagy & E. E. Alp. Nuclear resonant scattering of synchrotron radiation by multilayer structures. *Hyperfine Interact.* **123/124** p. 427, 1999.
- [Chu01] A. I. Chumakov, R. Ruffer, O. Leupold, A. Barla, H. Thiess, J. M. Gil, H. V. Alberto, R. C. Vilão, N. Ayres de Campos, V. G. Kohn, M. Gerken & M. Lucht. Nuclear Inelastic scattering with  $^{161}\text{Dy}$ . *Phys. Rev. B* **63** p. 172301, 2001.
- [Col04] E. Colineau, P. Jacorský, P. Boulet, J. C. Griveau, J. Rebizant, J. P. Sanchez & G. R. Stewart. Magnetic and electronic properties of the antiferromagnet  $\text{NpCoGa}_5$ . *Phys. Rev. B* **69** p. 184411, 2004.

- [CRL] <http://laue.physik.rwth-aachen.de/home.html.en>. RWTH Aachen. *crcalc-Program*. Compound refractive lens calculations based on [Len99].
- [Dal79] B. W. Dale, R. J. Dickinson & R. V. Parish. Quadrupole splitting in the  $^{61}\text{Ni}$  Mössbauer spectrum of a square-planar complex. *Chem. Phys. Lett.* **64** p. 375, 1979.
- [Dar14] C. G. Darwin. The Theory of X-Ray Reflexion. *Phil. Mag.* **27** p. 315, 1914.
- [deS74] A. deShalit & H. Feshbach. *Theoretical Nuclear Physics Volume I: Nuclear Structure*. John Wiley & Sons, Inc., 1974. Chapter VIII.
- [Dot81] F. Doty & P. D. Ellis. Design of high speed cylindrical NMR sample spinners. *Rev. Sci. Instrum.* **52** p. 1868, 1981.
- [Duk00] P. J. Duke. *Synchrotron Radiation*. Oxford University Press, 2000.
- [Dun72] B. D. Dunlap. An Introduction to Electric Quadrupole Interactions in Mössbauer Spectroscopy. In J. G. Stevens & V. E. Stevens, editors, *Mössbauer Effect Data Index 1970*, p. 25. Adam Hilger, London, 1972.
- [Eld48] F. R. Elder, R. V. Langmuir & H. C. Pollock. Radiation from Electrons Accelerated in a Synchrotron. *Phys. Rev.* **74** p. 52, 1948.
- [Ell98] P. Elleaume. Optimization of compound refractive lenses for X-rays. *Nucl. Instr. Meth. Phys.* **A412** p. 482, 1998.
- [Eri69] U. Erich. Mössbauereffekt am  $^{61}\text{Ni}$ . *Z. Physik* **227** p. 25, 1969.
- [ESRFa] <http://www.esrf.fr/Accelerators/Operation/Statistics/FillingModes>. *Filling modes in 2002*.
- [ESRFb] <http://www.esrf.fr>. European Synchrotron Radiation Facility.
- [ESRFc] <http://www.esrf.fr/Accelerators/Operation/Modes>. *Operating modes at the ESRF*.
- [Fen93] Y. P. Feng, S. K. Sinha, H. W. Deckman, J. B. Hastings & D. P. Siddons. X-Ray Flux Enhancement in Thin-Film Waveguides Using Resonant Beam Couplers. *Phys. Rev. Lett.* **71** p. 537, 1993.
- [Fir96] R. B. Firestone & V. S. Shirley. *Table of Isotopes*, vol. I and II. John Wiley & Sons, Inc. New York, eighth edition, 1996.
- [Fra63] H. Frauenfelder. *The Mössbauer Effect*. W. A. Benjamin Inc. New York, 1963.
- [Fra68] H. Frauenfelder & R. M. Steffen. Angular Correlations. In K. Siegbahn, editor, *Alpha-, Beta- and Gamma-Ray Spectroscopy*, p. 997. North Holland, 1968.
- [Fre93] A. Freund. X-Ray Optics for Synchrotron Radiation. In Baruchel et al. [Bar93].
- [Ger85] E. Gerdau, R. Rüffer, H. Winkler, W. Tolksdorf, C. P. Klages & J. P. Hannon. Nuclear Bragg Diffraction of Synchrotron Radiation in Yttrium Iron Garnet. *Phys. Rev. Lett.* **54** p. 835, 1985.
- [Ger02] M. Gerken. *Kernresonante Streuung von Synchrotronstrahlung an  $^{161}\text{Dy}$  und  $^{61}\text{Ni}$* . Dissertation, Universität Hamburg, 2002.
- [Ges04] K. Geske & H.-C. Wille, 2004. private communications.
- [Gla91] O. Glatter. Small-angle scattering and light scattering. In P. Lindner & T. Zemb, editors, *Neutron, X-Ray and Light Scattering*, p. 33. Elsevier Science Publishers, 1991.
- [Gol68] V. I. Goldanskii & E. F. Makarov. Fundamentals of Gamma-Resonance Spectroscopy. In V. I. Goldanskii & R. H. Herber, editors, *Chemical Applications of Mössbauer Spectroscopy*. Academic Press, New York, 1968.
- [Gör71] J. Göring. The Nuclear Moments of the 67.4 keV Level in  $^{61}\text{Ni}$ . *Z. Naturforsch.* **26 a** p. 1931, 1971.
- [Gör73] J. Göring. The Concentration Dependence of the Hyperfine Fields in NiPd and NiPt Alloys. *phys. stat. sol. (b) Short Notes* **57** p. K7, 1973.
- [Got98] R. Gottschall, R. Schöllhorn, M. Muhler, N. Jansen, D. Walcher & P. Gülich. Electronic State of Nickel in  $\text{BaNiO}_3$ . *Inorg. Chem.* **37** p. 1513, 1998.

- [Gra93] U. Gradmann. Magnetism in ultrathin transition metal films. In K. H. J. Buschow, editor, *Handbook of Magnetic Materials*, vol. 7, p. 1. Elsevier Science, 1993.
- [Gry89] D. Gryffroy, R. E. Vandenberghe & E. de Grave. Magnetic hyperfine fields at  $^{61}\text{Ni}$  in some ferrimagnetic spinel compounds. *Hyperfine Interact.* **50** p. 631, 1989.
- [Güt78] P. Gütlich, R. Link & A. Trautwein. *Mössbauer Spectroscopy and Transition Metal Chemistry*. Springer Verlag, 1978.
- [Güt84] P. Gütlich, K. M. Hasselbach, H. Rummel & H. Spiering.  $^{61}\text{Ni}$  Mössbauer spectroscopy of magnetic hyperfine interaction in nickel spinels. *J. Chem. Phys.* **81** p. 1396, 1984.
- [Güt99] P. Gütlich, K.-J. Range, C. Felser, C. Schultz-Münzenberg, W. Tremel, D. Walcher & M. Waldeck. The Valence States of Nickel, Tin and Sulfur and the Ternary Chalcogenide  $\text{Ni}_3\text{Sn}_2\text{S}_2$ . *Angew. Chem. Int. Ed.* **38** p. 2381, 1999.
- [Han99] J. P. Hannon & G. T. Trammell. Coherent  $\gamma$ -ray optics. *Hyperfine Interact.* **123/124** p. 127, 1999.
- [Has91] J. B. Hastings, D. P. Siddons, U. van Bürck, R. Hollatz & U. Bergmann. Mössbauer Spectroscopy Using Synchrotron Radiation. *Phys. Rev. Lett.* **66** p. 770, 1991.
- [Hau97] R. P. Hausinger. Metallocenter assembly in nickel-containing enzymes. *J. Biol. Inorg. Chem.* **2** p. 279, 1997.
- [Ing75] R. Ingalls, F. van der Woude & G. A. Sawatzky. Iron and Nickel. In G. K. Shenoy & F. E. Wagner, editors, *Mössbauer Isomer Shifts*. North Holland, 1975.
- [Iwa44] D. Iwanenko & I. Pomeranchuk. On the Maximal Energy Attainable in a Betatron. *Phys. Rev.* **65** p. 343, 1944.
- [Jan96] N. Jansen, D. Walcher, P. Gütlich, D. Häußinger, B. Hannebauer, R. Kniep, K. Lutar, P. C. Schmidt, D. Sellmann & B. Žemva. Application of  $^{61}\text{Ni}$  Mössbauer spectroscopy to chemical problems. *Il Nuovo Cim. D* **18** p. 231, 1996.
- [Joh95] D. E. Johnson, D. P. Siddons, J. Z. Larase & J. B. Hastings. Observation of nuclear forward scattering from  $^{83}\text{Kr}$  in bulk and monolayer films. *Phys. Rev. B* **51** p. 7909, 1995.
- [Kag78] Y. Kagan, A. M. Afanas'ev & V. G. Kohn. Time delay in the resonance scattering of synchrotron radiation by nuclei in a crystal. *Phys. Lett.* **68A** p. 339, 1978.
- [Kag79] Y. Kagan, A. M. Afanas'ev & V. G. Kohn. On excitation of isomeric nuclear states in a crystal by synchrotron radiation. *J. Phys. C: Solid State Phys.* **12** p. 615, 1979.
- [Kho04] A. L. Kholmetskii, W. Potzel, R. Röhlberger, U. van Bürck & E. Gerdau. Nuclear Resonant Scattering of Synchrotron Radiation as a Method for Distinction between Covariant Ether Theories and Special Relativity. *Hyperfine Interact.* **156/157** p. 9, 2004.
- [Kik94] S. Kikuta. Studies of nuclear resonant scattering at TRISTAN-AR. *Hyperfine Interact.* **90** p. 335, 1994.
- [Kir48] P. Kirkpatrick & A. Baez. Formation of Optical Images by X-Rays. *J. Opt. Soc. Am.* **38** p. 766, 1948.
- [Kis92] S. Kishimoto. High time resolution x-ray measurements with an avalanche photodiode detector. *Rev. Sci. Instrum.* **63** p. 824, 1992.
- [Kis00] S. Kishimoto, Y. Yoda, M. Seto, S. Kitao, R. Haruki, T. Kawauchi, K. Fukutani & T. Okano. Observation of Nuclear Excitation by Electron Transition in  $^{197}\text{Au}$  with Synchrotron X Rays and an Avalanche Photodiode. *Phys. Rev. Lett.* **85** p. 1871, 2000.
- [Kit96] C. Kittel. *Einführung in die Festkörperphysik*. R. Oldenbourg Verlag GmbH München, 11. Auflage, 1996. English original: *Introduction to Solid State Physics*, 6th edition.
- [Kit00] S. Kitao, T. Mitsui & M. Seto. Nuclear Resonant Scattering of Synchrotron Radiation by  $^{121}\text{Sb}$  and  $^{149}\text{Sm}$ . *J. Phys. Soc. Jap.* **69** p. 683, 2000.
- [Kit03] S. Kitao. private communications, 2003.

- [Kle04] T. Klein. private communications, 2004.
- [Koc83] E.-E. Koch, D. E. Eastman & Y. Farge. Synchrotron radiation - a powerful tool in science. In E.-E. Koch, editor, *Handbook of Synchrotron Radiation*, vol. 1A. North-Holland, 1983.
- [Koy96] I. Koyoma, Y. Yoda, X. W. Zhang, M. Ando & S. Kikuta. Nuclear Resonant Excitation of  $^{161}\text{Dy}$  and  $^{151}\text{Eu}$  by Synchrotron Radiation. *Jpn. J. Appl. Phys.* **35** p. 6297, 1996.
- [KPNR] Part of the program package CONUSS, see [Stu94].
- [Kri76] G. Krill, M. F. Lapierre, F. Gautier, C. Robert, G. Czjzek, J. Fink & H. Schmidt. Electronic and magnetic properties of the pyrite-structure compound  $\text{NiS}_2$ : Influence of vacancies and copper impurities. *J. Phys. C: Solid State Phys.* **9** p. 761, 1976.
- [Kri83] S. Krinsky, M. L. Perlman & R. E. Watson. Characteristics of synchrotron radiation and of its sources. In E.-E. Koch, editor, *Handbook of Synchrotron Radiation*, vol. 1A. North-Holland, 1983.
- [Kse02] V. Ksenofontov, S. Reiman, D. Walcher, Y. Garcia, N. Doroshenko & P. Gütlich. Stoichiometry of  $\text{LiNiO}_2$  Studied by Mössbauer Spectroscopy. *Hyperfine Interact.* **139/140** p. 107, 2002.
- [Lam39] W. E. Lamb. Capture of Neutrons by Atoms in a Crystal. *Phys. Rev.* **55** p. 190, 1939.
- [Lan88] J. R. Lancaster Jr., editor. *The Bioinorganic Chemistry of Nickel*. Wiley, 1988.
- [Lax51] M. Lax. Multiple Scattering of Waves. *Rev. Mod. Phys.* **23** p. 287, 1951.
- [Len99] B. Lengeler, C. Schroer, J. Tümmler, B. Benner, M. Richwin, A. Snigirev, I. Snigireva & M. Drakopoulos. Imaging by parabolic refractive lenses in the hard X-ray range. *J. Synchr. Rad.* **6** p. 1153, 1999.
- [Leo94] W. R. Leo. *Techniques for Nuclear and Particle Physics Experiments*. Springer-Verlag, 1994.
- [Leu96] O. Leupold, J. Pollmann, E. Gerdau, H. D. Rüter, G. Faigel, M. Tegze, G. Bortel, R. Ruffer, A. I. Chumakov & A. Q. R. Baron. Nuclear resonance scattering of synchrotron radiation at the 21.5 keV resonance of  $^{151}\text{Eu}$ . *Europhys. Lett.* **35** p. 671, 1996.
- [Leu97] O. Leupold, E. Gerdau, M. Gerken & H. D. Rüter. Experiment number HE 286. *ESRF User Reports*, 1997. [http://ftp.esrf.fr/pub/UserReports/9321\\_A.pdf](http://ftp.esrf.fr/pub/UserReports/9321_A.pdf).
- [Leu99] O. Leupold & H. Winkler. Relaxation experiments with synchrotron radiation. *Hyperfine Interact.* **123/124** p. 571, 1999.
- [Lev89] J. R. Levinne, J. B. Cohen, Y. W. Chung & P. Georgopoulos. Grazing-Incidence Small-Angle X-ray Scattering: New Tool for Studying Thin Film Growth. *J. Acta. Cryst.* **22** p. 528, 1989.
- [Lip60] H. J. Lipkin. Some Simple Features of the Mössbauer Effect. *Ann. Physics* **9** p. 332, 1960.
- [Lov68] J. Love, G. Czjzek, J. J. Spijkerman & D. K. Snediker. Mössbauer experiments with  $^{61}\text{Ni}$ . In E. Matthias & D. A. Shirley, editors, *Hyperfine Structure and Nuclear Radiations*, p. 125. North-Holland, Amsterdam, 1968.
- [Lov71] J. C. Love, F. E. Obenshain & G. Czjzek. Mössbauer Spectroscopy with  $^{61}\text{Ni}$  in Nickel-Transition-Metal Alloys and Nickel Compounds. *Phys. Rev. B* **3** p. 2827, 1971.
- [Łuk85] M. Łukasiak, T. Zemčik, J. Suwalski & J. Piekoszewski. Study of long range order parameter in  $\text{Ni}_3\text{Fe}$  by means of  $^{61}\text{Ni}$  and  $^{57}\text{Fe}$  Mössbauer spectroscopy. *Acta Phys. Polonica* **A68** p. 79, 1985.
- [Mar88] G. Margaritondo. *Introduction to synchrotron radiation*. Oxford University Press, 1988.
- [Mar01] G. Martínez-Pinedo, P. Schwerdtfeger, E. Caurier, K. Langanke, W. Nazarewicz & T. Söhnel. Nuclear Quadrupole Moment of  $^{57}\text{Fe}$  from Microscopic Nuclear and Atomic Calculations. *Phys. Rev. Lett.* **87** p. 062701, 2001.
- [Mas98] V. F. Masterov, F. S. Nasredinov, N. P. Seregin & P. P. Seregin. Atomic Charge States in  $\text{Tl}_2\text{Ba}_2\text{Ca}_{n-1}\text{Cu}_n\text{O}_{2n+4}$  as Determined by  $^{61}\text{Cu}(^{61}\text{Ni})$ ,  $^{67}\text{Cu}(^{67}\text{Zn})$   $^{133}\text{Ba}(^{133}\text{Cs})$  Emission Mössbauer Spectroscopy. *phys. stat. sol. (b)* **207** p. 223, 1998.

- [May94] T. Mayer-Kuckuk. *Kernphysik*. Teubner Stuttgart, 6. Auflage, 1994.
- [Met90] J. Metge, R. Ruffer & E. Gerdau. A  $\gamma$ -ray detector with good time resolution and high signal-to-noise ratio. *Nucl. Instr. Meth. Phys. Res. A* **292** p. 187, 1990.
- [Mey78] R. A. Meyer, A. L. Prindle, W. A. Myers, P. K. Hopke, D. Dieterly & J. E. Koops. Multiparticle configurations in the odd-neutron nuclei  $^{61}\text{Ni}$  and  $^{67}\text{Zn}$  populated by decay of  $^{61}\text{Cu}$ ,  $^{67}\text{Cu}$  and  $^{67}\text{Ga}$ . *Phys. Rev. C* **17** p. 1822, 1978.
- [Moh00] P. J. Mohr & B. N. Taylor. CODATA recommended values of the fundamental physical constants: 1998. *Rev. Mod. Phys.* **72** p. 351, 2000.
- [Möb58] R. L. Mößbauer. Kernresonanzfluoreszenz von Gammastrahlung in  $\text{Ir}^{191}$ . *Z. Phys.* **151** p. 124, 1958.
- [Möb59] R. L. Mößbauer. Kernresonanzabsorption von  $\gamma$ -Strahlung in  $\text{Ir}^{191}$ . *Z. Naturforsch.* **14 a** p. 211, 1959.
- [Möb67] R. L. Mößbauer. Recoilless absorption of gamma rays and studies of nuclear hyperfine interactions in solids. In A. J. Freeman & R. B. Frankel, editors, *Hyperfine Interactions*. Academic Press, New York, 1967.
- [Mot51] H. Motz. Applications of the Radiation from Fast Electron Beams. *J. Appl. Phys.* **22** p. 527, 1951.
- [Mül03] G. A. Müller. *Ion-beam induced changes of magnetic and structural properties in thin Fe films*. Dissertation, Universität zu Göttingen, 2003.
- [Nas93] F. S. Nasredinov, P. P. Seregin, V. F. Masterov & C. S. Saidov. Combined magnetic and electric quadrupole hyperfine interaction at the copper sites in high-temperature superconductor lattices investigated by  $^{61}\text{Cu}$ ( $^{61}\text{Ni}$ ) emission Mössbauer spectroscopy. *Phys. Solid State* **35** p. 1088, 1993.
- [NDS] *Nuclear Data Sheets*, J. K. Tuli, editor, Academic Press.
- [Nie98] L. Niesen, A. Mugarza, M. F. Rosu, R. Coehoorn, R. M. Jungblut, F. Roozeboom, A. Q. R. Baron, A. I. Chumakov & R. Ruffer. Magnetic behaviour of probe layers of  $^{57}\text{Fe}$  in thin Fe films observed by means of nuclear resonant scattering of synchrotron radiation. *Phys. Rev. B* **58** p. 8590, 1998.
- [Obe61] F. E. Obenshain & H. F. Wegener. Mössbauer Effect with  $^{61}\text{Ni}$ . *Phys. Rev.* **121** p. 1344, 1961.
- [Obe73] F. E. Obenshain. Nuclear gamma resonance with  $^{61}\text{Ni}$ . In Stevens and Stevens [Ste73], p. 13.
- [Obe76] F. E. Obenshain, J. C. Williams & L. W. Houk. Hyperfine interactions at  $^{61}\text{Ni}$  in ionic nickel compounds. *J. Inorg. Nucl. Chem.* **38** p. 19, 1976.
- [Oka95] T. Okada, Y. Noro, Y. Kobayashi, H. Kitazawa & F. Ambe. Huge hyperfine magnetic field of  $^{61}\text{Ni}$  in spinel chromites  $\text{Cu}_{0.9}\text{Ni}_{0.1}\text{Cr}_2\text{O}_4$  and  $\text{Co}_{0.9}\text{Ni}_{0.1}\text{Cr}_2\text{O}_4$ . *Phys. Lett. A* **209** p. 241, 1995.
- [Për87] G. A. Përez Alcazar & E. Galvão da Silva. Mössbauer effect study of magnetic properties of  $\text{Fe}_{1-q}\text{Al}_q$ ,  $0 < q \leq 0.5$ , alloys in the disordered phase. *J. Phys. F: Met. Phys.* **17** p. 2323, 1987.
- [PKP] <http://www.pkp.de>. PKP Prozessmesstechnik GmbH.
- [Por82] G. Porod. General Theory. In O. Glatter & O. Kratky, editors, *Small Angle X-ray Scattering*, p. 17. Academic Press, 1982.
- [Qua02] K. Quast. *Der experimentelle Nachweis des nuklearen Leuchtturmeffektes und erste Anwendungen*. Dissertation, Universität Rostock, 2002.
- [Rao93] D. Raoux. Introduction to synchrotron radiation and to the physics of storage rings. In Baruchel et al. [Bar93].
- [Rie77] P. C. Riedi. Temperature dependence of the magnetization of nickel using  $^{61}\text{Ni}$  NMR. *Phys. Rev. B* **15** p. 5197, 1977.

- [Röh94] R. Röhlsberger, O. Leupold, J. Metge, H. D. Rüter, W. Sturhahn & E. Gerdau. Nuclear forward scattering of synchrotron radiation from unmagnetized  $\alpha$ - $^{57}\text{Fe}$ . *Hyperfine Interact.* **92** p. 1107, 1994.
- [Röh97] R. Röhlsberger, E. Gerdau, R. Ruffer, W. Sturhahn, T. S. Toellner, A. I. Chumakov & E. E. Alp. X-ray optics for  $\mu\text{eV}$ -resolved spectroscopy. *Nucl. Instr. Meth. Phys. Res. A* **394** p. 251, 1997.
- [Röh98] R. Röhlsberger. Spektroskopie im  $\mu\text{eV}$ -Bereich: Instrumentierung, Beispiele. In E. Burkel, editor, *Erforschung der Dynamik kondensierter Materie mit Synchrotronstrahlung*. WE Heraeus - Ferienkurs Manuskripte, 1998.
- [Röh99a] R. Röhlsberger. Nuclear resonant scattering of synchrotron radiation from thin films. *Hyperfine Interact.* **123/124** p. 455, 1999.
- [Röh99b] R. Röhlsberger. Theory of X-ray grazing incidence reflection in the presence of nuclear resonance excitation. *Hyperfine Interact.* **123/124** p. 301, 1999.
- [Röh99c] R. Röhlsberger, E. E. Alp, E. Gerdau, O. Leupold, K. W. Quast, R. Ruffer, W. Sturhahn, T. Toellner & E. Burkel. Techniques for inelastic X-ray spectroscopy with  $\mu\text{eV}$ -resolution. *Physica B* **263-264** p. 574, 1999.
- [Röh00a] R. Röhlsberger. Resonant X-Ray scattering from a rotating medium: The Nuclear Lighthouse Effect. *Hyperfine Interact.* **126** p. 425, 2000.
- [Röh00b] R. Röhlsberger. Techniques for inelastic X-ray scattering with  $\mu\text{eV}$ -resolution. *Hyperfine Interact.* **125** p. 69, 2000.
- [Röh00c] R. Röhlsberger, T. S. Toellner, W. Sturhahn, K. W. Quast, E. E. Alp, A. Bernhard, E. Burkel, O. Leupold & E. Gerdau. Coherent Resonant X-Ray Scattering from a Rotating Medium. *Phys. Rev. Lett.* **84** p. 1007, 2000.
- [Röh01a] R. Röhlsberger. Vibrational spectroscopy of thin films and nanostructures by inelastic nuclear resonant scattering. *J. Phys.: Cond. Mat.* **13** p. 7659, 2001.
- [Röh01b] R. Röhlsberger, K. W. Quast, T. S. Toellner, P. L. Lee, W. Sturhahn, E. E. Alp & E. Burkel. Imaging the temporal evolution of nuclear resonant x-ray scattering. *Appl. Phys. Lett.* **78** p. 2970, 2001.
- [Röh01c] R. Röhlsberger, K. W. Quast, T. S. Toellner, P. L. Lee, W. Sturhahn, E. E. Alp & E. Burkel. Observation of the 22.5-keV Resonance in  $^{149}\text{Sm}$  by the Nuclear Lighthouse Effect. *Phys. Rev. Lett.* **87** p. 047601, 2001.
- [Röh01d] R. Röhlsberger, T. S. Toellner, K. W. Quast, W. Sturhahn, E. E. Alp & E. Burkel. The nuclear lighthouse effect: a new tool for high-resolution X-ray spectroscopy. *Nucl. Instr. Meth. Phys. Res. A* **467** p. 1473, 2001.
- [Röh02a] R. Röhlsberger. Imaging the Magnetic Structure of Thin Films and Nanoparticles. *Hyperfine Interact.* **144/145** p. 33, 2002.
- [Röh02b] R. Röhlsberger, H. Thomas, K. Schlage, E. Burkel, O. Leupold & R. Ruffer. Imaging the Magnetic Spin Structure of Exchange-Coupled Thin Films. *Phys. Rev. Lett.* **89** p. 237201, 2002.
- [Röh03] R. Röhlsberger, J. Bansmann, V. Senz, K. L. Jonas, A. Bettac, K. H. Meiwes-Broer & O. Leupold. Nanoscale magnetism probed by nuclear resonant scattering of synchrotron radiation. *Phys. Rev. B* **67** p. 245412, 2003.
- [Röh04a] R. Röhlsberger. *Nuclear Condensed Matter Physics with Synchrotron Radiation*. Springer, 2004.
- [Röh04b] R. Röhlsberger, T. Klein, K. Schlage, O. Leupold & R. Ruffer. Coherent X-ray scattering from ultrathin probe layers. *Phys. Rev. B* **69** p. 235412, 2004.
- [Roo75] S. Roodbergen, H. Visser, W. Molendijk, H. S. Bedet & H. Verheul. Transition Probabilities in the Ni-Zn Region. *Z. Physik A* **275** p. 45, 1975.

- [Rub74] S. L. Ruby. Mössbauer experiments without conventional sources. *J. Physique* **35** p. C6–209, 1974.
- [Rum82] H. Rummel, R. L. Cohen, P. Gütlich & K. W. West.  $^{61}\text{Ni}$  Mössbauer measurements of nickel microprecipitates produced in  $\text{LaNi}_5$  by cyclic hydrogen absorption and desorption. *Appl. Phys. Lett.* **40** p. 477, 1982.
- [Sam02] A. Samoson. Extended Magic-Angle Spinning. In D. M. Grant & R. K. Harris, editors, *Encyclopedia of Nuclear Magnetic Resonance*, vol. 9, p. 59. John Wiley & Sons, 2002.
- [San98] M. Sanchez del Rio & R. J. Dejus. XOP: Recent Developments. *SPIE proc.* **3448** p. 340, 1998.
- [Sch49] J. Schwinger. On the Classical Radiation of Accelerated Electrons. *Phys. Rev.* **75** p. 1912, 1949.
- [Sch73] K. P. Schmidt, R. Coussement, G. Langouche & J. P. Lafaut. A Mössbauer parity experiment on  $^{61}\text{Ni}$  and the determination of the  $^{61}\text{Co}$  ground state spin. *Nucl. Phys.* **A204** p. 279, 1973.
- [Sch91] P. Schmidt. Small-Angle Scattering Studies of Disordered, Porous and Fractal Systems. *J. Appl. Cryst.* **24** p. 414, 1991.
- [Sch92] G. Schatz & A. Weidinger. *Nukleare Festkörperphysik*. Teubner Stuttgart, 2. Auflage, 1992.
- [Ser02] I. Sergueev, H. Franz, T. Asthalter, W. Petry, U. van Bürck & G. V. Smirnov. Structural relaxation in a viscous liquid studied by quasielastic nuclear forward scattering. *Phys. Rev. B* **66** p. 184210, 2002.
- [Ser03] I. Sergueev, U. van Bürck, A. I. Chumakov, T. Asthalter, G. V. Smirnov, H. Franz, R. Rüffer & W. Petry. Rotational and Translational Glass Dynamics Studied by Nuclear Resonant Scattering. *ESRF Highlights* p. 12, 2003.
- [Ser04] I. Sergueev. *Nuclear Resonant Scattering for the Study of Dynamics of Viscous Liquids and Glasses*. Dissertation, Technische Universität München, 2004.
- [Ser05] I. Sergueev *et al.* Synchrotron radiation based perturbed angular correlation applied to investigate rotational dynamics in soft matter, 2005. to be published.
- [Set95] M. Seto, Y. Yoda, S. Kikuta, X. W. Zhang & M. Ando. Observation of Nuclear Resonant Scattering Accompanied by Phonon Excitation Using Synchrotron Radiation. *Phys. Rev. Lett.* **74** p. 3828, 1995.
- [Set00] M. Seto, S. Kitao, Y. Kobayashi, R. Haruki, T. Mitsui, Y. Yoda, X. W. Zhang & Y. Maeda. Nuclear Resonant Scattering of Synchrotron Radiation by  $^{40}\text{K}$ . *Phys. Rev. Lett.* **84** p. 566, 2000.
- [Set02] M. Seto, S. Kitao, Y. Kobayashi, R. Haruki, T. Mitsui, Y. Yoda, X. W. Zhang, S. Kishimoto & Y. Maeda. Nuclear Resonant Inelastic and Forward Scattering of Synchrotron Radiation by  $^{40}\text{K}$ . *Hyperfine Interact.* **141/142** p. 99, 2002.
- [Set03] M. Seto, S. Kitao, Y. Kobayashi, R. Haruki, Y. Yoda, T. Mitsui & T. Ishikawa. Site-Specific Phonon Density of States Discerned using Electronic States. *Phys. Rev. Lett.* **91** p. 185505, 2003.
- [Sey65] D. Seyboth, F. E. Obenshain & G. Czjzek. Observation of recoilless emission of  $^{61}\text{Ni}$  gamma rays following coulomb excitation. *Phys. Rev. B* **14** p. 954, 1965.
- [Sha80] M. Shaham, J. Barak, U. El-Hanany & J. W. W. Warren. NMR study of the 3d ferromagnetic metals: Critical region and paramagnetic phase. *Phys. Rev. B* **22** p. 5400, 1980.
- [Shi69] E. N. Shipley, R. E. Holland & F. J. Lynch. Lifetimes and Excited States of  $\text{V}^{51}$ ,  $\text{Ni}^{61}$ ,  $\text{Ga}^{69}$ ,  $\text{As}^{75}$ ,  $\text{Br}^{79}$ ,  $\text{Rb}^{85}$ , and  $\text{Sb}^{123}$ . *Phys. Rev.* **182** p. 1165, 1969.
- [Shv99] Y. V. Shvyd'ko. Nuclear resonant forward scattering of x rays: Time and space picture. *Phys. Rev. B* **59** p. 9132, 1999.
- [Shv00] Y. Shvyd'ko, M. Lerche, J. Jäschke, M. Lucht, E. Gerdau, M. Gerken, H. D. Rüter, H.-C. Wille, P. Becker, E. E. Alp, W. Sturhahn, J. Sutter & T. S. Toellner.  $\gamma$ -Ray Wavelength Standard for Atomic Scales. *Phys. Rev. Lett.* **85** p. 495, 2000.



- [Shv01] Y. V. Shvyd'ko, M. Gerken, H. Franz, M. Lucht & E. Gerdau. Nuclear resonant scattering of synchrotron radiation from  $^{161}\text{Dy}$  at 25.61 keV. *Europhys. Lett.* **56** p. 309, 2001. Preliminary results in HASYLAB Annual Report 1999, p. 573, by the same authors.
- [Sid99] D. P. Siddons, U. Bergmann & J. B. Hastings. Polarization effects in resonant nuclear scattering. *Hyperfine Interact.* **123/124** p. 681, 1999.
- [SLAC] <http://www-ssrl.slac.stanford.edu/absorb.html>. Stanford Linear Accelerator Center. Fortran 77 program *absorb*. Calculations based on Cromer and Liberman and McMasters. The values cited in chapter 3 are for natural nickel and iron, obtained using  $\sigma_{el} = A N_A^{-1} l_{abs}^{-1} \rho^{-1}$ .
- [Smi99] G. V. Smirnov. General properties of nuclear resonant scattering. *Hyperfine Interact.* **123/124** p. 31, 1999.
- [Sni96] A. Snigirev, V. Kohn, I. Snigireva & B. Lengeler. A compound refractive lens for focusing high-energy X-rays. *Nature* **384** p. 49, 1996.
- [Sos81] M. Sostarich, S. Dey, P. Deppe, M. Rosenberg, G. Czjzek, V. Oestreich, H. Schmidt & F. E. Luborsky. Magnetic and Mössbauer investigation of amorphous  $(\text{Fe}_x\text{Ni}_{1-x})_{80}\text{B}_{20}$  alloys. *IEEE Trans. Magnetics* **MAG-17** p. 2612, 1981.
- [Spa80] C. J. Sparks, B. S. Borie & J. B. Hastings. X-ray monochromator geometry for Focusing Synchrotron Radiation above 10 keV. *Nucl. Instr. Meth.* **172** p. 237, 1980.
- [Spi68] J. J. Spijkerman. Mössbauer Spectroscopy of  $^{61}\text{Ni}$ . In *The Mössbauer effect (Symposium of the Faraday Society No.1)*, p. 134. Butterworth, London, 1968.
- [Spi74] E. Spiller & A. Segmüller. Propagation of x rays in waveguides. *Appl. Phys. Lett.* **24** p. 60, 1974.
- [Spr-8] <http://www.spring8.or.jp>. Spring-8, Japan Synchrotron Radiation Research Institute.
- [Sta87] Z. M. Stadnik, P. Griesbach, G. Dehe, P. Gütlich, T. Kohara & G. Stroink.  $^{61}\text{Ni}$  Mössbauer study of the hyperfine magnetic field near the Ni surface. *Phys. Rev. B* **35** p. 6588, 1987.
- [Sta88] Z. M. Stadnik, P. Griesbach, P. Gütlich & G. Stroink.  $^{61}\text{Ni}$  Mössbauer study of the surface hyperfine field in nickel. *Hyperfine Interact.* **41** p. 705, 1988.
- [Sta89] Z. M. Stadnik & G. Stroink. Local magnetic moments in crystalline and amorphous alloys. *Hyperfine Interact.* **47** p. 275, 1989.
- [Sta92] F. Stanglmeier, B. Lengeler, W. Weber, H. Göbel & M. Schuster. Determination of the Dispersive Correction  $f'(E)$  to the Atomic Form Factor from X-ray Reflection. *Acta Cryst.* **A48** p. 626, 1992.
- [Ste73] J. Stevens & V. Stevens, editors. *Mössbauer Effect Data Index 1972*. Plenum Press New York, 1973.
- [Ste75] R. M. Steffen & K. Alder. Angular Distribution and Correlation of Gamma Rays (chapter 12); Extranuclear Perturbations of Angular Distributions and Correlations (chapter 13). In W. D. Hamilton, editor, *Nuclear Spectroscopy*, p. 505–582; 583–643. North-Holland, 1975.
- [Str63] R. L. Streever & L. H. Bennett. Line Shapes, Saturation Behavior, and Temperature Studies in the Nuclear Resonance of Nickel. *Phys. Rev.* **131** p. 2000, 1963.
- [Stü63] D. Stünkel. Die Magnetisierung sehr dünner Eisenschichten. *Z. Physik* **176** p. 207, 1963.
- [Stu91] W. Sturhahn, E. Gerdau, R. Hollatz, R. Rüffer, H. D. Rüter & W. Tolksdorf. Nuclear Bragg Diffraction of Synchrotron Radiation at the 8.41 keV Resonance of Thulium. *Europhys. Lett.* **14** p. 821, 1991.
- [Stu94] W. Sturhahn & E. Gerdau. Evaluation of time-differential measurements of nuclear-resonance scattering of x rays. *Phys. Rev. B* **49** p. 9285, 1994. That is the basis of the program CONUSS.
- [Stu95] W. Sturhahn, T. S. Toellner, E. E. Alp, X. Zhang, M. Ando, Y. Yoda, S. Kikuta, M. Seto, C. W. Kimball & B. Dabrowski. Phonon Density of States Measured by Inelastic Nuclear Resonant Scattering. *Phys. Rev. Lett.* **74** p. 3832, 1995.

- [Stu04] W. Sturhahn. Nuclear resonant spectroscopy. *J. Phys.: Condens. Matter* **16** p. S497, 2004.
- [Tan72] J. E. Tansil, F. E. Obenshain & G. Czjzek.  $^{61}\text{Ni}$  Mössbauer effect in Ni-Pd Alloys. *Phys. Rev. B* **6** p. 2796, 1972.
- [Toe00] T. S. Toellner. Monochromatization of synchrotron radiation for nuclear resonant scattering experiments. *Hyperfine Interact.* **125** p. 3, 2000.
- [Tom56] D. H. Tomboulia & P. L. Hartman. Spectral and Angular Distribution of Ultraviolet Radiation from the 300-MeV Cornell Synchrotron. *Phys. Rev.* **102** p. 1423, 1956.
- [Tom77] K. Tomala, G. Czjzek, J. Fink & H. Schmidt. Hyperfine interactions in intermetallic compounds between Gd and 3d transition metals. *Solid State Commun.* **24** p. 857, 1977.
- [Tra68] J. C. Travis & J. J. Spijkerman. Mössbauer Spectroscopy with Ni $^{61}$ . In I. J. Gruwerman, editor, *Mössbauer Effect Methodology*, vol. 4. Plenum Press, 1968.
- [Tra78] G. T. Trammel & J. P. Hannon. Quantum beats from nuclei excited by synchrotron pulses. *Phys. Rev. B* **18** p. 165, 1978.
- [Var88] D. A. Varshalovich, A. N. Moskalev & V. K. Khersonskii. *Quantum Theory of Angular Momentum*. World Scientific Singapore, 1988.
- [Vog99] G. Vogl & B. Sepiol. Diffusion in crystalline materials. *Hyperfine Interact.* **123/124** p. 595, 1999.
- [Wal94] J. C. Walker. Mössbauer spectroscopy as a Means of Characterizing Surfaces, Thin Films, and Superlattices. In Bland and Heinrich [Bla94]. Vol. II, Chapter 5.
- [Weg61] H. H. F. Wegener & F. E. Obenshain. Mössbauer Effect for  $^{61}\text{Ni}$  with Applied Magnetic Fields. *Z. Physik* **163** p. 17, 1961.
- [Weg66] H. Wegener. *Der Mössbauer-Effekt und seine Anwendungen in Physik und Chemie*. Bibliographisches Institut AG Mannheim, 2. Auflage, 1966.
- [Wil93] C. E. Williams. Small Angle Scattering from solids and solutions. In Baruchel et al. [Bar93].
- [Wil02] H.-C. Wille, M. Gerken, E. Gerdau, Y. V. Shvyd'ko, H. D. Rüter & H. Franz. Excitation of the nuclear resonance in  $^{61}\text{Ni}$  at 67.4 keV by Synchrotron Radiation. *Hyperfine Interact.* **C5** p. 1, 2002.
- [Wil03] H.-C. Wille. *Der anomale Effekt der Isotopenmasse auf den Gitterparameter in Silizium und Germanium*. Dissertation, Universität Hamburg, 2003.
- [Wil04a] H.-C. Wille. ESRF ID18 group seminar. *Applications of Bragg Backscattering*, 2004.
- [Wil04b] H.-C. Wille. private communications, 2004.
- [Win83] H. Winkler. *Stochastic Models for Dynamic Hyperfine Interactions - Applications to Perturbed Angular Correlation and Mössbauer spectroscopy*. Habilitationsschrift, Hamburg, 1983.
- [Yod02] Y. Yoda, S. Kishimoto, X. W. Zhang, M. Seto & S. Kikuta. Nuclear Excitation of  $^{127}\text{I}$  using Synchrotron Radiation. *Hyperfine Interact.* **C5** p. 17, 2002.
- [Zab04] H. Zabel. Thin film magnetism. *Lectures, Ruhr-Universität Bochum*, 2004. [www.ep4.rub.de/fk/people/zabel/lectures-Vorlesungen/thin\\_film\\_magnetism.htm](http://www.ep4.rub.de/fk/people/zabel/lectures-Vorlesungen/thin_film_magnetism.htm).
- [Zeiss] Zeiss Oberkochen, Germany. Optik-Planfertigung und Sonderaufträge. Extension from DIN 4762 and DIN 4768 to surfaces, the integration going over the surface and not a direction:  

$$S_q = \sqrt{\frac{1}{x_m y_m} \int_0^{x_m} \int_0^{y_m} z^2(x, y) dx dy}$$
- [Zha02] J. Y. Zhao, T. S. Toellner, M. Y. Hu, W. Sturhahn, E. E. Alp, G. Y. Shen & H. K. Mao. High-energy-resolution monochromator for  $^{83}\text{Kr}$  nuclear resonant scattering. *Rev. Sci. Instrum.* **73** p. 1608, 2002.

# Acknowledgements

This thesis was not always a huge fun. Exploding rotors, wrongly mounted stators, huge background radiation and many other things threatened to make me sometimes sad and beaten. But there was warmth and happiness when I came back from work, and a huge encouragement that I did not get from anywhere else. Thank you Claire for this and the support when I wrote the thesis and days kept passing. I also thank my parents and my brother in this regard and for making me feel to be part of the family besides the geographic distance between us since seven years.

Concerning the almost five years at the laboratory, I like to thank the following persons:

- Special sincere thanks go to Olaf Leupold, who was always there: at the preparations and during the measurements, while thinking about the problems, or to calculate any kinds of estimations. Whatever your question, he will take the time to explain you; and of course, he will know the answer! Also, he was always happy to share a beer at the end of a late night at work, which was very much appreciated.
- Many thanks to Rudolf Ruffer. He proposed me the subject, especially for exploring the high energy region of the beamline. I was very happy for the fact that I got one week of 16 bunch mode of valuable in-house research time. I still don't know if I made a record as the PhD student who has spent the biggest amount of money in his thesis, but I definitely want to say that I am happy we could reach consent on most items that I wanted to buy.
- Ralf Röhlsberger, the inventor of the Nuclear Lighthouse Effect, was my real, (in?)official supervisor. Without his invention, I would not have had the chance to overcome all the problems and would miss this particular experience. Most enjoyable were the bicycle races at DESY and the ESRF, to get the fastest to the canteen. Of course, we rushed as much when driving back to the experiment, believe me!
- Without the agreement of Eberhard Burkel to take the part as responsible Professor at the University of Rostock, this thesis would have never started. Thank you very much of giving me that opportunity. Not only you had to care of all the administration, but you had to read all this thesis. I hope you don't regret. Thanks again.
- Klaus Quast genius tips and hints on all kinds of technical problems concerning the lighthouse tower assembly were of greatest importance. He even came especially to Grenoble to discuss with me and Keith or Santiago, which steps to undertake to improve the performance of the setup. Thank you for this support.
- Hans-Christian Wille helped me a lot in reading all the first versions of all my chapters and Alessandro in reading some of them. This must have been very annoying, but you did it without complaining and humour, thanks! I am further indebted to Gerhard Wortmann and Sunil Sinha who accepted to read the final version as external referees.

- Uwe van Bürck together with Ralf managed to employ me an extra 6 month after the three years paid by the ESRF. This was very helpful for the success of this thesis. Further, his openness and his huge general knowledge made it very pleasant to discuss with him.
- Thanks to Werner Schmid and Terrence Manning for their perfect support concerning any kind of urgent machining or welding. Mostly, the pieces were then machined by Keith Baldock, Benoit Picut and Dominique Rolhion, whom I thank also for kindly according me the use of his workshop. I did not destroy too many tools, I hope!
- Aleksandr Chumakov knows everything about our instrumentation at ID18. Thanks a lot for helping me whenever I did not know enough about the monochromator or the CRLs or whatever. I also enjoyed very much when we had lunch and discussed other things than the beamline or skiing, although skiing is a very interesting topic at lunchtime.
- Keith Martel and Santiago Becerril helped me a lot in designing the lighthouse tower, as well as Jean-Philippe concerning the in-vacuum slit chambers. I am very happy also about the support from Ricardo Steinmann when I started to modify the Bruker stator block and discussed about many details concerning the cooling of the sample.
- Torsten Klein managed to prepare thin iron layers on my polished rotors, some of them in world record time. Thanks a lot for that. It's a pity that first, the rotor top surface was so badly tilted, but you even gave it a second chance again, after Zeiss repolished. Torsten also managed all delivery problems between Grenoble and Rostock, especially when the final thesis version did not arrive a friday evening as expected.
- Thank you, Bryan Doyle, for the friendly reception when I started in the Nuclear Resonance Group. It's a pity that you are so far away from the French Alps, we could have been having some other epics on a ski tour! And thanks for taking care of all my beginners computer problems and my many English mistakes, although your South-African English is not too good neither! Just kidding!
- I am very grateful to Cornelius Strohm and Christophe Thirion, with whom I shared so many days in the mountains, evenings with good music and drinks, and many discussions about the future, politics, and physics. In particular, your hints were very valuable and motivated me during the pursuit of my thesis.
- Thanks again to Alessandro, the master of fits, for showing me some basics of CONUSS and thanks Ilia Sergueev, for all help with any kind of mathematical problem and the use of mathematica. Thanks to Shinji Kitao for keeping an eye on the spinner control during cooled experiments. All three of you, together with Ernst Schreier and Svetoslav Stankov, Hans-Christian, Cornelius, Than Hai Deschaux-Beaume, Andrea Monaco and Ulrich Ponkratz made life very pleasant at work.
- Merci à Laurence Aeschelmann pour faire passer mes commandes toujours "super-urgentes" au plus vite, et pour toutes tentatives pour améliorer mon français. Très agréable aussi la sortie de ski quand il y avait la visite du grand chef à la ligne ;-)
- Jean-Marie Rigal took quite an effort to solder me a tiny in-vacuum APD with amplifier and Holger Witsch to implementation my lighthouse controller into spec. Thanks a lot.

And of course a lot of thanks to the continental drifts that built the marvellous Alps around Grenoble and the thick clouds of snow that come here in winter time. Nothing helps more to get over problems with exploding rotors than skiing over virgin slopes full of powder. There are

the remote places where I can relax and get back to my forces. That's hopefully where I am right now!



# Eidesstattliche Erklärung

Hiermit versichere ich, daß ich die vorliegende Arbeit selbständig angefertigt und ohne fremde Hilfe verfaßt habe, keine außer den von mir angegebenen Hilfsmitteln und Quellen dazu verwendet habe und die den benutzten Werken inhaltlich und wörtlich entnommenen Stellen als solche kenntlich gemacht habe.

Thomas Roth

Grenoble, der 21.4.2005





# Curriculum Vitæ

Dipl.-Phys. Thomas Roth  
8 rue Marceau  
38000 Grenoble  
France

- October 2000 - April 2005 Ph.D.-thesis at the University Rostock and in the Nuclear Resonance Group of the European Synchrotron Radiation Facility. “Development and Applications of the Nuclear Lighthouse Effect at high energies and at grazing incidence”
- January 2000 - September 2000 Investigations of the Magneto-Electric Linear birefringence at the Grenoble High Magnetic Field Laboratory (Phys. Rev. Lett. 88, p. 063001, 2002)
- June 2000 Reception of the “Diplom Physiker” degree at the Technische Universität Darmstadt, very good
- November 1998 - January 2000 “Diplomarbeit” at the Grenoble High Magnetic Field Laboratory, joint laboratory of the Centre National de la Recherche Scientifique and the Max-Planck-Institut für Festkörperforschung. Experimental verification of the Jones birefringence induced in liquids (Phys. Rev. Lett. 85, p. 4478, 2000)
- Spring 1998 studies at Joint Universities Accelerator School, Geneva
- Summer 1997 trainee period at the European Synchrotron Radiation Facility, Grenoble. “Focusing of synchrotron radiation and undulator calculations”
- September 1996 - July 1997 exchange student at the Ecole Nationale Supérieure de Grenoble, part of the Institut National Polytechnique de Grenoble, France
- October 1993 start of studies in physics, Technische Universität Darmstadt
- June 1992 Abitur at the Viktoriaschule Darmstadt, final mark 1.2
- Prizes Best poster prize at ESRF User meeting 2004, Grenoble  
Best poster prize at Mössbauer conference May 2002, Seeheim  
Best oral presentation at Bianisotropics conference September 2000, Lisbon

